



# Magneto-spectroscopy of Dirac matter : graphene and topological insulators

Thanyanan Phuphachong

## ► To cite this version:

Thanyanan Phuphachong. Magneto-spectroscopy of Dirac matter : graphene and topological insulators. Materials Science [cond-mat.mtrl-sci]. Université Pierre et Marie Curie, 2017. English. NNT : . tel-01763417

**HAL Id: tel-01763417**

**<https://theses.hal.science/tel-01763417>**

Submitted on 11 Apr 2018

**HAL** is a multi-disciplinary open access archive for the deposit and dissemination of scientific research documents, whether they are published or not. The documents may come from teaching and research institutions in France or abroad, or from public or private research centers.

L'archive ouverte pluridisciplinaire **HAL**, est destinée au dépôt et à la diffusion de documents scientifiques de niveau recherche, publiés ou non, émanant des établissements d'enseignement et de recherche français ou étrangers, des laboratoires publics ou privés.

**THESE DE DOCTORAT**  
**DE L'UNIVERSITE PIERRE ET MARIE CURIE**

**Spécialité : Physique de la matière condensée**  
**Ecole doctorale 397 Physique et Chimie des Matériaux**

Réalisée au **Laboratoire Pierre Aigrain**  
**Département de Physique de l'Ecole Normale Supérieure**



**Magneto-spectroscopy of Dirac matter :  
graphene and topological insulators**

Présentée par **Thanyanan PHUPHACHONG**

Pour obtenir le grade de  
**DOCTEUR DE L'UNIVERSITE PIERRE ET MARIE CURIE**

Soutenue le 20 Septembre 2017

Devant le jury composé de :

M. Gwendal FEVE

Mme Hélène BOUCHIAT

M. Frédéric TEPPE

M. Milan ORLITA

M. Yves GULDNER

M. Louis-Anne de VAULCHIER

Président de jury

Rapporteur

Rapporteur

Examineur

Directeur de thèse

Co-directeur de thèse



---

# Abstract

---

This thesis reports on the study under magnetic field of the electronic properties of relativistic-like Dirac fermions in two Dirac systems: graphene and topological insulators. Their analogies with high-energy physics and their potential applications have attracted great attention for fundamental research in condensed matter physics. The carriers in these two materials obey a Dirac Hamiltonian and the energy dispersion is analogous to that of the relativistic particles. The particle rest mass is related to the band gap of the Dirac material, with the Fermi velocity replacing the speed of light. Graphene has been considered as a “*model system*”, among quantum solids, that allows us to study the relativistic behavior of massless Dirac fermions satisfying a linear dispersion. When a Dirac system possesses a nonzero gap, we have massive Dirac fermions. Massless and massive Dirac fermions were studied in high-mobility multilayer epitaxial graphene and in topological crystalline insulators  $\text{Pb}_{1-x}\text{Sn}_x\text{Se}$  and  $\text{Pb}_{1-x}\text{Sn}_x\text{Te}$ . The latter system is a new class of topological materials where the bulk states are insulating but the surface states are conducting. This particular aspect results from the inversion of the lowest conduction and highest valence bulk bands having different parities, leading to a topological phase transition. Infrared magneto-spectroscopy is an ideal technique to probe these zero-gap or narrow gap materials since it provides quantitative information about the bulk parameters via the Landau quantization of the electron states. In particular, the topological phase transition can be characterized by a direct measurement of the topological index.

**Keywords:** Dirac fermions, graphene, topological crystalline insulator, topological phase transition, magneto-spectroscopy, Landau quantization.



---

# Résumé

---

Ce travail consiste en l'étude sous champ magnétique des propriétés électroniques des fermions de Dirac relativistes dans deux systèmes: graphène et isolants topologiques. Leur analogie avec la physique des hautes énergies et leurs applications potentielles ont suscité récemment de nombreux travaux. Les états électroniques sont donnés par un Hamiltonien de Dirac et la dispersion est analogue à celle des particules relativistes. La masse au repos est liée au gap du matériau avec une vitesse de Fermi remplaçant la vitesse de la lumière. Le graphène a été considéré comme un « *système école* » qui nous permet d'étudier le comportement relativiste des fermions de Dirac sans masse satisfaisant une dispersion linéaire. Quand un système de Dirac possède un gap non nul, nous avons des fermions de Dirac massifs. Les fermions de Dirac sans masse et massifs ont été étudiés dans le graphène épitaxié et les isolants topologiques cristallins  $\text{Pb}_{1-x}\text{Sn}_x\text{Se}$  et  $\text{Pb}_{1-x}\text{Sn}_x\text{Te}$ . Ces derniers systèmes sont une nouvelle classe de matériaux topologiques où les états de bulk sont isolants mais les états de surface sont conducteurs. Cet aspect particulier résulte de l'inversion des bandes de conduction et de valence du bulk ayant des parités différentes, conduisant à une transition de phase topologique. La magnéto-spectroscopie infrarouge est une technique idéale pour sonder ces matériaux de petit gap car elle fournit des informations quantitatives sur les paramètres du bulk via la quantification de Landau des états électroniques. En particulier, la transition de phase topologique est caractérisée par une mesure directe de l'indice topologique.

**Mots clés:** fermions de Dirac, graphène, isolants topologiques cristallins, transition de phase topologique, magnéto-spectroscopie, quantification de Landau.




---

# Acknowledgements

---

First and foremost, I would like to begin by acknowledging the members of my thesis committee: Gwendal Fève, Hélène Bouchiat, Frédéric Teppe, and Milan Orlita. I thank them for taking the time out of their works and busy schedules to read this manuscript and participate in the thesis defense. I am extremely grateful to Frédéric and Milan who traveled very early in the morning from Montpellier and Grenoble to Paris, respectively, for being present at the thesis defense.

Secondly, my heart-felt thanks go to all the members (Yves Guldner, Louis-Anne de Vaultier, Badih A. Assaf, and Gauthier Krizman) of the infrared and terahertz magneto-spectroscopy group at Laboratoire Pierre Aigrain (LPA), Department of Physics, Ecole Normale Supérieure, in Paris, France. Without their support, this work would not have been accomplished with extraordinary satisfaction that it was.

-  The first important person is Yves Guldner, my thesis supervisor, who provided me numerous great opportunities to do research on a fascinating topic in condensed matter physics. I thank him for his patience to supervise me and useful advice he gave me during three and a half years, since my master internship. He is a role model for hard work and determination. He showed me how to grow as a scientist, as a professional, as a teacher and as a person. He is more than a supervisor! I respect him as my grandfather and I feel always happy to go to work because this group is my second home.
-  The second one is Louis-Anne de Vaultier, my thesis co-supervisor, who dedicated his time at the beginning of my research to teach me how the experimental setup works. He constantly encouraged me when experiments failed. He occasionally taught me some French slang words and phrases during our discussions or helium transfer. However, my academic French is usually corrected by his attention. It was amusing to spend time with him apart from physics discussion to discover French cultures and share Thai traditions. Most importantly, he always listens to me when I need to talk and never leaves my side in the most difficult times. This is the reason why I respect him as my father. His remarkably generous support is one of essential factors which brings me success.
-  The third one is Badih A. Assaf, postdoctoral fellow - Junior Research Chair at Ecole Normale Supérieure, who spent much time with me in the topological crystalline insulator part of my thesis. He could be considered as an idol for young scientists thanks

## Acknowledgements

---

to his remarkable characteristics. He is extremely active, always motivated by new interesting things in his research area, and enthusiastic about puzzling topics in physics. Most importantly, he always has positive attitude to overcome any problem encountered. I learned a lot from him how to bring out my potential to do my best in order to reach any goal.

- ✚ The last one is Gauthier Krizman who joined the group for his master internship. He is very nice, generous, and disciplined. With his strong academic background in physics and mathematics, I am sure that he will move forward the research of the group and will be successful in his Ph.D. thesis.

Thirdly, I would like to convey my sincere gratitude to all the principle collaborators in France and in Austria who have prepared high-quality Dirac matter samples allowing me to accomplish this thesis.

- ✚ Paola Atkinson and Mahmoud Eddrief from Institut des Nanosciences de Paris (INSP) fabricated thin films of  $\text{Bi}_2\text{Se}_3$  topological insulator.
- ✚ Abdelkarim Ouerghi from Laboratoire de Photonique et de Nanostructures (LPN), at Marcoussis, not far from Paris, prepared high-quality multilayer epitaxial graphene.
- ✚ Günther Bauer, Valentine Volobuev and Gunther Springholz from Johannes Kepler University (JKU) Linz, in Austria, fabricated high-quality films of  $\text{Pb}_{1-x}\text{Sn}_x\text{Se}$  and  $\text{Pb}_{1-x}\text{Sn}_x\text{Te}$  topological crystalline insulators.

I would also like to show my appreciation to the following individuals, working at Ecole Normale Supérieure, for their help and support.

- ✚ Olivier Andrieu and Florent Perrin from cryogenic service of LPA prepared liquid helium for all the experiments carried out at low temperatures.
- ✚ Anne Matignon, Olga Hodges, Fabienne Renia, Cécile Margossian, Alina Corches, Julie Loussier and Marie Chayla from administration team facilitated my administrative documents.
- ✚ Pascal Morfin and Jules Silembo from technical service constructed and repaired experimental setup and essential equipment of the group.
- ✚ I thank Juliette Mangeney for the opportunity she gave me to work with her team and Robson Ferreira for the theoretical explanations of my experimental results of graphene.

## *Acknowledgements*

---

✚ I especially thank Ph.D. students (Sylvain Massabeau, Rémi Bisognin, Valentino Pistore, Holger Graef, Danijela Markovic, and Christophe Raynaud), postdoctoral fellows (Federico Valmorra and Hanond Nong), and young doctors (Omblin Lafont, Sarah Houver, Adrien Jeantet, Arthur Marguerite, Andreas Inhofer, Laure Bruhat, and Feihu Wang) for their help and friendship, and I also thank all the members of Ecole Normale Supérieure that I could not put their names on this page.

In addition, I would also like to thank my friends in Paris, in Europe and in Thailand for their help, strong friendship and spiritual support.

✚ French friends from Université Pierre et Marie Curie (UPMC Paris VI) since 2009 who taught me how to take notes, study, and write scientific reports in French style: Tabatha Sauvaget, Suzanne Dang, Myriam Rollat, Marina Vannier, Lucas Grosset, and Abderrezak Torche.

✚ Thai friends in Paris who hung out, chilled out and strolled out in Paris with me: Suwanna Dolparadorn, Kantika Lohawiboonkij, Saroch Leedumrongwatthanakul, Nathassidh Comson, Theera Rungtheera, Teerawat Kulsuwan, Yotsakorn Klaewkla, Arinch Tanunkat, and Possathorn Sriya.

✚ France alumni/Thai students in Europe/Mahidol Wittayanusorn friends/Buriram friends.

In completing this independent study with the foremost success, I could not have accomplished this work without financial support and spiritual support from the following organizations.

✚ “Mahidol Wittayanusorn” scholarship of Thai government which financially supported my whole life during memorable period (almost ten years) in France.

✚ “Franco-Thai” scholarship of French government which financially supported my studies in doctoral degree and my accommodation during my last three years in France.

✚ Office of the Education Council, Royal Thai Embassy in Paris, which took care of me about ten years in France.

The last three important people of my life to thank are 1<sup>st</sup> LTN Sekson Somnam and my beloved parents. I thank the first one for his encouragement and driving force he gave me to write this manuscript, and his spiritual support in tough periods during the last year in France. Last but not least, I would like to thank my beloved parents, Mr. Wattanai Phuphachong and Mrs. Kodchanawan Phuphachong, very much for their spiritual support and permission to go to

## *Acknowledgements*

---

France, when I was just an eighteen-year-old girl, to study physics during a really long period. This chance allows me to discover Europe, and to gain very precious and unforgettable experiences.

Again, I would like to express that I am very grateful to have had received encouragement and supports from all of these individuals whose names are written down above, including some not mentioned here. Without them, I would not have been able to accomplish this solid work the way I have.

*Vouloir, c'est pouvoir.*

ความพยายามอยู่ที่ไหน ความสำเร็จย่อมอยู่ที่นั่น

---

## List of abbreviations

---

Acronym	Definition
AFM	atomic force microscopy
ARPES	angle-resolved photoemission spectroscopy
BHZ	Bernevig-Hughes-Zhang
BZ	Brillouin zone
CR	cyclotron resonance
CVD	chemical vapor deposition
DFT	density functional theory
FCC	face-centered-cubic
FIR	far-infrared
FIR-MT	far-infrared magneto-transmission
FTIR	Fourier transform infrared interferometer
IQHE	integer quantum Hall effect
IR	infrared
LL	Landau level
MBE	molecular beam epitaxy
MDC	momentum distribution curve
MEG	multilayer epitaxial graphene
MIR	mid-infrared

## *List of abbreviations*

---

NEXAFS	near-edge X-ray absorption fine structure
PMMA	Poly(methyl methacrylate)
QAHE	quantum anomalous Hall effect
QSHE	quantum spin Hall effect
RHEED	reflection high energy electron diffraction
STEM	scanning tunneling electron microscopy
STI	strong topological insulator
STM	scanning tunneling microscope
SWM	Slonczewski-Weiss-McClure
TCI	topological crystalline insulator
TI	topological insulator
TKNN	Thouless-Kohmoto-Nightingale-Nijs
TSS	topological surface states
UHV	ultra-high vacuum
VTI	variable temperature insert
WTI	weak topological insulator
XPS	X-ray photoelectron spectroscopy
XRD	X-ray diffraction
ZDP	zero path difference

---

# Contents

---

<b>Introduction</b>	<b>1</b>
<b>Chapter 1 – Investigation techniques of Dirac matter: ARPES and IR magneto-spectroscopy</b>	<b>5</b>
<b>1. Angle-resolved photoemission spectroscopy (ARPES)</b>	<b>7</b>
<b>2. Magneto-optical absorption spectroscopy</b>	<b>11</b>
<b>2.1. Sample preparation for measurement</b>	<b>12</b>
2.1.1. Sample probe	12
2.1.2. Sample holder	13
2.1.3. Bolometer	14
<b>2.2. Fourier transform infrared (FTIR) interferometer</b>	<b>14</b>
2.2.1. Operating principle of the FTIR interferometer	14
2.2.2. Infrared light sources	16
<b>2.3. Cryostat and superconducting coil</b>	<b>17</b>
<b>2.4. Data acquisition</b>	<b>18</b>
<b>References</b>	<b>21</b>
<b>Chapter 2 – Magneto-optics in multilayer epitaxial graphene</b>	<b>23</b>
<b>1. Electronic properties of graphene</b>	<b>25</b>
1.1. Ideal graphene	26
1.2. Bilayer graphene	30
1.3. Trilayer graphene	32
1.4. Multilayer graphene	35
<b>2. Fabrication methods of graphene</b>	<b>36</b>
2.1. Mechanical exfoliation	36
2.2. Chemical exfoliation	37
2.3. Chemical vapor deposition	38
2.4. Epitaxy by thermal decomposition of SiC substrate	40



## *Contents*

---

<b>3. Magneto-spectroscopy in graphene</b>	<b>41</b>
<b>3.1. Ideal graphene</b>	<b>41</b>
<b>3.2. Bilayer graphene</b>	<b>44</b>
<b>3.3. Trilayer graphene</b>	<b>45</b>
<b>4. Experimental results</b>	<b>46</b>
<b>4.1. C-terminated face multilayer epitaxial graphene</b>	<b>46</b>
4.1.1. Fabrication of C-terminated MEG samples	46
4.1.2. Dirac Landau level spectroscopy in monolayer and bilayer graphenes	47
4.1.3. Disorder effect on magneto-optical transitions	53
<b>4.2. Si-terminated face multilayer epitaxial graphene</b>	<b>58</b>
4.2.1. Fabrication of Si-terminated MEG samples	58
4.2.2. Electronic band structure of trilayer graphene from ARPES experiment	59
4.2.3. Infrared magneto-transmission results of trilayer graphene	62
<b>5. Conclusion</b>	<b>64</b>
<b>References</b>	<b>67</b>
 <b>Chapter 3 – A brief overview of topological matter</b>	 <b>71</b>
<b>1. Topological insulators</b>	<b>73</b>
<b>1.1. Historical overview</b>	<b>73</b>
1.1.1. Quantum Hall effect	73
1.1.2. Quantum spin Hall effect	76
<b>1.2. Theoretical notions of topological states of matter</b>	<b>77</b>
1.2.1. Berry phase	78
1.2.2. Topological invariants	79
<b>1.3. Theoretical prediction and experimental realization of <math>Z_2</math> topological insulators</b>	<b>81</b>
1.3.1. 2D topological insulator: QSHE in CdTe/HgTe/CdTe quantum wells	82
1.3.2. 3D topological insulator: Bi-based compounds	84
<b>2. Topological crystalline insulators</b>	<b>89</b>
<b>2.1. Crystal structure</b>	<b>90</b>
<b>2.2. Band inversion</b>	<b>90</b>
<b>2.3. Topological surface Dirac cones in different bulk Brillouin zone orientations</b>	<b>93</b>

---

<b>2.4. Electronic band structure of <math>\text{Pb}_{1-x}\text{Sn}_x\text{Se}</math> and <math>\text{Pb}_{1-x}\text{Sn}_x\text{Te}</math></b>	<b>94</b>
2.4.1. Electronic band structure of nontrivial $\text{Pb}_{1-x}\text{Sn}_x\text{Te}$ alloy	95
2.4.2. Electronic band structure of nontrivial $\text{Pb}_{1-x}\text{Sn}_x\text{Se}$ alloy	97
<b>2.5. Valley anisotropy</b>	<b>100</b>
<b>3. Bernevig-Hughes-Zhang Hamiltonian for topological matter</b>	<b>102</b>
<b>References</b>	<b>105</b>
<b>Chapter 4 – Magneto-optical investigation of topological crystalline insulators: IV-VI compounds</b>	
<b>1. Dirac Landau levels of IV-VI semiconductors</b>	<b>111</b>
1.1. Landau levels of the longitudinal valley	111
1.2. Landau levels of the oblique valleys	116
1.3. Landau levels of the topological surface states	116
<b>2. Growth and characterization of (111) <math>\text{Pb}_{1-x}\text{Sn}_x\text{Se}</math> and <math>\text{Pb}_{1-x}\text{Sn}_x\text{Te}</math> epilayers</b>	<b>117</b>
2.1. Molecular beam epitaxy growth	117
2.2. X-ray diffraction	118
2.3. Electrical transport characterization	119
<b>3. Magneto-optical Landau level spectroscopy of Dirac fermions in (111) <math>\text{Pb}_{1-x}\text{Sn}_x\text{Se}</math></b>	<b>121</b>
3.1. Bulk states in (111) $\text{Pb}_{1-x}\text{Sn}_x\text{Se}$	121
3.2. Topological surface states in (111) $\text{Pb}_{1-x}\text{Sn}_x\text{Se}$	131
<b>4. Magneto-optical Landau level spectroscopy of Dirac fermions in (111) <math>\text{Pb}_{1-x}\text{Sn}_x\text{Te}</math></b>	<b>133</b>
4.1. Bulk states in (111) $\text{Pb}_{1-x}\text{Sn}_x\text{Te}$	133
4.2. Topological surface states in (111) $\text{Pb}_{1-x}\text{Sn}_x\text{Te}$	142
<b>5. Magneto-optical determination of a topological index</b>	<b>145</b>
5.1. (111) $\text{Pb}_{1-x}\text{Sn}_x\text{Se}$	146
5.2. (111) $\text{Pb}_{1-x}\text{Sn}_x\text{Te}$	149
<b>6. Validity of the massive Dirac approximation</b>	<b>151</b>
<b>7. Valley anisotropy in IV-VI compounds</b>	<b>153</b>

## ***Contents***

---

<b>7.1. <math>\text{Pb}_{1-x}\text{Sn}_x\text{Se}</math></b>	<b>154</b>
<b>7.2. <math>\text{Pb}_{1-x}\text{Sn}_x\text{Te}</math></b>	<b>155</b>
<b>8. Absence of the band gap closure across the topological phase transition in <math>\text{Pb}_{1-x}\text{Sn}_x\text{Te}</math></b>	<b>157</b>
<b>9. Conclusion and perspectives</b>	<b>159</b>
<b>References</b>	<b>162</b>
<b>Conclusion and outlook</b>	<b>165</b>
<b>Appendix</b>	<b>167</b>



# Introduction

This thesis focuses on the magneto-optical study of the electronic properties of Dirac fermions and their relativistic behavior in two extensively studied Dirac materials: graphene (Nobel Prize 2010) and topological insulators (Nobel Prize 2016). Such materials have recently become of great interest in solid state physics owing to their analogies with high-energy physics and their potential for promising technological applications.

The first Dirac system studied in this work is graphene known as the first truly two-dimensional crystal, composed of carbon atoms, ever found in nature. In condensed matter physics, graphene has been considered as "*the model system*" for studying the behavior of relativistic-like electrons known as massless Dirac fermions owing to its gapless and linearly dispersing electronic band structure at low energies. These massless Dirac particles in the vicinity of the corners of the hexagonal Brillouin zone of graphene (Dirac cone) can be described by a Dirac Hamiltonian with a Fermi velocity 300 times smaller than the speed of light.

Recently, the search for other solid systems of which the carriers exhibit relativistic-like properties as those in graphene has become very active. Topological insulator is a new class of materials that provides access to the description of both relativistic massless and massive Dirac fermions. Note that the energy dispersion of massive Dirac fermions resembles that of graphene but there exists a mass term corresponding to the energy gap of the material. A notable characteristic of such material is that its bulk insulating states are coexisting with its surface conducting states occurring at the boundaries of the solid. This intriguing particular aspect originates directly from the spin-orbit coupling which invert the lowest conduction and the highest valence bulk bands of the material. The band inversion results in linearly dispersing spin-momentum locked topological surface states which are protected by time-reversal symmetry.

# INTRODUCTION

---

Such a physical phenomenon can be observed in narrow gap semiconductors where the role of the spin-orbit interaction is important enough to invert the bulk band ordering. The topological nature of condensed materials is thus fundamentally governed by the parity and orbital ordering of the conduction and valence bands. The material is in the trivial regime when the bands are normal (with positive band gap) and is in the nontrivial regime when the bands are inverted (with negative band gap). The material must undergo a topological phase transition for changing the band ordering from trivial phase to nontrivial phase.

Another novel class of topological matter, so-called topological crystalline insulator, has been shown to display similar bulk and topological surface state properties as in the case of topological insulator, but the topological surface states are protected by the crystalline symmetry of the system. Narrow gap rocksalt IV-VI semiconductors such as  $\text{Pb}_{1-x}\text{Sn}_x\text{Se}$  and  $\text{Pb}_{1-x}\text{Sn}_x\text{Te}$  were demonstrated to exhibit these topological properties. In this thesis, we chose these lead-tin chalcogenides as the second Dirac system to study the relativistic behavior of their massless and massive Dirac fermions, owing to their mirror-like conduction and valence bands. The topological phase transition resulting from the bulk band inversion can be studied by tuning the chemical Sn composition. For a given temperature, there exists a critical Sn content  $x_c$  at which the topological phase transition occurs in  $\text{Pb}_{1-x}\text{Sn}_x\text{Se}$  and  $\text{Pb}_{1-x}\text{Sn}_x\text{Te}$ . For  $x < x_c$ , the system is trivial and has a positive gap, while it is nontrivial and has a negative gap when  $x > x_c$ .

In this work, magneto-optical absorption spectroscopy in the infrared domain (4-930 meV) is the principal technique used to investigate these zero gap (graphene) and narrow gap (topological crystalline insulators) semiconductors having the energy gap less than 1 eV. When a magnetic field is applied perpendicular to the crystal surface, the electron states are quantized into Landau levels. Optical transitions between Landau levels can be observed at the minima of the transmission spectra. This allows us to extract the band parameters, i.e. the Dirac mass or the energy gap and the Dirac velocity, of the material using the Dirac fermion model analysis. The obtained physical quantities of the bulk bands allow us to study the bulk band inversion or equivalently the topological phase transition of the topological system, making magneto-spectroscopy an ideal tool for probing topological material. Additionally, magneto-transport experiment, presented in the Appendix, can also be used as a technique to examine the topological character of a topological material via its bulk properties. Moreover, transport technique was used by M. König et al. in 2007 to demonstrate the quantum spin Hall effect in  $\text{Hg}_{1-x}\text{Cd}_x\text{Te}/\text{HgTe}$  quantum wells, classified later as the first two-dimensional topological insulator.

The present thesis is organized in two major parts, dealing successively with two Dirac matter systems: graphene and topological crystalline insulators. The magneto-optical study of relativistic-like Dirac fermions accommodated in these two quantum materials will be presented in this manuscript as follows:

1. The first chapter presents two investigation techniques that can be used to study the electronic properties of Dirac fermions: angle-resolved photoemission spectroscopy (ARPES) and IR magneto-optical absorption measurement. ARPES is a surface sensitive probe, while magneto-spectroscopy is essentially a bulk sensitive probe. The latter is the principal technique employed to realize this work and it allows us to investigate not only the bulk states, but also the surface states of solid materials.
2. The second chapter is completely devoted to graphene. The electronic properties of single-layer graphene and graphene stacks (bilayer, trilayer, and multilayer) will be introduced. Several methods of graphene fabrication will be briefly described. The Landau quantization, in the presence of an external magnetic field, of the energy of Dirac fermions in different types of graphene stacking will be given. Magneto-optical results were mainly obtained from high-quality multilayer epitaxial graphene prepared by thermal decomposition of SiC substrates on both the C- and Si-terminated surfaces.
3. The third chapter briefly overviews the characteristic aspects of topological matter: topological insulators and topological crystalline insulators. The first section regarding topological insulators starts with historical overview, then theoretical notions of topological states of matter, and finishes with presenting some well-known two-dimensional and three-dimensional  $Z_2$  topological insulators. We then describe topological crystalline insulator in the second section. This new kind of topological matter consists of narrow gap rocksalt IV-VI semiconductors such as  $\text{Pb}_{1-x}\text{Sn}_x\text{Se}$  and  $\text{Pb}_{1-x}\text{Sn}_x\text{Te}$  alloys. The electronic band structure of different surface orientations and the valley anisotropy in both systems will be described in details. This facilitates the interpretation of the transmission spectra shown in the upcoming chapter. The last section shows a Bernevig-Hughes-Zhang Hamiltonian model, equivalent to a three-dimensional Dirac Hamiltonian, that can be used to describe the topological nature of relativistic-like massive Dirac fermions in both topological insulators and topological crystalline insulators.

# INTRODUCTION

---

4. The heart of this thesis is presented in the last chapter. This chapter shows the magneto-optical experimental findings of high-quality (111)-oriented  $\text{Pb}_{1-x}\text{Sn}_x\text{Se}$  and  $\text{Pb}_{1-x}\text{Sn}_x\text{Te}$  films grown on  $\text{BaF}_2$  substrates by molecular beam epitaxy. A systematic study, using Dirac Landau level magneto-spectroscopy, of the topological character of these chemical tuning systems across the topological phase transition is presented in details. From the bulk band parameters extracted, the valley anisotropy in  $\text{Pb}_{1-x}\text{Sn}_x\text{Se}$  and  $\text{Pb}_{1-x}\text{Sn}_x\text{Te}$  can be studied in the vicinity of the topological phase transition. The most important aspect of our analysis is the ability to verify whether a material is trivial or nontrivial via its topological index that can be measured experimentally by magneto-spectroscopy. This important result demonstrates that the topological character of the material can be directly determined via the bulk properties.
5. Finally, we will conclude the ensemble of main results presented in this thesis and confirm that magneto-spectroscopy is a powerful investigation technique for Dirac matter. We will also give a few perspectives for future magneto-optical studies of the topological phase transition in various Dirac systems that can be described by a Bernevig-Hughes-Zhang Hamiltonian.
6. Another approach to determine the topological character via the bulk band properties of solids is represented in the Appendix. Performing magneto-transport experiment, high-quality (111)  $\text{Pb}_{1-x}\text{Sn}_x\text{Se}$  epilayers were demonstrated to exhibit the topological phase transition when the negative longitudinal magnetoresistance is observed and the system is in the nontrivial regime. The origin of this phenomenon will be described.

# *Chapter 1*

## **Investigation techniques of Dirac matter: ARPES and IR magneto-spectroscopy**

Numerous investigation techniques are efficient to study the electronic band structure of quantum solids. In this chapter, we present two representative techniques used to probe Dirac fermions and allowing us to study the band dispersion in Dirac matter. The first one is the angle-resolved photoemission spectroscopy which allows a direct experimental study of the electron distribution in the reciprocal space. It is a surface sensitive probe for the electron surface states. The second one, which is essentially a bulk sensitive probe, is the magneto-optical spectroscopy in the infrared domain. We will show in the Chapter 4 that this technique can be used to probe not only the bulk states, but also the surface states of solid materials.



# **CHAPTER 1**

## ***Investigation techniques of Dirac matter: ARPES and IR magneto-spectroscopy***

---

### **Chapter 1 - Investigation techniques of Dirac matter: ARPES and IR magneto-spectroscopy**

<b>1. Angle-resolved photoemission spectroscopy (ARPES)</b>	<b>7</b>
<b>2. Magneto-optical absorption spectroscopy</b>	<b>11</b>
<b>2.1. Sample preparation for measurement</b>	<b>12</b>
2.1.1. Sample probe	12
2.1.2. Sample holder	13
2.1.3. Bolometer	14
<b>2.2. Fourier transform infrared (FTIR) interferometer</b>	<b>14</b>
2.2.1. Operating principle of the FTIR interferometer	14
2.2.2. Infrared light sources	16
<b>2.3. Cryostat and superconducting coil</b>	<b>17</b>
<b>2.4. Data acquisition</b>	<b>18</b>
<b>References</b>	<b>21</b>

## 1. Angle-resolved photoemission spectroscopy (ARPES)

Angle-resolved photoemission spectroscopy (ARPES) is one of the photoelectron spectroscopy techniques based on the photoelectric effect first observed by H. Hertz <sup>1</sup> and later explained by A. Einstein for the quantum description of light <sup>2</sup>. In other words, this technique relies fundamentally on the detection of photoemitted electrons allowing to probe directly the momentum-dependent electronic band structure and provide detailed information about the band dispersion and Fermi surface of solids. To obtain ARPES spectra, the kinetic energy and angular distribution of the electrons photoemitted from a material under sufficiently high-energy illumination are measured and analyzed. Up to now, ARPES reaches 2 meV energy resolution and 0.2° angular resolution <sup>3</sup> which lead to better reveal the behavior of the electrons propagating inside a material through a penetration length of a few nanometers. This improvement has played a key role in enhancing the potential of ARPES to become a more sophisticated precision tool for the investigation of complex phenomena.

As mentioned earlier, the fundamental objective of an ARPES experiment is to detect the photoemission from the photoelectric effect occurring in a material. Within the non-interacting electron scheme and the energy conservation law, one can thus relate the kinetic energy ( $E_{kin}$ ) of the photoelectron in vacuum to the binding energy ( $E_B$ ) of the electronic state inside the material by the following expression:

$$E_{kin} = h\nu - \phi - |E_B| \quad (1.1)$$

where  $h$  is the Planck constant,  $\nu$  is the photon frequency, and  $\phi$  is the material work function. The latter represents the potential barrier at the surface that prohibits the valence electrons from escaping.

Fig. 1.1 schematically illustrates the photoemission occurring in a sample using ARPES probe under ultra-high vacuum (UHV) condition ( $P < 4 \times 10^{-11}$  mbar) in order to minimize surface contamination and maximize the mean free path of the emitted electrons <sup>3</sup>. A monochromatized light beam of energy  $h\nu$  is incident on the sample. Light sources of energy between 10 and 200 eV are, for example, plasma helium discharge lamp, synchrotron radiation, or lasers. As a consequence, the electrons will be emitted by photoelectric effect and escape in all directions in vacuum. The hemispherical electron energy analyzer is employed to collect the photoelectrons (denoted as  $e^-$  in Fig. 1.1). Such photoelectrons are directed onto a 2D multi-channel plate. The kinetic energy  $E_{kin}$  of the photoemitted electrons can then be measured for a given emission direction specified by the azimuthal ( $\varphi$ ) and polar ( $\theta$ ) angles.

# CHAPTER 1

## Investigation techniques of Dirac matter: ARPES and IR magneto-spectroscopy

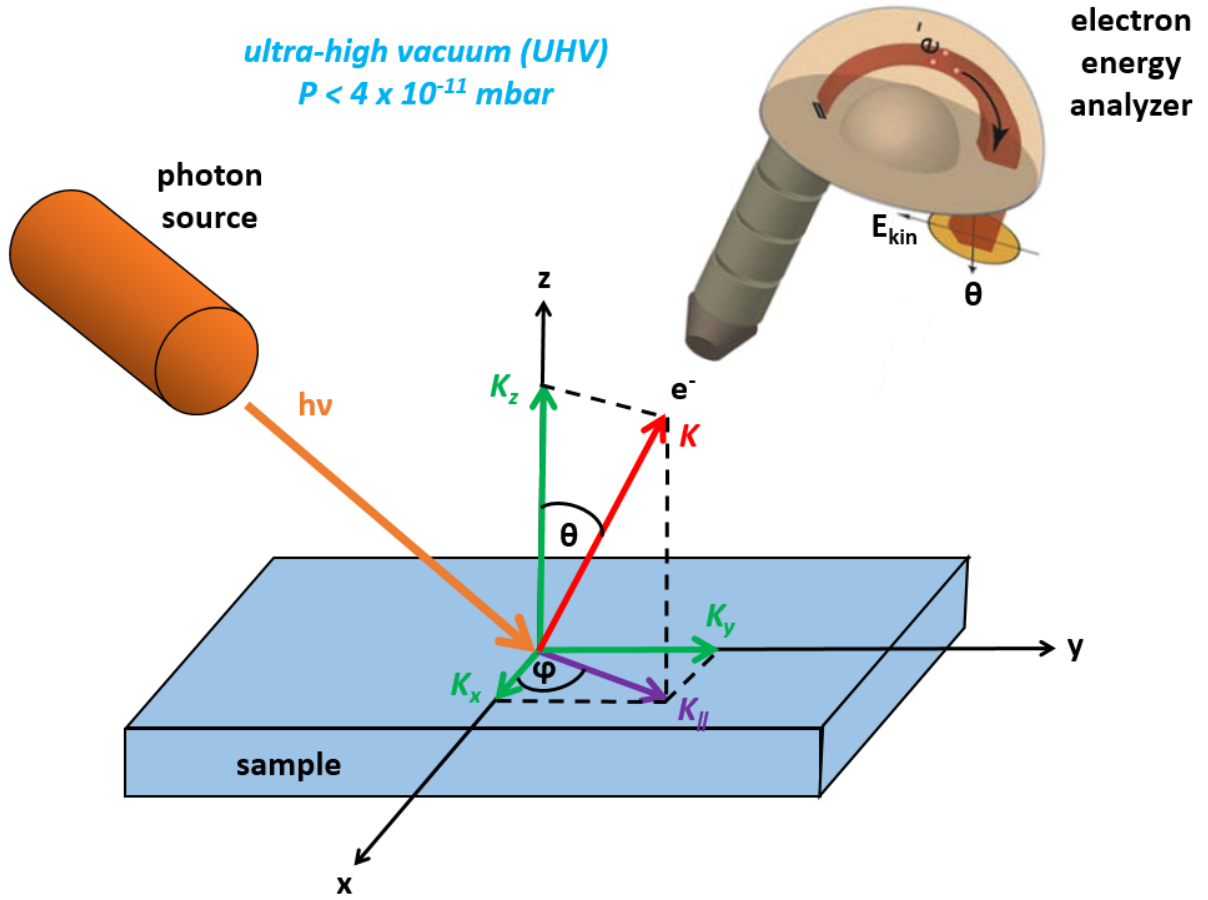


**Figure 1.1. Photoemission geometry of an ARPES experiment.** The incident photon of energy  $h\nu$  causes the photoemitted electron ( $e^-$ ) escaping from the sample in vacuum. The emission direction of the photoelectron is identified by the azimuthal ( $\phi$ ) and polar ( $\theta$ ) angles. An electron energy analyzer collects the photoelectrons.

The wave vector or momentum of the photoelectrons in vacuum can be determined as  $\vec{K} = \vec{p}/\hbar$  and its modulus is equal to  $K = \sqrt{2m_0E_{kin}}/\hbar$ , where  $\hbar$  is the reduced Planck constant and  $m_0$  is the electron rest mass. The components parallel ( $\vec{K}_{\parallel} = \vec{K}_x + \vec{K}_y$ ) and perpendicular ( $\vec{K}_{\perp} = \vec{K}_z$ ) to the sample surface can be obtained in terms of the emission angles ( $\phi$  and  $\theta$ ) defined in Fig. 1.1 as follows:

$$K_x = \frac{1}{\hbar} \sqrt{2m_0E_{kin}} \sin(\theta) \cos(\phi) \quad (1.2a)$$

$$K_y = \frac{1}{\hbar} \sqrt{2m_0E_{kin}} \sin(\theta) \sin(\phi) \quad (1.2b)$$

$$K_z = \frac{1}{\hbar} \sqrt{2m_0E_{kin}} \cos(\theta) \quad (1.2c)$$

Since the objective of ARPES measurement is to construct the electronic dispersion relation between the binding energy  $E_B$  and the wave vector or momentum  $\vec{k}$  of the electrons propagating inside the material, we have to determine the two components of  $\vec{k}$  which are  $\vec{k}_{\parallel}$  and  $\vec{k}_{\perp}$ . Here  $\vec{k}_{\parallel} = \vec{k}_x + \vec{k}_y$  is the component parallel to the material surface while  $\vec{k}_{\perp} = \vec{k}_z$  is the component perpendicular to the material surface. Note that ARPES measurement requires sufficiently clean surfaces in order to establish a definite relationship between the crystal wave vector ( $\vec{k}$ ) and the measured wave vector ( $\vec{K}$ ) of the extracted photoelectron.  $\vec{k}_{\parallel}$  is conserved in the process. For a pristine sample,  $k_{\parallel}$  reads:

$$k_{\parallel} = K_{\parallel} = \frac{1}{\hbar} \sqrt{2m_0 E_{kin}} \sin(\theta) \quad (1.3)$$

Contrary to  $\vec{k}_{\parallel}$ ,  $\vec{k}_{\perp}$  is not conserved but is necessary to map the electronic band structure. To calculate  $k_{\perp}$ , we can adopt a nearly-free-electron description for the final bulk Bloch states <sup>4</sup>. We thus get:

$$E_{kin} + \phi = \frac{\hbar^2 \vec{k}^2}{2m_0} - |E_0| = \frac{\hbar^2 (\vec{k}_{\parallel}^2 + \vec{k}_{\perp}^2)}{2m_0} - |E_0| \quad (1.4)$$

Here,  $E_0$  corresponds to the energy at the bottom of the band with respect to the Fermi energy. As we can calculate the value of  $\vec{k}_{\parallel}^2$  from Eq. 1.3, the expression of  $k_{\perp}$  can thus be written as:

$$k_{\perp} = \frac{1}{\hbar} \sqrt{2m_0 (E_{kin} \cos^2(\theta) + V_0)} \quad (1.5)$$

where the inner potential  $V_0 = |E_0| + \phi$  represents the energy of the bottom of the band referenced to the vacuum level.

The electronic band structure of a material can be established by studying the momentum-dependent binding energy ( $E_B(\vec{k})$ ). Only occupied electronic states can be observed by ARPES. Fig. 1.2 represents ARPES spectra obtained from different Dirac systems accommodating 2D and 3D topological Dirac fermions. These ARPES data clearly show the surface electronic structure dispersion map for the 2D topological surface Dirac cone in 3D topological insulator  $\text{Bi}_2\text{Se}_3$  <sup>5</sup>, 3D tunable topological insulators  $\text{TlBi}(\text{S}_{1-x}\text{Se}_x)_2$  with  $x = 0.5$  <sup>6</sup> and  $(\text{Bi}_{1-x}\text{In}_x)_2\text{Se}_3$  with  $x = 0.04$  <sup>7</sup>, and the 3D bulk Dirac cone in 3D Dirac semimetal  $\text{Cd}_3\text{As}_2$  <sup>8</sup>. Moreover, ARPES measurement allows us to estimate the surface state band velocity from the experimental slope of the Dirac cone structure.

## CHAPTER 1

### Investigation techniques of Dirac matter: ARPES and IR magneto-spectroscopy

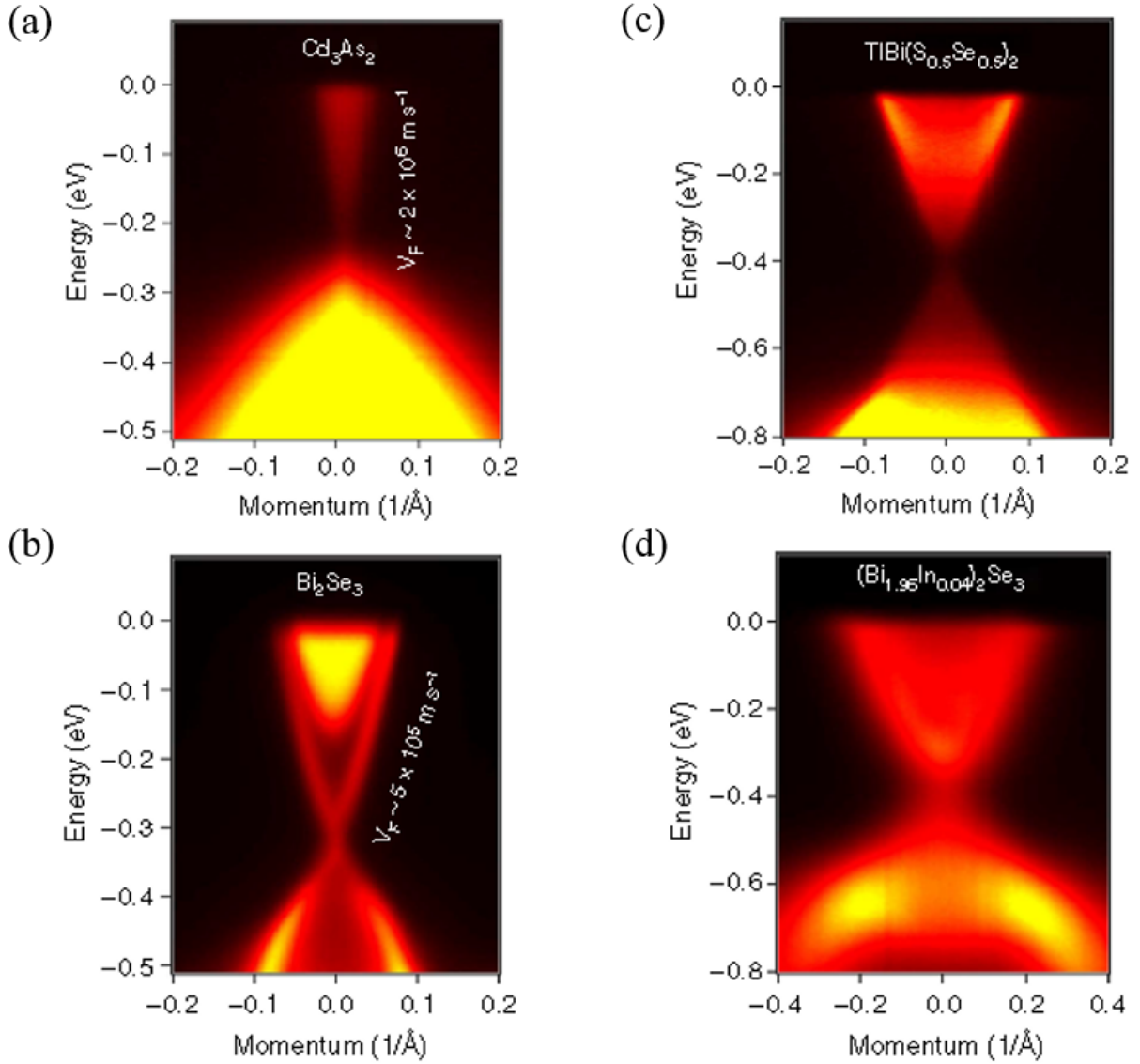


**Figure 1.2. ARPES measurements in different Dirac systems.** ARPES spectra show the surface electronic band structure of (a) 3D topological Dirac semimetal  $\text{Cd}_3\text{As}_2$  <sup>8</sup>, (b) 3D topological insulators  $\text{Bi}_2\text{Se}_3$  <sup>5</sup>, (c)  $\text{TlBi}(\text{S}_{0.5}\text{Se}_{0.5})_2$  <sup>6</sup> and (d)  $(\text{Bi}_{0.96}\text{In}_{0.04})_2\text{Se}_3$  <sup>7</sup> in topologically nontrivial phase. Modified from <sup>8</sup>.

In summary, ARPES is an ideal surface sensitive probe used to investigate the electronic band structure of quantum materials due to the improvements of energy and angle resolutions and data acquisition efficiency. There are also many exciting developments trying to add new dimensions into this technique leading to the spin-resolved ARPES and time-resolved ARPES. With the efforts put into its development, this powerful tool will continue playing an irreplaceable role in the search for novel phenomena of complex materials. The ARPES results that will be presented later in this work were obtained by our collaborators.

## 2. Magneto-optical absorption spectroscopy

In the previous section, ARPES as surface sensitive probe is shown to be a powerful tool allowing us to study the electronic band structure of Dirac materials. In this section, infrared magneto-optical absorption spectroscopy, the technique we used in this thesis to probe and characterize Dirac matter, will be described. When the crystal surface is subjected perpendicular to an applied magnetic field  $B$ , the electron states will be quantized into relativistic Landau levels dispersing as  $\sqrt{B}$  or  $\sqrt{\alpha^2 + \beta B}$ , where  $\alpha$  and  $\beta$  are band parameters. This is a typical characteristic feature of Dirac fermions. The optical transitions occurring between these Landau levels give important information about the physical parameters of the electronic band structure of bulk states as well as surface states. Infrared spectral range is chosen thanks to the energy compatibility for probing semiconductors of which the energy gap is less than 1 eV. This is the primary reason why magneto-optical absorption spectroscopy in the infrared domain is primarily used in this thesis to investigate Dirac matter.



**Figure 1.3.** Photo of magneto-optical spectroscopy experimental setup.



## CHAPTER 1

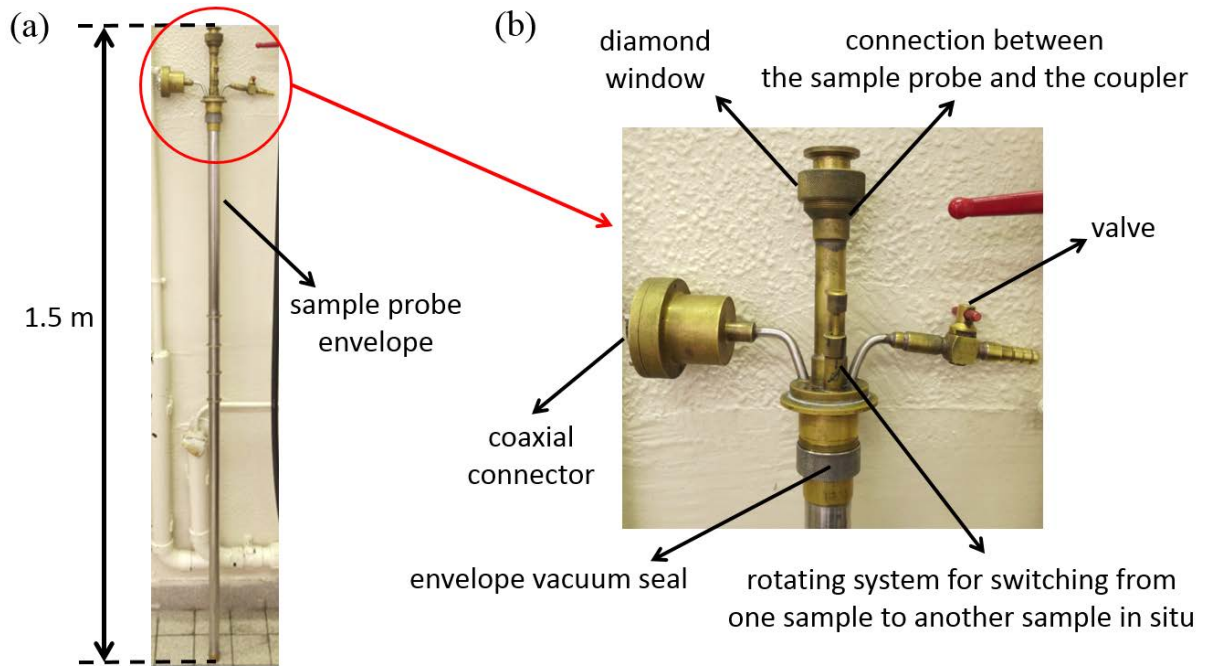
### *Investigation techniques of Dirac matter: ARPES and IR magneto-spectroscopy*

Fig. 1.3 shows the whole experimental setup used to probe Dirac fermions. The principal element is the Oxford Instruments 1.5K/17T cryostat, situated at the center of the photo, equipped with a superconducting coil. It allows us to do experiments in the temperature range  $1.5 \text{ K} < T < 220 \text{ K}$  and under magnetic fields  $B = 0\text{-}17 \text{ T}$ . The Fourier transform infrared (FTIR) interferometer (Bruker VERTEX 80V), located in the upper left hand corner of the photo, is employed as the infrared light source and the spectral analysis apparatus at the same time. These two essential elements are connected by a coupler containing a parabolic mirror. Detailed information about the experimental setup and the data acquisition will be described in the following subsections.

## 2.1. Sample preparation for measurement

Samples are first prepared and attached at the bottom of the sample probe for magneto-optical absorption measurement. In this subsection, three important parts will be described: the sample probe, the sample holder and the bolometer used as a detector of transmitted signals.

### 2.1.1. Sample probe



**Figure 1.4. Different parts of the sample probe.** (a) The sample is placed at the bottom of the sample probe for measurement. The sample probe envelope is used to avoid any contact between the sample and the exterior environment. (b) Zoom of the top of the sample probe.

A 1.5 m long sample probe was designed to mount samples for magneto-optical absorption measurement and to maintain three electrical channels carried by two nonmagnetic coaxial cables (Fig. 1.4(b)). The inner walls of the sample probe guide the incident infrared light reaching towards the sample. The three channels are used for the  $\pm 18 \text{ V}$  bolometer power supply, the signal acquisition of the bolometer and the ground. The sample probe envelope (Fig.

1.4(a)) is necessary for protecting the cables, the bolometer and the sample from the exterior environment when the sample probe is immersed in the cryostat filled with liquid helium. After the sample is mounted and sealed, the sample probe is primarily evacuated down to  $\sim 1 \times 10^{-2}$  mbar. It is then filled with helium exchange gas, up to a pressure of 80-800 mbar at room temperature to ensure sample thermalisation, before being put into the variable temperature insert (VTI) of the cryostat for measurement. The pressure in the sample probe is maintained owing to a diamond window located at the connection between the sample probe and the coupler. The diamond window enables also an optimal passage of the transmitted signals throughout the infrared range. For the investigation of Dirac fermions in graphene and topological insulators, the pressure of the helium exchange gas is about 100-120 mbar at room temperature.

### 2.1.2. Sample holder

Fig. 1.5(a) shows two kinds of sample holders: sample holder with one hole and rotating sample holder with two holes. The sample holder used for the transmission experiment has several diameters. An appropriate diameter for a given sample is chosen for maximizing the transmitted signals. Fig. 1.5(b) shows a sample bonded on a sample holder. The rotating sample holder can mount two pieces of samples as seen in Fig. 1.5(c). The rotating system (Fig. 1.4(b)) joining the rotating sample holder allows switching from one sample to another sample in situ. This is very practical for a measurement requiring a normalization between two consecutive transmission spectra at the same applied field. To glue a sample on a sample holder, we use silver paste or PMMA (Poly(methyl methacrylate)).

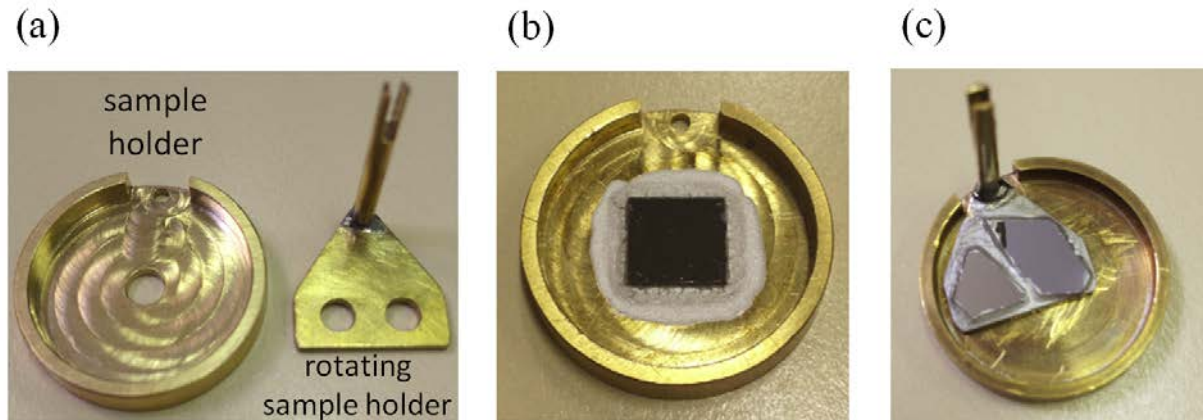


**Figure 1.5. Examples of sample holders.** (a) Examples of a sample holder (with one hole) and a rotating sample holder (with two holes). There are several diameters adapting to the dimension of the sample. (b) A sample glued with silver paste to the sample holder. (c) A sample and a substrate glued with silver paste to the rotating sample holder.



## CHAPTER 1

### *Investigation techniques of Dirac matter: ARPES and IR magneto-spectroscopy*

#### 2.1.3. Bolometer

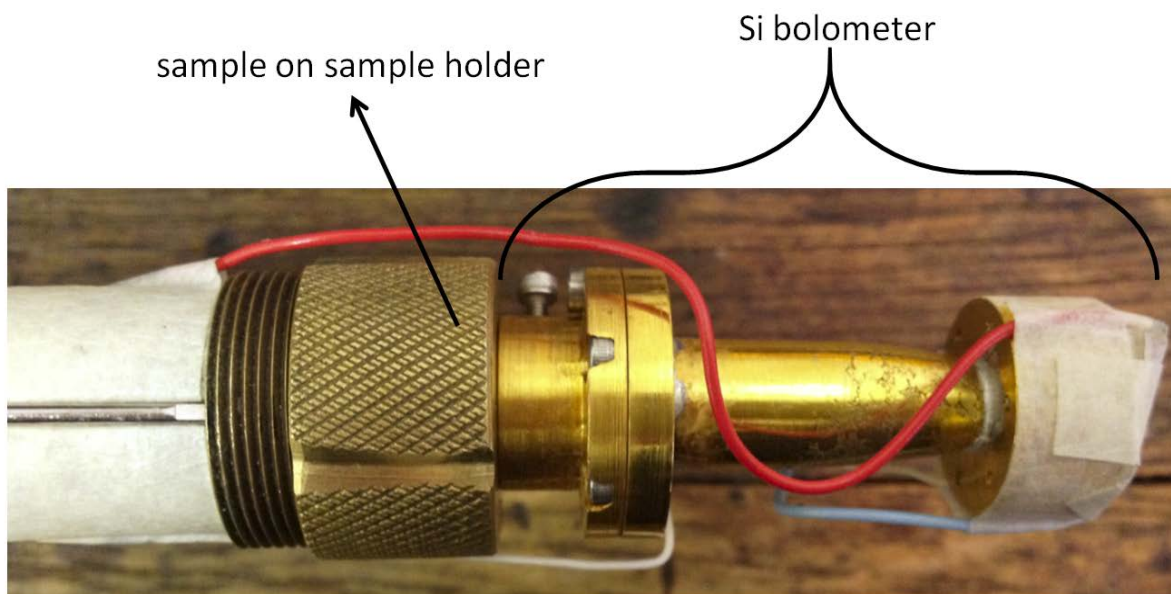


**Figure 1.6. Infrared Si-composite bolometer with a diamond window.** The Si bolometer and the sample are attached to the bottom of the sample probe.

The bolometer is a photo-detector used for spectrum measurement. Its operating principle is to convert the energy of the incident electromagnetic radiation on the surface of a metallic or semiconductor absorber into heat. A Si-composite bolometer (Infrared Laboratories) equipped with a diamond window was used in this thesis for infrared magneto-optical absorption measurement. It is used to collect the transmitted light directly below the sample (Fig. 1.6). The signal from the bolometer passes through an external preamplifier before being transmitted to the FTIR interferometer for analysis. It is possible to adjust the amplification factor (200, 2,000 and 5,000) of the preamplifier to obtain satisfying signal intensity.

## 2.2. Fourier transform infrared (FTIR) interferometer

Infrared magneto-optical spectroscopy is a technique employed to obtain transmission spectra of a sample (intensity as a function of energy) in the infrared domain ( $30\text{-}7500\text{ cm}^{-1}$  or  $4\text{-}930\text{ meV}$ ). The laboratory is equipped with a Bruker VERTEX 80V Fourier transform infrared (FTIR) interferometer monitored by the OPUS operating software. This spectrometer plays two essential roles as infrared light source and spectral analysis tool.

### 2.2.1. Operating principle of the FTIR interferometer

As represented in Fig. 1.7, The FTIR interferometer possesses two infrared light sources: far-infrared (FIR) source for  $30\text{-}700\text{ cm}^{-1}$  and mid-infrared (MIR) source for  $700\text{-}7500\text{ cm}^{-1}$ . The light beam is collimated and directed towards a beam splitter and a system of

associated mirrors. The half portion of the signal is transmitted to a mobile mirror which can move on nitrogen cushion thanks to a motor. When the mirror moves, each wavelength is periodically blocked or transmitted by the interferometer by interference phenomenon. Finally, the light emerging from the spectrometer is sent towards the cryostat using a vacuum coupler with a parabolic mirror. The incident light is then focused on the sample placed above the bolometer. The detector measures the light intensity remaining after passing through the sample and sends the transmitted signal, after amplification, to the FTIR interferometer for spectral analysis.

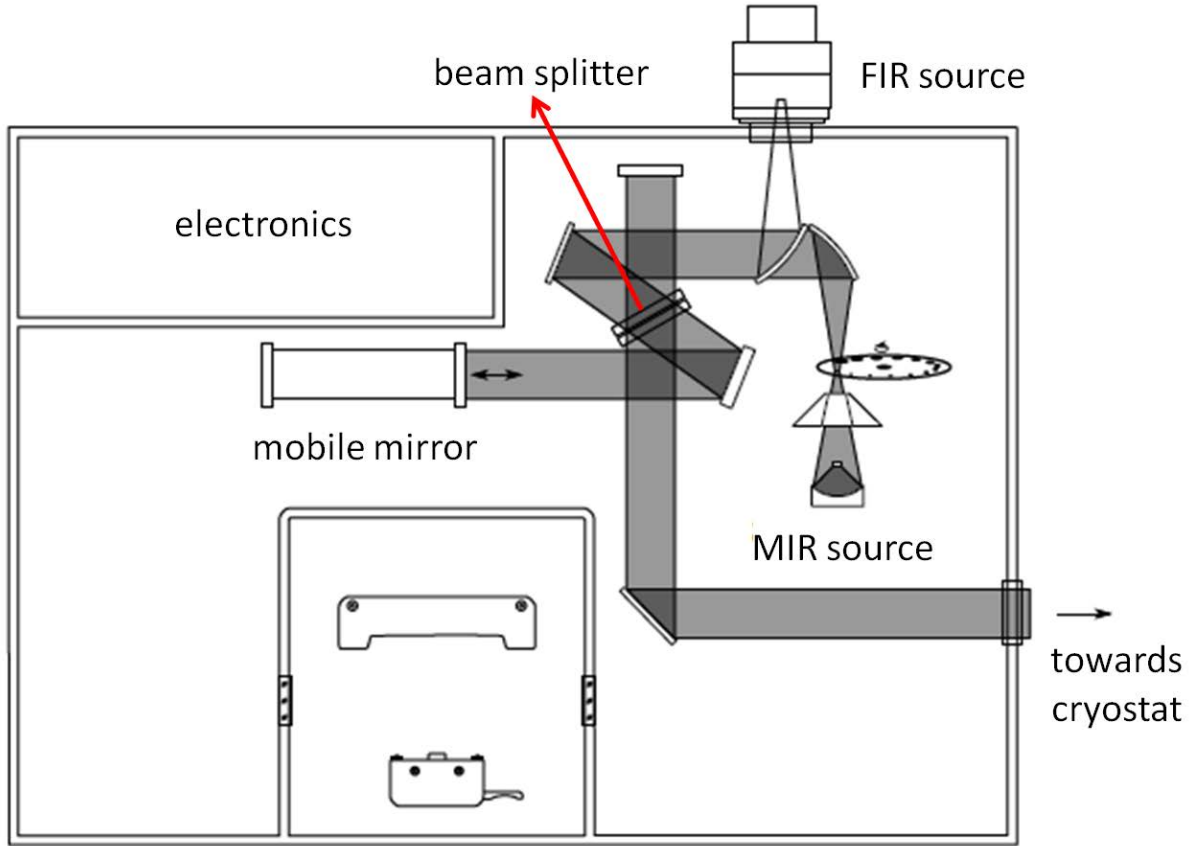


**Figure 1.7. Schematic representation of the FTIR interferometer (Bruker VERTEX 80V).**

The FTIR interferometer obtains the signal from the bolometer as an interferogram (the transmitted light as a function of mobile mirror position) (Fig. 1.8) and then changes it into a spectrum (the transmitted light as a function of energy) using the calculation of the Fourier transform (Eq. 1.6). Here,  $D(\delta)$  is the intensity of the interferogram as a function of phase difference proportional to the mobile mirror displacement  $\delta$ .  $I(\nu)$  refers to the intensity of the spectrum as a function of frequency  $\nu$ .

$$I(\nu) = \int_{\delta_{min}}^{\delta_{max}} D(\delta) \cos(2\pi\delta\nu) d\delta \quad (1.6)$$

# CHAPTER 1

## Investigation techniques of Dirac matter: ARPES and IR magneto-spectroscopy

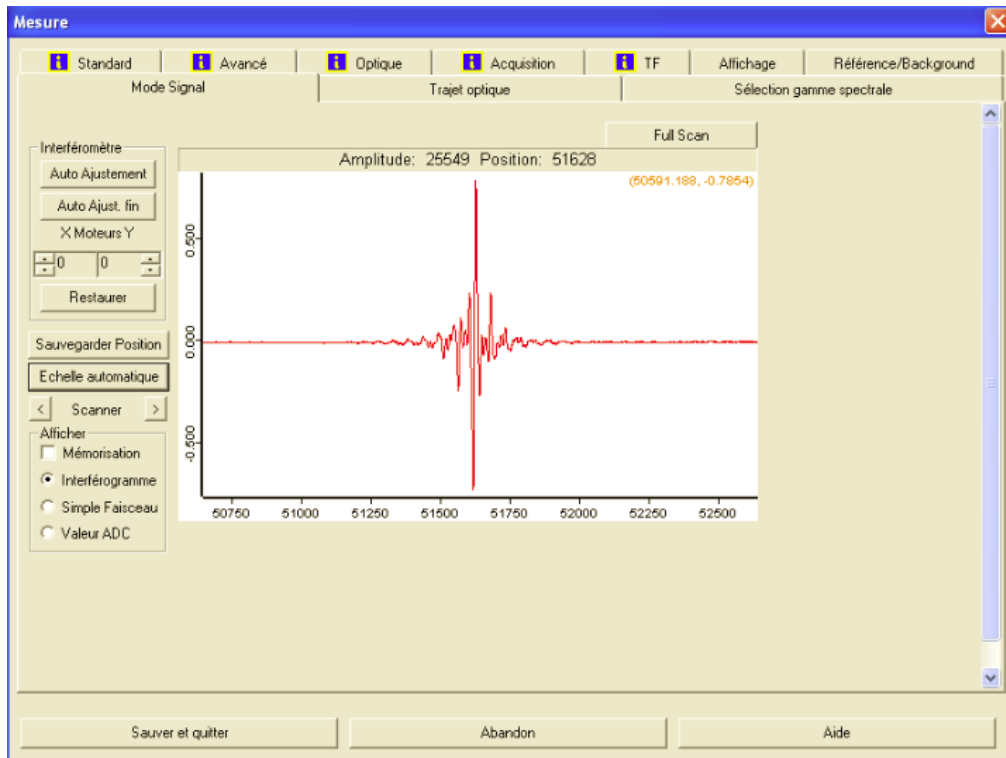


**Figure 1.8. OPUS control window showing an interferogram.** The central peak corresponds to the zero path difference (ZPD) position of the mobile mirror at which the maximum of light passes through the interferometer towards the detector.

In order to get a good signal/noise ratio, each final spectrum is obtained after acquisition and average of several spectra. The number of averaged spectra is proportional to a parameter which is the number of scans. It can typically be selected among the values of 64, 128 or 256 scans. Furthermore, the maximal spectral resolution can be adjusted up to  $0.2 \text{ cm}^{-1}$ . The spectral resolution chosen for our magneto-optical absorption experiment is  $5 \text{ cm}^{-1}$ . Note that the vacuum is essential during the measurement in the FTIR interferometer, the entire optical path and inside the coupler in order to avoid the absorption of the infrared light beam by the atmospheric gases ( $\text{H}_2\text{O}$ ,  $\text{O}_2$ ,  $\text{CO}_2$ , etc.).

### 2.2.2. Infrared light sources

The typical characteristics of FIR and MIR light sources of the FTIR interferometer are summarized in Table 1.1.

Characteristics	Far-infrared (FIR)	Mid-infrared (MIR)
Source	mercury vapor lamp	SiC rod heated to $T > 100$ °C
Beam splitter	Mylar-Multilayer (CsI)	KBr
Filter	polyethylene	diaphragm of adjustable diameter
Wavenumber range	30-700 $\text{cm}^{-1}$	700-7500 $\text{cm}^{-1}$
Wavelength range	14-333 $\mu\text{m}$	1.3-14 $\mu\text{m}$
Energy range	4-87 meV	87-930 meV

Table 1.1. Characteristics of FIR and MIR light sources.

The operating software OPUS represents a spectrum in a function of wavenumber  $\sigma$ . Some useful formulas regarding the conversion between the energy  $E$ , the wavelength  $\lambda$ , the wavenumber  $\sigma$  and the frequency  $\nu$  are written in Table 1.2.

Energy ( $E$ )	Wavelength ( $\lambda$ )	Frequency ( $\nu$ )
$E(J) = \frac{hc}{\lambda(m)}$	$\lambda(m) = \frac{1}{\sigma(m^{-1})}$	$\nu(Hz) = \frac{E(J)}{h}$
$E(meV)$ $= \frac{hc \times 1000}{\lambda(cm) \times 10^{-2} \times 1.6 \times 10^{-19}}$ $= \frac{0.124}{\lambda(cm)}$	$\lambda(\mu m) = \frac{10000}{\sigma(cm^{-1})}$	$\nu(THz)$ $= \frac{E(meV) \times 10^{-3} \times 1.6 \times 10^{-19}}{h \times 10^{12}}$ $= \frac{E(meV)}{4.1}$

Table 1.2. Conversion formulas between  $E$ ,  $\lambda$ ,  $\sigma$  and  $\nu$ .

Here,  $h$  is the Planck constant ( $h = 6.626 \times 10^{-34}$  J.s) and  $c$  is the speed of light in vacuum ( $c = 2.997 \times 10^8$  m/s).

## 2.3. Cryostat and superconducting coil

As illustrated in Fig. 1.9(a), the cryogenic storage dewar of total volume of 85 L contains a superconducting coil at the bottom of the cryostat and a variable temperature insert (VTI), resulting finally in a capacity of 46 L of liquid helium. The VTI is separated from the exterior container by the inner vacuum shield, consequently, the temperature of the sample can be varied to be different from the temperature of liquid helium (4.2 K). To decrease the temperature below 4.2 K, we introduce liquid helium from the exterior container into the VTI via the needle valve and then pump out the pressure in the VTI. To increase the temperature above 4.2 K, we use the Oxford Instruments ITC503 automated control/heater apparatus that allows us to fix the desired temperature. The sample at the bottom of the sample probe is placed at the heart of the

## CHAPTER 1

### *Investigation techniques of Dirac matter: ARPES and IR magneto-spectroscopy*

superconducting coil as seen in Fig. 1.9(b). The sample holder is surrounded by the sample probe envelope to avoid any direct contact between the sample and liquid helium. The control and power supply of the superconducting coil are provided by the Oxford Instruments IPS120-10 apparatus, enabling to work at fixed magnetic fields and to sweep the field with a maximum speed of 1 T/minute.

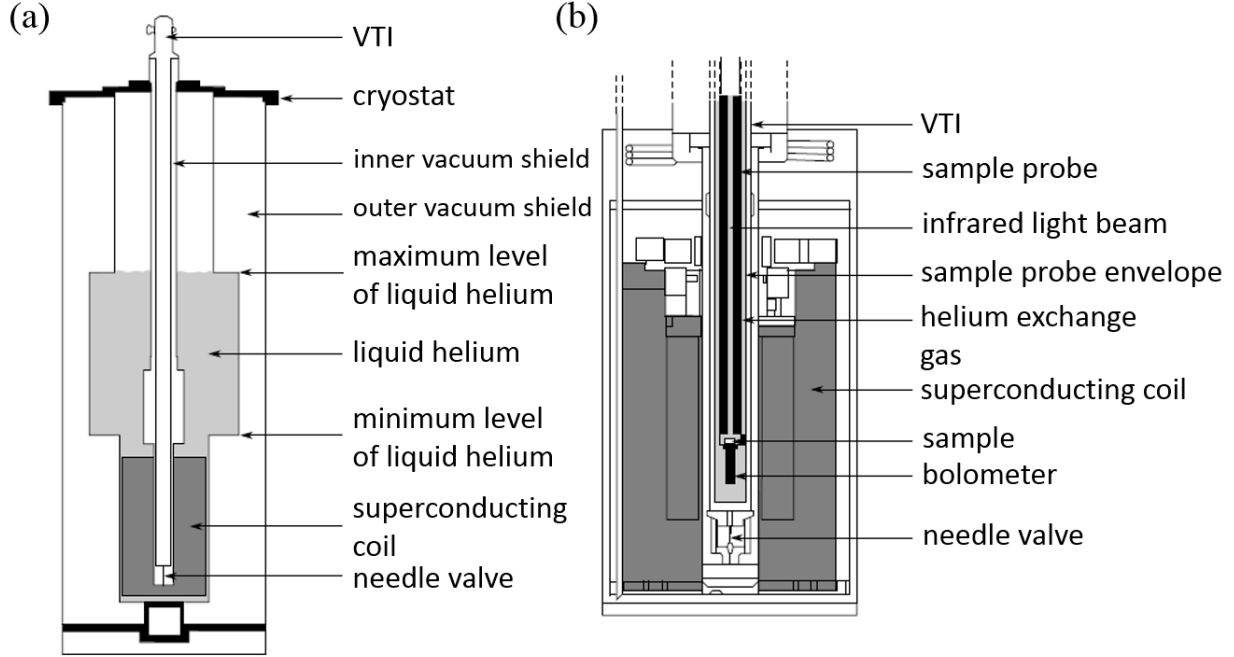


**Figure 1.9. Schematics of the cryostat equipped with a superconducting coil.** (a) The dewar consists of two containers: an interior one or the variable temperature insert (VTI) and an exterior one containing the superconducting coil immersed in liquid helium. The maximum and minimum filling levels of liquid helium are indicated. The opening of the needle valve lets flow liquid helium from the exterior container into the VTI. (b) Zoom of the superconducting coil and the bottom of the sample probe. The heat exchange between the sample and the VTI is via a helium exchange gas of a pressure of 80-800 mbar at room temperature.

## 2.4. Data acquisition

In this thesis, all experimental results were obtained from infrared magneto-optical absorption measurement. Fig. 1.10 displays the whole experimental setup used to probe Dirac fermions in graphene and topological insulators. The process of spectra acquisition is as follows. The infrared light beam generated from FIR or MIR sources passes by the beam splitter and the system of associated mirrors in the vacuum FTIR interferometer and is then transmitted to the entrance of the sample probe using the vacuum coupler. The parabolic mirror inside the coupler bends the light beam to propagate directly to the sample placed at the center of the superconducting coil. The magnetic field is oriented perpendicular to the sample surface in Faraday geometry and can be varied up to  $B = 17$  T. Each measurement is performed at a constant magnetic field. The temperature is fixed at 4.5 K. The Si bolometer detects the transmitted light directly below the sample. The transmission signals are acquired, then amplified and sent to the FTIR interferometer for spectral analysis. The corresponding

interferogram is obtained after the analysis and will then be converted by Fourier transform calculation to the transmission spectrum.

The transmission spectra measured at different magnetic fields will be manipulated in order to obtain and analyze the relative transmission and the transmittance. As a result, we are able to extract valuable quantitative information about the physical properties, for instance, the Dirac velocity, the Dirac mass or the energy gap of a Dirac material. The relative transmission is defined to be the normalization of the sample transmission at a given magnetic field  $T(B)$  by a zero-field sample transmission  $T(0)$ . This indicates the absorption due to the transitions of carriers between different Landau levels. The transmittance at a fixed magnetic field is defined as the sample transmission  $T_{sam}(B)$  normalized by the corresponding substrate transmission  $T_{sub}(B)$ . This allows us to gain the information about the absorption of the free carriers and to determine the absorption threshold of the sample.

Infrared magneto-optical absorption spectroscopy represents the powerful ability to investigate the volume of a quantum solid. It is shown to be a bulk efficient sensitive probe, yet not blind to the surface, used to reveal the electronic band structure of solids via physical parameters obtained from the measurement.

## CHAPTER 1

### *Investigation techniques of Dirac matter: ARPES and IR magneto-spectroscopy*

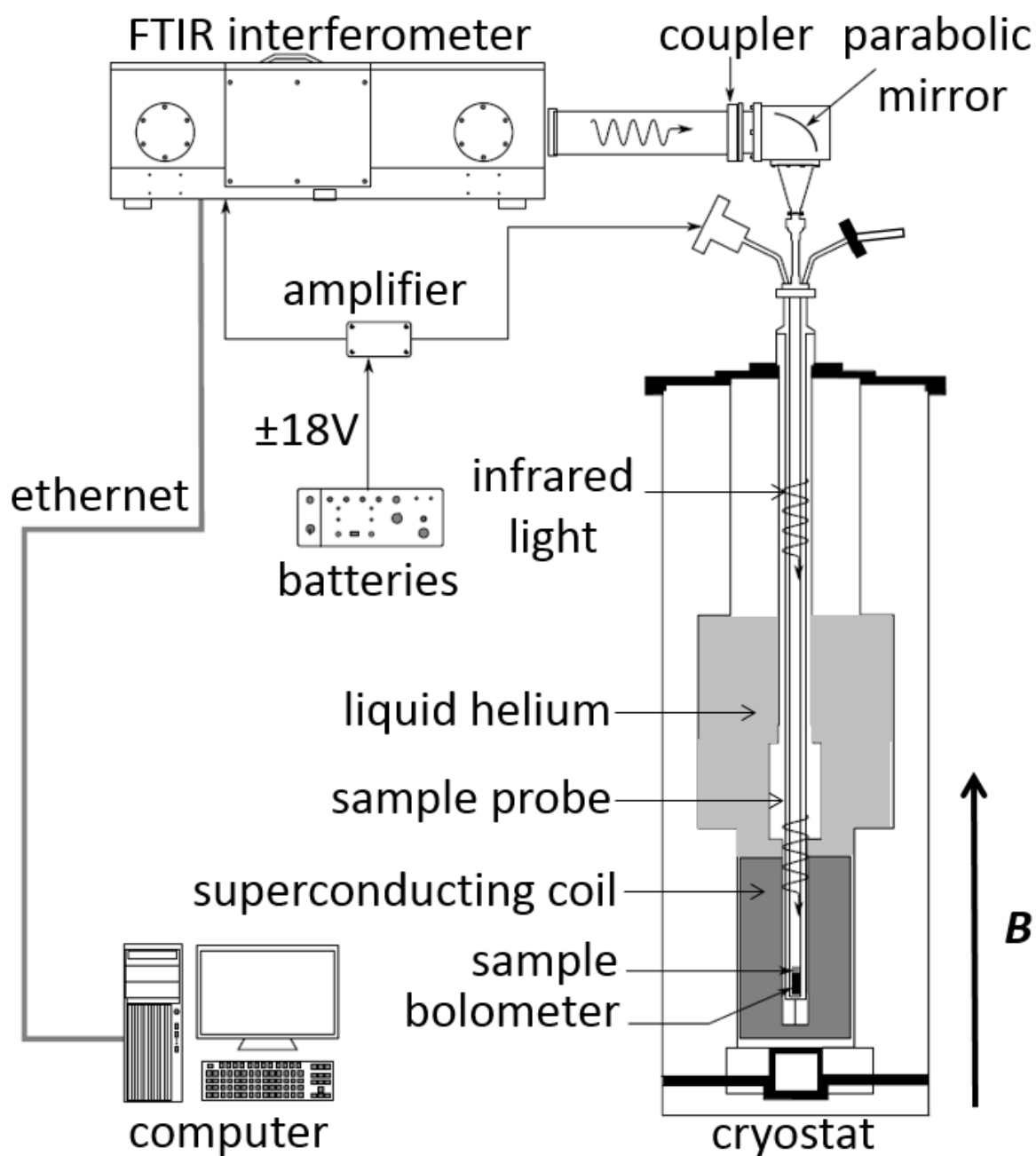


Figure 1.10. Experimental setup of infrared magneto-optical absorption measurement.

## References

1. Hertz, H. *Ann. Phys.* **17**, 983 (1887).
2. Einstein, A. *Ann. Phys.* **31**, 132 (1905).
3. Lee, W. S., Vishik, I. M., Lu, D. H. & Shen, Z.-X. A brief update of angle-resolved photoemission spectroscopy on a correlated electron system. *J. Phys. Condens. Matter* **21**, 164217 (2009).
4. Damascelli, A. Probing the Electronic Structure of Complex Systems by ARPES. *Phys. Scr.* **T109**, 61–74 (2004).
5. Xia, Y. *et al.* Observation of a large-gap topological-insulator class with a single Dirac cone on the surface. *Nat. Phys.* **5**, 398–402 (2009).
6. Xu, S.-Y. *et al.* Topological Phase Transition and Texture Inversion in a Tunable Topological Insulator. *Science* **332**, 560–564 (2011).
7. Brahlek, M. *et al.* Topological-metal to band-insulator transition in  $(\text{Bi}_{1-x}\text{In}_x)_2\text{Se}_3$  thin films. *Phys. Rev. Lett.* **109**, 186403 (2012).
8. Neupane, M. *et al.* Observation of a three-dimensional topological Dirac semimetal phase in high-mobility  $\text{Cd}_3\text{As}_2$ . *Nat. Commun.* **5**, 3786 (2014).



## **CHAPTER 1**

### ***Investigation techniques of Dirac matter: ARPES and IR magneto-spectroscopy***

---

## Chapter 2

# Magneto-optics in multilayer epitaxial graphene

In this work, the study of Dirac matter was first devoted to graphene: the first truly two-dimensional crystal, composed of carbon atoms, ever found in nature. The fundamental study of the theoretical aspects and experimental realization of graphene has always retained this research area active in condensed matter physics after the 2010 Nobel Prize in Physics was awarded jointly to A. K. Geim and K. S. Novoselov for "*groundbreaking experiments regarding the two-dimensional material graphene*". In particular, the most intriguing typical characteristic of graphene, at low energies, is that its unusual linear energy-momentum dispersion is similar to the physics of quantum electrodynamics for massless fermions but the Dirac velocity of these particles is 300 times smaller than the speed of light. This completely differs from ordinary electrons when subjected to magnetic fields. Graphene is thus a model system of Dirac matter allowing us to study the relativistic behavior of Dirac fermions in analogy with high-energy physics.

In this chapter, the electronic properties of an ideal graphene and graphene stacks will be addressed by magneto-optical spectroscopy. Different methods of graphene fabrication will be briefly described. We will essentially focus on the behavior of Dirac fermions in multilayer epitaxial graphene, fabricated by thermal decomposition of SiC substrates, which were investigated using infrared magneto-optical absorption measurements. Experimental results of multilayer epitaxial graphene on the C-terminated and Si-terminated faces of SiC substrates will be shown.

## **CHAPTER 2**

### ***Magneto-optics in multilayer epitaxial graphene***

---

## **Chapter 2 – Magneto-optics in multilayer epitaxial graphene**

<b>1. Electronic properties of graphene</b>	<b>25</b>
1.1. Ideal graphene	26
1.2. Bilayer graphene	30
1.3. Trilayer graphene	32
1.4. Multilayer graphene	35
<b>2. Fabrication methods of graphene</b>	<b>36</b>
2.1. Mechanical exfoliation	36
2.2. Chemical exfoliation	37
2.3. Chemical vapor deposition	38
2.4. Epitaxy by thermal decomposition of SiC substrate	40
<b>3. Magneto-spectroscopy in graphene</b>	<b>41</b>
3.1. Ideal graphene	41
3.2. Bilayer graphene	44
3.3. Trilayer graphene	45
<b>4. Experimental results</b>	<b>46</b>
4.1. C-terminated face multilayer epitaxial graphene	46
4.1.1. Fabrication of C-terminated MEG samples	46
4.1.2. Dirac Landau level spectroscopy in monolayer and bilayer graphenes	47
4.1.3. Disorder effect on magneto-optical transitions	53
4.2. Si-terminated face multilayer epitaxial graphene	58
4.2.1. Fabrication of Si-terminated MEG samples	58
4.2.2. Electronic band structure of trilayer graphene from ARPES experiment	59
4.2.3. Infrared magneto-transmission results of trilayer graphene	62
<b>5. Conclusion</b>	<b>64</b>
<b>References</b>	<b>67</b>

## 1. Electronic properties of graphene

From a purely theoretical point of view, graphene is a two-dimensional (2D) one-atom-thick allotrope of carbon. As represented in Fig 2.1(a), graphene is the mother for other carbon materials in different dimensionalities owing to the flexibility of the carbon-carbon bonding present in its honeycomb lattice structure. One can obtain a fullerene molecule (0D) from wrapped-up graphene with the introduction of pentagons (Fig. 2.1(b)), a carbon nanotube (1D) by rolling up graphene along a chosen direction (Fig. 2.1(c)), and a graphite (3D) by stacking many graphene layers connected by van der Waals force (Fig. 2.1(d)).

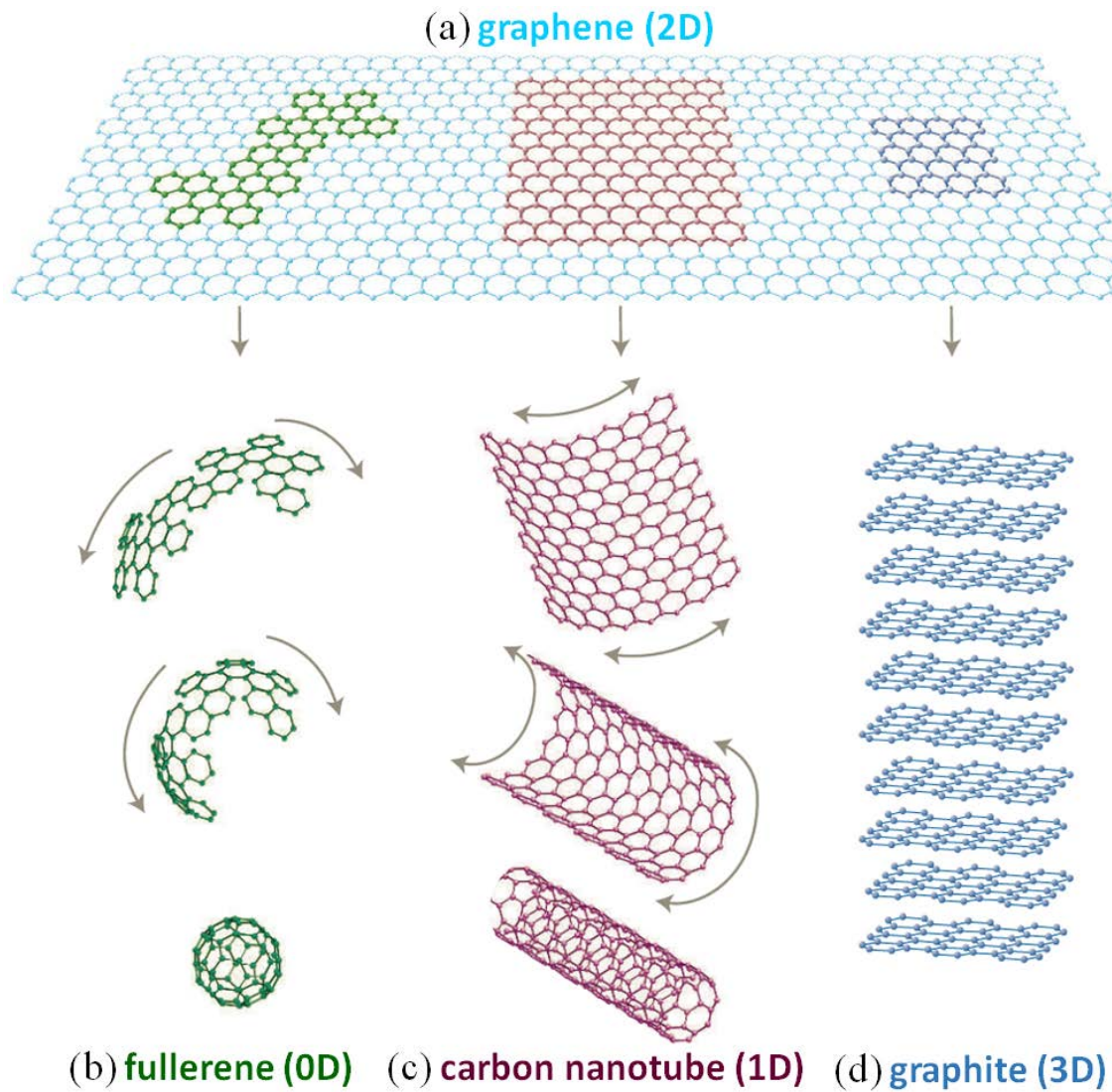


**Figure 2.1. Allotropes of carbon.** (a) Graphene is a 2D honeycomb lattice structure of carbon atoms. It is a mother building material for carbon materials in other dimensionalities. (b) Fullerene ( $C_{60}$ ) is a 0D buckyball molecule constructed by wrapping graphene with the introduction of pentagons on the hexagonal lattice. (c) Carbon nanotube is a 1D material that can be obtained by rolling up a graphene layer. (d) Graphite is a 3D structure consisting of several graphene layers electronically connected by van der Waals force. Adapted from <sup>2</sup>.

## CHAPTER 2

### *Magneto-optics in multilayer epitaxial graphene*

---

Graphene was isolated for the first time, in the experiment carried out by K. S. Novoselov and A. K. Geim in 2004, by repeated peeling or mechanical exfoliation of pyrolytic graphite allowing to obtain few-layer graphene to measure its optical effects on top of the Si/SiO<sub>2</sub> substrate<sup>1</sup>. They found that the electronic properties of their graphene with few layers on the Hall bar devices are different from those of 3D graphite. After this discovery, graphene has attracted great interest in both its fundamental physics study and enormous range of promising applications<sup>2–7</sup>. Graphene was shown to possess remarkable physical properties which are fundamentally different from those of metals and conventional semiconductors such as transparency, elasticity, impermeability to any gases, outstanding intrinsic strength, high electronic and thermal conductivities, and high carrier mobility. As a consequence, graphene has become a candidate material for a wide range of applications, for example, a new generation of nanoscale ultra-fast transistors or flexible displays.

As seen previously, graphene presents generally in the form of a stack of several monolayers electronically disconnected from each other. However, stacking in a regular order can change considerably the electronic properties of layered graphene. In this section, the electronic properties of graphene corresponding to the number of graphene sheets and their stacking order will be described.

#### **1.1. Ideal graphene**

An ideal graphene is a 2D single crystal layer consisting of carbon atoms arranged in a hexagonal lattice structure shown in Fig. 2.1(a) as a honeycomb. The physical properties of graphene can be explained by the special arrangement of carbon atoms.

Interestingly, four valence electrons of a carbon atom ( $1s^2 2s^2 2p^2$ ) in graphene have a particular electron configuration. In other words, three of them form an  $sp^2$  hybridization between one s orbital and two p orbitals, and the last electron is arranged in the other p orbital as shown in Fig. 2.2(a). The robustness of the honeycomb lattice structure of graphene results from the formation of a  $\sigma$  bond, owing to the  $sp^2$  hybridization, between two carbon atoms separated by a distance  $a \sim 1.42 \text{ \AA}$  as shown in Fig. 2.2(b). Three  $\sigma$  bonds construct a trigonal planar structure with the angle  $120^\circ$  among them. Since the  $\sigma$  bond is fully filled of electrons, this covalent bonding between two adjacent carbon atoms is thus strong. The p orbital perpendicular to the trigonal planar structure will be bound with the p orbitals of neighboring carbon atoms, forming a half-filled  $\pi$  bond which is not strong (Fig. 2.2(b)).

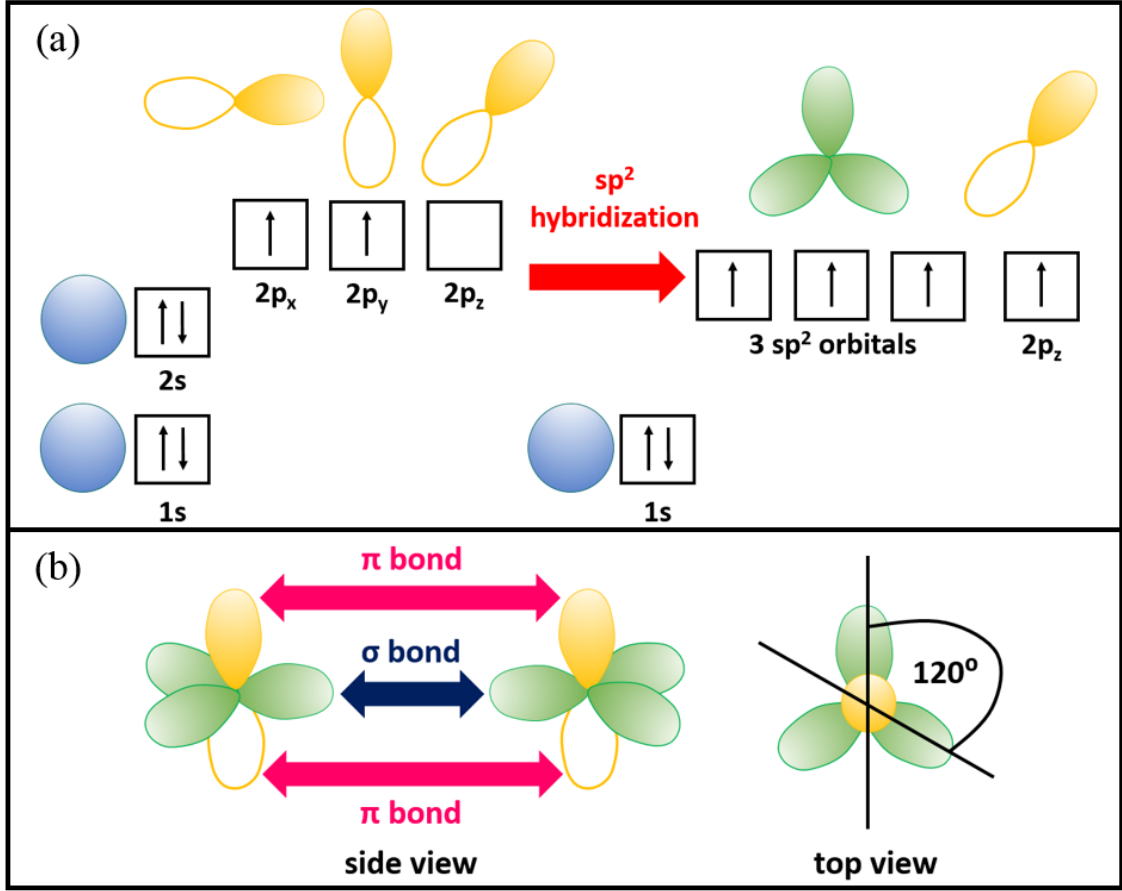


**Figure 2.2. Origin of the robustness of graphene.** (a) Orbital hybridization of a carbon atom in graphene. Four valence electrons ( $2s^2 2p^2$ ) form three  $sp^2$  hybridized orbitals and one half-filled p orbital. (b)  $\sigma$  and  $\pi$  bonds between two neighboring carbon atoms separated by a distance  $a \sim 1.42 \text{ \AA}$ . The angle between two  $\sigma$  bonds is  $120^\circ$ , yielding a trigonal planar structure.

The electronic band structure of single-layer of graphene was first proposed by P. R. Wallace in 1947 via tight-binding approach for band description in bulk graphite<sup>8</sup>. He considered the perpendicular p orbital, forming the  $\pi$  bond (Fig. 2.2(b)), that is responsible for the electronic band structure of graphene. Fig. 2.3(a) shows the hexagonal crystalline structure of graphene composed of carbon atoms arranged in two different sites: A and B. In the tight-binding approximation, the nearest-neighbor hopping energy or the necessary energy for electrons to hop from one site to both nearest- ( $t$ ) and next-nearest-neighbor ( $t'$ ) sites is defined. A unit cell (green shaded area in Fig. 2.3(a)) contains two carbon atoms (A and B) and its lattice vectors can be written in the  $(e_x, e_y)$  basis as:

$$\vec{a}_1 = \frac{a}{2} (3, \sqrt{3}) \text{ and } \vec{a}_2 = \frac{a}{2} (3, -\sqrt{3}) \quad (2.1)$$

where  $a \sim 1.42 \text{ \AA}$  is the distance between the nearest two carbon atoms. The lattice parameter can then be defined as  $a_0 = |\vec{a}_1| = |\vec{a}_2| = \sqrt{3}a \sim 2.46 \text{ \AA}$ .

## CHAPTER 2

### Magneto-optics in multilayer epitaxial graphene

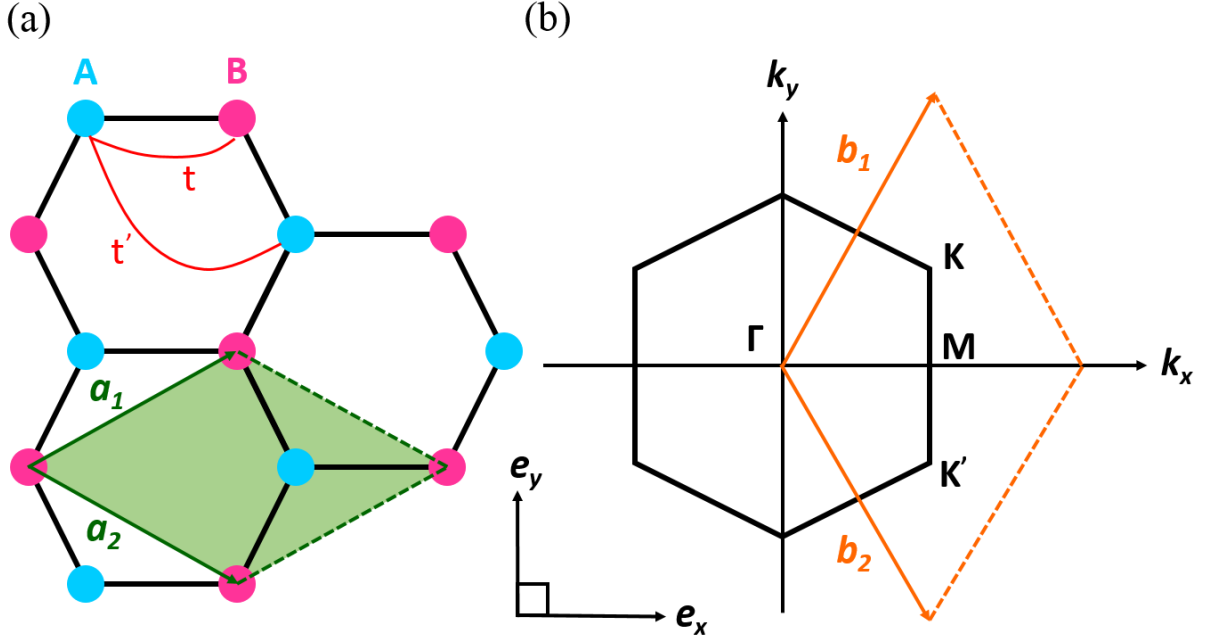


**Figure 2.3. Ideal graphene crystalline structure.** (a) Hexagonal lattice structure of graphene in the real space. Carbon atoms are arranged in two different sites A and B. The unit cell of graphene is represented in the green shaded area containing two atoms (A and B) and can be identified by two lattice vectors  $\vec{a}_1$  and  $\vec{a}_2$ . (b) Corresponding hexagonal Brillouin zone centered at the  $\Gamma$ -point in the reciprocal space. High-symmetry points  $K$ ,  $K'$  and  $M$  are also shown. The reciprocal lattice vectors  $\vec{b}_1$  and  $\vec{b}_2$  form a unit cell enclosing the  $K$  and  $K'$  points where the Dirac cones are located.

The corresponding Brillouin zone is also hexagonal (Fig. 2.3(b)). Its reciprocal lattice vectors  $\vec{b}_1$  and  $\vec{b}_2$ , verifying  $\vec{a}_i \cdot \vec{b}_j = 2\pi\delta_{ij}$  with  $\delta_{ij} = 0$  for  $i \neq j$  and  $\delta_{ij} = 1$  for  $i = j$ , can be expressed in the  $(\vec{e}_x, \vec{e}_y)$  basis as follows:

$$\vec{b}_1 = \frac{2\pi}{3a}(1, \sqrt{3}) \text{ and } \vec{b}_2 = \frac{2\pi}{3a}(1, -\sqrt{3}) \quad (2.2)$$

The fundamental physics of graphene occurs at the high-symmetry points  $K$  and  $K'$  situated at the corners of the Brillouin zone (Fig. 2.3(b)). Their positions in the  $(\vec{e}_x, \vec{e}_y)$  basis are given by:

$$\vec{K} = \left(\frac{2\pi}{3a}, \frac{2\pi}{3\sqrt{3}a}\right) \text{ and } \vec{K}' = \left(\frac{2\pi}{3a}, -\frac{2\pi}{3\sqrt{3}a}\right) \quad (2.3)$$

The energy dispersion in the momentum space derived from the tight-binding calculation reads:

$$E_{\pm}(\vec{k}) = \pm t \sqrt{3 + f(\vec{k})} - t' f(\vec{k}) \quad (2.4a)$$

$$\text{with } f(\vec{k}) = 2 \cos(\sqrt{3}k_y a) + 4 \cos(\frac{\sqrt{3}}{2}k_y a) \cos(\frac{3}{2}k_x a) \quad (2.4b)$$

where  $\pm$  signs refer to the upper  $\pi$  band energy and the lower  $\pi$  band energy, respectively. Generally, the band structure of graphene is asymmetric because of the nonzero values of  $t$  and  $t'$ . Most theoretical calculations found  $t \sim 3$  eV<sup>3,4</sup>, while the value of  $t'$  is not well known and it could be  $0.02t \leq t' \leq 0.2t$ <sup>9</sup>. We notice that if we neglect the hopping energy between two same sublattices  $t' = 0$ , the band structure will become symmetric around zero energy as displayed in Fig. 2.4.

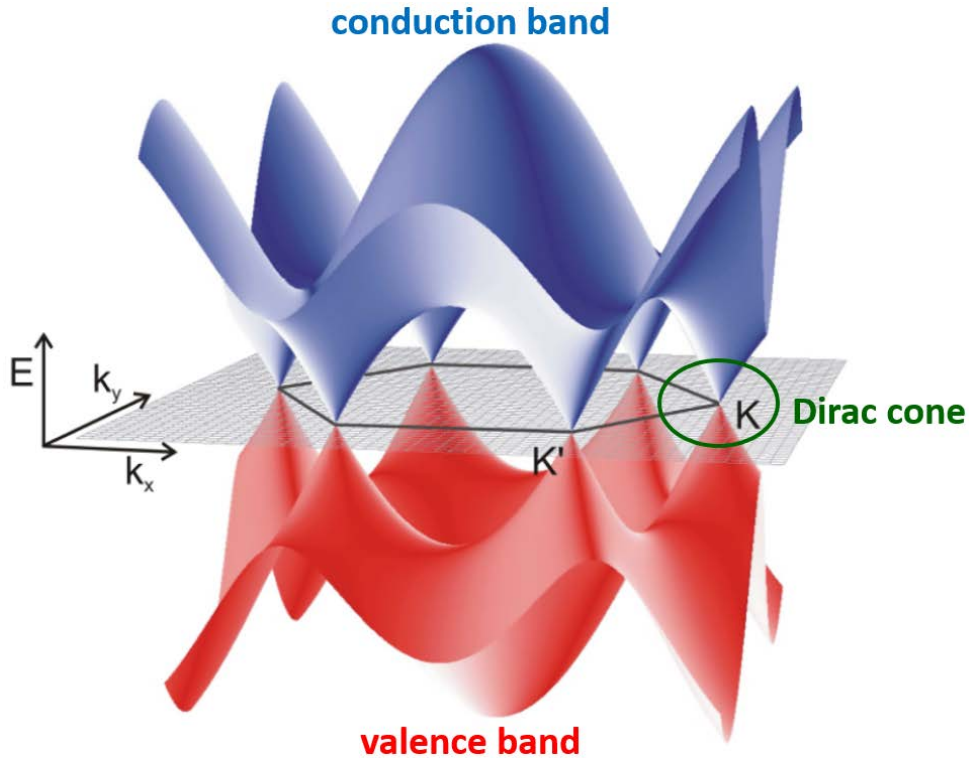


**Figure 2.4. Electronic band structure of graphene.** The band structure of graphene in the momentum space is symmetric when  $t' = 0$ . The upper  $\pi$  band and lower  $\pi$  band correspond respectively to the conduction and valence bands. In the vicinity of the Dirac points ( $K$  or  $K'$ ), the energy dispersion is linear and forms a Dirac cone as can be seen in the green circle. Adapted from<sup>4</sup>.

Now, we consider the graphene band structure in the vicinity of the  $K$  or  $K'$  points. To do this, we write  $\vec{k} = \vec{K} + \vec{q}$ . Here,  $\vec{q}$  is the momentum measured relatively to the  $K$  or  $K'$  points and  $|\vec{q}| \ll |\vec{K}|$ . We thus get:

$$E_{\pm}(\vec{q}) \approx \pm \hbar v_F |\vec{q}| \quad (2.5)$$

Here,  $\hbar$  is the reduced Planck constant. This shows that the energy-momentum dispersion given in Eq. 2.4a (for  $t' = 0$ ) becomes nearly linear and rotationally symmetric close to the  $K$  or  $K'$  points, yielding a Dirac cone as can be seen in the green circle of Fig. 2.4. Hence, graphene can exhibit the zero-bandgap semiconductor or semimetal character for which the



## CHAPTER 2

### *Magneto-optics in multilayer epitaxial graphene*

conduction and valence bands touch or cross at the  $K$  or  $K'$  points, named as Dirac points. Note that in pristine graphene, the Fermi energy is situated at the Dirac points.

The parameter  $v_F$  having a dimension of a velocity is known as Fermi velocity. This physical quantity is directly related to the coupling strength between the adjacent carbon atoms or the nearest-neighbor hopping energy  $t$ . The expression of  $v_F$  is given by:

$$v_F = \frac{3ta}{2\hbar} \quad (2.6)$$

One can estimate the value of  $v_F \sim 1 \times 10^6$  m/s for  $t \sim 3$  eV. The Fermi velocity is approximately 300 times smaller than the speed of light  $c \sim 3 \times 10^8$  m/s. This shows the unusual semimetallic behavior of charge carriers in graphene. In other words, they behave as relativistic particles moving with the Fermi velocity  $v_F$  and their rest mass is zero. These particles are known as massless Dirac fermions that can be described by a Dirac Hamiltonian. Interestingly, these important results analogous to high-energy physics show that quantum relativistic phenomena can also be investigated and observed in low-energy physics. The particular properties seen in an ideal graphene are therefore an essential starting point to study the electronic properties of carbon-based materials in other dimensionalities.

### 1.2. Bilayer graphene

The electronic properties of a single layer of graphene or monolayer graphene have been described in the previous subsection. In reality, a monolayer graphene is very difficult to be isolated experimentally. Naturally, graphene presents in the form of several monolayers stacked in a regular order. Fig. 2.5 clearly shows three possible orientations of graphene layers: A, B and C. The influence of particular stacking orders on the electronic properties of graphene will be discussed later in the text<sup>10,11</sup>.

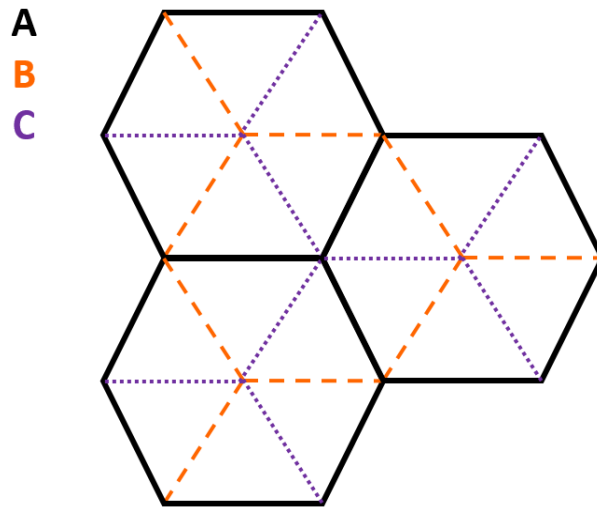


**Figure 2.5. Schematic of three different orientations of graphene layers.** ABA (Bernal) stacking is found in bilayer and trilayer graphenes. ABC (rhombohedral) stacking can be found in trilayer graphene.

Bilayer graphene is constituted of two monolayers of graphene with the AB stacking structure (Fig. 2.5). Since the crystalline structure of bilayer graphene can be considered as an elementary brick for constructing the whole lattice structure of graphite (Fig. 2.6(a)), the Slonczewski-Weiss-McClure (SWM) model developed for describing the electronic band structure of graphite<sup>12,13</sup> can thus be applied in bilayer graphene<sup>14</sup>. In contrast to monolayer graphene seen earlier, the electrons in bilayer graphene are massive Dirac fermions satisfying a parabolic energy dispersion<sup>15</sup> and they exhibit interesting quantum phenomena such as the integer quantum Hall effect with anomalies<sup>16</sup>. In the SWM model, six electronic hopping energies associated with overlap and transfer integrals calculated for nearest neighboring atoms are  $t$ ,  $t_1$ ,  $t_2$ ,  $t_3$ ,  $t_4$  and  $t_5$ . Only the parameters  $t$ ,  $t_1$ ,  $t_3$  and  $t_4$  denoted by red arrows (Fig. 2.6(a)) are considered in the calculation of the band structure of bilayer graphene. In bilayer graphene, interesting physical phenomena take place at the high-symmetry  $K$  and  $K'$  points of the Brillouin zone.

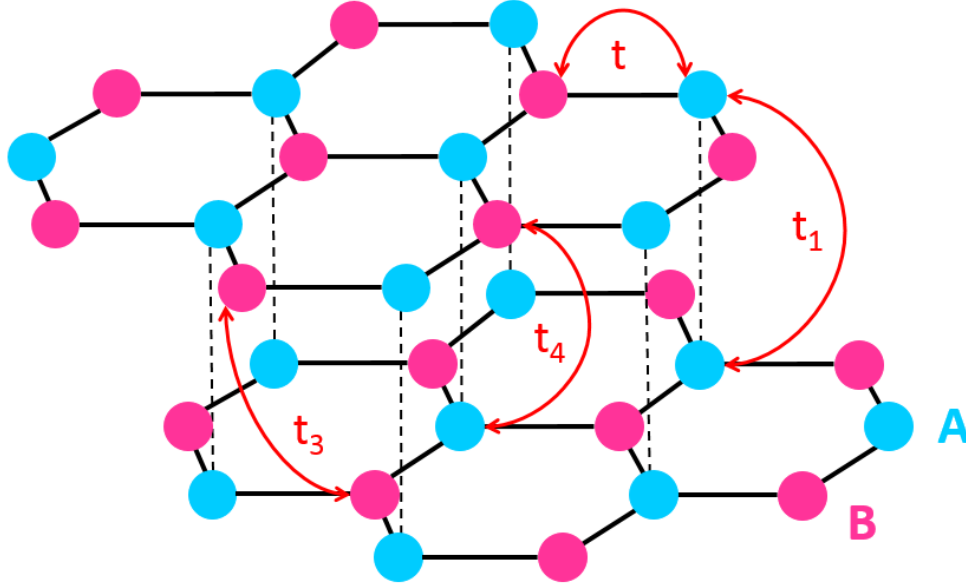


**Figure 2.6. Crystalline structure of bilayer graphene.** Bilayer graphene lattice structure in the AB stacking order as an elementary brick of graphite lattice structure. The A atoms of each layer are over each other. Only the Slonczewski-Weiss-McClure (SWM) parameters  $t$ ,  $t_1$ ,  $t_3$ , and  $t_4$  corresponding to the hopping energies of nearest neighboring atoms are presented.

The SWM parameters can be determined by various investigation techniques<sup>17</sup>. Typically,  $t_1 \sim 0.4$  eV,  $t_3 \sim 0.3$  eV, and  $t_4 \sim 0.04$  eV. The simplest way to calculate the band structure of bilayer graphene is to neglect the parameters  $t_3$  and  $t_4$ , and consider only the parameter  $t_1$ . Under these conditions, the electronic band structure of bilayer graphene at the  $K$  and  $K'$  points is constituted of four bands (Fig. 2.7). Their energy dispersions are parabolic at low energies and can be expressed as:

## CHAPTER 2

### Magneto-optics in multilayer epitaxial graphene

$$E_{4,3}(\vec{k}) = \pm \frac{t_1}{2} + \sqrt{\frac{t_1^2}{4} + \hbar^2 v_F^2 k^2} \quad (2.7a)$$

and

$$E_{2,1}(\vec{k}) = \pm \frac{t_1}{2} - \sqrt{\frac{t_1^2}{4} + \hbar^2 v_F^2 k^2} \quad (2.7b)$$

Here, the Fermi velocity  $v_F$  has the same definition and the same value as that in the case of a single-layer graphene (Eq. 2.6). The bands numbered 3 and 4 constitute the conduction bands, while the bands 1 and 2 correspond to the valence bands. We notice that the band structure is symmetric with respect to the point where the bands 2 and 3 touch each other. At the  $K$  and  $K'$  points, the band 4 is shifted upwards by the energy  $t_1$  from the band 3, and the band 1 is shifted downwards by the same energy from the band 2. Note that if there is no interlayer coupling constant  $t_1 = 0$ , we will obtain the band structure of ideal monolayer graphene at the  $K$  and  $K'$  points (Eq. 2.5).

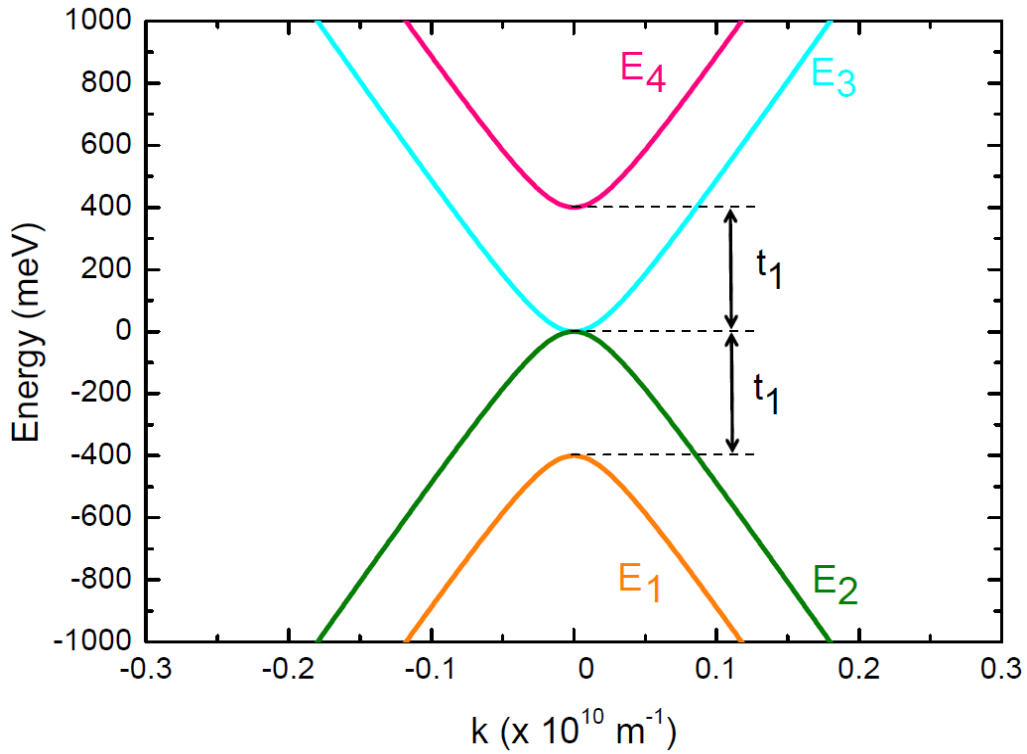


**Figure 2.7. Scheme of the electronic band structure of bilayer graphene.** The electronic band structure around the  $K$  and  $K'$  points of bilayer graphene schematically shown here is calculated with  $v_F = 1 \times 10^6$  m/s by taking into account only the principal parameter  $t_1 = 0.4$  eV and when the interlayer potential is not considered. The energy dispersion of all four bands is parabolic at low energies.

### 1.3. Trilayer graphene

Trilayer graphene is composed of three graphene monolayers stacked in the ABA (Bernal) or ABC (rhombohedral) sequences as represented in Fig. 2.8. Trilayer graphene has

been experimentally realized by several fabrication methods and theoretically studied, leading to explore its remarkably interesting electronic properties<sup>18–24</sup>. Importantly, the electronic properties of graphene trilayers depend drastically on how the three stacked layers are rearranged<sup>10,11</sup>.

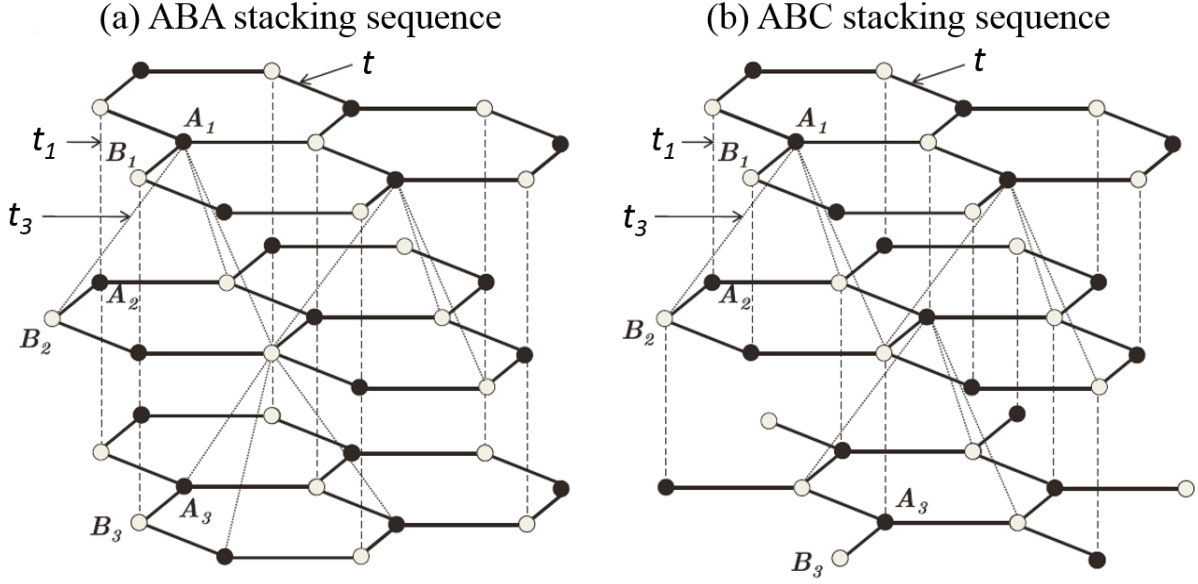


**Figure 2.8. Crystalline structure of trilayer graphene.** Trilayer graphene possesses three graphene monolayers. These three layers can be stacked in the ABA sequence (a) or ABC sequence (b). Some hopping energy parameters are also denoted. Adapted from<sup>25</sup>.

The low-energy electronic band structures of ABA- and ABC-stacked trilayer graphene in the vicinity of the  $K$  point of the Brillouin zone are different and their energy dispersions are written as<sup>25</sup>:

- For the ABA stacking sequence:

$$E_{\alpha}(\vec{k}) = \pm \sqrt{t_1^2 + \hbar^2 v_F^2 k^2 + \alpha \sqrt{t_1^4 + 2t_1^2 \hbar^2 v_F^2 k^2}} \quad (2.8a)$$

and

$$E_0(\vec{k}) = \pm \hbar v_F |\vec{k}| \quad (2.8b)$$

Here,  $v_F$  and  $t_1$  have the same definition as described previously for the monolayer and bilayer graphenes. Fig. 2.9(a) schematically shows the trilayer graphene band structure around the  $K$  point in the ABA stacking order with six energy bands in total. In the expression of  $E_{\alpha}(\vec{k})$ ,  $\alpha = +1$  refers to the energy bands that do not touch each other at the  $K$  point (green lines) and  $\alpha = -1$  refers to the energy bands touching each other at the  $K$  point (red lines).  $E_0(\vec{k})$  represents two linear band dispersions (black lines). We notice that the low-energy band structure of ABA trilayer graphene is a combination of two massless monolayer

## CHAPTER 2

### Magneto-optics in multilayer epitaxial graphene

graphene-like subbands with linear dispersion and four massive bilayer graphene-like subbands with parabolic dispersion.

- For the ABC stacking sequence:

$$E_{1,\alpha}(\vec{k}) = 2\sqrt{Q} \cos\left(\frac{\theta+2\pi}{3}\right) - \alpha \frac{v_F |\vec{k}|}{3} \quad (2.9a)$$

$$E_{2,\alpha}(\vec{k}) = 2\sqrt{Q} \cos\left(\frac{\theta+4\pi}{3}\right) - \alpha \frac{v_F |\vec{k}|}{3} \quad (2.9b)$$

$$E_{3,\alpha}(\vec{k}) = 2\sqrt{Q} \cos\left(\frac{\theta}{3}\right) - \alpha \frac{v_F |\vec{k}|}{3} \quad (2.9c)$$

Here, new parameters are  $\theta = \cos^{-1}\left(\frac{\alpha R}{\sqrt{Q^3}}\right)$ ,  $R = \frac{8v_F^3 k^3}{27} - \frac{v_F k t_1^2}{6}$ , and  $Q = \frac{3t_1^2 + 4v_F^2 k^2}{9}$ .  $v_F$ ,  $t_1$  and  $\alpha = \pm 1$  have the same definition as in the ABA stacking order. Fig. 2.9(b) schematically shows the ABC trilayer graphene band structure around the  $K$  point with six different energy bands.

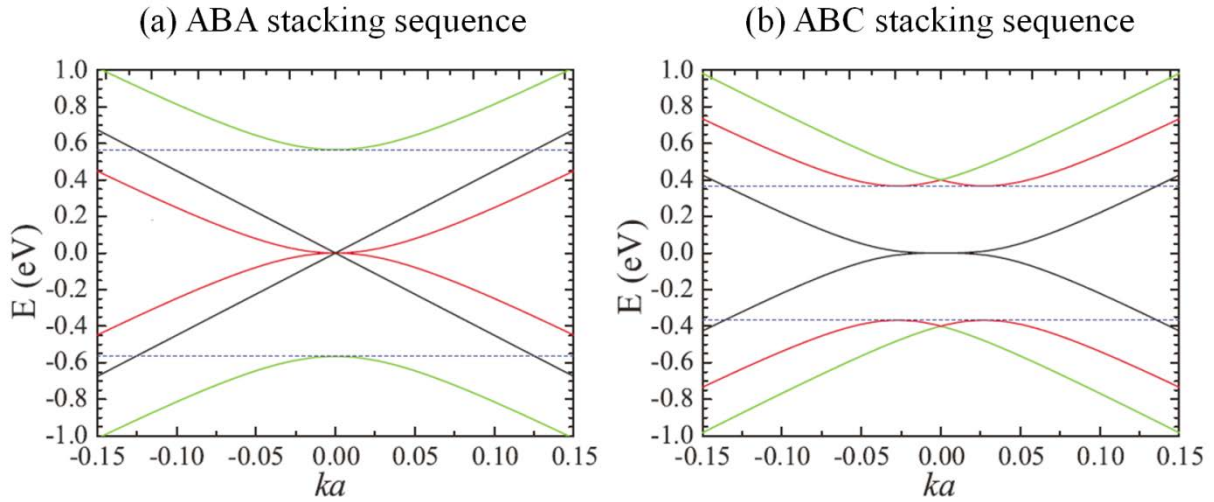


**Figure 2.9. Low-energy electronic band structure of trilayer graphene around the  $K$  point.** (a) The band structure of ABA-stacked trilayer graphene exhibits two massless monolayer graphene-like dispersions (black lines) and four massive bilayer graphene-like dispersions (red and green lines). (b) The band structure of ABC-stacked trilayer graphene with six subbands in total. These band structures are calculated with  $v_F \sim 1 \times 10^6$  m/s (for  $t = 3$  eV) and  $t_1 = 0.4$  eV. The dashed horizontal lines indicate the position of the bottom (top) of the upper (lower) bands. Adapted from <sup>25</sup>.

Interestingly, trilayer graphene with the Bernal stacking possesses lower energy configuration than that in the rhombohedral stacking, therefore the Bernal trilayer graphene is energetically more favorable than the rhombohedral one <sup>26</sup>. Consequently, an energy barrier is required for moving carbon atoms assembled in the Bernal sequence to be rearranged in the rhombohedral order. Furthermore, the rhombohedral trilayer graphene exhibits a tunable

narrow gap semiconductor character due to the gap opening in the presence of a perpendicular electric field <sup>11,19,22,23</sup>.

## 1.4. Multilayer graphene

Multilayer graphene consists of many graphene layers stacked in a particular sequence following three inequivalent orientations shown in Fig. 2.5. The most common observed stacking sequence is ABA, whereas the ABC order can also be found but less frequently due to the higher energy configuration <sup>26</sup>. In this thesis, we will mainly focus on multilayer epitaxial graphene (MEG) fabricated by thermal decomposition on the C-terminated or Si-terminated faces of SiC substrates that we will describe later in the subsection 2.4. The electronic properties of MEG were shown by several investigation techniques to be predominantly similar to those of single-layer graphene <sup>27–30</sup>. ARPES spectra in Fig. 2.10 show the Dirac cones as the band structure of the graphene layers in a MEG sample. This can be explained by the existence of a rotational stacking occurring in each pair of two adjacent graphene sheets that make all the graphene layers electronically decoupled and satisfy the Dirac linear dispersion <sup>29,30</sup>. The MEG sometimes contains a small contribution of bilayer graphene feature and one can thus observe the signature of the electronic band structures stemming from both monolayer and bilayer graphenes <sup>31–33</sup>.

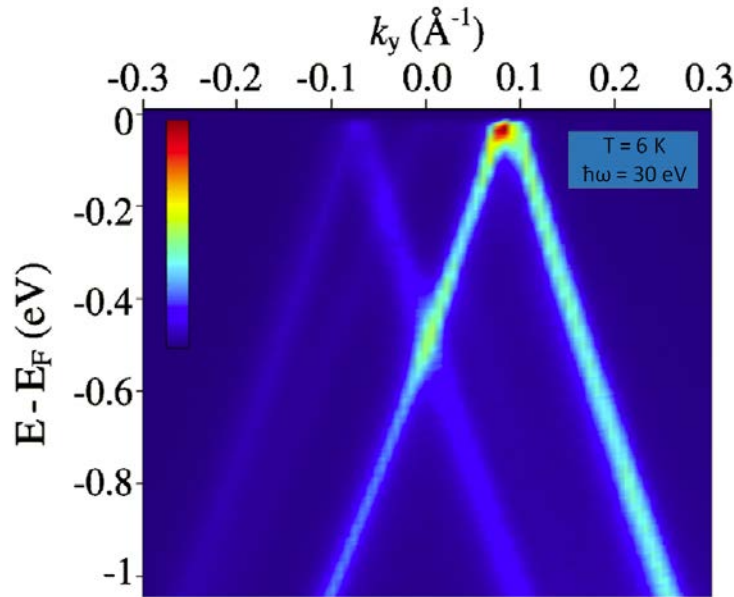


**Figure 2.10. ARPES spectra showing the band structure of an 11-layer epitaxial graphene grown on the C-face of 6H-SiC substrate.** ARPES measurement shows the top three graphene layers of the sample. Two unperturbed Dirac cones with  $v_F \sim 1 \times 10^6$  m/s were observed, evidencing that the graphene layers are electronically decoupled and the MEG sample behaves like an isolated graphene sheet. Adapted from <sup>30</sup>.

## **2. Fabrication methods of graphene**

Graphene has long been theoretically and experimentally demonstrated to exhibit outstanding physical properties as mentioned previously. However, the production of graphene to attain the required properties for applications is extremely challenged. To this day, a large number of existing fabrication methods have been employed and continuously developed in order to prepare graphene with specific properties suitable for applications. Such methods are mainly categorized into two classes: bottom-up and top-down methods. The first one is based on the formation of 2D graphene lattice resulting from the covalent bonding between carbon atoms. The last one depends on the direct exfoliation of graphite. As a result, graphene samples obtained by different methods are in various dimensions and their quality is distinguishing. In this section, we will focus only on certain essential techniques producing scalable graphene samples. The four following production methods of graphene will be described as well as their advantages leading to the feasibility of numerous graphene applications.

### **2.1. Mechanical exfoliation**

The first method to fabricate graphene is mechanical exfoliation. There are several mechanical exfoliation techniques<sup>34</sup> but at this stage we will concentrate only on micromechanical cleavage of graphite generating the first graphene flakes in the real world<sup>1</sup>. This technique allows to obtain monolayers of graphene from natural graphite thanks to its particular structure in stacked graphene sheets. Fig. 2.11 shows how to create graphene by this process. One can easily make mechanically exfoliated graphene by peeling a great number of times in different orientations some natural graphite grains on an adhesive piece (Fig. 2.11(b)). The normal force from the peeling applied on the graphite surface plays a dominant role of the exfoliation mechanism (Fig. 2.11(a)). The main objective of the peeling is to mechanically overcome the van der Waals attraction force between two adjacent graphene layers. One will then get on the surface of the adhesive a quasi-homogeneous distribution of graphene monolayers, bilayers, multilayers or graphite micro-grains (Fig. 2.11(c)). Finally, the graphene sample will be transferred to the surface of a substrate for measurements.

The mechanical exfoliation technique is one of the most promising platforms to achieve high-quality graphene with the electron mobility  $> 2 \times 10^5 \text{ cm}^2/(\text{V.s})$  at ambient temperature or  $> 1 \times 10^6 \text{ cm}^2/(\text{V.s})$  at low temperatures. The dimension of exfoliated graphene is typically  $> 1 \text{ mm}^2$ . Importantly, the graphene production using this technique can be effectuated at an extremely low cost compared to other fabrication methods. However, the research on mechanically exfoliated graphene always remains in laboratories because this technique is highly time-consuming, exfoliated graphene samples extracted from graphite have uncontrollable dimensions and defects, and they are impossible to be scaled up for industrial production. Therefore, it is substantial to improve the mechanical exfoliation efficiency.



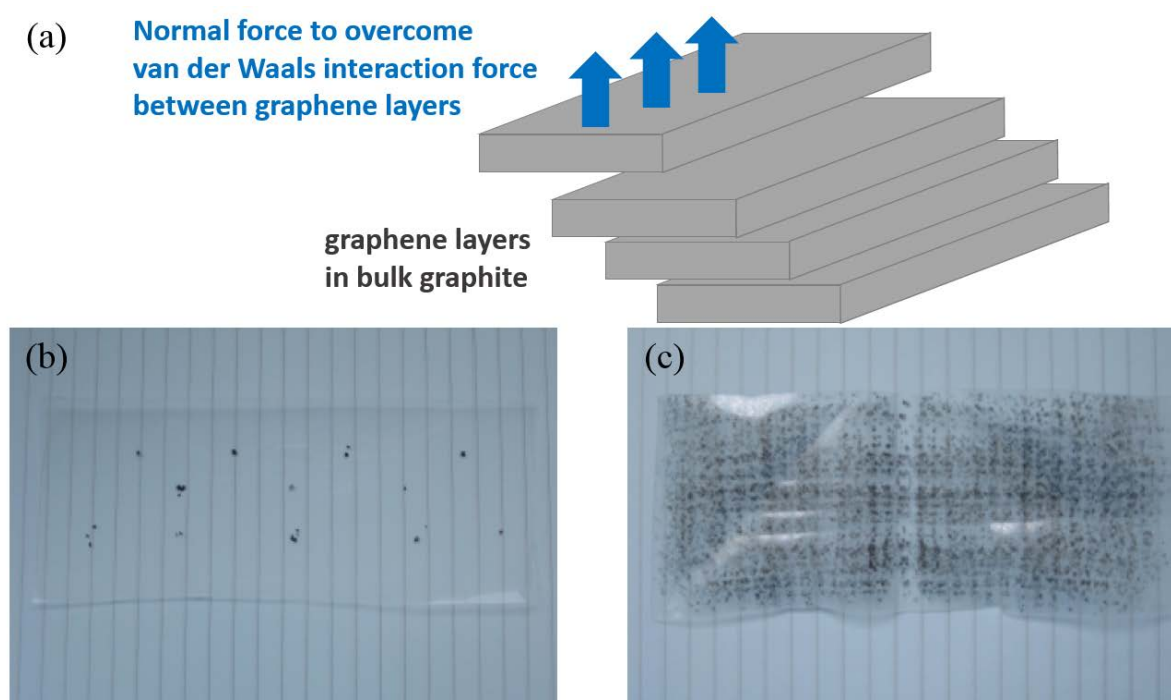


**Figure 2.11. Illustration of graphene production by mechanical exfoliation: micromechanical cleavage.** (a) Normal force denoted by blue arrows is applied on the surface of bulk graphite during the peeling. To exfoliate graphite into graphene flakes, the normal force has to overcome the van der Waals interaction force between two adjacent graphene layers. (b) Natural graphite grains are deposited on an adhesive sheet. (c) Exfoliated graphene flakes obtained from the repeated peeling in different oriented axes. (b) and (c) are adapted from the Ph.D. thesis of J. Guignard defended in 2011.

## 2.2. Chemical exfoliation

Graphene flakes can also be prepared from graphite via a variety of chemical approaches followed by exfoliation such as liquid-phase exfoliation, graphene from graphite oxide, electrochemical exfoliation, and supercritical fluid exfoliation<sup>35</sup>. These various techniques rely in principle on the intercalation procedure of specific molecules between graphene layers stacked in graphite in order to provoke the delamination through chemical reactions. The most straightforward chemical method allowing the reduction of the van der Waals forces is to dip graphite into a liquid medium. Fig. 2.12 schematically elucidates the liquid-phase exfoliation process of graphite<sup>36</sup>. The molecules in N-methylpyrrolidone solvent will insert between two adjacent graphene sheets. Ultrasonication is then used to induce exfoliation, leading to the splitting of graphite into individual graphene layers in the suspension. Nevertheless, the interactions between the solvent and the graphene flakes need to compensate the attractive forces among the graphene sheets. Hence, surfactant or intercalator molecules can be sometimes added in a solvent to avoid graphene re-aggregation caused by van der Waals forces after the sonication.



## CHAPTER 2

### *Magneto-optics in multilayer epitaxial graphene*

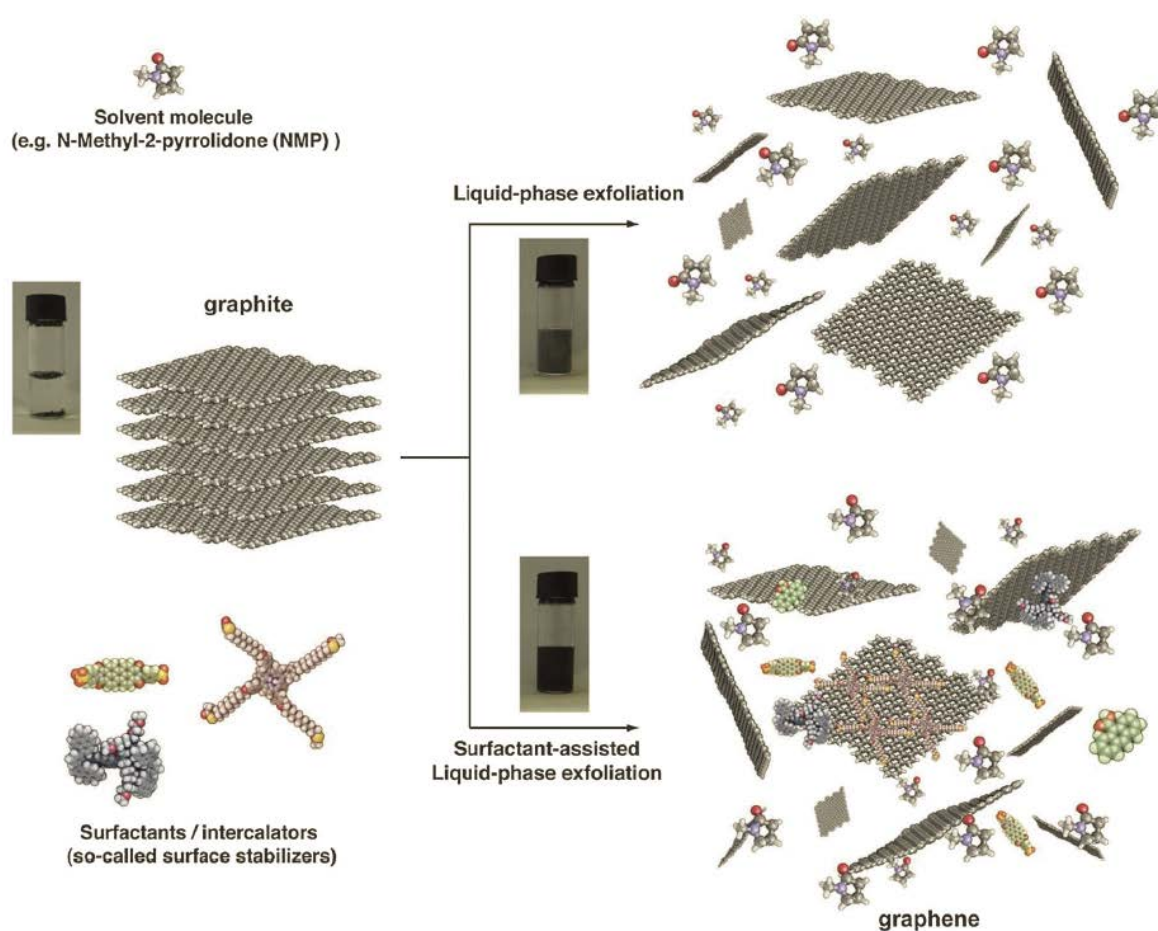


**Figure 2.12. Schematic illustration of graphene production by chemical exfoliation: liquid-phase exfoliation.** Graphite is immersed in N-methylpyrrolidone solvent. The solvent molecules will intervene between graphene layers of graphite. With the aid of sonication, graphite will split into individual graphene sheets. The liquid-phase exfoliation process can be carried out with or without surfactant or intercalator molecules, helping to avoid the re-aggregation of graphene after the chemical exfoliation. Adapted from <sup>36</sup>.

Since the graphene flakes obtained by this technique flow in a solvent, they are thus free of any substrate. This means that there is no charge transfer from substrates to the graphene flakes. Moreover, the graphene flakes have possibilities to be deposited onto many different substrate materials. Chemical exfoliation method provides potentially up-scalable graphene samples with the electron mobility of about  $100 \text{ cm}^2/(\text{V.s})$  even if, for example, the controls of lateral size and layer number have to be improved. A wide range of applications of chemically exfoliated graphene are, for instance, printing inks, coatings, graphene-based composites, thin film transistors, transparent conductive layers and photovoltaics.

### 2.3. Chemical vapor deposition

Another method to produce graphene is chemical vapor deposition (CVD) of which the principal aims at growing graphene layers using hydrocarbon gas precursors ( $\text{CH}_4$ ) which

decompose at high temperatures  $\sim 1,000$  °C to carbon radicals forming at the surface of various transition metal substrates (for example Ni or Cu)<sup>37–39</sup>. After cooling with an appropriate rate, the formation of graphene layers at the surface of the metal substrates can occur. The as-grown CVD graphene can be transferred onto other insulator substrates (for example Si/SiO<sub>2</sub>, glass or h-BN) for characterizations or applications. Fig. 2.13(a) schematically represents the CVD growth of graphene. Fig. 2.13(b) shows briefly the transfer process of the CVD-graphene using polymethyl methacrylate (PMMA) onto a substrate.

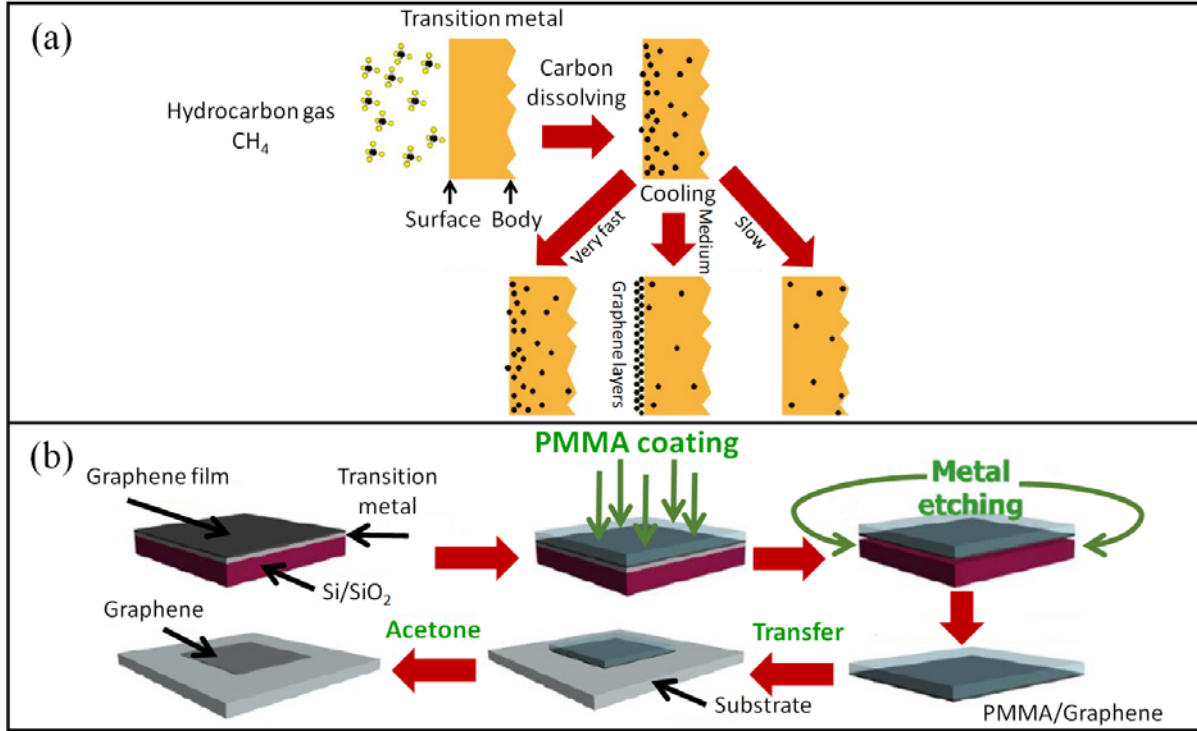


**Figure 2.13. Schematic representation of graphene preparation by chemical vapor deposition (CVD).** (a) CVD growth of graphene on a transition metal using hydrocarbon gas precursors at high temperatures. When cooling with an appropriate rate, graphene layers can form at the surface of the metal substrate. (b) Transfer process of CVD-graphene onto an insulator targeting substrate. A thin layer of polymethyl methacrylate (PMMA) is usually used as coating on the CVD-graphene. The metal substrate is then etched from the sample. PMMA/graphene thin film is then transferred onto a substrate. Acetone is used at the final stage to remove PMMA, leaving only graphene layers on the substrate. (a) is adapted from<sup>37</sup> and (b) is adapted from<sup>39</sup>.

The CVD technique provides single-layer and few-layer graphenes with the electron mobility of approximately  $10,000 \text{ cm}^2/(\text{V.s})$  and the small number of defects. Large-scale area of CVD-graphene can be obtained with the dimension between  $1 \text{ cm}^2$  to  $1 \text{ m}^2$ . However, the number of layers and stacking order of CVD-graphene have to be controlled because these can change completely the graphene properties with respect to monolayer graphene. In addition, the removal of metallic substrates used in the CVD growth and the graphene transfer process onto other targeting substrates are big challenges to be improved and optimized in order to diminish the damage to graphene layers. All the advantages of graphene fabricated by CVD method give rise to possible applications such as coatings against corrosion, photonics,

## CHAPTER 2

### *Magneto-optics in multilayer epitaxial graphene*

sensors, field effect transistors, touch screen and flexible transparent conductive electrodes for organic photovoltaics.

#### 2.4. Epitaxy by thermal decomposition of SiC substrate

It has long been known that graphene could be grown epitaxially by thermal decomposition of materials consisting carbon atoms, for instance, hydrocarbons, carbon oxide<sup>40–43</sup>, nanodiamonds<sup>44</sup> and silicon carbide (SiC)<sup>27–30,45–47</sup>. In this thesis, we are particularly interested in multilayer epitaxial graphene or MEG grown on SiC substrates by this fabrication method. When heating at high temperatures, silicon atoms from the top layers of SiC desorb and carbon atoms left will then form in graphene lattice structure (Fig. 2.14(a)). Rotational stacking occurs during the process, leading to the electronic decoupling between the graphene layers (Fig. 2.14(b)). As a result, several layers of graphene are grown on the SiC substrates (Fig. 2.14(c)). The number of graphene monolayers (up to 100 layers) depends on the duration or temperature of the heating process.

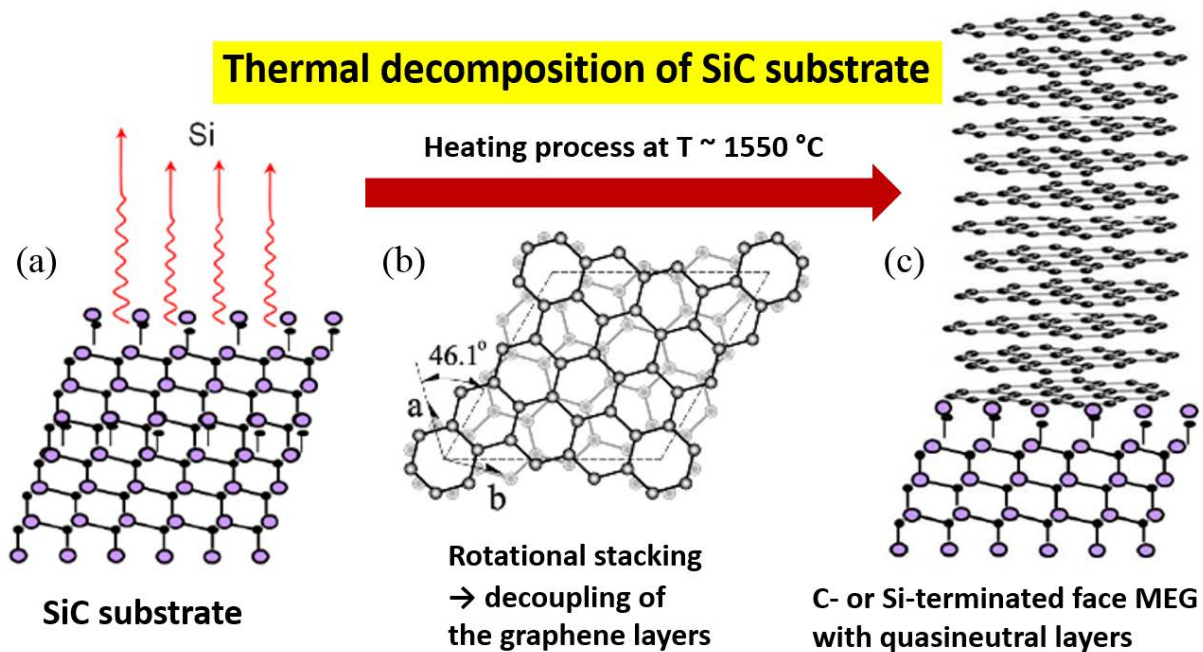


**Figure 2.14. Multilayer epitaxial graphene (MEG) prepared by thermal decomposition of SiC substrate.** (a) The SiC substrate is used in the heating treatment at temperature  $T \sim 1550^\circ\text{C}$ . Si atoms desorb from the substrate and carbon atoms left form several graphene layers. (b) Rotational stacking occurs during the epitaxial growth, leading to the electronic decoupling among graphene monolayers. (b) is adapted from<sup>29</sup>. (c) Multilayer epitaxial graphene is obtained after the thermal decomposition process on the C- or Si-face.

Two surfaces of SiC are possible for the epitaxial growth: C-terminated or Si-terminated surfaces. The graphene growth rate on the Si-terminated face is slower than that on the C-terminated face. Additionally, the number of layers and the quality of the samples grown on the C-face differ from those grown on the Si-face<sup>46,47</sup>. Lower mobility (typically  $\sim 1,000\text{--}10,000\text{ cm}^2/(\text{V}\cdot\text{s})$ <sup>47,48</sup>) samples with few layers can be obtained on the Si-face, whereas

on the C-face higher mobility (up to 250,000 cm<sup>2</sup>/(V.s) at room temperature <sup>49</sup>) samples with more layers than the first case will be obtained. This is mainly due to the fact that it is easier to control the graphene growth on the Si-face as well as the number of graphene layers which can be limited to one, two or few layers over a large area <sup>50</sup>. Furthermore, the choice of SiC substrates has an impact on the formation of epitaxial trilayer graphene in Bernal or rhombohedral stackings <sup>51,52</sup>. The dimension of the samples fabricated on both surfaces by this method is about 1 cm<sup>2</sup>. One of the typical characteristics of MEG is that the first few layers next to the SiC substrates are highly doped because of the charge transfer from the substrates to these layers but the remaining quasi-neutral layers have much more lower carrier density <sup>47</sup>.

### 3. Magneto-spectroscopy in graphene

Infrared magneto-optical spectroscopy is an efficient technique allowing the study of electronic properties of graphene. M. Orlita and his colleagues at the Laboratoire National des Champs Magnétiques Intenses (LNCMI) in Grenoble, have studied profoundly the Dirac electronic states in graphene systems <sup>4,31,49,53–58</sup>. When a magnetic field  $B$  is applied parallel to the propagation direction of light, in the Faraday geometry, and perpendicular to the graphene plane, the electron energy will be quantized into discrete Landau levels (LLs) which do not vary linearly with  $B$  due to the relativistic behavior of Dirac fermions. To calculate LLs of ideal graphene, bilayer graphene and trilayer graphene, one can proceed the Peierls substitution by replacing the wave vector  $\vec{k}$  of a considered Hamiltonian by  $i\vec{\nabla} + e\vec{A}/\hbar$ , where  $\vec{A}$  is the vector potential generating  $\vec{B} = \vec{\nabla} \times \vec{A}$  <sup>5</sup>. This is valid for electrons on a lattice system as long as the lattice parameter is much smaller than the magnetic length  $l_B = \sqrt{\hbar/eB}$ . The LLs of the system are thus given by the eigenenergies of the obtained Hamiltonian. Optical transitions between LLs can be observed in transmission spectra. This allows us to extract the physical information about the electronic band structure of graphene such as the Fermi velocity, the Fermi energy and the carrier mobility.

#### 3.1. Ideal graphene

The LL energies of ideal monolayer graphene are given by <sup>4,5,59</sup>:

$$E_n^{c,v} = \pm v_F \sqrt{2\hbar e B n} = \pm E_1 \sqrt{n} \quad (2.10)$$

where  $n \geq 0$  is the LL index. The signs  $\pm$  refer to the conduction band energies ( $E_n^c$ ) and the valence band energies ( $E_n^v$ ), respectively.  $v_F$  is the Fermi velocity as defined before and  $v_F \sim 1 \times 10^6$  m/s.  $\hbar$  and  $e$  have their usual meaning. Here,  $E_1 = v_F \sqrt{2\hbar e B}$  is defined to be a characteristic energy introduced by the magnetic field. LL energy dispersion of ideal graphene depending on  $B$  is represented in Fig. 2.15. The energy spacing between two adjacent LLs is not constant for each couple of  $n$  and  $n + 1$ . We notice that the LLs of pure graphene evolve as a function of  $\sqrt{B}$  as a consequence of the linearity of its band structure and the only one

## CHAPTER 2

### Magneto-optics in multilayer epitaxial graphene

parameter to be adjusted is  $v_F$ . The  $\sqrt{Bn}$ -dependence of the graphene LLs is in contrast to what occurs in conventional 2D electrons where  $E_n = \left(n + \frac{1}{2}\right) \hbar e B / m$ , with  $m$  is the cyclotron mass, which corresponds to equidistant LLs.

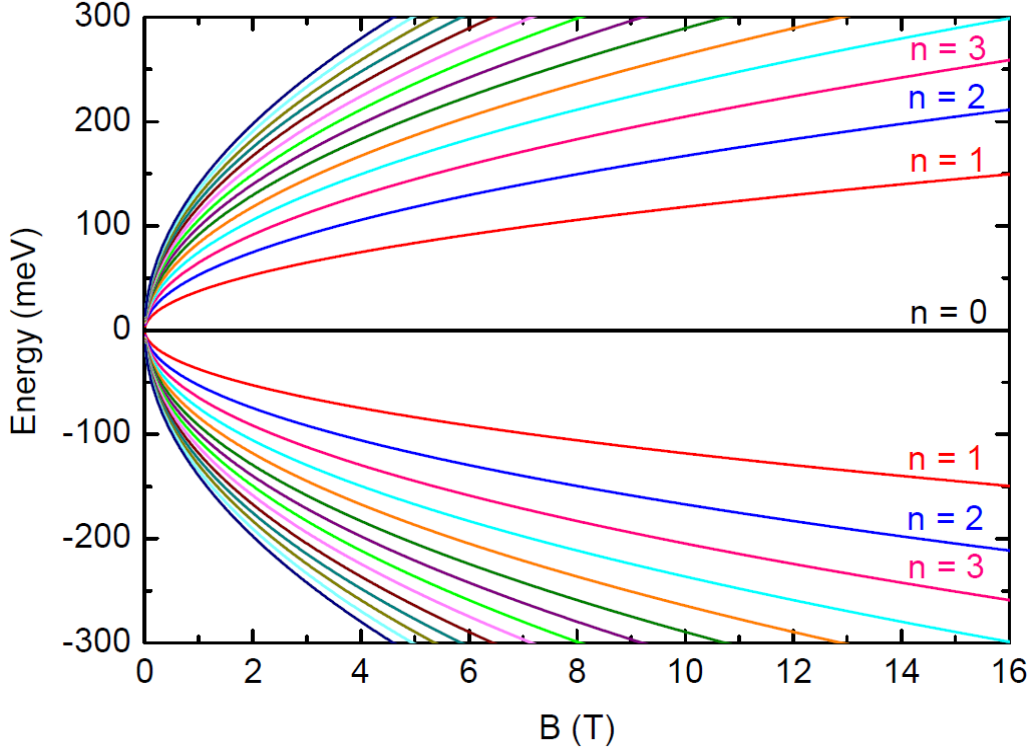


**Figure 2.15. Landau levels of ideal monolayer graphene as a function of magnetic field.** Ideal graphene Landau levels of the conduction ( $E \geq 0$ ) and valence ( $E \leq 0$ ) bands are calculated with the Fermi velocity  $v_F = 1.03 \times 10^6$  m/s.

Magneto-optical absorption experiments consist in sending infrared light beam through a graphene sample subjected to a perpendicular magnetic field in order to observe the absorption lines due to optical transitions between LLs. The selection rules governing these transitions in the Faraday geometry are  $\Delta n = \pm 1$ . Such selection rules authorize two types of transitions: intraband transitions and interband transitions. The former transitions, also called cyclotron resonances, are transitions between two LLs of the same band. The latter transitions regard transitions from a LL of the valence band to a LL of the conduction band. Fig. 2.16 illustrates, for a given Fermi energy  $E_F$  (green line), possible intraband (blue arrows) and interband (red arrows) transitions between LLs of ideal monolayer graphene calculated for  $v_F = 1.03 \times 10^6$  m/s with the selection rules  $\Delta n = \pm 1$ . Note that all the transitions can occur when the starting level is populated with electrons ( $E < E_F$ ) and the arrival level is at least partially depopulated ( $E > E_F$ ).



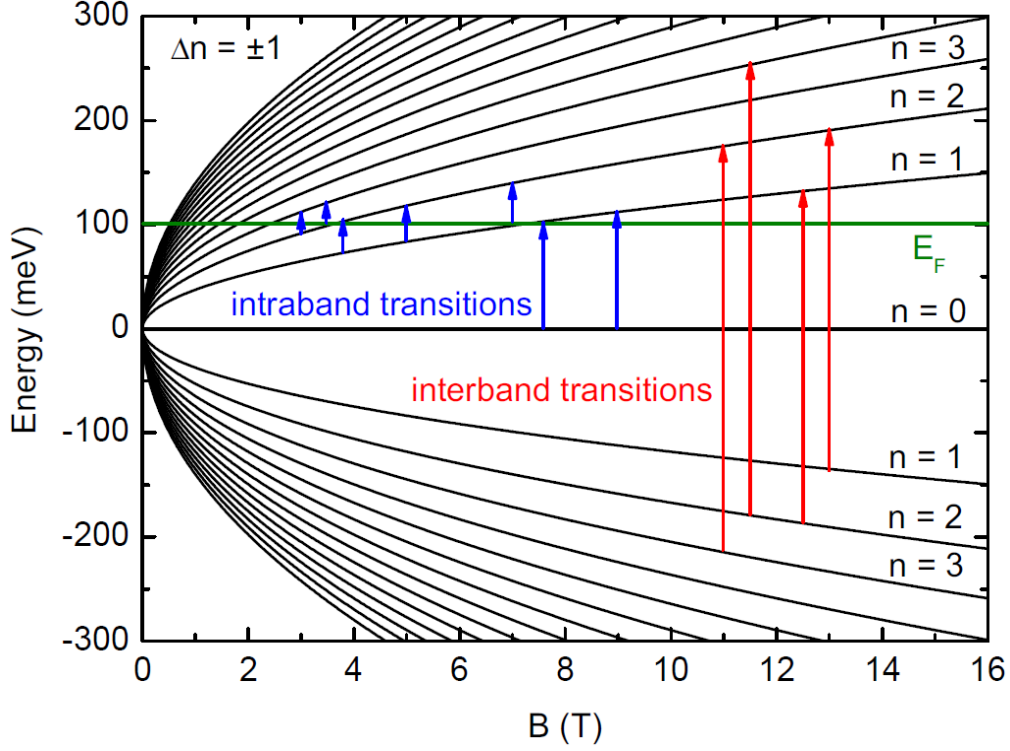


**Figure 2.16. Optical transitions in ideal monolayer graphene in the Faraday geometry.** Intraband (blue arrows) and interband (red arrows) transitions between Landau levels of ideal graphene with the Fermi velocity  $v_F = 1.03 \times 10^6$  m/s are shown for the Fermi energy  $E_F = 100$  meV. The selection rules in the Faraday geometry is given by  $\Delta n = \pm 1$ .

Intraband or cyclotron resonance transition energies from the level  $n$  to the level  $n + 1$  of the conduction or valence bands can be written as:

$$\text{For n-type samples: } E_{n+1}^c - E_n^c = v_F \sqrt{2\hbar e B} (\sqrt{n+1} - \sqrt{n}) \quad (2.11a)$$

$$\text{For p-type samples: } E_n^v - E_{n+1}^v = v_F \sqrt{2\hbar e B} (\sqrt{n+1} - \sqrt{n}) \quad (2.11b)$$

Interband transition energies from the level  $n$  of the valence band to the level  $n \pm 1$  of the conduction band are expressed as:

$$E_{n\pm 1}^c - E_n^v = v_F \sqrt{2\hbar e B} (\sqrt{n \pm 1} + \sqrt{n}) \quad (2.12)$$

Note that, in our model, the transitions  $n(v) \rightarrow n + 1(c)$  and  $n + 1(v) \rightarrow n(c)$  have the same transition energy.

## CHAPTER 2

### Magneto-optics in multilayer epitaxial graphene

#### 3.2. Bilayer graphene

The LLs of bilayer graphene read as follows <sup>4,60</sup>:

$$E_{n,\alpha}^{c,v} = \pm \frac{1}{\sqrt{2}} \sqrt{t_1^2 + (2n+1)E_1^2 + \alpha \sqrt{t_1^4 + 2(2n+1)t_1^2 E_1^2 + E_1^4}} \quad (2.13)$$

where  $n \geq 0$  is the LL index,  $E_{n,\alpha}^c \geq 0$  and  $E_{n,\alpha}^v \leq 0$ ,  $t_1$  is the hopping energy as defined in the subsection 1.2,  $E_1 = v_F \sqrt{2\hbar e B}$ , and  $v_F$  is the Fermi velocity having the same definition as for single-layer graphene.  $\alpha$  is the value indicating which conduction and valence bands of bilayer graphene will be considered in the LL calculation.  $\alpha = -1$  gives the LLs of the highest valence band and the lowest conduction band that touch each other at the  $K$  or  $K'$  points ( $E_2$  and  $E_3$  bands in Fig. 2.7). We notice that if  $t_1 = 0$ , the above LLs will become exactly equal to those of single-layer graphene. Fig. 2.17 displays the LLs of bilayer graphene as a function of magnetic field calculated with  $v_F = 1.03 \times 10^6$  m/s,  $t_1 = 0.4$  eV, and  $\alpha = -1$ .

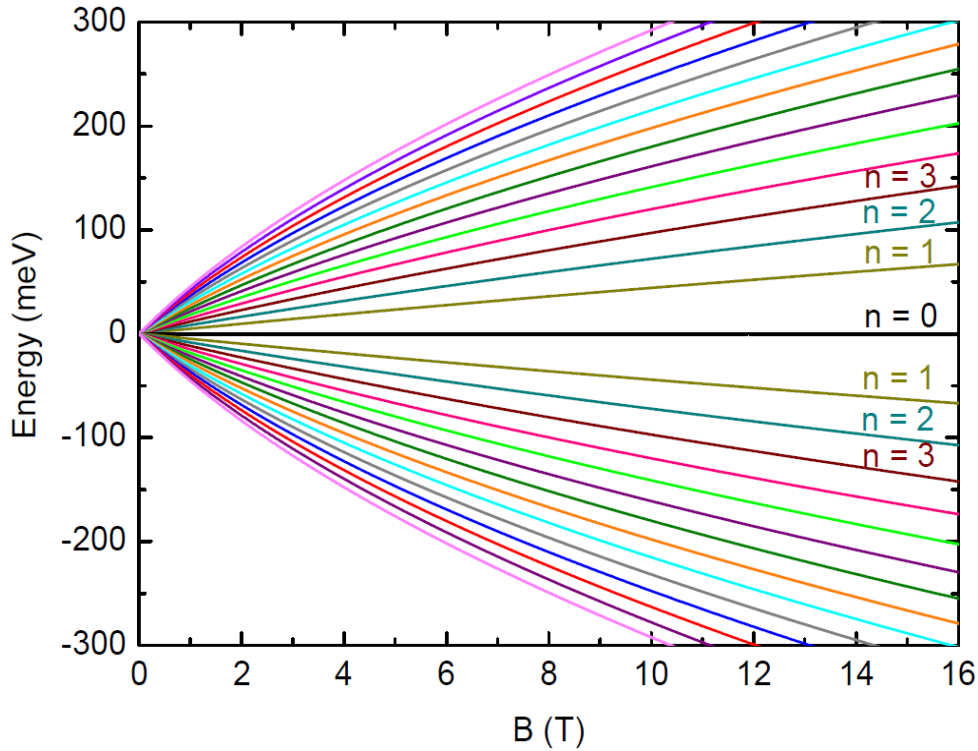


**Figure 2.17. Landau levels of bilayer graphene as a function of magnetic field.** Bilayer graphene Landau levels are calculated with the Fermi velocity  $v_F = 1.03 \times 10^6$  m/s and the hopping energy  $t_1 = 0.4$  eV for  $\alpha = -1$  corresponding to the lowest lying conduction band and the highest lying valence band touching each other at the  $K$  or  $K'$  points.

### 3.3. Trilayer graphene

The fundamental research on the electronic properties of trilayer graphene has previously demonstrated that there exist two different electronic band structures depending on the stacking sequences: ABA (Bernal) or ABC (rhombohedral). As a consequence, the corresponding LLs of graphene trilayers stacked in these two orders are different. Here, we will only describe the LLs of the ABA configuration which are expressed as <sup>25</sup>:

$$E_{n,\alpha}^{c,v} = \pm \frac{1}{\sqrt{2}} \sqrt{2t_1^2 + (2n+1)E_1^2 + \alpha \sqrt{4t_1^4 + 4(2n+1)t_1^2 E_1^2 + E_1^4}} \quad (2.14a)$$

and

$$E_{n,0}^{c,v} = \pm E_1 \sqrt{n} \quad (2.14b)$$

where  $n \geq 0$  is the LL index,  $E_{n,\alpha}^c \geq 0$ ,  $E_{n,\alpha}^v \leq 0$ ,  $E_{n,0}^c \geq 0$ ,  $E_{n,0}^v \leq 0$ ,  $E_1 = v_F \sqrt{2\hbar eB}$ , and  $v_F$  is the Fermi velocity having the same definition as for single-layer graphene. For the LLs  $E_{n,\alpha}^{c,v}$ ,  $\alpha = \pm 1$  are respectively defined for the contribution of the parabolic bands that do not touch each other and the parabolic bands touching each other at the  $K$  point, as seen previously in the band structure of trilayer graphene presented in the subsection 1.3. The remaining LLs are written as  $E_{n,0}^{c,v}$  that are exactly equivalent to those for monolayer graphene in the subsection 3.1. To summarize, the LL spectrum of ABA-stacked trilayer graphene can be studied by considering the summation of both the LLs of monolayer and bilayer graphenes. Fig. 2.18 shows ABA trilayer graphene LLs only for the positive energies.

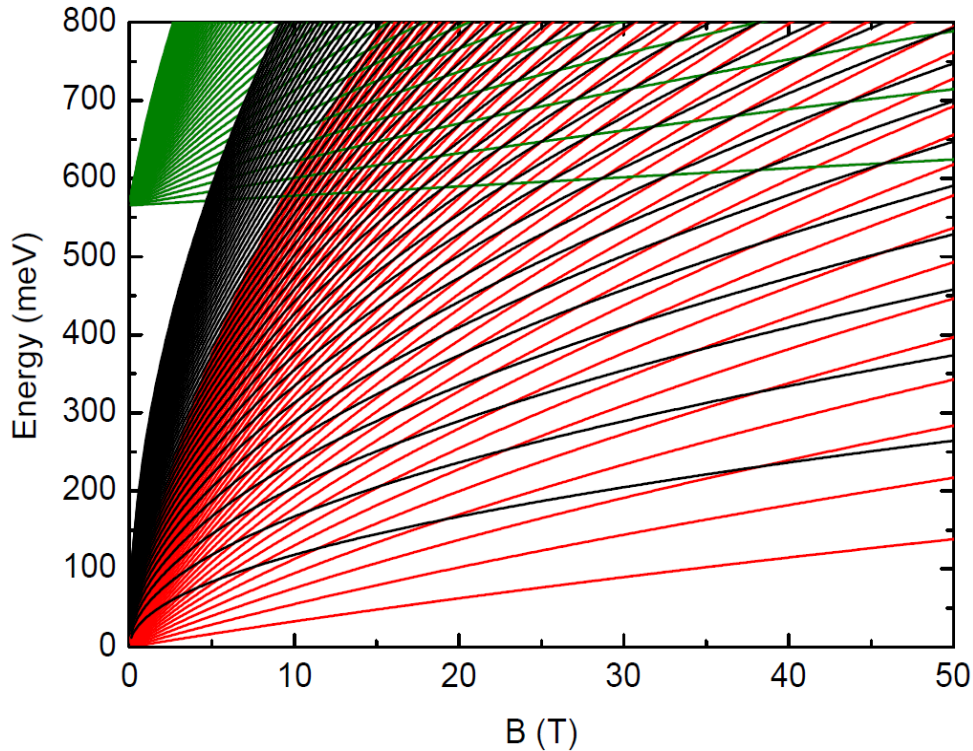


**Figure 2.18. Positive Landau level spectrum of ABA-stacked trilayer graphene.** ABA trilayer graphene Landau levels:  $E_{n,0}$  (black lines),  $E_{n,\alpha=-1}$  (red lines), and  $E_{n,\alpha=+1}$  (green lines). The energy origin of



## CHAPTER 2

### *Magneto-optics in multilayer epitaxial graphene*

$E_{n,\alpha=+1}$  is very high. Thus, the Landau levels at low energies are only combined with  $E_{n,0}$  and  $E_{n,\alpha=-1}$ . The parameters used in the calculations of these first 50 Landau levels in each band are  $v_F = 1.03 \times 10^6$  m/s and  $t_1 = 0.4$  eV.

## 4. Experimental results

In this section, experimental results obtained from magneto-optical absorption measurement performed on MEG samples grown on the C- and Si-terminated faces of SiC substrates will be presented and discussed. Our C- and Si-face MEG samples were fabricated by A. Ouerghi at the Laboratoire de Photonique et de Nanostructures (LPN-CNRS), Marcoussis, France.

### 4.1. C-terminated face multilayer epitaxial graphene

#### 4.1.1. Fabrication of C-terminated MEG samples

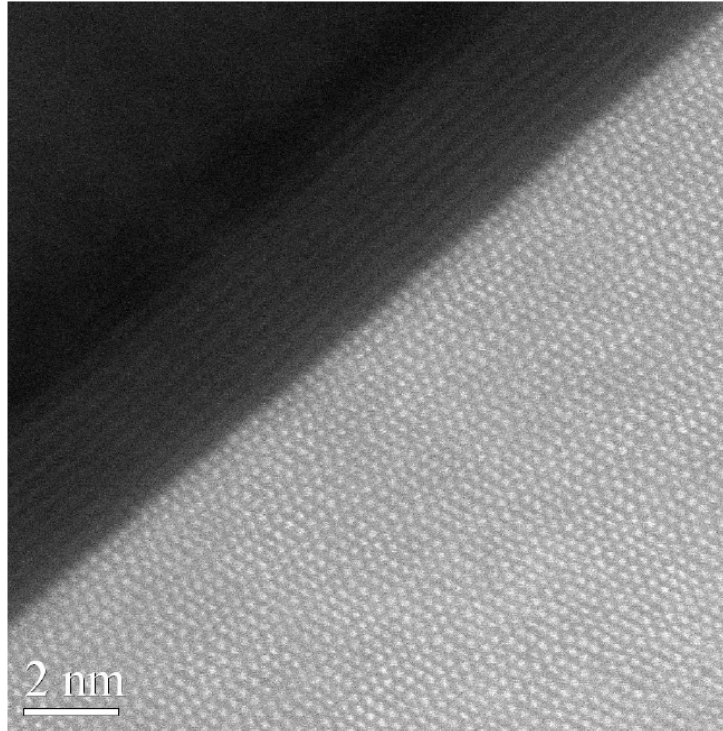


**Figure 2.19. Representative image of our C-terminated MEG samples obtained by scanning tunneling electron microscopy (STEM).** The darker region corresponds to a MEG sample of which  $\sim 8$ -10 graphene layers grown by thermal decomposition of SiC substrate on the C-terminated surface can be clearly seen. The lighter region represents the surface of the SiC substrate at the atomic level. This image was taken by G. Patriarche (LPN-CNRS).

The high-quality MEG samples investigated by magneto-spectroscopy measurement were prepared at LPN-CNRS using thermal decomposition, as described in the subsection 2.4, from the C-terminated surface of semi-insulating oriented  $(000\bar{1})$  4H-SiC substrate. First of

all, the SiC substrate was etched in a hydrogen flux at temperature  $T = 1,500$  °C and under pressure  $P = 200$  mbar for 15 minutes in order to remove any damage derived from the polishing of the SiC surface and to construct a step-ordered structure on the surface. The graphene layers were then grown in a closed radio-frequency (RF) induction furnace at  $T \sim 1,550$  °C and at  $P = 1 \times 10^{-5}$  mbar. The number of graphene layers was intentionally chosen to be  $\sim 8$ -10 layers which were confirmed by scanning tunneling electron microscopy (STEM) analysis (Fig. 2.19). A few graphene layers close to the SiC substrate are significantly doped due to the charge transfer from the substrate to the sample, whereas the remaining layers are quasi-neutral. The dimension of our C-terminated MEG samples is typically  $5 \times 5$  mm<sup>2</sup>.

#### **4.1.2. Dirac Landau level spectroscopy in monolayer and bilayer graphenes**

We have performed infrared magneto-optical transmission measurement on C-face MEG samples to determine the band parameters of our graphene layers. In this investigation, the magnetic field  $B$  can be varied up to 15 T and the temperature was held to be at  $T = 4.5$  K. FIR and MIR light sources were used to generate the spectral range between 4 and 750 meV. To measure the relative transmission spectrum of the sample, the transmission at a given magnetic field  $T(B)$  is normalized by the zero-field transmission  $T(0)$ .

Fig. 2.20 shows typical transmission spectra of a representative C-terminated MEG sample taken at different magnetic fields in the MIR range. The transmission minima indicated by different arrows disperse as a function of magnetic field and correspond to optical transitions between LLs of the sample. We have seen the calculation of optical transitions in the subsection 3.1 for the LL index  $n \geq 0$ . For the following, an intraband transition will be written as  $n^{c(v)} - (n + 1)^{c(v)}$  for a transition from the level  $n$  to the level  $n + 1$  of the conduction ( $c$ ) or valence ( $v$ ) bands. An interband transition is written as  $n^v - (n \pm 1)^c$  for a transition from the level  $n$  of the valence band to the level  $n \pm 1$  of the conduction band. A large number of strong transmission minima that satisfy the  $\sqrt{B}$ -dependence (black arrows) are attributed to the interband transitions originating from the excitation of massless Dirac fermions in monolayer graphene. Other weaker transmission minima that are linearly dependent on  $B$  (red arrows) are associated with the transitions resulting from the excitation of massive Dirac fermions in bilayer graphene. The orange arrows depict additional transitions that follow the  $\sqrt{B}$ -dependence as the transitions in monolayer graphene. Such transitions will be discussed later on the text. Narrow absorption lines were observed down to low fields, evidencing the high quality and high mobility of the sample.

## CHAPTER 2

### Magneto-optics in multilayer epitaxial graphene

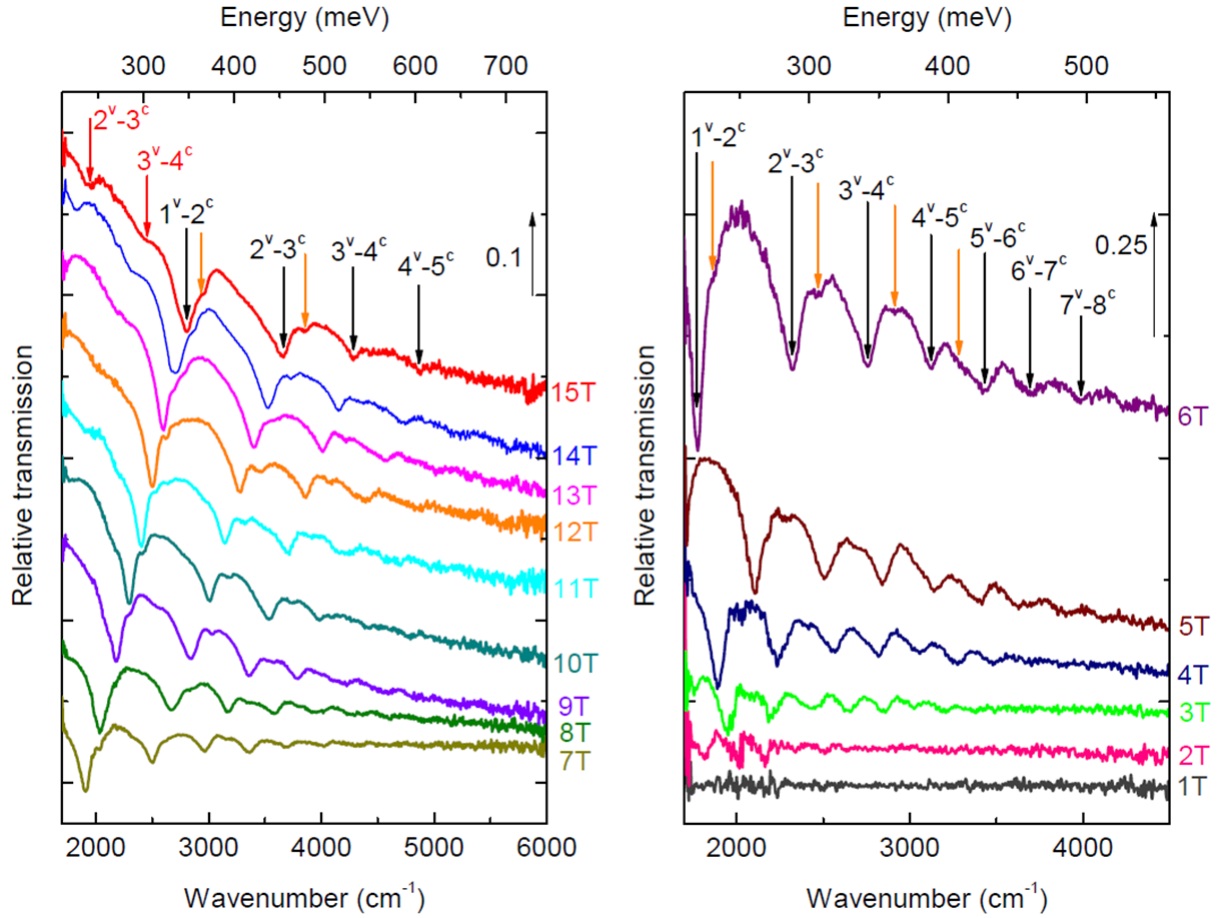


**Figure 2.20. MIR transmission spectra of a representative C-face MEG measured at different magnetic fields.** Transmission minima corresponding to optical transitions between Landau levels disperse as a function of magnetic field. Interband transitions in monolayer graphene and bilayer graphene are respectively depicted by black and red arrows. Narrow absorption lines were observed down to low fields, evidencing the high quality and high mobility of the sample. Additional transmission minima indicated by orange arrows cannot be interpreted by the Dirac Landau level transitions in monolayer or bilayer graphene.

Fig. 2.21 shows FIR transmission spectra of the same C-face MEG sample measured at different magnetic fields. The dispersion of various transitions with increasing fields was also observed as in the MIR range.

The principle absorption in the FIR range is the ground cyclotron resonance transition  $CR\ 0^c - 1^c$  (blue arrows) satisfying the  $\sqrt{B}$ -dependence. Hence, this transition originates from the excitation of massless Dirac fermions in monolayer graphene. Since the band structure of single-layer graphene is gapless, therefore the  $CR\ 0^c - 1^c$  can also be considered as the first interband transition. Such a transition appears up to 4.5 T in the FIR range. After this field any transmission associated with the  $CR\ 0^c - 1^c$  can be observed between 85 and 210 meV (reststrahlen band) due to the opacity of the SiC substrate caused by the phonon-related absorption. The  $CR\ 0^c - 1^c$  is narrow and disappears below  $B \sim 0.05$  T, evidencing the high quality and high carrier mobility of this C-face MEG sample. As we know that the necessary

condition for electrons to create a cyclotron orbit is given by  $\mu B \geq 1$ , we can thus deduce, for  $B = 0.05$  T, that the electron mobility of our graphene is very high:  $\mu \geq 200,000$  cm<sup>2</sup>/(V.s). This agrees with the measurements on MEG samples carried out by M. Orlita et al.<sup>49</sup>. Furthermore, the CR  $0^c - 1^c$  that is visible for the magnetic fields higher than 0.05 T allows us to determine the Fermi energy  $E_F$ . By considering the level  $1^c$  ( $n = 1$ ) that is depopulated from  $B = 0.05$  T, we can thus estimate using Eq. 2.10 with  $v_F = 1.03 \times 10^6$  m/s that  $E_F \leq E_1 \sim 8$  meV above the Dirac point. This method was used to determine  $E_F$  in all the MEG samples<sup>61,62</sup>.

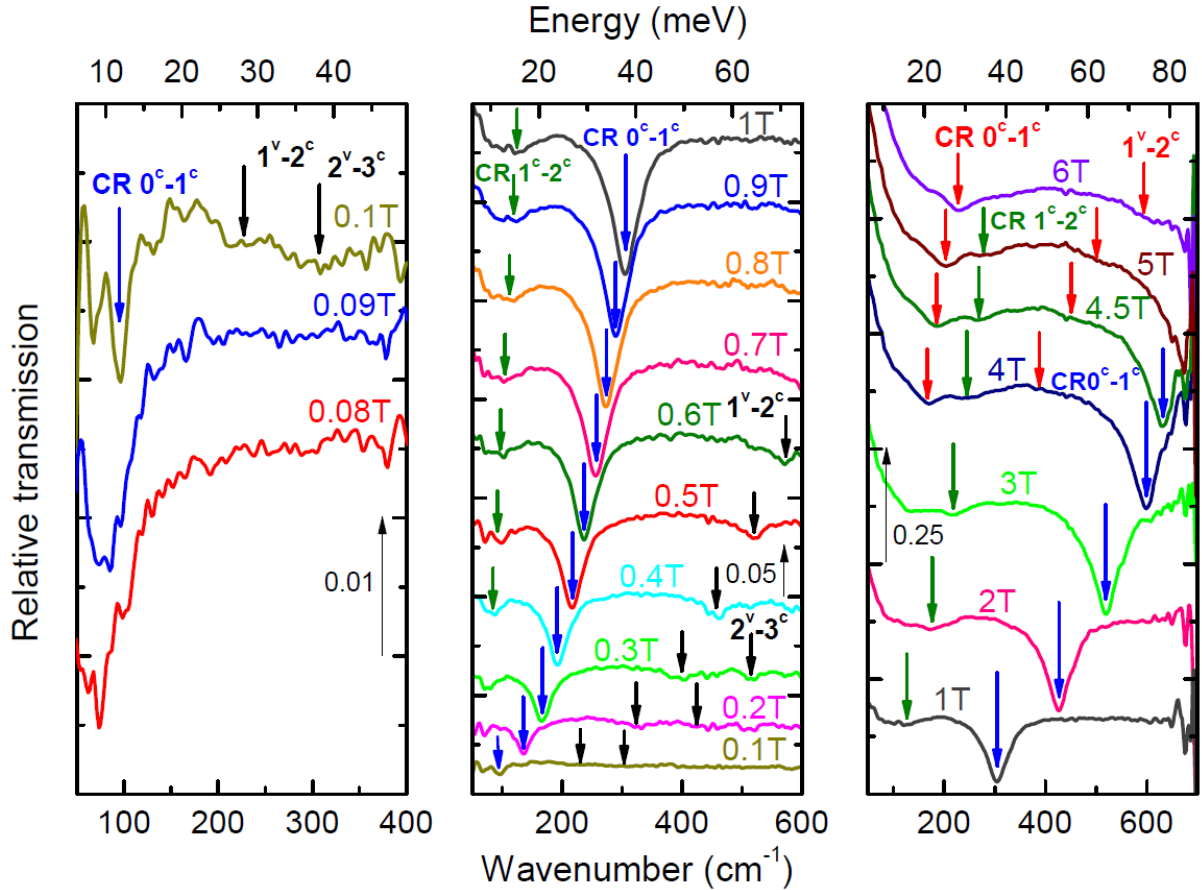


**Figure 2.21. FIR transmission spectra of a representative C-face MEG measured at different magnetic fields.** The minima of transmission spectra dispersing as a function of magnetic field correspond to optical transitions between Landau levels of various features of our graphene layers (denoted by arrows of different colors). The principle transition in this energy range is the ground cyclotron resonance CR  $0^c - 1^c$  (marked by blue arrows) of graphene monolayers. This transition is narrow and can be followed down to a very low field, indicating the high mobility of the sample.

Besides the main absorption lines originating from monolayer graphene (blue arrows), we observed also weaker transmission minima (red arrows) observed from 4 T to higher fields that are linearly dependent on  $B$ . Such transitions can thus be associated with the ground CR  $0^c - 1^c$  of massive Dirac fermions accommodated in bilayer graphene.

## CHAPTER 2

### *Magneto-optics in multilayer epitaxial graphene*

---

Interband transitions in monolayer graphene (black arrows) and bilayer graphene (red arrows indicating  $1^v - 2^c$ ) were also observed in this low-energy range. High intensity of these transitions can be seen clearer in the transmission spectra measured in the MIR range.

We observed also a very small absorption corresponding to the intraband transition  $1^c - 2^c$  between 0.4 and 5 T indicated by green arrows. Actually, this transition cannot occur because we have seen before that the level  $1^c$  is depopulated from 0.05 T. If there exists the CR  $1^c - 2^c$ , it should only occur below 0.05 T when the level  $1^c$  is populated. This indicates that there are some graphene layers of which their properties differ from those of the monolayers investigated earlier. Using Eq. 2.10 with  $v_F = 1.03 \times 10^6$  m/s to calculate  $E_F$  of these layers for the level  $1^c$  ( $n = 1$ ) that is populated up to  $B = 5$  T, we get  $E_F \sim E_1 \sim 85$  meV above the Dirac point. These layers have higher Fermi level energy and lower carrier mobility with respect to those of the monolayers seen before. Therefore, we propose that the observed CR  $1^c - 2^c$  arises from the few doped layers close to the SiC substrate.

To extract the band parameters of the graphene sample, the energy positions of the transmission minima seen previously were plotted versus magnetic field and were analyzed using the calculation of intraband and interband transitions between LLs in monolayer and bilayer graphenes as shown in the subsections 3.1 and 3.2. Fig. 2.22 displays the LL transition diagram of the C-face MEG sample. Blue dots represent the transmission minima interpreted as the ground CR  $0^c - 1^c$  of the graphene monolayers stacked in the sample. The corresponding blue curve fit was calculated with  $v_F = 1.03 \times 10^6$  m/s. The transmission minima denoted by black dots are attributed to the interband transitions occurring in the graphene monolayers. Black lines were calculated with  $v_F = 1.03 \times 10^6$  m/s to fit all these transitions. Red dots refer to the transmission minima associated with the ground CR  $0^c - 1^c$  and interband transitions of bilayer graphene present in the sample. The curve fits are in red and were calculated with  $v_F = 1.03 \times 10^6$  m/s and  $t_1 = 0.4$  eV. The latter parameter obtained by means of magneto-optics is in good agreement with several theoretical and experimental studies shown before. The stacking faults are frequently observed in the rotationally ordered MEG. The ratio between bilayers and monolayers in MEG has been reported to be typically 10% by M. Orlita et al.<sup>31</sup>. Green dots mark the transmission minima that can be interpreted by the CR  $1^c - 2^c$  of monolayer graphene represented in green line. As already explained before, such a transition and the ground CR  $0^c - 1^c$  in monolayer graphene cannot occur at the same time. This is an evidence for the existence of the few highly doped graphene monolayers close to the SiC substrate, having high Fermi energy and low electron mobility. Gray shaded rectangle represents the reststrahlen band of SiC substrate between 85 and 210 meV which limits our magneto-optical investigation because no transition can be observed in this spectral range. Overall, an excellent agreement between theory and experimental data is obtained for describing the electronic properties of different graphene layers stacked in our C-face MEG.

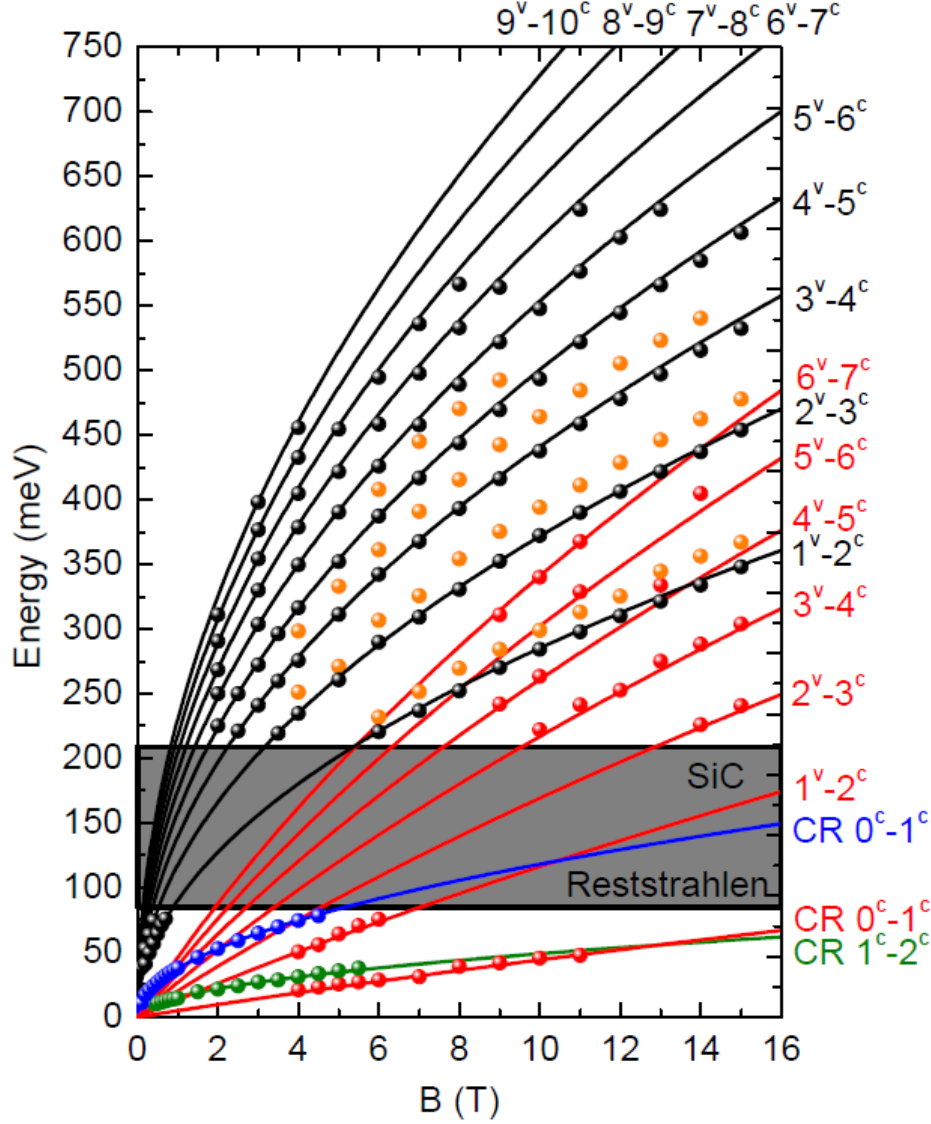


**Figure 2.22. Landau level transition diagram of a representative C-face MEG.** Transmission minima denoted by dots were plotted as a function of magnetic field. Solid lines are curve fits calculated for intraband and interband transitions that can occur in monolayer (with  $v_F = 1.03 \times 10^6$  m/s) and bilayer (with  $v_F = 1.03 \times 10^6$  m/s and  $t_1 = 0.4$  eV) graphenes. Blue color is used to represent the ground CR  $0^c - 1^c$  transition in monolayer graphene. Black color is used for interband transitions in the graphene monolayers. Red color shows the ground CR  $0^c - 1^c$  and interband transitions occurring in bilayer graphene. An excellent agreement theory/experiment is obtained. The emergence of the CR  $1^c - 2^c$  shown in green corresponds to the transition resulting from the few highly doped graphene layers close to the SiC substrate, having high Fermi level and low mobility. Gray shaded region is the reststrahlen band of SiC substrate where no transition can be observed. Orange symbols mark the transitions that will be attributed to the structural disorder present in our C-face MEG.

The additional  $\sqrt{B}$ -dispersing transmission minima observed near the interband transitions in the graphene monolayers are denoted by orange dots on the fan chart (Fig. 2.22). From the above analysis, we found that these transitions do not obey neither the Dirac LL transitions in monolayer (with  $v_F = 1.03 \times 10^6$  m/s) nor bilayer (with  $v_F = 1.03 \times 10^6$  m/s and

## CHAPTER 2

### *Magneto-optics in multilayer epitaxial graphene*

$t_1 = 0.4$  eV) graphenes. However, we did not completely forget that our magneto-optical absorption technique probes all the graphene layers and these supplementary transitions could be due to the interband transitions with different  $v_F$  in monolayer graphene grown on the other face of the SiC substrate. To verify this hypothesis, we etched the excessive graphene layers on this face and examined the sample once again by magneto-optics. The results obtained from this process remain unchanged. Hence, the supplementary transitions originate from the graphene layers on the C-face. Moreover, as seen in Fig. 2.20, the width of the additional absorption lines (orange arrows) is comparable to that of the principle absorptions (black arrows). This means that these two types of absorption peaks were caused by the same graphene monolayers. The physics of these additional transitions in our C-face MEG samples will be clarified in the following subsection.

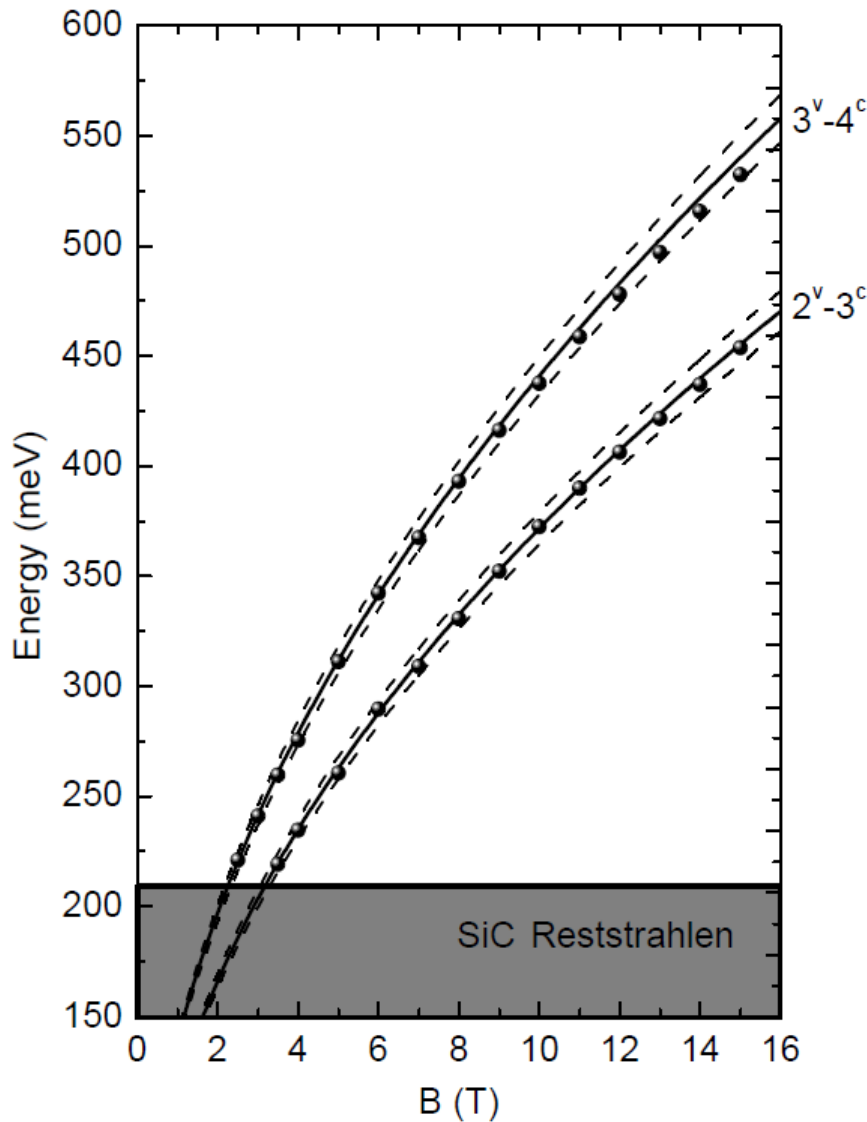


**Figure 2.23. Precise determination of the Fermi velocity of a representative C-face MEG sample using magneto-optical investigation.** Interband transitions  $2^v - 3^c$  and  $3^v - 4^c$  occurring in the graphene monolayers were fit with three values of  $v_F$ :  $v_F = 1.03 \times 10^6$  m/s (black solid lines),  $v_F = 1.05 \times 10^6$  m/s (upper black dashed lines), and  $v_F = 1.01 \times 10^6$  m/s (lower black dashed lines).



Our magneto-optical absorption investigation provides a precise determination of the Fermi velocity. As shown in Fig. 2.23, the interband transitions  $2^v - 3^c$  and  $3^v - 4^c$  occurring in the graphene monolayers were fit using the expression in Eq. 2.12 with  $v_F = 1.03 \times 10^6$  m/s, as represented by black solid lines. The black dashed lines at the energies higher than the experimental transition data were calculated with  $v_F = 1.05 \times 10^6$  m/s, while the black dashed lines at lower energies were calculated with  $v_F = 1.01 \times 10^6$  m/s. We see clearly that these two values of  $v_F$  do not fit the experimental data. As a consequence, the Fermi velocity of massless Dirac fermions in monolayer graphene determined from our method is accurately given by  $v_F = (1.03 \pm 0.02) \times 10^6$  m/s. Note that this value is in agreement with previous magneto-optical determination by M. Orlita et al.<sup>31,49</sup>.

### 4.1.3. Disorder effect on magneto-optical transitions

We have previously seen that the additional transitions dispersing with  $\sqrt{B}$  (depicted by orange symbols on Fig. 2.20 and 2.22) could not be associated with any excitation from massless Dirac fermions in pristine monolayer graphene. Furthermore, we checked that these transitions really occur in the graphene monolayers grown on the C-face. To explain this, we are interested in the structural disorder present in our graphene samples that can significantly modify their electronic properties<sup>63–65</sup>. In this scope, we will focus on the point defects that can perturb the LLs of ideal monolayer graphene. The following discussion regarding the perturbed LLs in graphene caused by the localized defects can also be found in our work<sup>62</sup>.

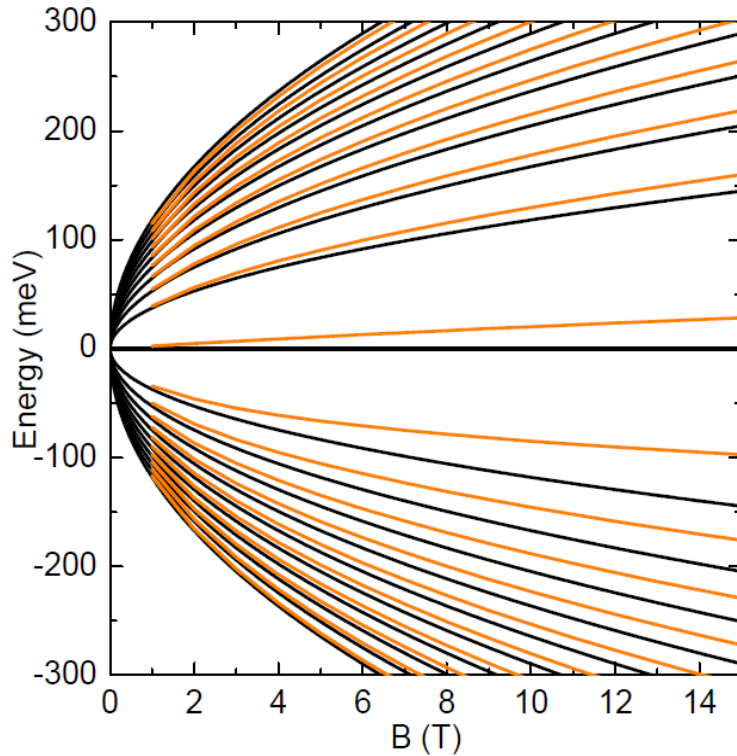


**Figure 2.24. Fan chart of perturbed Landau levels in the presence of point defects in graphene.** The perturbed Landau levels are obtained from the diagonalization of the Hamiltonian of graphene including a



## CHAPTER 2

### *Magneto-optics in multilayer epitaxial graphene*

short-range perturbation potential (delta-like)  $V(\vec{r}) = W_0\delta(\vec{r})$  in a truncated basis of unperturbed Landau levels, with  $W_0 = 20 \text{ eV.nm}^2$  and  $v_F = 1.03 \times 10^6 \text{ m/s}$ . Two kinds of states are obtained: in between (orange lines) and at the same energies (black lines) as the unperturbed Landau levels. Adapted from our paper <sup>62</sup>.

The origin of the supplementary transitions can be attributed to short-range defects in the graphene layers: C vacancies, Si isoelectric substitution or adatoms on a sublattice A or B site. To study the effect of these localized defects in our graphene, we collaborated with the theory group of our laboratory. We developed a model in the  $\mathbf{k} \cdot \mathbf{p}$  framework by taking into account a short-range potential (delta-like) in real space. We then considered  $V(\vec{r}) = W_0\delta(\vec{r})$  as the perturbation potential.  $W_0$  is a constant corresponding to the strength of the localized perturbation <sup>63</sup> and it is the only one parameter to be adjusted in the model in order to reproduce the experimental data. The diagonalization of the Hamiltonian  $H_0 + V(\vec{r})$ , for  $W_0 = 20 \text{ eV.nm}^2$  and  $v_F = 1.03 \times 10^6 \text{ m/s}$ , in a truncated basis of unperturbed Landau states gives the LLs in the presence of the point defects as represented in Fig. 2.24. For the sake of simplicity, we considered  $-10 < n < 10$ , resulting in 21 LLs in the basis.

The perturbed LLs obtained can be separated in two kinds of states: (i) the states placed in between the unperturbed LLs (orange lines) and (ii) the states placed at the same energies as the unperturbed LLs (black lines). The perturbed LL spectrum structure can be understood at the lowest order by retaining only the two unperturbed states of the same index  $n$  (different from zero) and derived from two different valleys. The eigenvalue equation to be solved is given by  $(E_n + \eta)I + \eta\sigma_x = EI$ , where  $E_n$  is the unperturbed LLs of ideal monolayer graphene,  $\eta = W_0/\lambda_B^2$  represents the intra- and intervalley coupling strengths which are equivalent and  $\lambda_B$  is the magnetic length,  $I = \begin{pmatrix} 1 & 0 \\ 0 & 1 \end{pmatrix}$  is the identity matrix, and  $\sigma_x = \begin{pmatrix} 0 & 1 \\ 1 & 0 \end{pmatrix}$  is the real nondiagonal Pauli matrix. The solutions of the above equation read:

$$E_{\pm} = E_n + \eta \pm |\eta| \quad (2.15)$$

For a given index  $n$ , we get a state at the same energy  $E_n$  as the unperturbed LL, and another either below or above  $E_n$ , depending on the sign of  $W_0$ .

In the following, we will demonstrate that the additional transitions observed in magneto-optical transmission spectra can be described by the transitions between the calculated LLs shown in Fig. 2.24. To do this, we calculated all the possible transition energies between all the available LLs to fit the orange data points on Fig. 2.22. Note that the selection rules  $\Delta n = \pm 1$  for an ideal graphene are no longer applied in the presence of defects. Finally, we found that the orange points are associated with the transitions between unperturbed (black lines) and defect-related (orange lines) LLs seen in Fig. 2.24.

In order to fit the experimental transmission spectra, we introduce a phenomenological broadening of the transitions of which the expression is written as:

$$T(E) = C - \frac{1}{E} \left[ \sum_{E_{LL-to-LL}} \frac{A}{\Gamma_{LL-to-LL}} e^{-\frac{(E-E_{LL-to-LL})^2}{2\Gamma_{LL-to-LL}}} + N_{def} \sum_{E_{LL-to-def}} \frac{A'(E_{LL-to-def})}{\Gamma_{LL-to-def}} e^{-\frac{(E-E_{LL-to-def})^2}{2\Gamma_{LL-to-def}}} \right] \quad (2.16)$$

Here, the first sum corresponds to the transitions between unperturbed LLs, noted as LL-to-LL, while the second sum is calculated for the transitions between unperturbed and defect-related states, denoted as LL-to-def.  $A$  and  $A'$  represent the amplitudes of the transitions and can be obtained with the Fermi golden rule.  $E_{LL-to-LL}$  and  $E_{LL-to-def}$  are the positions of transmission minima due to the transitions LL-to-LL and LL-to-def, respectively.  $\Gamma_{LL-to-LL}$  and  $\Gamma_{LL-to-def}$  refer to the broadenings of the transmission spectra.  $N_{def}$  is the area density of defects. The last three quantities are parameters to be adjusted.

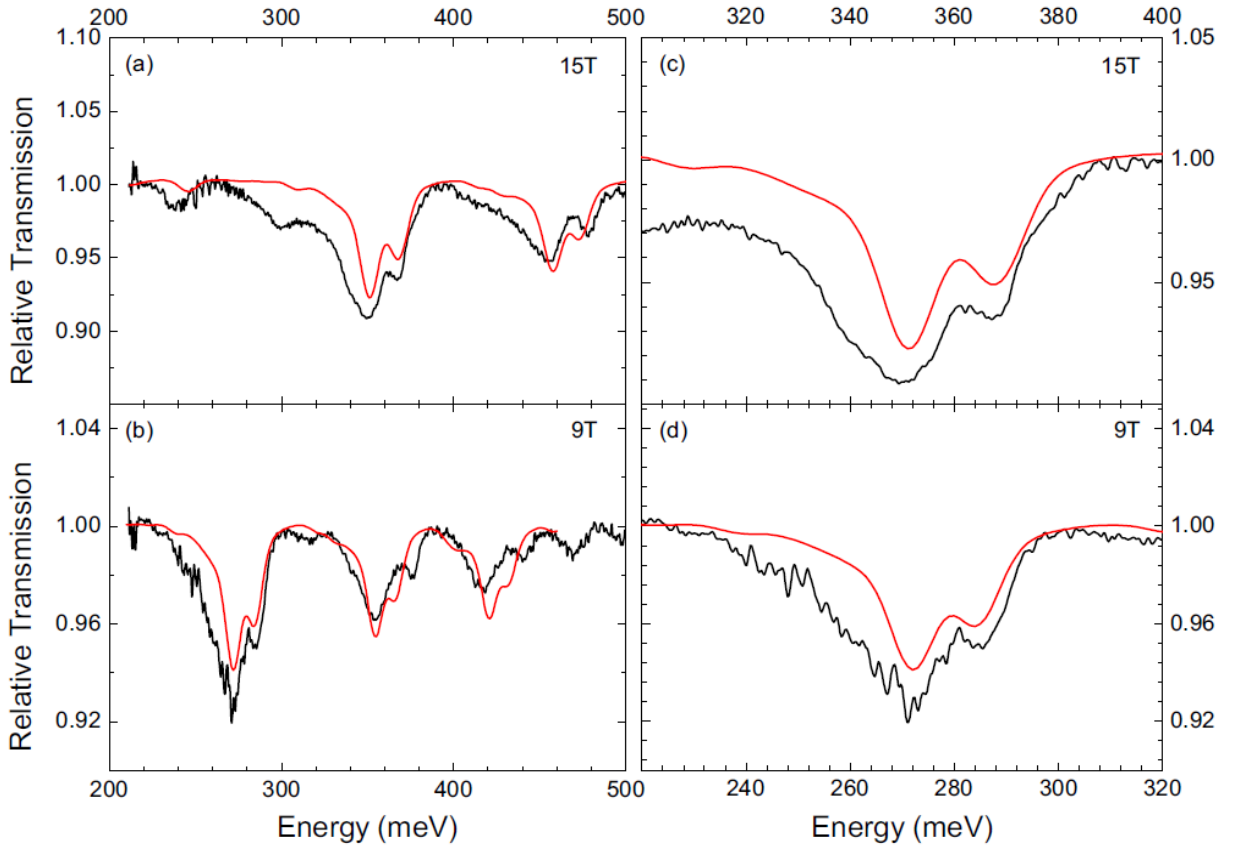


**Figure 2.25. Theory/experiment comparison.** Transmission spectra (black) measured in a representative C-face MEG at 15 T (a and c) and 9 T (b and d). Calculated absorption spectra (red) are superposed to the experimental data. (c) and (d) are zooms of (a) and (b), respectively. A good agreement between the theory and experimental transmission spectra is obtained. Adapted from our paper <sup>62</sup>.

## CHAPTER 2

### *Magneto-optics in multilayer epitaxial graphene*

Fig. 2.25 shows the comparison between theory and experiment. The calculated absorption spectra for 9 T and 15 T are represented by red curves. They correspond to the transitions of electrons initially in unperturbed valence states (black LLs with  $E \leq 0$ ) towards all accessible excited perturbed states (with  $E \geq 0$ ). Note that the level  $E = 0$  plays the twofold role of initial and final level as in the ideal graphene.

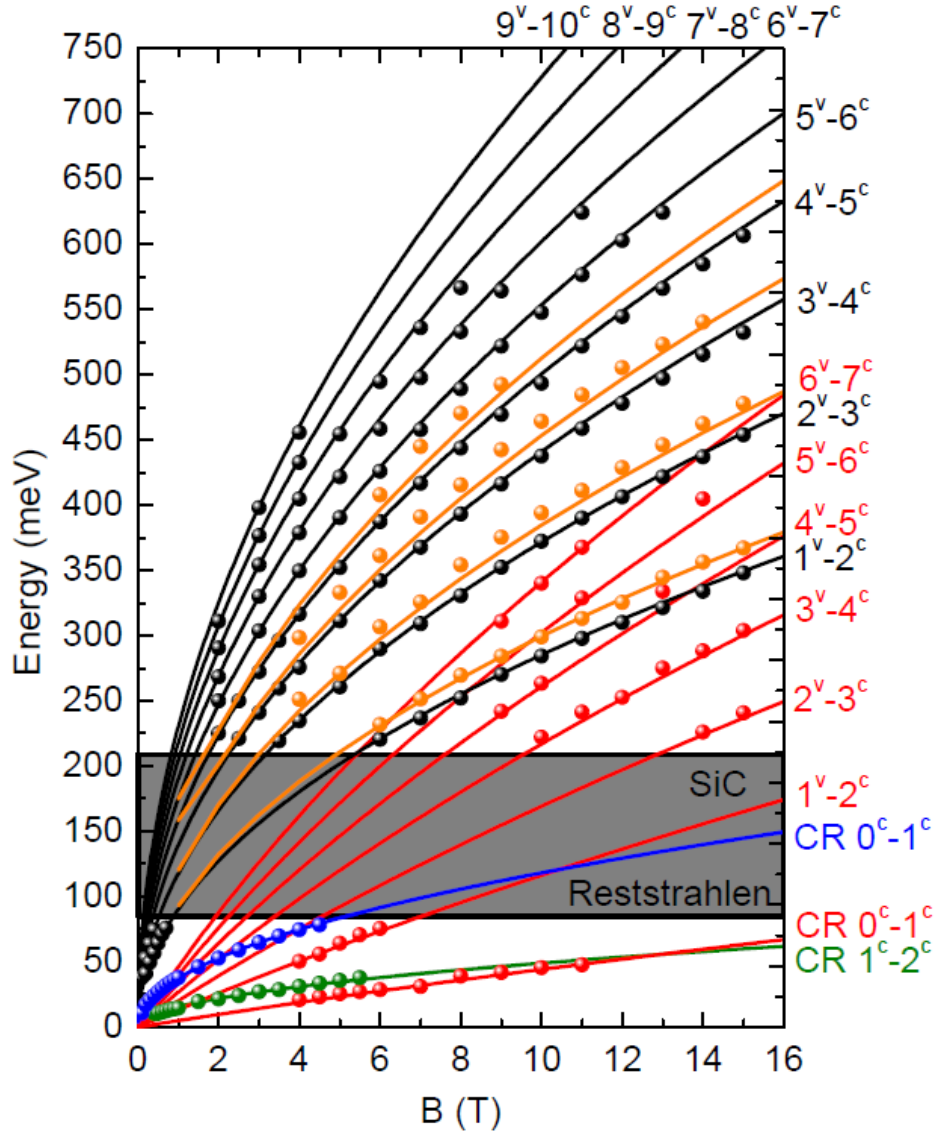


**Figure 2.26. Complete Landau level transition diagram of a representative C-face MEG.** In this sample, the rotational stacking results in the electronic decoupling between graphene monolayers. Their ground CR  $0^c - 1^c$  and interband transitions dispersing with  $\sqrt{B}$  are represented by blue and black circles, respectively. Blue and black solid lines are the corresponding curve fits calculated using  $v_F = 1.03 \times 10^6$  m/s. Stacking faults frequently occurring in the sample give rise to  $\sim 10\%$  of bilayer graphene. The associated transitions are marked by red dots and the corresponding curve fits shown in red solid lines are calculated with  $v_F = 1.03 \times 10^6$  m/s and  $t_1 = 0.4$  eV. Additional transitions depicted by orange dots were fit by orange lines calculated from the transitions between unperturbed (black lines in Fig. 2.24) and defect-related (orange lines in Fig. 2.24) Landau

## CHAPTER 2

### *Magneto-optics in multilayer epitaxial graphene*

levels in the presence of the point defects ( $W_0 = 20 \text{ eV.nm}^2$ ) in our C-face MEG. An excellent agreement theory/experiment is obtained. Adapted from our paper <sup>62</sup>.

All parameters were obtained in order to get the best fit. First, the energy positions of the weaker absorptions mostly depend on the potential strength  $W_0$ . We obtained  $W_0 = 20 \text{ eV.nm}^2$ . Second, we know that the intensity of a defect-related absorption peak is proportional to the number of defects present in the sample, while the strength of an intrinsic contribution depends on the sample surface. Therefore, the relative amplitudes between the main and weaker absorption lines mostly rely on the area density of defects  $N_{def}$ . As discussed earlier, certain defect-related states possess the same energies as the unperturbed LLs, thereby each main line contains both LL-to-LL and LL-to-def contributions. The best fit is obtained for  $N_{def} = 4.5 \times 10^{11} \text{ cm}^{-2}$  as shown in Fig. 2.25. Third, the energy-independent broadenings of the Gaussian fits were obtained:  $\Gamma_{LL-to-LL} = 10 \text{ meV}$  and  $\Gamma_{LL-to-def} = 5 \text{ meV}$ . The different broadenings ( $\Gamma_{LL-to-LL} \approx 2\Gamma_{LL-to-def}$ ) might be due to the fact that the width of the LL-to-LL transitions results from the convolution of two nearly equally broadened LLs, while we do not expect an important broadening for a spatially localized state in the gap between two LLs. For  $W_0 = 20 \text{ eV.nm}^2$  and  $v_F = 1.03 \times 10^6 \text{ m/s}$ , a good agreement between calculated transitions (black and orange lines) and the experimental results (black and orange symbols) is shown in Fig. 2.26.

The concentration of the defects in the graphene layers is very diluted since the ratio  $N_{def}/N_C \sim 1 \times 10^{-4}$ , where  $N_C = 2/S_{UC}$  is the area density of carbon atoms (two carbon atoms per unit cell) and  $S_{UC} = 0.052 \text{ nm}^2$  is the area of the graphene unit cell. This is consistent with the high electron mobility  $\mu \geq 200,000 \text{ cm}^2/(\text{V.s})$  deduced previously from the observation of the ground CR  $0^c - 1^c$  from  $B \sim 0.05 \text{ T}$ .

Interestingly, we observed in our samples a self-healing of the defects at room temperature. Fig. 2.27 shows the self-healing effect in a sample measured at 12 T at different times after the first measurement ( $t_0$ ) done right after the growth. This puzzling phenomenon has not been fully understood yet. It could be probably due to the diffusion of atmospheric molecules, for example  $\text{H}_2\text{O}$ , that penetrate between the graphene layers and place at the point defects, generating the LL-to-def transitions indicated by orange arrows. One month later ( $t_0 + 1m$ ), the intensity of these transitions diminishes but the broadening of the peaks remains unchanged:  $\Gamma_{LL-to-def} = 5 \text{ meV}$ . The other two experiments carried out later ( $t_0 + 4m$  and  $t_0 + 10m$ ) show the disappearance of the LL-to-def transitions. When the sample was heated to  $1,100 \text{ }^\circ\text{C}$  for 10 minutes, we reproduced all the transitions (at  $t_0 + 10m$  after the heating process) with comparable intensity as observed in the measurement at  $t_0$ . Hence, the heating process allows to get rid of the atmospheric molecules from the sample.

## CHAPTER 2

### Magneto-optics in multilayer epitaxial graphene

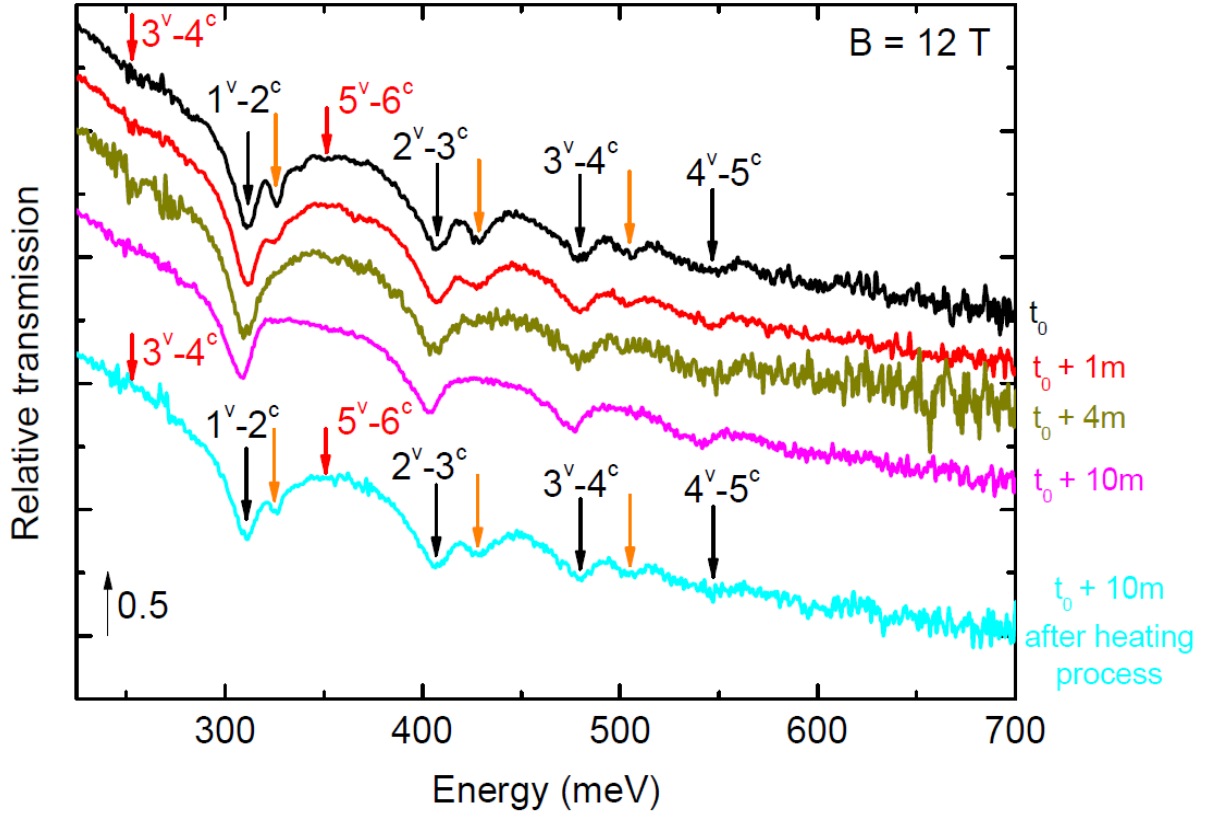


**Figure 2.27. Self-healing effect study in a representative C-face MEG.** The upper four transmission spectra were measured at 12 T at different times. The intensity of the additional transitions marked by orange arrows diminishes as a function of time and disappears about one month later after the first measurement ( $t_0$ ). The lowest transmission spectrum was reproduced at 12 T after the sample was heated to 1,100 °C for 10 minutes. The signature due to the localized defects comes back after the heating procedure.

## 4.2. Si-terminated face multilayer epitaxial graphene

### 4.2.1. Fabrication of Si-terminated MEG samples

It has been known that the Si-face of SiC substrates is more favorable than the C-face for controlling the epitaxial growth of a few graphene layers (1-3 layers), as described previously in the subsection 2.4. For instance, we discuss here the electronic properties of MEG samples (typically  $5 \times 5 \text{ mm}^2$ ) fabricated from a  $4^\circ$  off-axis 4H-SiC(0001) substrate via the method of thermal decomposition (A. Ouerghi, LPN-CNRS). Before the graphitization, the substrate was first etched in a hydrogen flux (100% of  $\text{H}_2$ ) at temperature  $T = 1,550^\circ\text{C}$  in order to prepare well-ordered atomic terraces of the SiC substrate. Secondly, the substrate was heated to  $T = 820^\circ\text{C}$  and deoxidized at  $T = 1,100^\circ\text{C}$  for removing the native oxide and any surface contamination. Then, the substrate was heated to  $T = 1,550^\circ\text{C}$  under an argon atmosphere of pressure  $P = 800 \text{ mbar}$  for 10 minutes. Epitaxially grown graphene layers were finally cooled down to room temperature and transferred ex-situ to perform further characterizations and measurements. Note that the first carbon layer (buffer layer in Fig. 2.28)

of a Si-terminated MEG is insulating. This can be explained by the fact that one third of the carbon atoms of the buffer layer are covalently bound to the SiC substrate. The real epitaxial graphene layers exhibiting graphene properties are therefore on top of this interfacial layer.

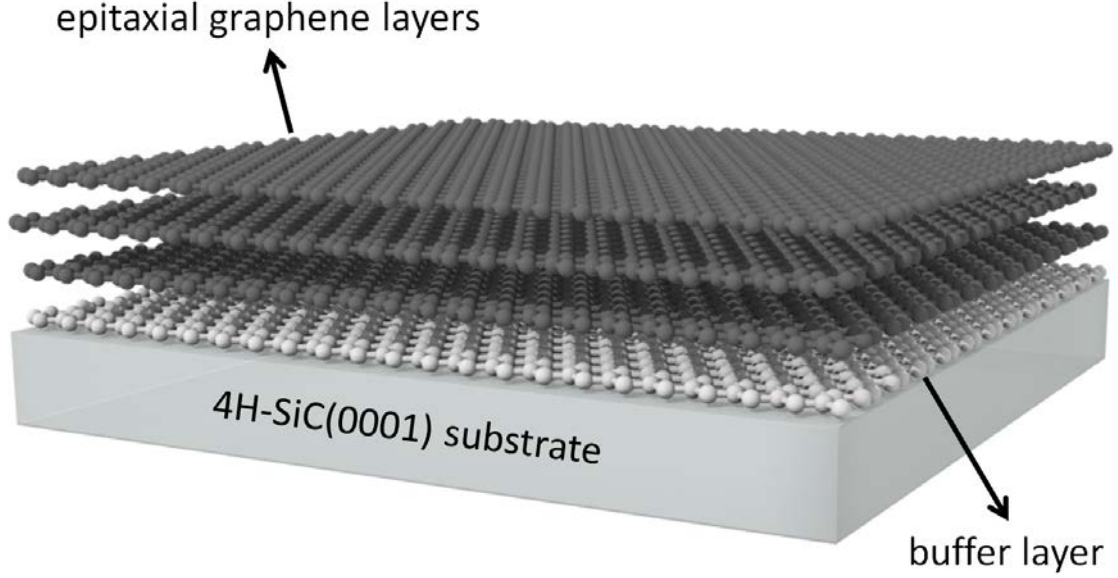


**Figure 2.28. Schematic structure of our Si-terminated MEG epitaxially grown on 4H-SiC(0001) substrate.** The first carbon layer, known as buffer layer, close to the SiC substrate is insulating due to the covalent bonding between the carbon atoms of this interfacial layer and the substrate. Epitaxial graphene layers that exhibit graphene properties correspond to the layers next to the buffer layer. Adapted from our paper <sup>66</sup>.

Various characterizations and measurements were carried out and they confirm that this Si-terminated MEG is a trilayer graphene. All the measurements were performed in collaboration with the research group of A. Ouerghi at LPN-CNRS and at Synchrotron-SOLEIL, Saint-Aubin, France. Characterization techniques used in this study were micro-Raman mappings, atomic force microscopy (AFM) and X-ray photoelectron spectroscopy (XPS). Different measurements were combined to study the electronic properties of this epitaxial trilayer graphene: near-edge X-ray absorption fine structure (NEXAFS), angle-resolved photoemission spectroscopy (ARPES) and far-infrared magneto-transmission (FIR-MT). In this thesis, only ARPES and FIR-MT experimental results will be shown and discussed. Further details regarding the characterizations and other measurements of this epitaxial trilayer graphene can be found in our paper <sup>66</sup>.

#### 4.2.2. Electronic band structure of trilayer graphene from ARPES experiment

ARPES experiment was performed in our epitaxial graphene at Synchrotron-SOLEIL, Saint-Aubin, France. It is a powerful technique since it allows us to get directly the information about the electron energy band dispersion of our graphene sample. Fig. 2.29(a) displays ARPES spectra, measured at the energy  $\hbar\nu = 60$  eV, along the  $M$ - $K$ - $\Gamma$  direction of

## CHAPTER 2

### *Magneto-optics in multilayer epitaxial graphene*

---

the first Brillouin zone. The electronic band structure mostly shows the valence band energy. The Fermi energy  $E_F$  is placed in the conduction band at the zero energy as reference ( $E_F = 0$ ). As can be seen in Fig. 2.29(b), the momentum distribution curve (MDC) was extracted at the energy  $E - E_F = -1.32$  eV denoted by the horizontal red line in Fig. 2.29(a). Three maxima, indicated by black arrows, of the ARPES spectra intensity observed in the MDC evidence the existence of three valence bands. This is different from the band structure of monolayer graphene with a single valence band and bilayer graphene with double valence bands. As a consequence, our graphene sample epitaxially grown on the Si-face of 4H-SiC(0001) substrate is most probably a trilayer graphene. Clearer evidence for trilayer graphene can be found in the second derivative of the electronic band structure as shown in Fig. 2.29(c). The energy dispersion of three valence bands can be clearly seen and the bands (2) and (3) indexed in Fig. 2.29(b) touch each other at the  $K$  point. Density functional theory (DFT) calculation was also performed (Fig. 2.29(d)) to show the consistency of the trilayer graphene band structure with ARPES experimental data. The calculated band structure corresponds to the electronic band structure of trilayer graphene in Bernal or ABA stacking sequence. The Bernal stacking is energetically more preferable than the rhombohedral (ABC) stacking, as explained in the subsection 1.3, and this is finally confirmed by the ARPES results.

The ARPES spectra clearly evidencing the three valence bands (Fig. 2.29(a)) demonstrate the high crystalline quality of this epitaxial trilayer graphene. It is well known that the  $\pi$  bands of trilayer graphene form a Dirac cone and the  $\pi$  branches cross each other at the Dirac point ( $K$  point). For our sample, the Dirac point is located at the energy denoted as  $E_D \sim -320$  meV. From ARPES measurement, we can estimate the Fermi energy ( $E_F = 0$ ) with respect to the Dirac point to be  $\Delta E = E_F - E_D \sim 320$  meV above the Dirac point. Using a Fermi velocity  $v_F \sim 1 \times 10^6$  m/s, the carrier concentration can be estimated to be  $n \sim 9 \times 10^{12}$  cm<sup>-2</sup> per graphene layer.



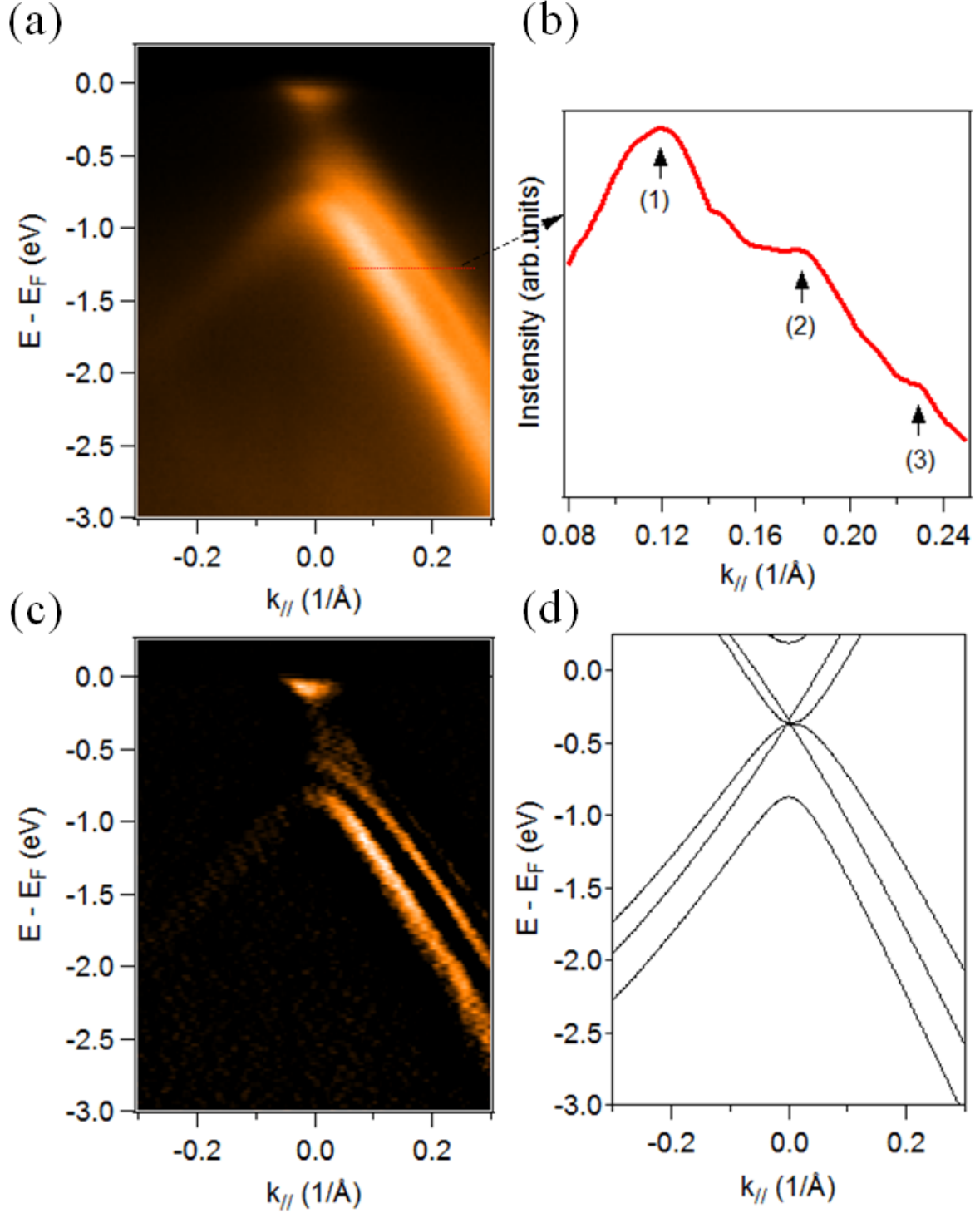


**Figure 2.29.** Electronic band structure measured by ARPES experiment of our Si-terminated MEG epitaxially grown on 4H-SiC(0001) substrate. (a) ARPES spectra of the epitaxial trilayer graphene measured along the  $M$ - $K$ - $\Gamma$  direction of the first Brillouin zone at the energy  $\hbar\nu = 60$  eV. (b) Momentum distribution curve (MDC) extracted from the ARPES spectra in (a) at the energy  $-1.32$  eV with respect to the Fermi energy at 0 eV. (c) Second derivative of the ARPES spectra in (a) showing clearer epitaxial trilayer graphene band structure. (d) Density functional theory (DFT) calculation for the band structure of trilayer graphene in Bernal stacking order. Adapted from our paper <sup>66</sup>.



## CHAPTER 2

### *Magneto-optics in multilayer epitaxial graphene*

#### 4.2.3. Infrared magneto-transmission results of trilayer graphene

We have performed FIR magneto-optical transmission measurement on this epitaxial trilayer graphene. Fig. 2.30 shows typical FIR relative transmission spectra measured at various magnetic fields at 4.5 K. For  $B \geq 3$  T, the broad absorption line of the sample indicated by black arrows disperses as a function of magnetic field. We notice that the transition energy minima are not linearly dependent on  $B$ . This is a typical characteristic of Dirac fermions.

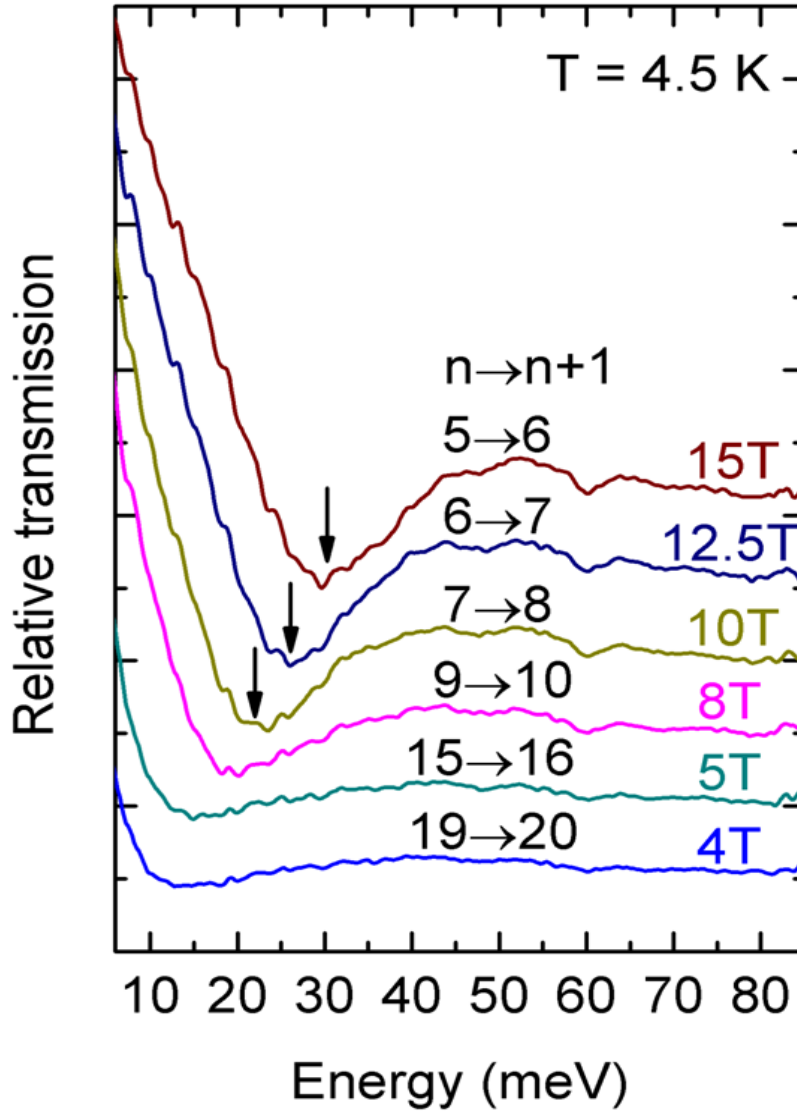


**Figure 2.30. Infrared magneto-optical relative transmission spectra of our epitaxial trilayer graphene.** Far-infrared transmission spectra of our trilayer graphene with Bernal stacking were measured at different magnetic fields at 4.5 K. Black arrows show the cyclotron resonance (CR) transitions. Each CR transition of the conduction band at a fixed field is denoted by  $n \rightarrow n + 1$ , where  $n \geq 0$  is the Landau level index, and has to satisfy the condition  $E_n < E_F < E_{n+1}$ , where  $E_F$  is the Fermi level. Adapted from our paper <sup>66</sup>.

As seen before in the subsection 3.3, the LLs of trilayer graphene can be decomposed in two LL origins: a monolayer graphene-like and a bilayer graphene-like LLs. This is expected since the trilayer graphene band structure exhibits two massless monolayer graphene-like subbands and four massive bilayer graphene-like subbands. The LL spectra for the conduction bands of a Bernal trilayer graphene are represented in Fig. 2.31. Only monolayer graphene-like LLs  $E_{n,0}^c$  (black curves) and bilayer graphene-like LLs  $E_{n,\alpha=-1}^c$  (red curves) are shown and they were calculated with  $v_F = 1 \times 10^6$  m/s and  $t_1 = 0.39$  eV. Note that the LLs  $E_{n,\alpha=+1}^c$  of bilayer graphene are situated at the energies higher than 400 meV (Fig. 2.18).

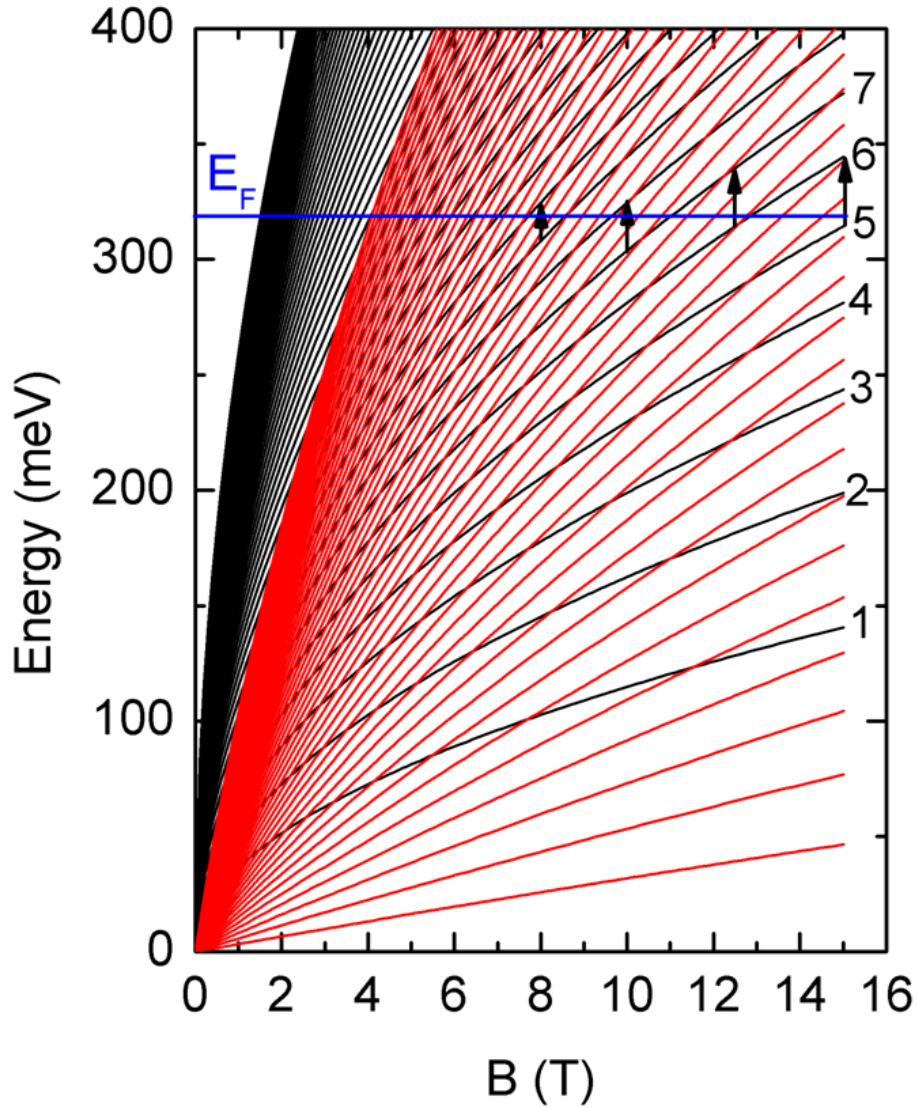


**Figure 2.31.** Calculated Landau level spectra for the conduction bands of a Bernal trilayer graphene. Landau levels of a Bernal trilayer graphene consist of monolayer graphene-like and bilayer graphene-like Landau levels represented respectively by black (for  $E_{n,0}^c$ ) and red (for  $E_{n,\alpha=-1}^c$ ) lines for the conduction bands. They were calculated with  $v_F = 1 \times 10^6$  m/s and  $t_1 = 0.39$  eV. The LLs  $E_{n,\alpha=+1}^c$  of bilayer graphene are located at the energies higher than 400 meV and are not represented. Black arrows depict the cyclotron resonance (CR) transition energies at each magnetic field between two adjacent monolayer graphene-like Landau

## CHAPTER 2

### *Magneto-optics in multilayer epitaxial graphene*

levels,  $n$  and  $n + 1$  with  $n \geq 0$ . Blue horizontal line indicates the Fermi energy  $E_F$  being satisfied by all the CR transitions. Adapted from our paper <sup>66</sup>.

Using the Fermi energy  $E_F = 320$  meV and place it as blue horizontal line on the calculated LL spectra in Fig. 2.31, we can calculate the intraband transition energies, respecting the selection rules  $\Delta n = \pm 1$  in the Faraday geometry, at each field between two adjacent LLs of monolayer graphene, as indicated by black arrows. We found that these transition energies correspond to the transmission minima dispersing with magnetic fields depicted by black arrows in Fig. 2.30. Therefore, the main observed absorption can be attributed to the electron cyclotron resonance (CR) of the linear conduction bands touching at the  $K$  point. At each  $B$ , the observed CR transition occurs between two adjacent LLs, the upper populated  $n$  and the lower unpopulated  $n + 1$  LLs with  $n \geq 0$ , of the conduction band and will be denoted as  $n \rightarrow n + 1$ . Note that the LL index  $n$  varies with  $B$  since the CR transition has to fulfill the condition  $E_n < E_F < E_{n+1}$ . The Fermi velocity was confirmed to be  $v_F \sim 1 \times 10^6$  m/s and the Fermi energy above the Dirac point can be experimentally determined to be  $E_F \sim 320$  meV by our magneto-spectroscopy, in agreement with ARPES measurement. In sum, we essentially measured the CR transitions of the monolayer graphene-like LLs. We did not observe any optical intraband transition from the bilayer graphene-like LLs having energies located around  $E_F$  since the transition energy between two adjacent LLs is probably too narrow to be experimentally resolved, as compared to the transition energy between two adjacent monolayer graphene-like LLs having larger LL width.

Magneto-spectroscopy allows to determine the electron mobility  $\mu$  of epitaxial trilayer graphene by considering the CR observation condition  $\mu B \geq 1$ . With the fact that clear absorption minima in Fig. 2.30 are only defined for  $B \geq 3$  T, the mobility of the Dirac fermions can thus be deduced to be  $\mu \geq 3,000$  cm<sup>2</sup>/(V.s) at 4.5 K.

## 5. Conclusion

We investigated C-terminated face MEG samples grown by means of thermal decomposition of SiC substrates using magneto-optical absorption measurement in the FIR and MIR ranges at 4.5 K and magnetic fields up to  $B = 15$  T. In spite of the SiC substrate reststrahlen band covering the energy range between 85 and 210 meV, the minima of transmission spectra dispersing as a function of  $B$  can be followed down to low fields. This evidences the high electron mobility of the C-face MEG samples:  $\mu \geq 200,000$  cm<sup>2</sup>/(V.s) at 4.5 K. Narrow absorption lines observed in the spectra indicate the high quality of these samples. The minima were extracted from the spectra and plotted versus  $B$  in order to construct Dirac LL transition diagrams. The minima of high absorption intensity were observed to vary with  $\sqrt{B}$  and therefore analyzed using the Dirac LL transitions of massless Dirac fermions in monolayer graphene. Other weaker transmission minima are dependent on  $B$  and they were analyzed by the Dirac LL transitions of massive Dirac fermions in bilayer graphene. We are able to extract the band parameters of our samples from the best fit. Magneto-spectroscopy allows us to accurately determine the Fermi velocity  $v_F = (1.03 \pm$

$0.02) \times 10^6$  m/s for massless Dirac fermions of graphene monolayers and massive Dirac fermions of graphene bilayers. The hopping energy between two adjacent layers in bilayer graphene was found to be  $t_1 = 0.4$  eV, in good agreement with previous theoretical and experimental studies. The very low Fermi energy from the Dirac point was estimated to be  $E_F \leq 8$  meV. Our graphene samples were shown to exhibit essentially the electronic properties of monolayer graphene owing to the electronic decoupling among the layers caused by the rotational stacking during the SiC thermal decomposition. The presence of bilayer graphene  $\sim 10\%$  resulting from stacking faults was also observed in our samples. We observed the few graphene monolayers situated next to the SiC substrate, as commonly known, which are highly doped with  $E_F \sim 85$  meV from the Dirac point. Their mobility at 4.5 K is much smaller than that of the graphene monolayers.

We also observed additional transmission minima that are located near the energies of the interband transitions in monolayer graphene investigated earlier and disperse as a function of  $\sqrt{B}$ . It is experimentally known that thermal decomposition of SiC substrates gives residual graphene layers on the undesirable face of SiC. After having been etched the excessive layers, the samples were examined once again and these additional transitions still occur. Therefore, they really result from the monolayers grown on the C-face of SiC. We attributed these supplementary transitions to the structural disorder: short-range impurities or point defects. Such localized defects can perturb the LLs of ideal single-layer graphene. The developed model using a delta-like potential perturbation successfully describes in the  $\mathbf{k} \cdot \mathbf{p}$  framework the experimental transmission spectra. The disorder-perturbed LLs are found to be placed in between and at the same energies as the unperturbed LLs of ideal monolayer graphene. The additional transmission minima were shown to be associated with the transitions between unperturbed (black lines in Fig. 2.24) and defect-related (orange lines in Fig. 2.24) LLs. A phenomenological broadening of the transitions was used to fit the transmission spectra. From the analysis, we obtained the concentration of localized defects  $N_{def} = 4.5 \times 10^{11} \text{ cm}^{-2}$ . This concentration is very diluted ( $\sim 1 \times 10^{-4}$ ) which is relevant to the high carrier mobility  $\mu \geq 200,000 \text{ cm}^2/(\text{V.s})$  of the samples measured at 4.5 K. Interestingly, a self-healing effect of the defects in the samples kept at room temperature was observed. The additional transmission minima due to the transitions between unperturbed and defect-related LLs disappear about one month after the first measurement done right after the growth. This could be explained by the diffusion of atmospheric molecules, i.e.  $\text{H}_2\text{O}$ , that place at the point defects of the graphene layers, lowering the intensity of the additional transitions without modifying their broadening. We found that we can get rid of the atmospheric molecules by heating the samples to  $1,100^\circ \text{C}$  for 10 minutes. After the heating process, the additional transitions occur again with comparable intensity as observed in the first measurement.

Si-terminated face MEG samples grown by thermal decomposition of SiC substrates were shown to exhibit the electronic properties of graphene trilayers stacked in the Bernal or ABA sequence using magneto-spectroscopy and ARPES combined with other measurements and characterizations. The band structure obtained from ARPES experiment mostly shows three valence bands of which two bands touch each other at the  $K$  point, evidencing the

## CHAPTER 2

### *Magneto-optics in multilayer epitaxial graphene*

---

Bernal stacking. The Fermi energy was observed to be placed in the conduction bands, determining the n-type carriers in our samples. The ARPES results confirm the Bernal stacking in our trilayer graphene. The transmission minima observed in the FIR magneto-transmission experiments are found to correspond to the CR between two adjacent LLs of the linearly dispersing conduction band of the trilayer graphene (black lines in Fig. 2.9(a)). The observed CR transitions allow us to determine the Fermi velocity  $v_F = 1 \times 10^6$  m/s and the Fermi level  $E_F \sim 320$  meV above the Dirac point, in agreement with ARPES. The mobility of our epitaxial trilayer graphene is  $\mu \geq 3,000$  cm<sup>2</sup>/(V.s) at 4.5 K.

Finally, the experimental results shown in this chapter demonstrate that magneto-spectroscopy is a very powerful technique to characterize the very rich electronic properties of graphene stacks. The electronic properties of pristine stacks as well as the influence of defects (stacking faults, point defects, etc.) can be very accurately investigated.

## References

1. Novoselov, K. S. & Geim, A. K. Electric Field Effect in Atomically Thin Carbon Films. *Science* **306**, 666–669 (2004).
2. Geim, A. K. & Novoselov, K. S. The rise of graphene. *Nat. Mater.* **6**, 183–191 (2007).
3. Castro Neto, A. H., Guinea, F., Peres, N. M. R., Novoselov, K. S. & Geim, A. K. The electronic properties of graphene. *Rev. Mod. Phys.* **81**, 109–162 (2009).
4. Orlita, M. & Potemski, M. Dirac electronic states in graphene systems: Optical spectroscopy studies. *Semicond. Sci. Technol.* **25**, 063001 (2010).
5. Goerbig, M. O. Electronic properties of graphene in a strong magnetic field. *Rev. Mod. Phys.* **83**, 1193–1243 (2011).
6. Novoselov, K. S. *et al.* A roadmap for graphene. *Nature* **490**, 192–200 (2013).
7. Geim, A. K. Graphene: Status and Prospects. *Science* **324**, 1530–1534 (2009).
8. Wallace, P. R. The Band Theory of Graphite. *Phys. Rev.* **71**, 622–634 (1947).
9. Reich, S., Maultzsch, J., Thomsen, C. & Ordejón, P. Tight-binding description of graphene. *Phys. Rev. B* **66**, 035412 (2002).
10. Guinea, F., Castro Neto, A. H. & Peres, N. M. R. Electronic states and Landau levels in graphene stacks. *Phys. Rev. B* **73**, 245426 (2006).
11. Aoki, M. & Amawashi, H. Dependence of band structures on stacking and field in layered graphene. *Solid State Commun.* **142**, 123–127 (2007).
12. McClure, J. W. Band structure of graphite and de hass-van alphen effect. *Phys. Rev.* **108**, 612–618 (1957).
13. Slonczewski, J. C. & Weiss, P. R. Band Structure of Graphite. *Phys. Rev.* **109**, 272–279 (1958).
14. McCann, E. & Fal’ko, V. I. Landau-level degeneracy and quantum Hall effect in a graphite bilayer. *Phys. Rev. Lett.* **96**, 086805 (2006).
15. Malard, L. M. *et al.* Probing the electronic structure of bilayer graphene by Raman scattering. *Phys. Rev. B* **76**, 201401(R) (2007).
16. Novoselov, K. S. *et al.* Unconventional quantum Hall effect and Berry’s phase of  $2\pi$  in bilayer graphene. *Nat. Phys.* **2**, 177 (2006).
17. Dresselhaus, M. S. & Dresselhaus, G. Advances in Physics Intercalation compounds of graphite. *Adv. Phys.* **51**, 1–186 (2002).
18. Kumar, A. *et al.* Integer quantum Hall effect in trilayer graphene. *Phys. Rev. Lett.* **107**, 126806 (2011).
19. Jhang, S. H. *et al.* Stacking-order dependent transport properties of trilayer graphene. *Phys. Rev. B* **84**, 161408(R) (2011).
20. Freitag, M. Graphene: Trilayers unravelled. *Nat Phys* **7**, 596–597 (2011).
21. Taychatanapat, T., Watanabe, K., Taniguchi, T. & Jarillo-Herrero, P. Quantum Hall effect and Landau-level crossing of Dirac fermions in trilayer graphene. *Nat Phys* **7**, 621–625 (2011).
22. Lui, C. H., Li, Z., Mak, K. F., Cappelluti, E. & Heinz, T. F. Observation of an electrically tunable band gap in trilayer graphene. *Nat Phys* **7**, 944–947 (2011).
23. Bao, W. *et al.* Stacking-dependent band gap and quantum transport in trilayer

## CHAPTER 2

### *Magneto-optics in multilayer epitaxial graphene*

---

- graphene. *Nat Phys* **7**, 948–952 (2011).
24. Zhang, L., Zhang, Y., Camacho, J., Khodas, M. & Zaliznyak, I. The experimental observation of quantum Hall effect of  $l=3$  chiral quasiparticles in trilayer graphene. *Nat Phys* **7**, 953–957 (2011).
  25. Yuan, S., Roldán, R. & Katsnelson, M. I. Landau level spectrum of ABA- and ABC-stacked trilayer graphene. *Phys. Rev. B* **84**, 125455 (2011).
  26. Xu, P. *et al.* A pathway between Bernal and rhombohedral stacked graphene layers with scanning tunneling microscopy. *Appl. Phys. Lett.* **100**, 201601 (2012).
  27. Berger, C. *et al.* Electronic Confinement and Coherence in Patterned Epitaxial Graphene. *Science* **312**, 1191–1196 (2006).
  28. Sadowski, M. L., Martinez, G., Potemski, M., Berger, C. & De Heer, W. A. Landau level spectroscopy of ultrathin graphite layers. *Phys. Rev. Lett.* **97**, 266405 (2006).
  29. Hass, J. *et al.* Why multilayer graphene on 4H-SiC(000-1) behaves like a single sheet of graphene. *Phys. Rev. Lett.* **100**, 125504 (2008).
  30. Sprinkle, M. *et al.* First direct observation of a nearly ideal graphene band structure. *Phys. Rev. Lett.* **103**, 226803 (2009).
  31. Orlita, M. *et al.* Magneto-optics of bilayer inclusions in multilayered epitaxial graphene on the carbon face of SiC. *Phys. Rev. B* **83**, 125302 (2011).
  32. Koshino, M. & Ando, T. Orbital diamagnetism in multilayer graphenes: Systematic study with the effective mass approximation. *Phys. Rev. B* **76**, 085425 (2007).
  33. Koshino, M. & Ando, T. Magneto-optical properties of multilayer graphene. *Phys. Rev. B* **77**, 115313 (2008).
  34. Yi, M. & Shen, Z. A review on mechanical exfoliation for the scalable production of graphene. *J. Mater. Chem. A* **3**, 11700–11715 (2015).
  35. Parvez, K., Yang, S., Feng, X. & Müllen, K. Exfoliation of graphene via wet chemical routes. *Synth. Met.* **210**, 123–132 (2015).
  36. Ciesielski, A. & Samorì, P. Graphene via sonication assisted liquid-phase exfoliation. *Chem. Soc. Rev.* **43**, 381–398 (2014).
  37. Yu, Q. *et al.* Graphene segregated on Ni surfaces and transferred to insulators. *Appl. Phys. Lett.* **93**, 91–94 (2008).
  38. Li, X. *et al.* Large-area synthesis of high-quality and uniform graphene films on copper foils. *Science* **324**, 1312–1314 (2009).
  39. Zhang, Y., Zhang, L. & Zhou, C. Review of chemical vapor deposition of graphene and related applications. *Acc. Chem. Res.* **46**, 2329–2339 (2013).
  40. Shelton, J. C., Patil, H. R. & Blakely, J. M. Equilibrium segregation of carbon to a nickel (111) surface: A surface phase transition. *Surf. Sci.* **43**, 493–520 (1974).
  41. Sinitsyna, O. V. & Yaminsky, I. V. Atomic resolution probe microscopy of the graphite surface. *Russ. Chem. Rev.* **75**, 23 (2006).
  42. Oshima, C. & Nagashima, A. Ultra-thin epitaxial films of graphite and hexagonal boron nitride on solid surfaces. *J. Phys. Condens. Matter* **9**, 1 (1997).
  43. Eizenberg, M. & Blakely, J. M. Carbon monolayer phase condensation on Ni(111). *Surf. Sci.* **82**, 228–236 (1979).
  44. Affoune, A. *et al.* Experimental evidence of a single nano-graphene. *Chem. Phys. Lett.*

- 348**, 17–20 (2001).
45. Berger, C. *et al.* Ultrathin Epitaxial Graphite: 2D Electron Gas Properties and a Route toward Graphene-based Nanoelectronics. *J. Phys. Chem. B* **108**, 19912–19916 (2004).
  46. de Heer, W. A. *et al.* Large area and structured epitaxial graphene produced by confinement controlled sublimation of silicon carbide. *Proc. Natl. Acad. Sci. U. S. A.* **108**, 16900–16905 (2011).
  47. de Heer, W. A. *et al.* Epitaxial graphene. *Solid State Commun.* **143**, 92–100 (2007).
  48. Pallecchi, E. *et al.* High Electron Mobility in Epitaxial Graphene on 4H-SiC(0001) via post-growth annealing under hydrogen. *Sci. Rep.* **4**, 4558 (2014).
  49. Orlita, M. *et al.* Approaching the Dirac point in high-mobility multilayer epitaxial graphene. *Phys. Rev. Lett.* **101**, 267601 (2008).
  50. Riedl, C., Coletti, C. & Starke, U. Structural and electronic properties of epitaxial graphene on SiC(0001): a review of growth, characterization, transfer doping and hydrogen intercalation. *J. Phys. D. Appl. Phys.* **43**, 374009 (2010).
  51. Pierucci, D. *et al.* Evidence for flat bands near the Fermi level in epitaxial rhombohedral multilayer graphene. *ACS Nano* **9**, 5432–5439 (2015).
  52. Coletti, C. *et al.* Revealing the electronic band structure of trilayer graphene on SiC: An angle-resolved photoemission study. *Phys. Rev. B* **88**, 155439 (2013).
  53. Orlita, M. *et al.* Resonant Excitation of Graphene K-Phonon and Intra-Landau-Level Excitons in Magneto-Optical Spectroscopy. *Phys. Rev. Lett.* **108**, 247401 (2012).
  54. Orlita, M. *et al.* Carrier scattering from dynamical magnetoconductivity in quasineutral epitaxial graphene. *Phys. Rev. Lett.* **107**, 216603 (2011).
  55. Neugebauer, P., Orlita, M., Faugeras, C., Barra, A.-L. & Potemski, M. How Perfect Can Graphene Be? *Phys. Rev. Lett.* **103**, 136403 (2009).
  56. Orlita, M. *et al.* Magneto-transmission of multi-layer epitaxial graphene and bulk graphite: A comparison. *Solid State Commun.* **149**, 1128–1131 (2009).
  57. Faugeras, C. *et al.* Tuning the Electron-Phonon Coupling in Multilayer Graphene with Magnetic Fields. *Phys. Rev. Lett.* **103**, 186803 (2009).
  58. Plochocka, P. *et al.* High-Energy Limit of Massless Dirac Fermions in Multilayer Graphene using Magneto-Optical Transmission Spectroscopy. *Phys. Rev. Lett.* **100**, 087401 (2008).
  59. McClure, J. W. Diamagnetism of graphite. *Phys. Rev.* **104**, 666–671 (1956).
  60. Henriksen, E. A. *et al.* Cyclotron resonance in bilayer graphene. *Phys. Rev. Lett.* **100**, 087403 (2008).
  61. Massabeau, S. *et al.* Evidence of Fermi level pinning at the Dirac point in epitaxial multilayer graphene. *Phys. Rev. B* **95**, 085311 (2017).
  62. Maëro, S. *et al.* Disorder-perturbed Landau levels in high-electron-mobility epitaxial graphene. *Phys. Rev. B* **90**, 195433 (2014).
  63. Ando, T. & Nakanishi, T. Impurity Scattering in Carbon Nanotubes – Absence of Back Scattering –. *J. Phys. Soc. Japan* **67**, 1704–1713 (1998).
  64. Shon, N. H. & Ando, T. Quantum Transport in Two-Dimensional Graphite System. *J. Phys. Soc. Japan* **67**, 2421–2429 (1998).
  65. Peres, N. M. R., Guinea, F. & Castro Neto, A. H. Electronic properties of disordered



## **CHAPTER 2**

### ***Magneto-optics in multilayer epitaxial graphene***

---

- two-dimensional carbon. *Phys. Rev. B* **73**, 125411 (2006).
66. Hajlaoui, M. *et al.* High Electron Mobility in Epitaxial Trilayer Graphene on Off-axis SiC(0001). *Sci. Rep.* **6**, 18791 (2016).

# Chapter 3

## A brief overview of topological matter

The second part of this thesis deals with the Dirac matter systems studied in the so-called "topological insulators". This research field has recently become renowned after the 2016 Nobel Prize in Physics was awarded to David J. Thouless, F. Duncan M. Haldane and J. Michael Kosterlitz for "*theoretical discoveries of topological phase transitions and topological phases of matter*". They identified a completely novel type of phase transition and theoretically developed methods to describe this new kind of quantum phase transition based on arguments inspired from topology. In the research area of condensed matter physics, theoretical and experimental physicists are particularly interested in how topology can be applied to band structure theory, and what topological phenomena are. Up to date, certain semiconductors in suitable conditions were theoretically and experimentally shown to exhibit topological properties that could lead to numerous promising technological applications, for example, data storage, terahertz sensors, spintronic devices and quantum computing.

In this chapter, the notion of topological insulators will be first introduced and some topological insulator materials recently discovered will be exemplified. Secondly, an extended class of topological materials called "topological crystalline insulators" will then be addressed. Finally, the Bernevig-Hughes-Zhang Hamiltonian model will be shown to be applicable in both topological insulators and topological crystalline insulators and to reliably describe the topological behavior of relativistic-like Dirac fermions residing in such Dirac topological matter.

## Chapter 3 – A brief overview of topological matter

<b>1. Topological insulators</b>	<b>73</b>
<b>1.1. Historical overview</b>	<b>73</b>
1.1.1. Quantum Hall effect	73
1.1.2. Quantum spin Hall effect	76
<b>1.2. Theoretical notions of topological states of matter</b>	<b>77</b>
1.2.1. Berry phase	78
1.2.2. Topological invariants	79
<b>1.3. Theoretical prediction and experimental realization of <math>Z_2</math> topological insulators</b>	<b>81</b>
1.3.1. 2D topological insulator: QSHE in CdTe/HgTe/CdTe quantum wells	82
1.3.2. 3D topological insulator: Bi-based compounds	84
<b>2. Topological crystalline insulators</b>	<b>89</b>
<b>2.1. Crystal structure</b>	<b>90</b>
<b>2.2. Band inversion</b>	<b>90</b>
<b>2.3. Topological surface Dirac cones in different bulk Brillouin zone orientations</b>	<b>93</b>
<b>2.4. Electronic band structure of <math>Pb_{1-x}Sn_xSe</math> and <math>Pb_{1-x}Sn_xTe</math></b>	<b>94</b>
2.4.1. Electronic band structure of nontrivial $Pb_{1-x}Sn_xTe$ alloy	95
2.4.2. Electronic band structure of nontrivial $Pb_{1-x}Sn_xSe$ alloy	97
<b>2.5. Valley anisotropy</b>	<b>100</b>
<b>3. Bernevig-Hughes-Zhang Hamiltonian for topological matter</b>	<b>102</b>
<b>References</b>	<b>105</b>

## 1. Topological insulators

In the quantum world, a very large number of microscopic constituents such as ions or electrons in atoms can form different ordered phases of matter by spontaneously breaking symmetries. In a crystalline solid structure, ions are periodically arranged due to their electrostatic interactions, as a consequence, the continuous symmetries of space under translations and rotations are broken. In a typical magnet, magnetic moments or electrons break some rotational symmetries. The discovery of topological insulators (TIs) has revolutionized our understanding of quantum phases of matter since it challenged the symmetry-centered paradigm of phase transitions. Fundamentally speaking, it has allowed us to understand how unconventional states of matter can emerge in systems where fundamental symmetries remain preserved<sup>1,2</sup>.

A TI is a novel quantum state of matter which behaves as an insulator in its interior but as a metal on its boundary<sup>3,4</sup>. In other words, a TI material exhibits semiconducting bulk states accompanied by conducting edge or surface states. Several narrow gap semiconductors, in which the energy gap is smaller than relativistic corrections to the band structure, with spin-orbit interactions have been studied and theoretically or experimentally demonstrated to show metallic edge or surface states topologically protected by time-reversal symmetry. The combination of spin-orbit coupling and time-reversal symmetry drives to exotic physical phenomena. Therefore, the search for TIs is of importance and holds great promise for novel fundamental physics revealed from various investigation techniques such as the quantum spin Hall effect, the quantum anomalous Hall effect and Majorana fermions.

This section is completely devoted to TIs. It starts with the historical overview from quantum Hall effect to quantum spin Hall effect. Then, theoretical notions of topological states of matter will be introduced. Finally, some examples of two-dimensional (2D) and three-dimensional (3D)  $Z_2$  topological materials will be presented.

### 1.1. Historical overview

#### 1.1.1. Quantum Hall effect

The notion of TIs has been evolved from the ordinary Hall effect observed by Edwin H. Hall in 1879<sup>5</sup>. He measured the resistance, bearing his name as Hall resistance  $R_H$ , in a thin conducting sample placed under an external perpendicular magnetic field  $B$  and in which charged particles can go through. The Hall resistance is expressed as  $R_H = B/q\rho$ , where  $\rho$  is the density of charge carriers and  $q$  is the particle charge ( $q = -e$  for electrons and  $q = e$  for holes, with  $e$  the elementary charge). We notice that  $R_H$  is linear in  $B$ .

In 1980, K. von Klitzing, G. Dorda and M. Pepper discovered experimentally the integer quantum Hall effect (IQHE) in electrons confined to two dimensions, at

## CHAPTER 3

### A brief overview of topological matter

semiconductor heterojunction, and subjected to a strong uniform perpendicular magnetic field at low temperatures <sup>6</sup>. In this experiment, the longitudinal conductance becomes zero because all charged particles circularly orbit in a cyclotron motion with cyclotron frequency  $\omega_c$  around the magnetic flux due to the Lorentz force and they are thus localized in the bulk (Fig. 3.1(a)). For electrons, their circular orbits are quantized and lead to quantized Landau levels with energy  $E_n = \hbar\omega_c(n + 1/2)$ , where  $\omega_c = eB/m$  with  $m$  the cyclotron mass,  $n \in \mathbb{N}$  and  $\hbar$  is the reduced Planck constant <sup>7</sup>. These Landau levels may be viewed as a band structure as represented in Fig. 3.1(b). We denote  $\nu$  as the filling factor, indicating how many Landau levels are filled. Unlike an insulator, the Hall conductance or the transverse electrical conductance can be measured and is found to be quantized as:

$$\sigma_{xy} = \nu e^2/h \quad (3.1)$$

Here,  $\sigma_{xy}$  is the quantized Hall conductivity,  $h$  is the Planck constant and  $\nu \in \mathbb{N}^+$ . Since the conductance found in this experiment is quantized, this result completely differs from what is observed in the classical Hall effect. The IQHE is thus a quantum mechanical version of the classical Hall effect.

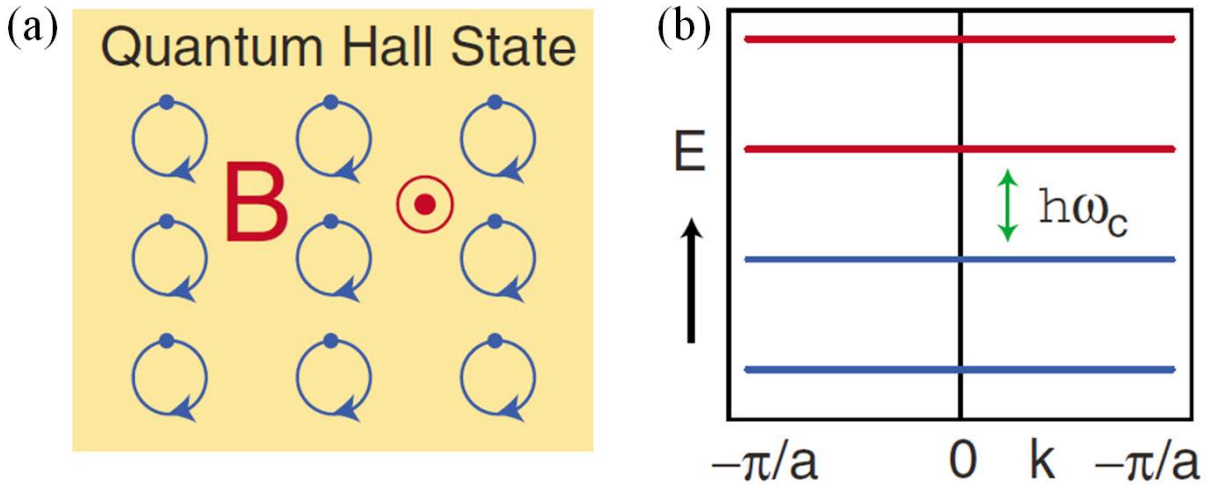


**Figure 3.1. Quantum Hall state.** (a) Circular cyclotron orbits of electrons confined to two dimensions and subjected to a strong perpendicular magnetic field, resulting in a quantum Hall state. (b) The quantized Landau levels of the electrons in (a) which may be viewed as a band structure. Adapted from <sup>3</sup>.

In a semiclassical scope, one can calculate the radius of the circular motion of a charged particle as  $R_n = \sqrt{\frac{\hbar}{eB}(2n + 1)}$ , varying as a function of magnetic field. Now, one may wonder what will happen when the particle moves close to the boundary. The answer is that the particle will bounce back from the rigid boundary and skip forward along the boundary (Fig. 3.2(a)). This physical phenomenon results in the formation of a one-dimensional (1D) conducting channel, called the edge state, in which the current flows in one direction with a quantum conductance  $e^2/h$  along the boundary. Each edge state occurs at the interface between two states of different filling factor values, for instance, an insulator with  $\nu$

$= 0$  and a quantum Hall state with  $\nu = 1$ . The electronic band structure of a single edge state connecting the conduction band and the valence band is illustrated in Fig. 3.2(b). Note that each Landau level will generate one edge channel and  $\nu$  filled Landau levels are thus equal to the number of edge channels. Consequently, the quantized Hall conductance is directly related to the number of edge channels present in a sample. Importantly, the charged particles in the bulk are localized by impurities or disorders, whereas the charge carriers in the edge channels are not affected by impurities or disorders and are thus very resistant to scattering. In other words, they move without energy dissipation. Such a dissipationless transport could be useful for semiconductor devices. Nevertheless, an applied strong magnetic field at low temperatures is required for realizing the QHE and thus limits the application potential of the QHE.

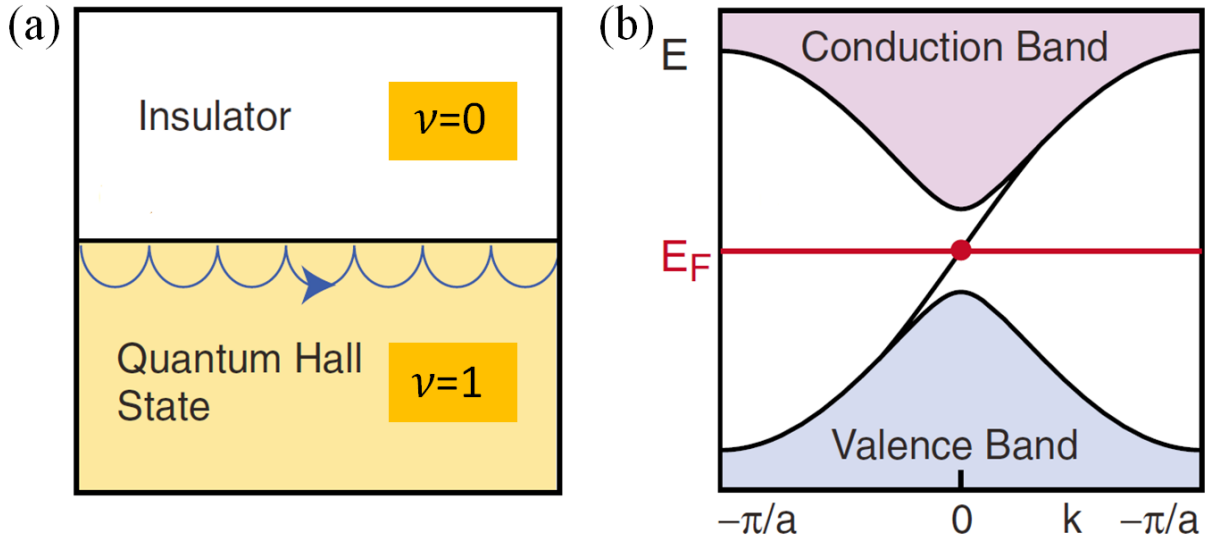


**Figure 3.2. Chiral edge state at the interface between an insulator and a quantum Hall state.** (a) Skipping cyclotron orbits of dissipationless transport electrons in a quantum Hall insulator. (b) The electronic band structure of a single edge state connecting the conduction band to the valence band. Adapted from <sup>3</sup>.

In 1988, F. Duncan M. Haldane theoretically proposed a model to describe the QHE that could break time-reversal symmetry without any magnetic flux in a 2D periodic system. The QHE occurring in the absence of an external magnetic field and without the associated Landau levels are referred to as the quantum anomalous Hall effect (QAHE) <sup>8</sup>. This can be explained by the fact that the lattice system is composed of spinless electrons in a periodic magnetic flux. The electrons are able to form a 1D conducting edge channel owing to the periodic magnetic flux even if the total magnetic flux is zero. As a consequence, the quantized Hall conductance originates from the band structure of electrons in the lattice instead of the discrete Landau levels generated by external magnetic field. Much attempt has been paid for investigating the QAHE in real materials <sup>9,10</sup> and it has been observed for example in magnetic TIs such as Cr-doped  $(\text{Bi,Sb})_2\text{Te}_3$  <sup>11</sup> and V-doped  $(\text{Bi,Sb})_2\text{Te}_3$  <sup>12</sup> films.

## CHAPTER 3

### A brief overview of topological matter

#### 1.1.2. Quantum spin Hall effect

We have previously seen in the earlier subsections that, in particular, the IQHE requires an external magnetic field, resulting in the broken time-reversal symmetry. The QAHE could also break the time-reversal symmetry by a periodic magnetic flux present in a 2D lattice system consisting of spinless electrons. In this part, a quantum state where the time-reversal symmetry is preserved will be introduced. Conducting edge states can generate, without any applied magnetic field, from the coupling between the spin and orbital angular momentum degrees of freedom (spin-orbit interactions) of electrons propagating in a 2D system.

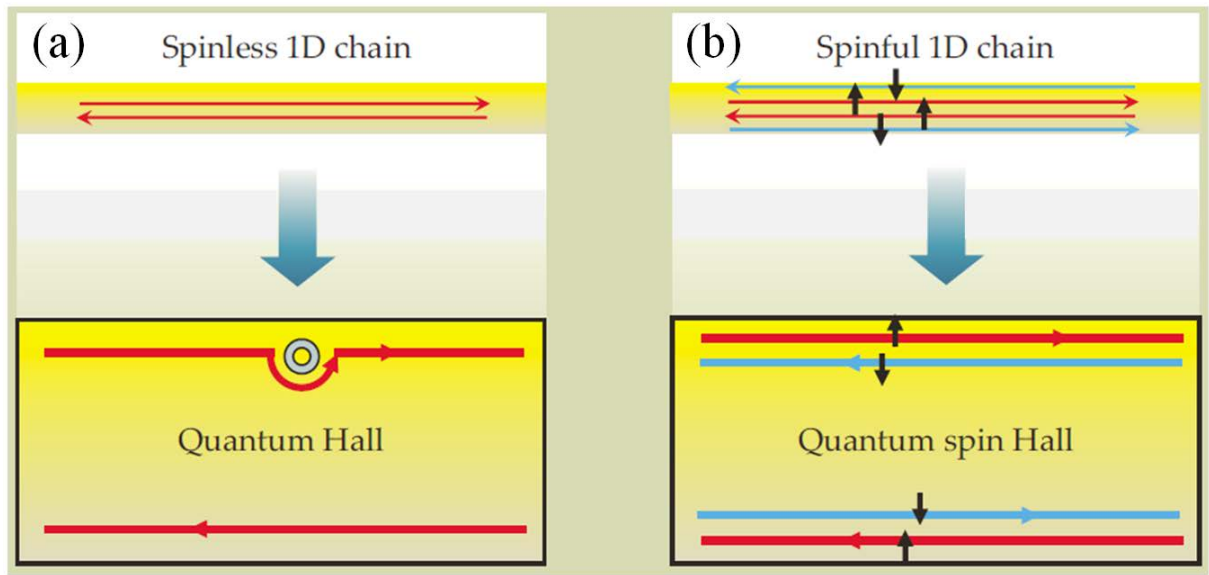


**Figure 3.3. Conducting edge states at the boundaries of the quantum Hall insulator and the quantum spin Hall insulator.** (a) 1D transport of spinless electrons in the quantum Hall insulator. The spinless electrons of the upper edge only move forward, while those of the lower edge only move backward. (b) 1D transport of spinful electrons in the quantum spin Hall insulator. The upper edge allows two helical conducting edge channels: spin up electrons move in the opposite direction of spin down electrons. The same situation occurs at the lower edge. In both cases, the conducting edge states are robust to impurities. The electrons move in one direction without backscattering, allowing dissipationless transport. Adapted from <sup>2</sup>.

In 2005, C. L. Kane and E. J. Mele generalized the Haldane model for the QAHE in a single plane of graphene consisting of spin-1/2 electrons by introducing the spin-orbit interactions in order to replace the periodic magnetic flux <sup>13</sup>. The effect of the spin-orbit coupling converts an ideal 2D semimetallic graphene to a quantum state having an energy gap in the electronic band structure and supporting the gapless states propagating at the graphene boundaries, known as quantum spin Hall effect (QSHE). This effect was also predicted to exist in 2D semiconductor systems <sup>14</sup> where different electron spins (spin up and spin down) experience opposite spin-dependent force while the electrons are moving through a crystal lattice. The intrinsic spin Hall conductance is quantized in units of  $2e^2/h$ . The QSHE is thus an analog of the QHE where spin currents flow at the boundaries instead of charge currents.

1D transport of the edge states is schematically illustrated in Fig. 3.3. A quantum Hall insulator has two conducting edge channels in which the spinless electrons move forward at the upper edge and move backward at the lower edge (Fig. 3.3(a)). In a QSH insulator, there are four conducting edge channels containing the spinful electrons (Fig. 3.3(b)). At each edge, the electrons of opposite spins flow in opposite directions, forming a pair of helical edge states. Such 1D electronic transport is dissipationless or without backscattering owing to the robustness of the electrons against impurities or geometric perturbations at the boundaries of the system. For the QSHE, the spinful electron backscattering in the two edge channels is prohibited due to the preserved time-reversal symmetry, which is not the case for the QHE.

A pair of helical edge states of the QSHE can be realized at the interface between a QSH insulator and an ordinary insulator (Fig. 3.4(a)). The corresponding electronic band structure is similar to that of a quantum Hall insulator but each single edge state links the conduction and the valence bands (Fig. 3.4(b)).

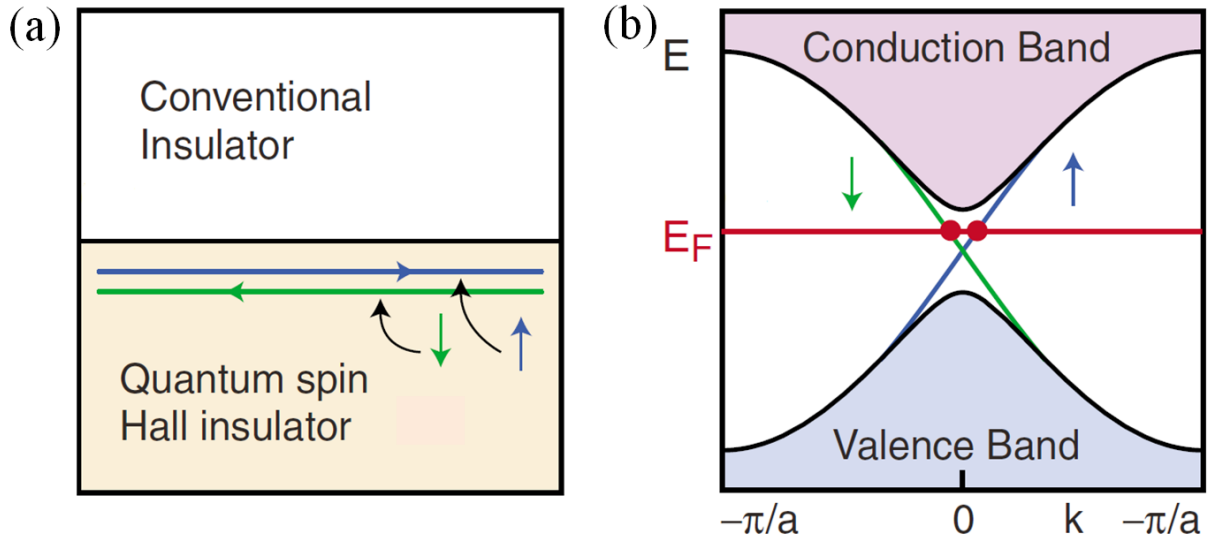


**Figure. 3.4. Helical edge states in the quantum spin Hall insulator.** (a) A pair of conducting edge channels that contain spin up and spin down electrons propagating in opposite directions at the interface between a quantum spin Hall insulator and a conventional insulator. (b) The dispersion of the helical edge states in the graphene model. Adapted from <sup>3</sup>.

## 1.2. Theoretical notions of topological states of matter

There exist a large number of materials that were demonstrated to host a topological phase. The classification of topological states (or phases) can be carried out by considering one or more indices, the so-called topological invariants. In this part, necessary theoretical notions regarding how topological states of matter can be distinguished and classified will be presented in the following subsections.



### 1.2.1. Berry phase

The emergence of topological states in a system originates directly from the influence of the Berry phase on the band structure. This concept was introduced by M. Berry in 1984<sup>15</sup>. He underlined the importance of geometric phases in mathematics that can be applied in classical and quantum physics. The Berry phase is thus a phase difference acquired during a cyclic adiabatic process of a system. In solid state physics, degeneracies of high-symmetry points in the Brillouin zone can be induced by the Berry phase. This leads to gapless states, states when the band structure has no energy gap, at the interface between two materials belonging to different topological classes. The Berry phase  $\phi_B$  in a closed contour  $C$  enclosing the  $\Gamma$ -point of the Brillouin zone (Fig. 3.5) can be expressed as the path integral:

$$\phi_B = \oint \langle u_m(\mathbf{k}) | i\nabla_{\mathbf{k}} | u_m(\mathbf{k}) \rangle \cdot d\mathbf{k} \quad (3.2)$$

Here,  $u_m(\mathbf{k})$  are the  $m^{\text{th}}$  eigenstates in the reciprocal space.  $\mathbf{A}_m(\mathbf{k}) = \langle u_m(\mathbf{k}) | i\nabla_{\mathbf{k}} | u_m(\mathbf{k}) \rangle$  is the Berry connection which plays the role of the vector potential.

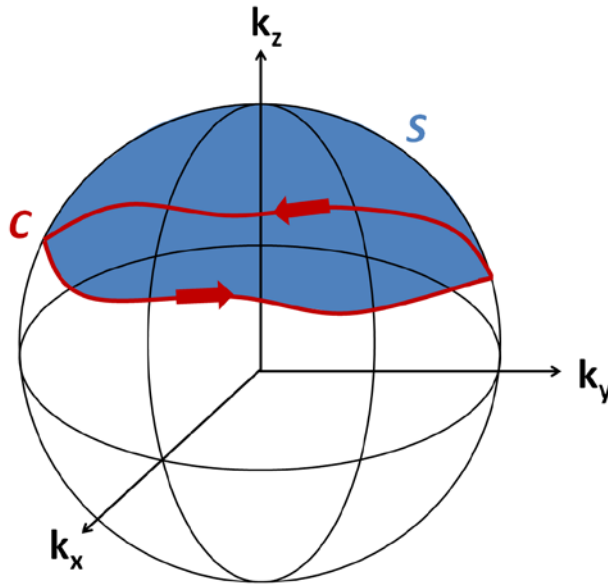


**Figure 3.5. Schematic representation relating to the Berry phase in the reciprocal space.** The projection of a closed path  $C$  enclosing a surface  $S$  on the Bloch sphere is represented. The Berry phase corresponds to the circulation of the Berry vector potential, or the Berry connection, on the closed path  $C$ . Equivalently, the Berry phase can be regarded as the flux of the Berry magnetic field, or the Berry curvature, passing through the surface  $S$ .

Note that we can define an equivalent Berry magnetic field, named as Berry curvature, from the Berry connection as  $\mathbf{B}(\mathbf{k}) = \nabla_{\mathbf{k}} \times \mathbf{A}_m(\mathbf{k})$ . Using the Stokes' theorem, the Berry phase can thus be rewritten as an area integral of the flux of the Berry magnetic field through the surface  $S$  of the Brillouin zone sited on the closed path  $C$  (Fig. 3.5):

$$\phi_B = \iint \mathbf{B}(\mathbf{k}) d^2\mathbf{k} \quad (3.3)$$

In a system where the time-reversal symmetry is preserved, the Berry phase can only take integer values of  $\pi$  modulo  $2\pi$ . For example, the Berry phase is equal to  $\pi$  for a TI material in topologically nontrivial phase (discussed in the subsection 1.3). This  $\pi$  Berry phase has a physical meaning which can be interpreted as the phase formed by closed trajectories of quasiparticles in a nontrivial TI system.

The Berry phase and the Berry curvature are directly related to the Hamiltonian of a system and they can thus reflect the physical properties of the system. Moreover, one can extract from the Berry phase a physical parameter known as topological invariant that is used as a classifier of topological materials.

### 1.2.2. Topological invariants

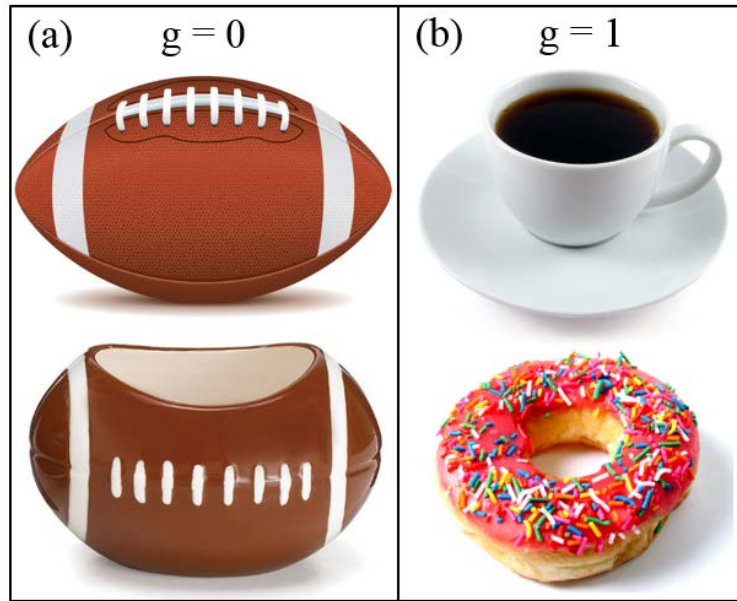


**Figure 3.6. Grouping of objects by the concept of topology for 3D surfaces.** Objects are classified by their genus  $g \in \mathbb{N}$  representing the number of holes they have. (a) A rugby ball and a bowl do not have hole and they are in the group  $g = 0$ . (b) A coffee cup and a donut have one hole and they belong to the group  $g = 1$ . Continuous deformations of an object into another one are allowed in the same group. When there exists a cutting during the transformation,  $g$  will change suddenly.

Topological invariants are physical indices used to distinguish topological systems and categorize them into different topological classes. The easiest intuitive way to understand the notion of topological invariant is the analogy with the topology of 3D surfaces<sup>1,3</sup>. In mathematics, topology is the study of the properties of objects that are invariant or remain unchanged under smooth deformations. The classification of objects is determined by genus  $g \in \mathbb{N}$  which is analogously equivalent to topological invariant and corresponds to the number

## CHAPTER 3

### *A brief overview of topological matter*

---

of holes that an object contains. Since this number is an integer and discrete, it cannot thus be changed continuously from one value to another value by simply deforming the surface of the object. Fig. 3.6(a,b) show two different groups of objects. A rugby ball and a bowl have no hole and belong to the same group of  $g = 0$  (Fig. 3.6(a)). One can thus transform a rugby ball into a bowl, and vice versa, by squeezing, stretching or twisting without cutting. These continuous deformations are also allowed in the group  $g = 1$  for transforming a coffee cup into a donut (Fig. 3.6(b)). If we consider the transformation between a bowl and a donut, it is unavoidable to cut the surface of a bowl to make a hole like in a donut. Consequently,  $g$  changes abruptly from 0 to 1 since no intermediate value is allowed. When a discontinuous deformation between two objects takes place, we assure that these two objects belong to two topologically distinct classes.

In solid state physics, similar considerations are taken into account for the electronic band structure of a system. Note that the band structure comes out of the Hamiltonian established by several symmetries. As a result, the band structures of two systems described by different Hamiltonians are not the same. Hence, these two systems are of distinguishing topological classes. It is impossible to transform continuously the Hamiltonian of the first system into that of the second system. Nevertheless, to make the transformation between both distinct systems possible, the closing of the band gap must occur at the interface between these two gapped materials, equivalently to changing the topological class and thus the topological invariant.

We describe in the following two examples of topological indices: the TKNN and the  $\mathbb{Z}_2$  topological invariants.

#### 1. The TKNN topological invariant or the Chern number

In 1982, D. J. Thouless, M. Kohmoto, M. P. Nightingale, and M. den Nijs (TKNN) demonstrated the difference between a conventional insulator and a quantum Hall insulator using the Kubo formula rewritten in an appropriate form to show the quantization of the Hall conductance in a 2D electron gas subjected to a uniform magnetic field and a periodic potential<sup>16</sup>. The obtained results lead to the definition of a number named as the Thouless-Kohmoto-Nightingale-Nijs or the TKNN topological invariant. It can also be understood in terms of the Berry phase. For the Bloch wave function  $|u_m(\mathbf{k})\rangle$ , the Berry phase or the area integral of the Berry curvature run over the first Brillouin zone is related to the Chern number  $n_m$  of the  $m^{\text{th}}$  occupied band, where  $n_m \in \mathbb{N}$ . The latter reads:

$$n_m = \frac{1}{2\pi} \iint \mathbf{B}(\mathbf{k}) d^2\mathbf{k} \quad (3.4)$$

The total Chern number denoted as  $N$  can be obtained by the summation of  $n_m$  for all occupied bands ( $M$  bands). We, thus, get:

$$N = \sum_{m=1}^M n_m \quad (3.5)$$

The Chern number  $N$  is equivalent to the TKNN topological invariant and is demonstrated to be equivalent to the integer filling factor  $\nu$  in Eq. 3.1 of the IQHE. The Chern invariant cannot change when the Hamiltonian of the system varies continuously and is used to characterize the topological nature of the Bloch states of the system.

## 2. The $Z_2$ topological invariant

The spin-orbit coupling is responsible for TIs accommodating spin-1/2 particles when the time-reversal symmetry is preserved<sup>13</sup>. This leads to at least twofold degenerate eigenstates of the Hamiltonian under the time-reversal symmetry. Such Hamiltonians belong to the TI class. Consequently, smooth deformations without the gap closing are authorized between such two Hamiltonians. The corresponding band structures are symmetric in each wave vector direction ( $k_x, k_y$ , and  $k_z$ ) with respect to the center ( $k_x = 0, k_y = 0, k_z = 0$ ) of the first Brillouin zone owing to the mirror image property of the time-reversal symmetry.

Now, we will turn our attention to the topological invariant of a spin-orbit coupled system where the time-reversal symmetry is preserved. In such a system, the TKNN topological invariant or the Chern number becomes zero. However, an additional topological invariant with two possible values  $\lambda = 0$  or  $1$  has to be considered, known as the  $Z_2$  topological invariant<sup>17</sup>, leading to two topologically distinct classes. In condensed matter, the parity ordering of the conduction and valence band wave functions is closely tight to the topological character of the band structure. Several narrow gap semiconductors are known to exhibit an inversion of this orbital ordering, whereby, an s-like conduction and a p-like valence bands can be inverted to yield a p-like conduction and an s-like valence bands, when a certain external physical parameter is varied (temperature, pressure, or chemical concentration). The topological invariant essentially characterizes the orbital character. Two different types of orbital orderings are associated different  $Z_2$  indices:  $Z_2 = 0$  for the trivial parity order and  $Z_2 = 1$  for the nontrivial one. A material with a nonzero  $Z_2$  index was also shown to host Dirac-dispersing edge or surface states when it is in junction with a material having  $Z_2 = 0$ , or even at its free surface when in contact with air or vacuum.

The  $Z_2$  topological class with only the unbroken time-reversal symmetry<sup>18</sup> consists of 2D TIs with topologically protected 1D conducting edge states and 3D TIs with topologically protected 2D conducting surface states. Further details about theoretical prediction and experimental realization of the  $Z_2$  TIs will be presented in the following subsection.

## **1.3. Theoretical prediction and experimental realization of $Z_2$ topological insulators**

A  $Z_2$  TI is a semiconductor that hosts a band inversion at time-reversal symmetric points in the Brillouin zone. It possesses insulating gapped bulk states and conducting gapless edge or surface states topologically protected by time-reversal symmetry. Such topological

## CHAPTER 3

### A brief overview of topological matter

gapless states occurring at the boundaries of the system stem from the spin-orbit interactions, playing the role of magnetic field. Hence, no external magnetic field is needed. The robustness of these topological gapless states against impurities and disorder makes TIs remarkable. Now, several  $Z_2$  TI systems theoretically predicted and experimentally realized will be exemplified in order to better understand their intrinsic physical properties.

#### 1.3.1. 2D topological insulator: QSHE in CdTe/HgTe/CdTe quantum wells

The QSHE theoretically predicted in a monolayer graphene by C. L. Kane and E. J. Mele in 2005<sup>13</sup> has inspired the search for real materials that can exhibit such a topological phase of matter. Actually, the QSH state requires a material composed of elements with high atomic number in order to generate the strong spin-orbit coupling in the system. In reality, the weak intrinsic spin-orbit coupling of carbon in graphene is not enough to observe the QSHE.

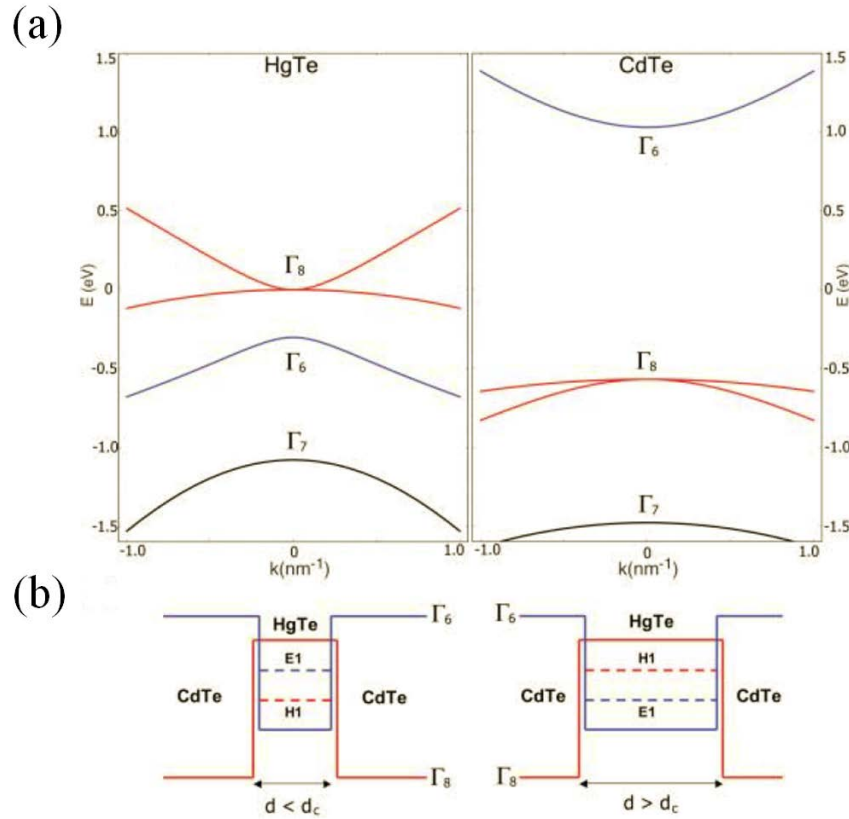


**Figure 3.7. Band structure and energy confinement of the CdTe/HgTe/CdTe heterostructure.** (a) Bulk band structure of the quantum well HgTe and the barrier CdTe at the  $\Gamma$ -point of the Brillouin zone. (b) The CdTe/HgTe/CdTe quantum well in the normal regime ( $E_1 > H_1$  and  $d < d_c$ ) and in the inverted regime ( $E_1 < H_1$  and  $d > d_c$ ), where  $d_c$  is the critical thickness at which the band inversion of the quantum well HgTe occurs. Adapted from<sup>19</sup>.

The first QSH state was successfully found in CdTe/HgTe/CdTe semiconductor quantum wells. In 2006, B. A. Bernevig, T. L. Hughes and S. C. Zhang theoretically demonstrated that helical conducting states of spin currents could occur in this sandwiched

heterostructure at the edges between the quantum well HgTe and the barrier CdTe<sup>19</sup>. The bulk energy bands of the barrier CdTe have a normal band structure with the s-type  $\Gamma_6$  band lying above the p-type  $\Gamma_8$  band, while these two bands are inverted in the quantum well HgTe (Fig. 3.7(a)). The  $\Gamma_7$  bands of both materials represent the far-band having negligible effects on the interaction between the  $\Gamma_6$  and  $\Gamma_8$  bands. When two semiconductors of different parity orderings of the bulk band structure are put alternatively next to each other, 1D topological gapless states can occur at the edges between these two materials under certain conditions. As shown in Fig. 3.7(b), by varying the thickness  $d$  of the well material, the energy confinement in the well can be altered from a normal regime ( $E_1 > H_1$ ) to an inverted one ( $E_1 < H_1$ ) when  $d \geq d_c \approx 64 \text{ \AA}$ , where  $d_c$  is the critical thickness at which the band inversion of the HgTe layer occurs. This band inversion leads to a topological quantum phase transition (at  $d = d_c$ ) of the whole structure between a conventional insulating state and a state exhibiting the QSHE.

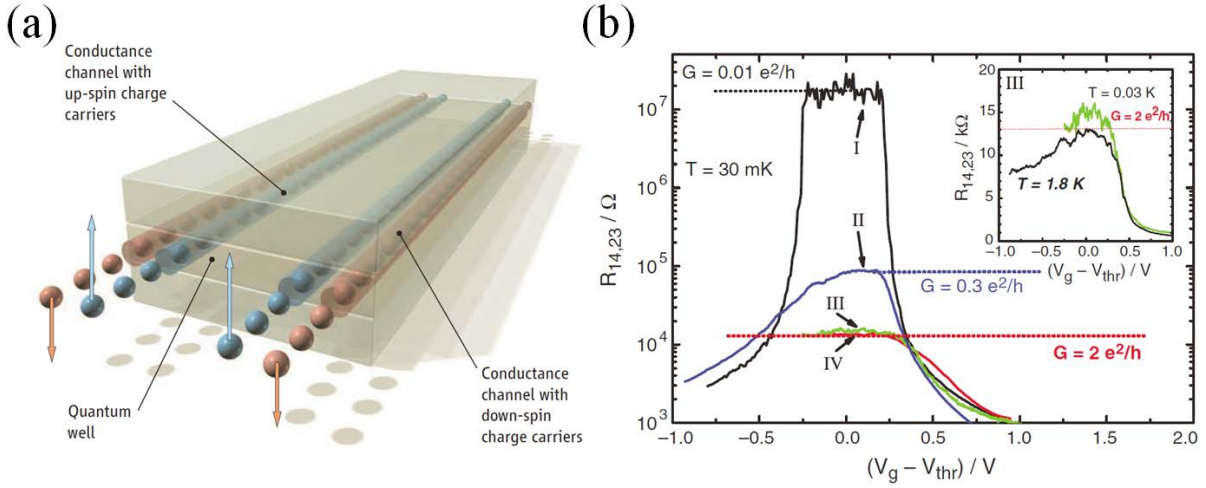


**Figure 3.8. Quantum spin Hall effect in the  $\text{Hg}_{0.3}\text{Cd}_{0.7}\text{Te}/\text{HgTe}/\text{Hg}_{0.3}\text{Cd}_{0.7}\text{Te}$  quantum wells.** (a) Schematic illustration of the helical conducting edge channels of the spin-polarized currents moving in opposite directions. (b) Zero-field transport measurements of the longitudinal resistance at  $T = 30 \text{ mK}$  in normal (I) and inverted (II, III and IV) quantum well samples as a function of normalized gate-voltage. Adapted from<sup>20</sup>.

The QSHE was later experimentally observed by König et al. in 2007 in low density and high mobility carriers residing in  $\text{Hg}_{0.3}\text{Cd}_{0.7}\text{Te}/\text{HgTe}/\text{Hg}_{0.3}\text{Cd}_{0.7}\text{Te}$  quantum wells<sup>20</sup>. Fig. 3.8(a) schematically illustrates the spin-polarized currents moving in opposite directions at the boundaries of the  $\text{Hg}_{0.3}\text{Cd}_{0.7}\text{Te}/\text{HgTe}/\text{Hg}_{0.3}\text{Cd}_{0.7}\text{Te}$  quantum well. In this experiment,  $\text{Hg}_{0.3}\text{Cd}_{0.7}\text{Te}$  exhibits a normal band structure as in the barrier CdTe seen previously and the critical thickness of the well HgTe is  $d_c \approx 63 \text{ \AA}$ . Fig. 3.8(b) shows the longitudinal resistance as a function of normalized gate-voltage of four quantum wells (I, II, III and IV) measured by transport experiment at zero magnetic field and at temperature  $T = 30 \text{ mK}$ . The length and width ( $L \times W$ ) of the samples are  $20 \times 13.3 \mu\text{m}^2$  for  $d < d_c$  (I),  $20 \times 13.3 \mu\text{m}^2$  for  $d > d_c$  (II),  $1 \times 1 \mu\text{m}^2$  for  $d > d_c$  (III) and  $1 \times 0.5 \mu\text{m}^2$  for  $d > d_c$  (IV). The sample I with  $G = 0.01 e^2/h$  shows the normal regime of the well HgTe for  $d < d_c$ . The samples III and IV reach  $G$  close to the predicted value  $2e^2/h$  for  $d > d_c$ , demonstrating the existence of the transport of

## CHAPTER 3

### *A brief overview of topological matter*

---

helical conducting states through edge channels which is independent of the width of the structure. This evidences the QSHE occurring in the inverted regime ( $E_1 < H_1$  and  $d > d_c$ ).

The  $\text{Hg}_{1-x}\text{Cd}_x\text{Te}/\text{HgTe}/\text{Hg}_{1-x}\text{Cd}_x\text{Te}$  quantum well that exhibits the QSHE with 1D helical conducting edge states is the first 2D TI. Nowadays, the QSHE has attracted great attention not only in the study of its fundamental physical properties, but also in its potential application in spintronic devices with low power dissipation.

#### **1.3.2. 3D topological insulators: Bi-based compounds**

The classification of topological materials began after the theoretical and experimental discoveries of the QSHE in the first 2D TI:  $\text{Hg}_{1-x}\text{Cd}_x\text{Te}/\text{HgTe}/\text{Hg}_{1-x}\text{Cd}_x\text{Te}$  quantum well. 3D TIs were predicted in 2007 by L. Fu, C. L. Kane and E. J. Mele<sup>21</sup> and demonstrated to be 3D bulk insulators coexisting with 2D metallic surface states surrounding materials that evolve from 1D helical conducting edge states in 2D TIs. In contrast to a 2D TI governed by only one  $Z_2$  topological invariant, a 3D TI is characterized by 4  $Z_2$  topological invariants<sup>22,23</sup>, yielding 16 distinguishing topological phases of TIs. They are categorized into two general classes: weak TIs (WTIs) and strong TIs (STIs). WTIs and STIs were shown to exhibit 2D conducting gapless surface states with an even and odd number of Dirac points, respectively. The STI state is robust against impurities, whereas the WTI state can be easily destroyed by disorder. In the following text, we will only focus on the STIs since they lead to a new topological surface phase at their interface with topologically trivial systems.

The Bi-based materials were proposed to be 3D STIs. Semiconducting alloy  $\text{Bi}_{1-x}\text{Sb}_x$  theoretically predicted by L. Fu and C. L. Kane in 2007 was prime candidate of the first generation of 3D TIs<sup>24</sup> and was verified experimentally via ARPES measurements by D. Hsieh et al. in 2008<sup>25</sup>. Additionally, Landau level magneto-infrared spectroscopy performed in a single crystal of  $\text{Bi}_{0.91}\text{Sb}_{0.09}$  provides evidence for the existence of topological surface states<sup>26</sup>. The second generation of 3D TIs was predicted by H. Zhang et al. in 2009 to be stoichiometric Bi-based compounds in the  $\text{Bi}_2\text{Se}_3$  family:  $\text{Bi}_2\text{Se}_3$ ,  $\text{Bi}_2\text{Te}_3$ , and  $\text{Sb}_2\text{Te}_3$ , hosting a single Dirac cone on their surface<sup>27</sup>. The latter is one of the characteristic features of such materials. ARPES experiments were subsequently performed in  $\text{Bi}_2\text{Se}_3$  by Y. Xia et al.<sup>28</sup> and in  $\text{Bi}_2\text{Te}_3$  by Y. L. Chen et al.<sup>29</sup> in 2009 and topological surface states were successfully observed. In order to get a better understanding of 3D TIs, only the most elementary form of 3D TI materials in the  $\text{Bi}_2\text{Se}_3$  family with a large bulk band gap and a single nondegenerate surface Dirac cone will be described.



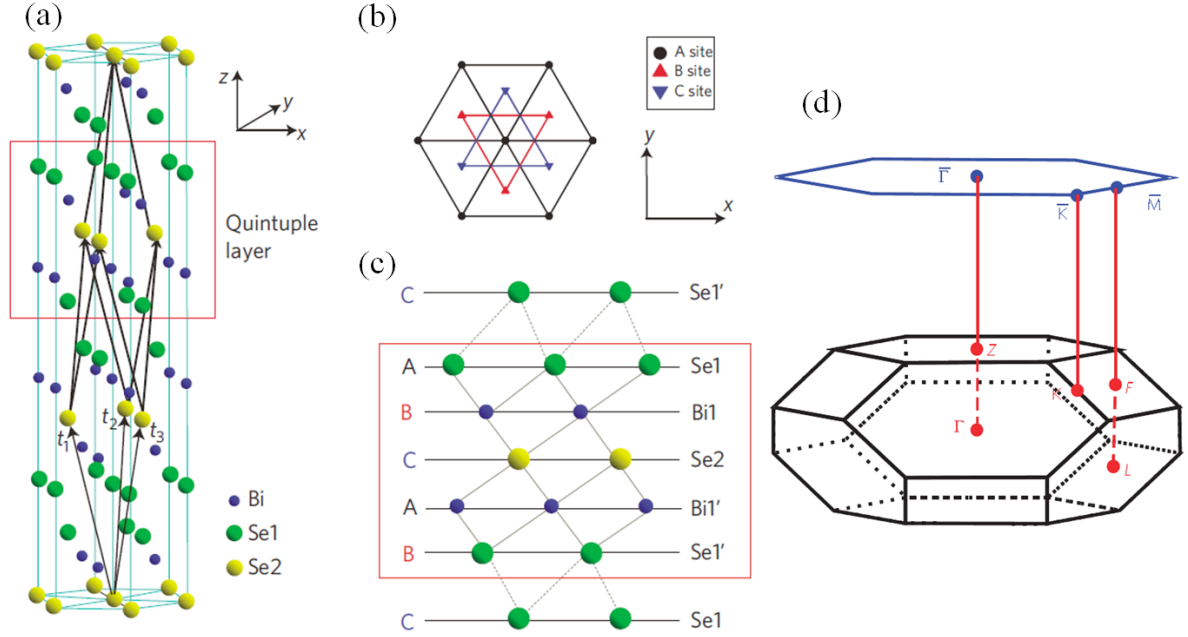


**Figure 3.9. Structural properties of Bi<sub>2</sub>Se<sub>3</sub>.** (a) Crystal structure of Bi<sub>2</sub>Se<sub>3</sub>. Three primitive lattice vectors  $\vec{t}_1$ ,  $\vec{t}_2$  and  $\vec{t}_3$  form a rhombohedral unit cell with five atoms in the space group  $D_{3d}^5$  ( $R\bar{3}m$ ). The red rectangle represents a quintuple layer composed of five atomic layers of Bi and Se. (b) Top view along the  $z$ -direction of three different positions (A, B and C) of the triangle lattice in a quintuple layer. (c) Side view along the  $z$ -direction of stacking order of Bi and Se atomic layers. In this configuration, Se2 atoms play the role of inversion centers. (d) Bulk Brillouin zone of Bi<sub>2</sub>Se<sub>3</sub> with four inequivalent time-reversal-invariant high-symmetry points  $\Gamma$ ,  $L$ ,  $F$  and  $Z$ . 2D Brillouin zone is represented by blue hexagon with high-symmetry points  $\bar{\Gamma}$ ,  $\bar{K}$ , and  $\bar{M}$ . Adapted from <sup>27</sup>.

Bi<sub>2</sub>Se<sub>3</sub>, Bi<sub>2</sub>Te<sub>3</sub>, Sb<sub>2</sub>Te<sub>3</sub> and Sb<sub>2</sub>Se<sub>3</sub> possess the same rhombohedral crystal structure in the space group  $D_{3d}^5$  ( $R\bar{3}m$ ) shown in Fig. 3.9(a) for a representative Bi<sub>2</sub>Se<sub>3</sub>. Five atomic layers of Bi and Se form a quintuple layer (Fig. 3.9(a,c)) in the sequence ...-A(Se1)-B(Bi1)-C(Se2)-A(Bi1')-B(Se1')-..., where A, B and C are three different positions of the triangle lattice (Fig. 3.9(b)). Here, Se2 plays the role of inversion centers by which the Se1 (Bi1) layer can be related to the Se1' (Bi1') layer. The interaction between two consecutive atomic layers within a quintuple layer is strong, while the van der Waals force is dominant between two consecutive quintuple layers. Fig. 3.9(d) shows the bulk Brillouin zone of Bi<sub>2</sub>Se<sub>3</sub> with four inequivalent time-reversal-invariant high-symmetry points  $\Gamma$ ,  $L$ ,  $F$  and  $Z$ . The projection of red high-symmetry points, represented by red solid lines, onto the corresponding 2D Brillouin zone gives rise to  $\bar{\Gamma}$ ,  $\bar{K}$ , and  $\bar{M}$  high-symmetry points.



## CHAPTER 3

### A brief overview of topological matter

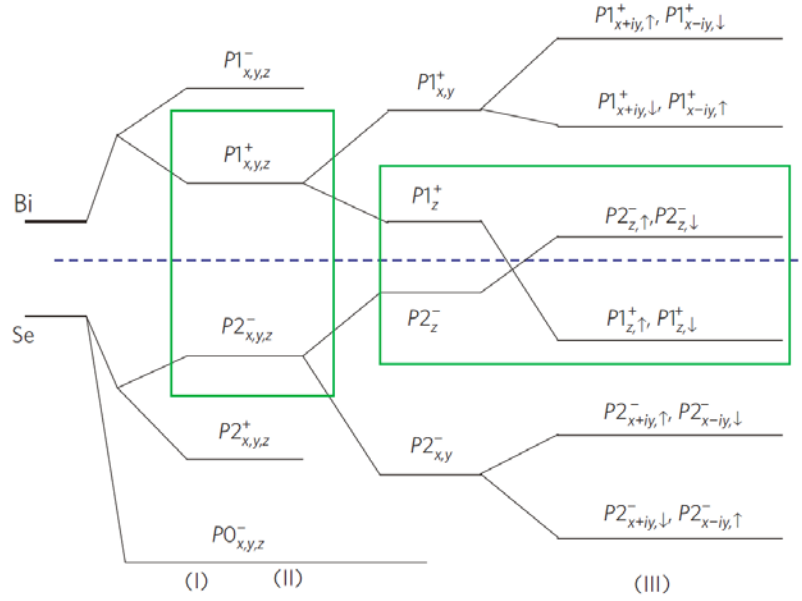


**Figure 3.10. Evolution from the atomic orbitals of Bi and Se into the conduction and valence bands of  $\text{Bi}_2\text{Se}_3$  at the  $\Gamma$ -point of the Brillouin zone.** The Fermi energy is indicated by blue dashed line. Three processes (I), (II) and (III) show respectively the effect of chemical bonding, crystal-field splitting and spin-orbit coupling on the energy levels. Two green rectangles highlight the levels undergone the effects near the Fermi energy. The level crossing in  $\text{Bi}_2\text{Se}_3$  occurs due to the spin-orbit coupling. Adapted from <sup>27</sup>.

We have previously seen that the spin-orbit interaction is responsible for the emergence of a TI phase in the system accommodating spin-1/2 particles when the time-reversal symmetry is preserved. Fig. 3.10 schematically shows the evolution of the atomic p orbitals of Bi ( $6s^26p^3$ ) and Se ( $4s^24p^4$ ). Here, the effect of their s orbitals is neglected since they are far from the Fermi energy, indicated by blue dashed line. The process (I) is related to the chemical bonding between Bi and Se atoms within a quintuple layer. This lifts up the Bi states from each p orbitals (one odd (-) and one even (+)) and pushes down the Si states from each p orbitals (two odd (-) and one even (+)). The process (II) corresponds to the crystal-field splitting between different p orbitals in the first green rectangle near the Fermi energy. This effect results in the splitting of the  $p_z$  orbital, to be near the Fermi energy, from the  $p_x$  and  $p_y$  orbitals. The process (III) is the effect of the spin-orbit coupling. The order of the two  $p_z$  orbitals of different parity obtained from the crystal-field splitting will be reversed if the spin-orbit coupling is strong enough. We notice that the TI phase at the  $\Gamma$ -point of the  $\text{Bi}_2\text{Se}_3$  system stems from the inversion between two levels of opposite parity due to the spin-orbit interaction. Similarly, the level crossing caused by the spin-orbit coupling occurs in  $\text{Bi}_2\text{Te}_3$  and  $\text{Sb}_2\text{Te}_3$ . In  $\text{Sb}_2\text{Se}_3$ , the scenario is different since the spin-orbit coupling is not strong enough.

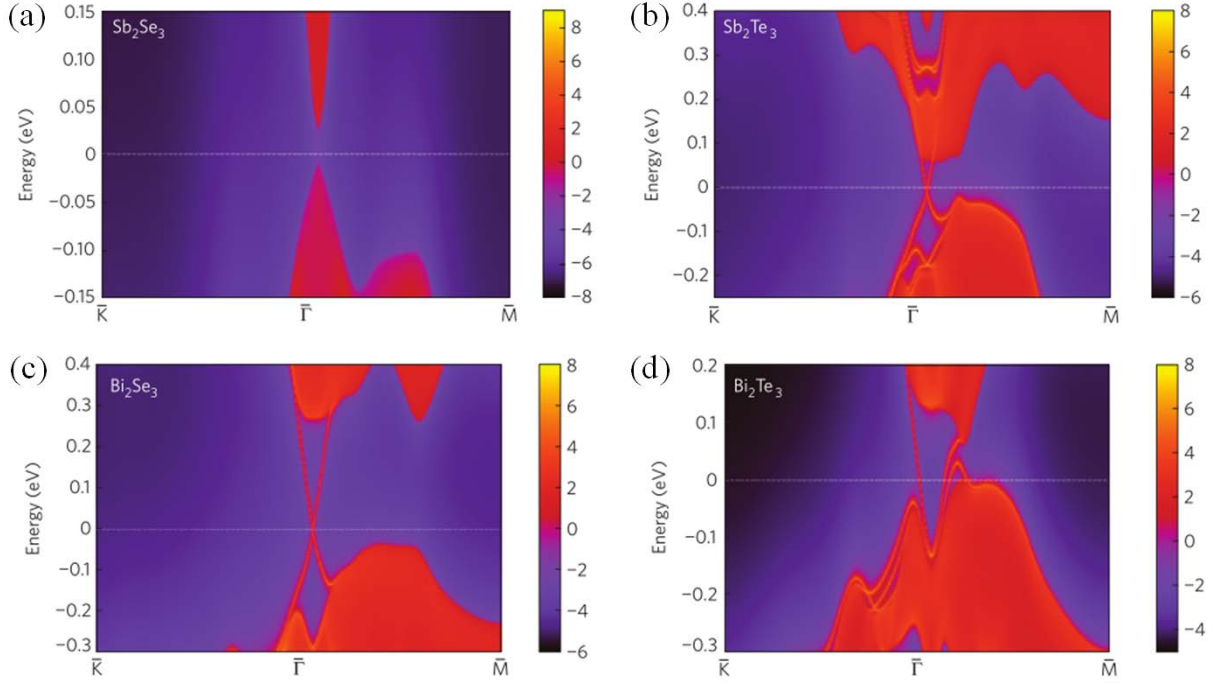


**Figure 3.11. Band structure calculations of Bi-based compounds in the  $\text{Bi}_2\text{Se}_3$  family.** Band structures of (a)  $\text{Sb}_2\text{Se}_3$ , (b)  $\text{Sb}_2\text{Te}_3$ , (c)  $\text{Bi}_2\text{Se}_3$  and (d)  $\text{Bi}_2\text{Te}_3$  along the  $\bar{K}$ - $\bar{\Gamma}$ - $\bar{M}$  direction on the 2D Brillouin zone. Red color indicates the regions of bulk energy bands and violet color indicates the regions of bulk energy gaps. The surface states can be clearly seen at the  $\bar{\Gamma}$ -point as red lines linearly dispersing in the bulk energy gap in  $\text{Bi}_2\text{Se}_3$ ,  $\text{Bi}_2\text{Te}_3$  and  $\text{Sb}_2\text{Te}_3$ . No evidence for the surface states in  $\text{Sb}_2\text{Se}_3$ . Adapted from <sup>27</sup>.

The most characteristic feature of 3D TI materials is the existence of topological surface states. Fig. 3.11 displays the study of the electronic band structures of  $\text{Bi}_2\text{Se}_3$ ,  $\text{Bi}_2\text{Te}_3$ ,  $\text{Sb}_2\text{Te}_3$  and  $\text{Sb}_2\text{Se}_3$  calculated using *ab initio* simulations along the  $\bar{K}$ - $\bar{\Gamma}$ - $\bar{M}$  direction on the 2D Brillouin zone <sup>27</sup>. One can clearly see at the  $\bar{\Gamma}$ -point a single linearly dispersive Dirac cone in the bulk energy gap associated with the topological surface states occurring in  $\text{Bi}_2\text{Se}_3$ ,  $\text{Bi}_2\text{Te}_3$  and  $\text{Sb}_2\text{Te}_3$ . These three materials are thus topologically nontrivial insulators. The Dirac velocity of the topological surface states was found to be  $\sim 5.0 \times 10^5$  m/s. On the contrary, no Dirac cone is observed in  $\text{Sb}_2\text{Se}_3$ , such a compound is thus a topologically trivial insulator.

The topological surface states of Bi-based materials in the  $\text{Bi}_2\text{Se}_3$  family were also experimentally evidenced by ARPES measurements. Fig. 3.12(b) shows high-resolution ARPES spectra of the surface electronic band dispersion in  $\text{Bi}_2\text{Se}_3$  along the  $\bar{M}$ - $\bar{\Gamma}$ - $\bar{M}$  and  $\bar{K}$ - $\bar{\Gamma}$ - $\bar{K}$  momentum-space cuts following the wave vector directions on the surface Brillouin zone shown in Fig. 3.12(a). The Dirac velocity of the topological surface state band is approximately  $5 \times 10^5$  m/s in the two linecut directions. This confirms the occurrence of the topological surface state feature that can be observed as a single nondegenerate Dirac cone at the  $\bar{\Gamma}$ -point, coexisting with the bulk states projected on the surface Brillouin zone. Moreover, another typical characteristic of TIs is the spin polarization of Dirac fermions on the surface.

## CHAPTER 3

### A brief overview of topological matter

As can be seen in Fig. 3.12(c), the spin angular momentum direction (red line) of helical Dirac fermions is perpendicular to its translational momentum direction and this results in the spin-momentum locked helical surface Dirac cone in  $\text{Bi}_2\text{Se}_3$ ,  $\text{Bi}_2\text{Te}_3$  and  $\text{Sb}_2\text{Te}_3$ <sup>30,31</sup>.

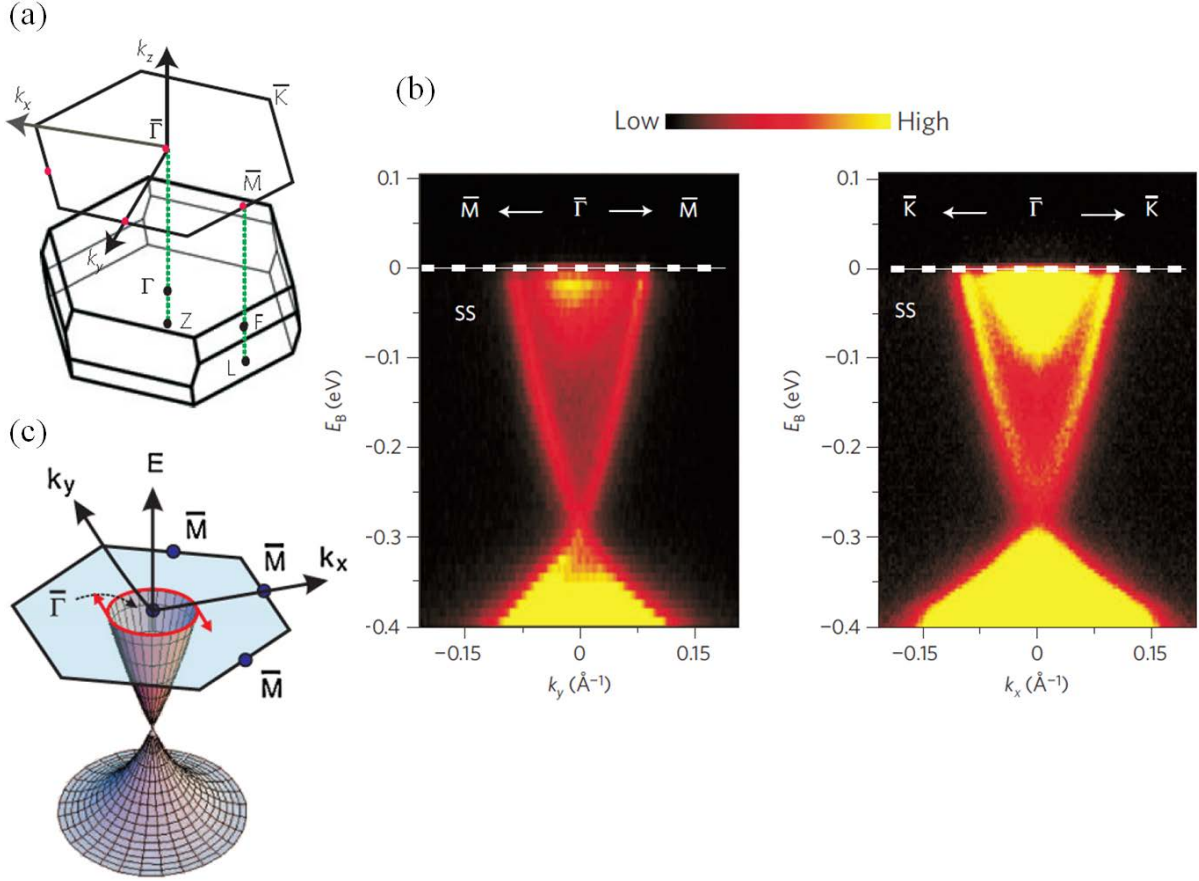


**Figure 3.12. Topological surface state properties of Bi-based materials in the  $\text{Bi}_2\text{Se}_3$  family.** (a) Bulk and surface Brillouin zones of Bi-based materials in the  $\text{Bi}_2\text{Se}_3$  family and three orthogonal directions of wave vectors of which the origin is located at the  $\bar{\Gamma}$ -point. (b) ARPES spectra of  $\text{Bi}_2\text{Se}_3$  showing the electronic band dispersion of bulk and topological surface states along the  $\bar{M}-\bar{\Gamma}-\bar{M}$  and  $\bar{K}-\bar{\Gamma}-\bar{K}$  linecuts on the surface Brillouin zone shown in (a). (a) and (b) are adapted from<sup>28</sup>. (c) Schematic of the spin-polarized surface state dispersion in the  $\text{Bi}_2\text{Se}_3$  family compounds. (c) is adapted from<sup>31</sup>.

Interestingly,  $\text{Bi}_2\text{Se}_3$  has a topologically nontrivial energy gap of approximately 300 meV predicted by theoretical calculations<sup>27</sup> and measured by ARPES experiments<sup>28,30</sup>. In contrast, optical studies report significantly lower values of about 200 meV for the energy gap of  $\text{Bi}_2\text{Se}_3$ <sup>32</sup>. There is still no consensus on the value of the energy gap of  $\text{Bi}_2\text{Se}_3$  and this discrepancy has not yet been clearly understood. Nevertheless, this could be explained by the fact that ARPES is a surface sensitive technique used to investigate the surface states of a material and it could take into account surface reconstruction effects, while optical methods probe the whole volume of the material. In  $\text{Bi}_2\text{Te}_3$ , the band gap is close to 170 meV<sup>29,31</sup>. The large band gap observed in the  $\text{Bi}_2\text{Se}_3$  family makes the topological surface states much more robust against any perturbations.

## 2. Topological crystalline insulators

Inspired by the discovery of TIs, topological crystalline insulators (TCIs) are a novel family of topological materials extended from the topological classification of band structures by including certain point group symmetry. In this thesis, the typical topological characteristics of massive and massless Dirac fermions in TCIs will be addressed. The notion of TCIs was first introduced by L. Fu in 2011. Such materials possess semiconducting bulk states accompanied by metallic gapless surface states as in the case of the well-known existing  $Z_2$  TIs<sup>33</sup>, but their topological surface states occur at an even number of high-symmetry points in the Brillouin zone. Contrary to TIs protected by time-reversal symmetry<sup>3,4,34</sup>, a TCI material is protected by mirror symmetry or reflection symmetry present in the crystal<sup>33,35</sup>. Such a reflection symmetry  $M$  is a combination of spatial inversion  $P$  ( $\vec{r} \rightarrow -\vec{r}$ ) and twofold rotation  $C_2$  (a rotation of an angle  $2\pi/n$ , where  $n = 2$ ) around the axis perpendicular to the plane of reflection:  $M = PC_2$ <sup>35</sup>. Moreover, for a TCI material, the total Chern number required by time-reversal symmetry is zero, but one can define a mirror Chern number which is a nonzero integer<sup>36</sup>. The latter becomes a new topological invariant determining a TCI state protected by mirror symmetry. Note that crystal symmetries can be broken by material surfaces. As a consequence, topological surface states of a TCI can only exist on some high-symmetry surfaces of the crystal, which is not the case in TI materials. The key role of mirror symmetry present in TCIs makes the study of different surface orientations very attractive.

The classification of TCI materials has not been completed yet. Therefore, the discovery of these topological states of matter is extremely intriguing and challenging in the research area of condensed matter physics. In 2012, Timothy H. Hsieh et al.<sup>37</sup> theoretically predicted the first class of TCI materials in narrow gap rocksalt IV-VI semiconductors and proposed SnTe as a representative by identifying its nonzero topological index or mirror Chern number. The first experimental observation of the topological surface states in SnTe single crystals was subsequently carried out by Y. Tanaka et al.<sup>38</sup>. ARPES experiment was performed in this compound and showed Dirac-like band dispersion originating from the metallic surface states. In contrast, the isostructural compound PbTe in the same IV-VI material family was demonstrated to be a conventional insulator<sup>37</sup>. However, PbTe can become a TCI by applying strain, pressure, temperature or alloying. Therefore, ARPES measurements were performed in related  $Pb_{1-x}Sn_xSe$ <sup>39</sup> and  $Pb_{1-x}Sn_xTe$ <sup>40</sup> alloys. The signature of topological surface states was also evidenced in transport and scanning tunneling microscopy (STM) experiments<sup>41–43</sup>. Henceforward, the study of the electronic band structures of the lead-tin salt  $Pb_{1-x}Sn_xSe$  and  $Pb_{1-x}Sn_xTe$  alloys has recently become an active field in the search for topological states of matter. A complete understanding of the behavior of surface Dirac fermions in such materials and the ability to reliably distinguish them from the bulk carriers is a necessary prerequisite to their development and implementation in potential devices<sup>44–47</sup>.

## 2.1. Crystal structure

$\text{Pb}_{1-x}\text{Sn}_x\text{Se}$  (for  $x \leq 0.4$ ) and  $\text{Pb}_{1-x}\text{Sn}_x\text{Te}$  alloys crystallize in a face-centered-cubic (FCC) structure as that of NaCl (space group  $Fm\bar{3}m$ )<sup>37,39,40</sup> represented in Fig. 3.13(a). In this structure, Pb/Sn and Te/Se form independently an FCC lattice. By interpenetrating these two lattices, we get a 3D checkerboard pattern. The first 3D Brillouin zone (3DBZ) or bulk Brillouin zone of these compounds is a truncated octahedron composed of six square faces and eight hexagonal faces<sup>40</sup> as illustrated in Fig. 3.13(b). As discussed in the subsection 2.2, ellipsoidal bulk carrier pockets are located at the  $L$ -points, the centers of the hexagonal faces.

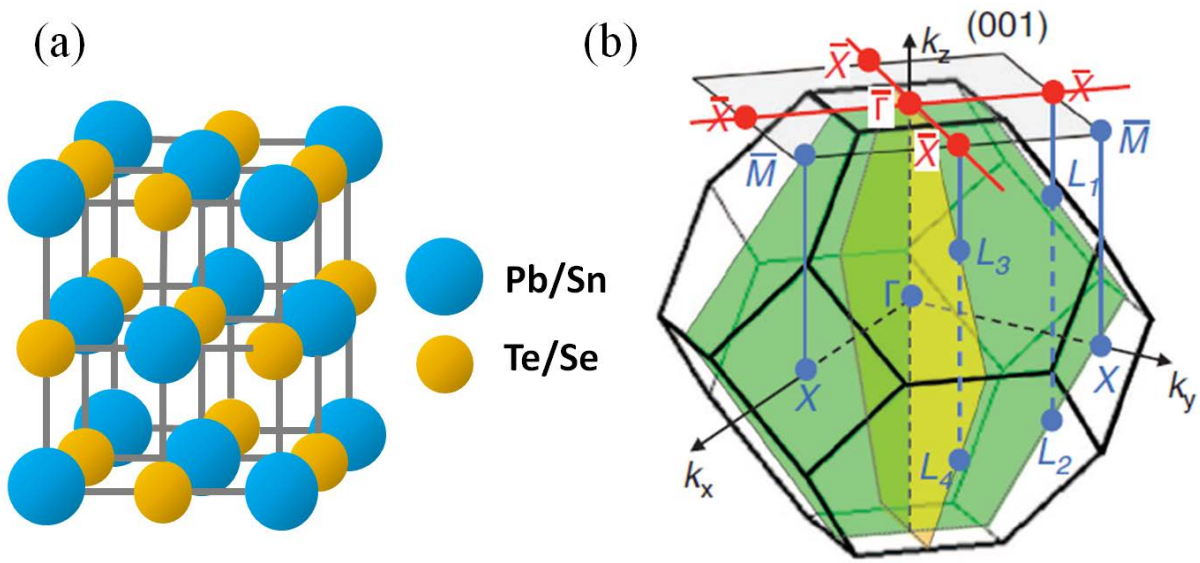


**Figure 3.13. Structural properties of  $\text{Pb}_{1-x}\text{Sn}_x\text{Se}$  and  $\text{Pb}_{1-x}\text{Sn}_x\text{Te}$  systems.** (a) Rocksalt (space group  $Fm\bar{3}m$ ) crystal structure. (b) The first 3D Brillouin zone (3DBZ) accompanied by a (001)-oriented 2D Brillouin zone (2DBZ). Two mirror crystallographic planes  $\{110\}$  are shown in yellow and green inside the bulk Brillouin zone. (b) is adapted from<sup>40</sup>.

## 2.2. Band inversion

Rocksalt IV-VI semiconductors  $\text{Pb}_{1-x}\text{Sn}_x\text{Se}$  and  $\text{Pb}_{1-x}\text{Sn}_x\text{Te}$  possess a small direct band gap that is found to be situated at the  $L$ -points of the 3DBZ. In a system having the conduction and valence bands of opposite parity, a band inversion (or equivalently a parity inversion) of bulk states can take place and gives rise to metallic gapless surface states<sup>19,24,27,33,37</sup>. The band inversion in such materials can be induced by varying temperature<sup>39,48,49</sup> or pressure<sup>50</sup> of the systems, applying strain to the crystal structure of the TCI layers grown on a specific substrate having different lattice constant<sup>51</sup>, and chemical composition alloying<sup>40,42,48,49,52–55</sup>.

In this thesis, we present the topological phase transitions induced by chemical alloying in TCIs. For the system of lead salts, the band inversion occurs as a function of



increasing Sn content at four equivalent  $L$ -points of the bulk Brillouin zone. As illustrated in Fig. 3.14(a), in the topologically trivial phase  $L_6^-$  is the lowest conduction band and  $L_6^+$  is the highest valence band that are of different parity. They form an energy gap  $E_g$  of the system. The band inversion at 4.5 K occurs at a critical value of the Sn composition  $x_c$  ( $x_c \approx 0.16$  for  $\text{Pb}_{1-x}\text{Sn}_x\text{Se}$  and  $x_c \approx 0.4$  for  $\text{Pb}_{1-x}\text{Sn}_x\text{Te}$ )<sup>48,49,53,54</sup> leading to a trivial to nontrivial topological phase transition. In the topologically trivial phase (normal regime), the energy gap ( $E_g > 0$ ) initially decreases with increasing Sn content, then closes at  $x = x_c$ , and finally re-opens as  $x > x_c$  ( $E_g < 0$ ) in the topologically nontrivial phase (inverted regime). This band inversion results in the emergence of the topological surface states (TSS) in the topologically nontrivial regime (blue shaded region), exhibiting zero gap Dirac-like dispersion. After the band inversion, the alloys remain direct band gap semiconductors.

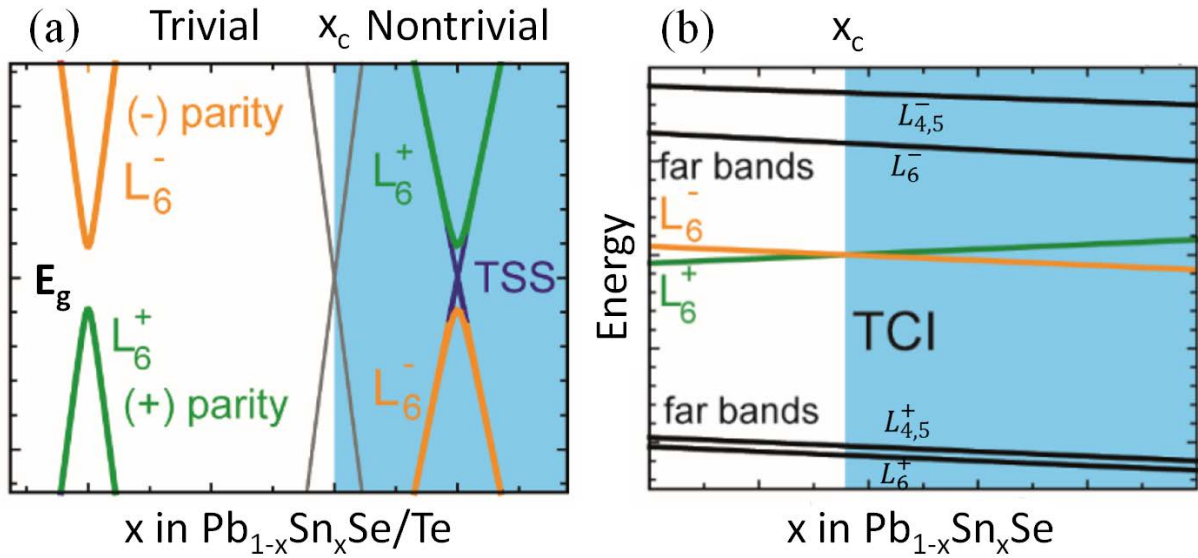


**Figure 3.14. Band inversion in narrow gap rocksalt IV-VI semiconductors.** (a) Schematic illustration of a topological phase transition in  $\text{Pb}_{1-x}\text{Sn}_x\text{Se}$  and  $\text{Pb}_{1-x}\text{Sn}_x\text{Te}$  systems, from topologically trivial regime to topologically nontrivial regime (blue region), occurring at a critical Sn concentration  $x_c$ . (a) is modified from our previous paper<sup>55</sup>. (b) Schematic illustration of the evolution of the conduction and valence band edges ( $L_6^\pm$ ) as a function of Sn content  $x$  for  $\text{Pb}_{1-x}\text{Sn}_x\text{Se}$  adapted from<sup>50</sup>. The far-bands represented above and below the  $L_6^\pm$  bands are very distant and do not deform too much the  $L_6^\pm$  bands, especially in the vicinity of the bulk band crossover point  $x_c$  where the band gap is really narrow.

Fig. 3.14(b) illustrates qualitatively the variation of the energies of the principal conduction and valence bands ( $L_6^\pm$ ) and four far-bands (represented by black lines) at the  $L$ -points for  $\text{Pb}_{1-x}\text{Sn}_x\text{Se}$ <sup>50</sup>. The conduction far-bands  $L_{4,5}^-$  and  $L_6^-$  and the valence far-bands  $L_{4,5}^+$  and  $L_6^+$  result from the spin-orbit interactions. Using the  $\mathbf{k} \cdot \mathbf{p}$  perturbation theory and taking into account the spin-orbit interactions, it was predicted that the band structures of PbSe and PbTe are quite similar, but only a difference in the spacing of various conduction and valence far-bands will be appeared<sup>56</sup>. Furthermore, theoretical calculations using a  $\mathbf{k} \cdot \mathbf{p}$  model of the band structures of  $\text{Pb}_{1-x}\text{Sn}_x\text{Se}$  and  $\text{Pb}_{1-x}\text{Sn}_x\text{Te}$  as a function of Sn composition were later performed<sup>57</sup>, showing the four far-bands in these two systems are distant from the main

## CHAPTER 3

### A brief overview of topological matter

conduction and valence bands ( $L_6^\pm$ ). These three conduction and three valence levels are of important because they lie in the energy interval spread of about 3-5 eV for PbSe, PbTe and PbS<sup>54</sup>.

It is important to note that the critical Sn content  $x_c$  of  $\text{Pb}_{1-x}\text{Sn}_x\text{Se}$  and  $\text{Pb}_{1-x}\text{Sn}_x\text{Te}$  alloys depends on the temperature of measurement. As shown in Fig. 3.15, the experimental data at temperatures  $T = 77, 195$  and  $300$  K obtained from infrared absorption and the p-n junction laser emission studies by A. J. Strauss in 1967<sup>49</sup> show a decrease in energy gap  $E_g$  of  $\text{Pb}_{1-x}\text{Sn}_x\text{Se}$  with increasing  $x$  through the topological phase transition. Black dashed line represents an extrapolation derived from known parameters ( $E_g = 0.165$  eV for PbSe and the composition dependence  $dE_g/dx = -0.89$  eV<sup>49</sup>) for measurement at 4 K. We notice that a temperature-driven experiment allows one to observe a topological phase transition in a given Sn content sample, for example in the compound with  $x = 0.23$  indicated by red dashed line. At low temperatures, the sample is in the nontrivial regime (yellow area) and has negative band gap ( $L_6^+$  is above  $L_6^-$  with the TSS in broken lines). Then, its band gap becomes closer to zero when temperature is increased and the 3D gapless Dirac state could occur at the critical temperature  $T_c$  (between 77 and 195 K). Beyond  $T_c$ , the energy gap of this sample changes sign from negative to positive ( $L_6^-$  is above  $L_6^+$  without the TSS) and the sample is in the trivial regime (white area).

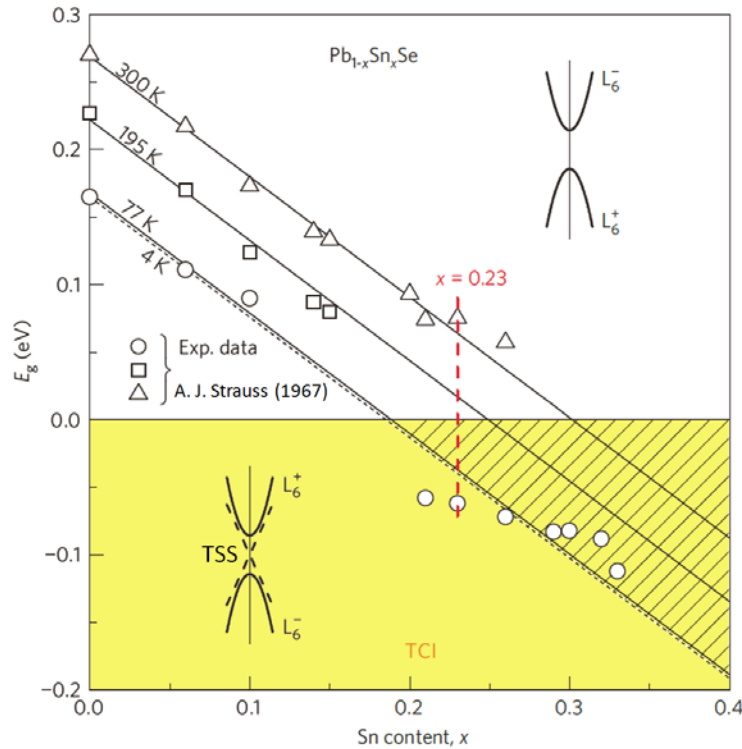


**Figure 3.15. Variation of the band gap in  $\text{Pb}_{1-x}\text{Sn}_x\text{Se}$  alloys as a function of Sn composition and temperature.** The experimental data points were obtained by A. J. Strauss in 1967<sup>49</sup> at 77, 195 and 300 K. An extrapolation at 4 K (black dashed line) is derived from known parameters. The band gap decreases as  $x$  is increased for all the temperatures. This figure demonstrates that the critical Sn content  $x_c$  depends on the

temperature of measurement and the topological phase transition of a given compound can be studied by varying temperature, as indicated by red dashed line for the sample with  $x = 0.23$ . White and yellow regions correspond to trivial (positive gap with  $L_6^-$  above  $L_6^+$ ) and nontrivial (negative gap with  $L_6^+$  above  $L_6^-$  and the TSS) phases, respectively. This figure is adapted from <sup>39</sup>.

### 2.3. Topological surface Dirac cones in different bulk Brillouin zone orientations

The crystalline mirror symmetry present in the rocksalt structure dictates that there only exist some surfaces residing topological gapless surface Dirac cones. As represented in Fig. 3.16, three 3DBZs of the rocksalt crystal are appropriately oriented to show the projections onto their corresponding (001), (110) and (111) surface Brillouin zones or 2DBZs shown in green <sup>58</sup>. Owing to the inversion symmetry of the crystal, the  $L$ -points are diagonally symmetric with respect to the six equivalent  $\{110\}$  mirror planes shown in yellow <sup>40</sup>. Thus, there are four equivalent  $L$ -points in total. For the (001)-oriented surface (Fig. 3.16(a)), there are two  $\{110\}$  mirror planes, there is only one for the (110) surface (Fig. 3.16(b)), and there are three such planes for the (111) surface (Fig. 3.16(c)). In all three cases, the projections of all high-symmetry  $L$ -points of the 3DBZs are located at the edges of each respective 2DBZ. The only one exception is the  $L_1$ -point in the (111)-oriented 3DBZ of which the projection is at the  $\bar{\Gamma}$ -point, the center of the (111)-2DBZ. Moreover, in a given configuration, each mirror plane can be projected onto the crystal surface arising in a corresponding mirror plane symmetry line shown on the 2DBZ.

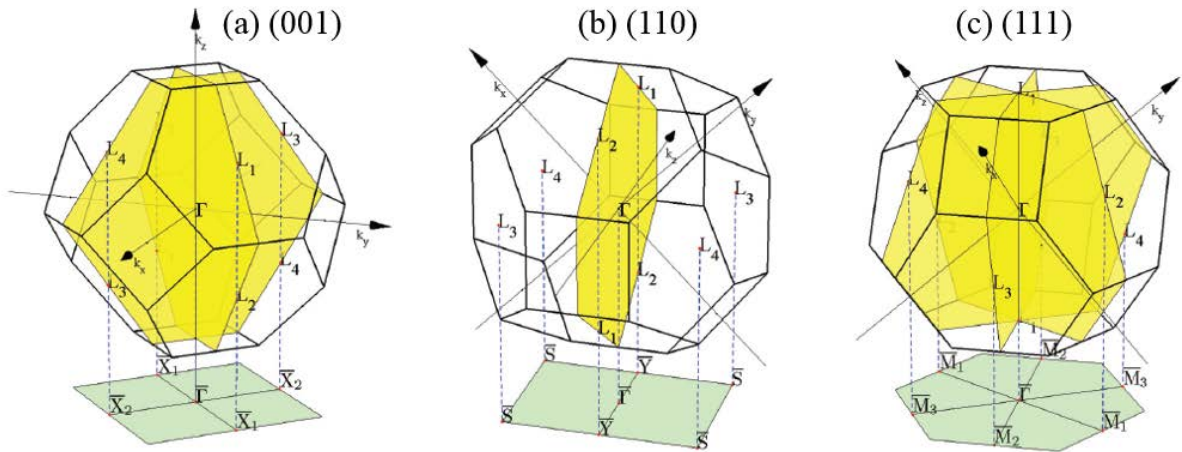


**Figure 3.16. The first three-dimensional Brillouin zones (3DBZs) of rocksalt crystal structure in various configurations.** (a) (001)-oriented surface. (b) (110)-oriented surface. (c) (111)-oriented surface. The six equivalent  $\{110\}$  mirror planes are shown in yellow. The mirror plane symmetry lines on each respective two-dimensional Brillouin zone (2DBZ) are depicted by black solid lines. Adapted from <sup>58</sup>.

In topologically nontrivial materials, the band inversion at the  $L$ -points of the bulk Brillouin zone with the crystalline mirror symmetry with respect to the  $\{110\}$  crystallographic planes leads to topologically protected band crossings at an even number of points (2 for (110) surface and 4 for (001) and (111) surfaces) on the 2DBZ <sup>33</sup>. This is in contrast to TIs



## CHAPTER 3

### A brief overview of topological matter

where the band crossings topologically protected by time-reversal symmetry occur at an odd number of high-symmetry points of the 3DBZ<sup>3,4,34</sup>. These points correspond to where the bulk  $L$ -points project on each respective surface. Thus, in each 3DBZ orientation, this band inversion results in the emergence of surface Dirac cones at points of the corresponding 2DBZ which are also mirror symmetric with respect to the mirror symmetry lines. Since all ellipsoidal bulk carrier pockets of the (001) 3DBZ are equivalently oriented with respect to the [001] direction, the (001)-oriented surface of  $\text{Pb}_{1-x}\text{Sn}_x\text{Se}$  and  $\text{Pb}_{1-x}\text{Sn}_x\text{Te}$  thus ends up having four similar Dirac cones along the  $\bar{\Gamma}$ - $\bar{X}$  linecuts of the 2DBZ (Fig. 3.17(a)). The (111)-oriented surface has one Dirac cone (blue) at the  $\bar{\Gamma}$ -point stemming from a bulk pocket (black) oriented along the [111] direction and three Dirac cones (green) at the  $\bar{M}$ -points resulting from the other three bulk pockets (red) similarly oriented with respect to the [111] direction (Fig. 3.17(b)). Ternary (001) and (111)  $\text{Pb}_{1-x}\text{Sn}_x\text{Se}$  and  $\text{Pb}_{1-x}\text{Sn}_x\text{Te}$  alloys are thus fourfold degenerate TCI where topology is governed by the symmetry of the crystal. Contrary to the (110)-oriented surface (twofold degenerate TCI), two Dirac cones occur along the  $\bar{\Gamma}$ - $\bar{Y}$  linecuts of the 2DBZ. In this thesis, we essentially consider the (111) orientation even if some measurements were performed on (001)-oriented samples.

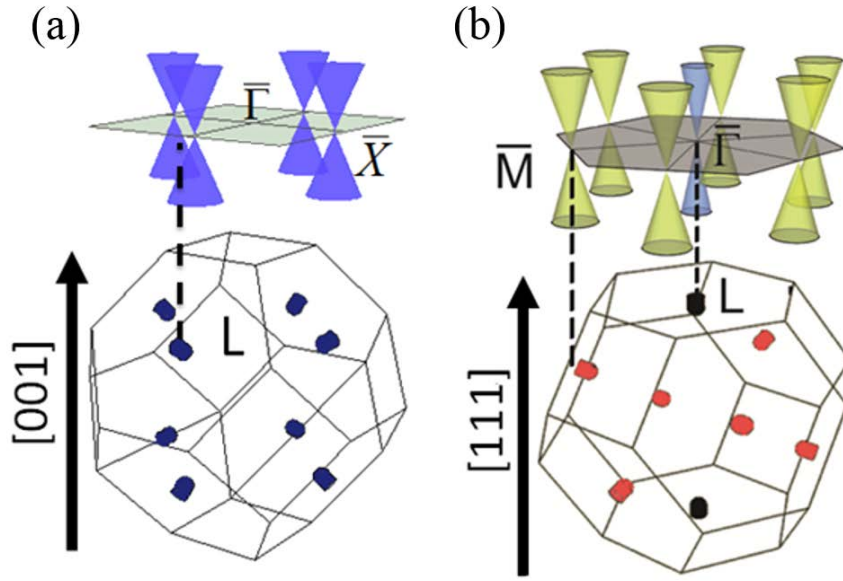


**Figure 3.17. Topological gapless surface Dirac cones of nontrivial  $\text{Pb}_{1-x}\text{Sn}_x\text{Se}$  and  $\text{Pb}_{1-x}\text{Sn}_x\text{Te}$  alloys.** (a) (001)-oriented and (b) (111)-oriented 3DBZs with respective 2DBZs shown on top. Ellipsoidal bulk carrier pockets at the  $L$ -points are represented in each configuration. All bulk pockets of the (001) 3DBZ are equivalently oriented from the [001] direction and give rise to four surface Dirac cones located along the mirror symmetry lines  $\bar{\Gamma}$ - $\bar{X}$ . The (111) 3DBZ has a bulk pocket (black) oriented along the [111] direction and this results in a surface Dirac cone (blue) at the  $\bar{\Gamma}$ -point. The other three bulk pockets (red) of the (111) 3DBZ are similarly oriented from the [111] direction and they lead to three surface Dirac cones (green) at the  $\bar{M}$ -point.

## 2.4. Electronic band structure of $\text{Pb}_{1-x}\text{Sn}_x\text{Se}$ and $\text{Pb}_{1-x}\text{Sn}_x\text{Te}$

Various bulk Brillouin zone configurations and corresponding topological surface Dirac cones have been previously described. In this part, the electronic band structure of  $\text{Pb}_{1-x}\text{Sn}_x\text{Se}$  and  $\text{Pb}_{1-x}\text{Sn}_x\text{Te}$  alloys are presented.

$x\text{Sn}_x\text{Se}$  and  $\text{Pb}_{1-x}\text{Sn}_x\text{Te}$  alloys in each 3DBZ orientation obtained from theoretical calculations, a tight-binding approach, as well as experimental observations will be presented.

### 2.4.1. Electronic band structure of nontrivial $\text{Pb}_{1-x}\text{Sn}_x\text{Te}$ alloy

According to <sup>58</sup>, the electronic band structures of three surface orientations, (001), (110) and (111), were calculated in  $\text{Pb}_{0.4}\text{Sn}_{0.6}\text{Te}$  alloy as shown in Fig. 3.18. This composition was chosen to assure the band inversion and the TCI phase.

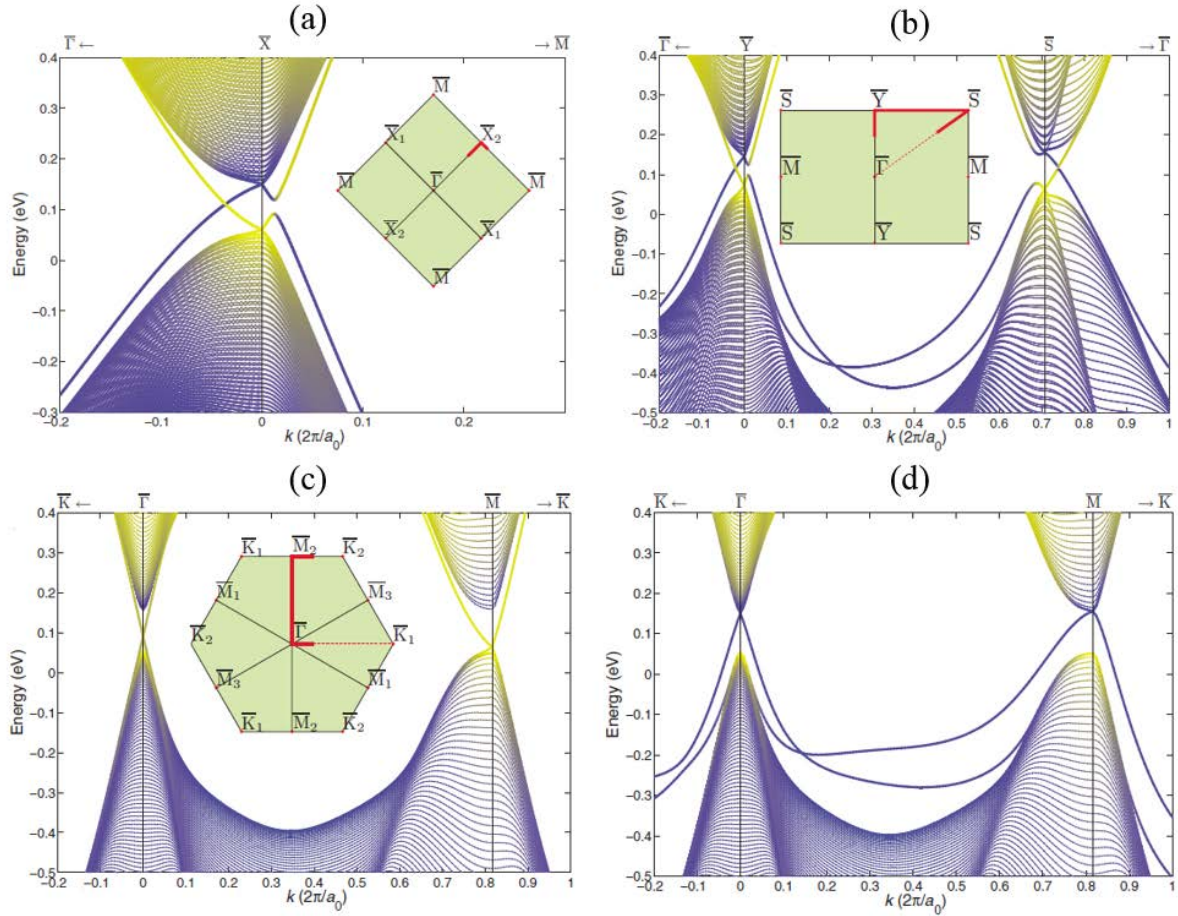


**Figure 3.18. Theoretical calculations of the electronic band structure of  $\text{Pb}_{0.4}\text{Sn}_{0.6}\text{Te}$ .** (a) The calculated band structure of the (001)-oriented surface along the  $\bar{\Gamma}-\bar{X}-\bar{M}$  direction. (b) The calculated band structure of the (110)-oriented surface along the  $\bar{\Gamma}-\bar{Y}-\bar{S}-\bar{\Gamma}$  direction. (c) The calculated band structure of the (111)-oriented surface for the  $\vec{k}$  wave vectors of the 2DBZ along the  $\bar{K}-\bar{\Gamma}-\bar{M}-\bar{K}$  direction with cations at the surfaces and (d) with anions at the surfaces. The yellow to blue color change depends on the cation (yellow) and anion (blue) p-type orbitals which dominantly contribute to the state's wave function. The  $k$  values are in the unity of  $2\pi/a_0$ , where  $a_0$  is the lattice parameter. Adapted from <sup>58</sup>.

The calculated band structure of the (001)-oriented surface is represented in Fig. 3.18(a) for the  $\vec{k}$  wave vectors of the 2DBZ along the  $\bar{\Gamma}-\bar{X}-\bar{M}$  direction (shown by the red line in the inset). The  $k = 0$  value corresponds to the  $\bar{X}_1$ -points where the  $L_1$  and  $L_2$  points are projected and the  $\bar{X}_2$ -points for the  $L_3$  and  $L_4$  points (Fig. 3.16(a)). A band crossing around

## CHAPTER 3

### A brief overview of topological matter

the  $\bar{X}$ -point is observed, evidencing the topological surface states. This is similar for all  $\bar{X}$ -points. Thus, four gapless Dirac cones occur in the inverted bulk band gap along the  $\bar{\Gamma}$ - $\bar{X}$  linecuts and inside the 2DBZ. We notice that these four Dirac cones are not located at time-reversal-invariant momenta and this can be explained by the interaction between the  $L$  valleys which are projected onto the same point of the 2DBZ. These theoretical calculations are in agreement with those in (001) SnTe<sup>37,59</sup> and (001) Pb<sub>0.6</sub>Sn<sub>0.4</sub>Te<sup>40</sup>. Furthermore, ARPES measurements in (001) SnTe crystal<sup>38</sup> and (001) Pb<sub>0.6</sub>Sn<sub>0.4</sub>Te crystal<sup>40</sup> (Fig. 3.19) reveal the observation of double Dirac cones around the  $\bar{X}$ -point<sup>37</sup>.

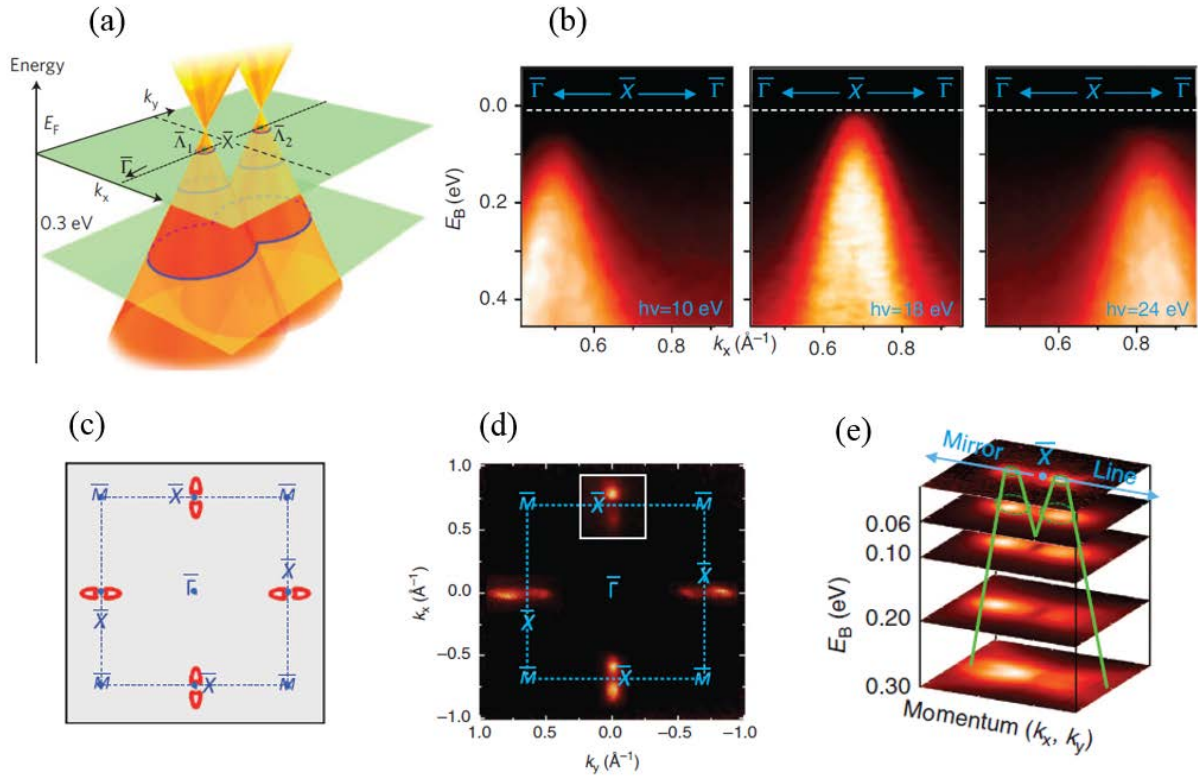


**Figure 3.19. Topological Dirac surface states in (001) Pb<sub>0.6</sub>Sn<sub>0.4</sub>Te crystal.** (a) Schematic surface band dispersion illustrating the evolution of double surface Dirac cones located at the  $\bar{L}_1$  and  $\bar{L}_2$  points lying along the  $\bar{\Gamma}$ - $\bar{X}$  linecuts. Blue circles depict energy contours of Fermi surface for a chosen binding energy. (a) is adapted from<sup>38</sup>. (b) ARPES low-energy electronic structure measurements on Pb<sub>0.6</sub>Sn<sub>0.4</sub>Te (for 10 eV, 18 eV and 24 eV of incident photon energy) showing the signature of double surface Dirac cones. (c) First-principles calculated surface states of SnTe at a given energy below the Dirac point are shown in red along the  $\bar{\Gamma}$ - $\bar{X}$  direction. (d) ARPES iso-energetic contour mapping of Pb<sub>0.6</sub>Sn<sub>0.4</sub>Te at the same energy in (c) (for an incident photon energy of 24 eV). (e) Energy contour mapping (green circles) of ARPES data at different binding energies. Green straight lines represent the guide to the eyes of the linear dispersion of the surface Dirac cones. (b-e) are adapted from<sup>40</sup>.

For the (110)-oriented surface, the calculated band structure along the  $\bar{\Gamma}$ - $\bar{Y}$ - $\bar{S}$ - $\bar{\Gamma}$  direction is shown in Fig. 3.18(b). The band inversion at the  $L_1$  and  $L_2$  points leads to the bulk and surface band structures around the  $\bar{Y}$ -points that are similar to those around the  $\bar{X}$ -points of the (001) surface. The surface states cannot exist around the  $\bar{S}$ -points where the  $L_3$  and  $L_4$  points are projected because these two  $L$ -points are not situated on the  $\{110\}$  mirror planes



(Fig. 3.16(b)). These theoretical calculations are in agreement with *ab initio* calculations demonstrated in (110) SnTe<sup>59</sup>.

The electronic band structure calculations of the (111)-oriented surface along the  $\bar{K}$ - $\bar{\Gamma}$ - $\bar{M}$ - $\bar{K}$  direction is displayed in Fig. 3.18(c) with cation-terminated (Pb or Sn) and in Fig. 3.18(d) with anion-terminated (Te) at the surfaces. For both situations, topologically protected Dirac cones (one isotropic at the  $\bar{\Gamma}$ -point and three anisotropic at the  $\bar{M}$ -points) are observed. The Dirac points of the cation surface states are located close to the top of the valence band, while they appear at the bottom of the conduction band for the anion surface states. In contrast to the (001) and (110) surfaces, we notice that all Dirac cones are situated exactly at the points of the 2DBZ where the projection of all single  $L$ -points takes place (Fig. 3.16(c)). These theoretical results agree with the  $\mathbf{k} \cdot \mathbf{p}$  theory combined with the band calculation on (111) SnTe<sup>59</sup>. The resolved spectra obtained from ARPES measurements on (111) SnTe crystal<sup>60</sup> and on high-quality epitaxial (111)  $\text{Pb}_{1-x}\text{Sn}_x\text{Te}$  films<sup>52</sup> exhibit the topological surface states satisfying the Dirac-like dispersion at the  $\bar{\Gamma}$ -point and the  $\bar{M}$ -points.

### 2.4.2. Electronic band structure of nontrivial $\text{Pb}_{1-x}\text{Sn}_x\text{Se}$ alloy

As shown in Fig. 3.20, the electronic band structures of nontrivial  $\text{Pb}_{1-x}\text{Sn}_x\text{Se}$  in (001) and (111) surface orientations were theoretically studied.

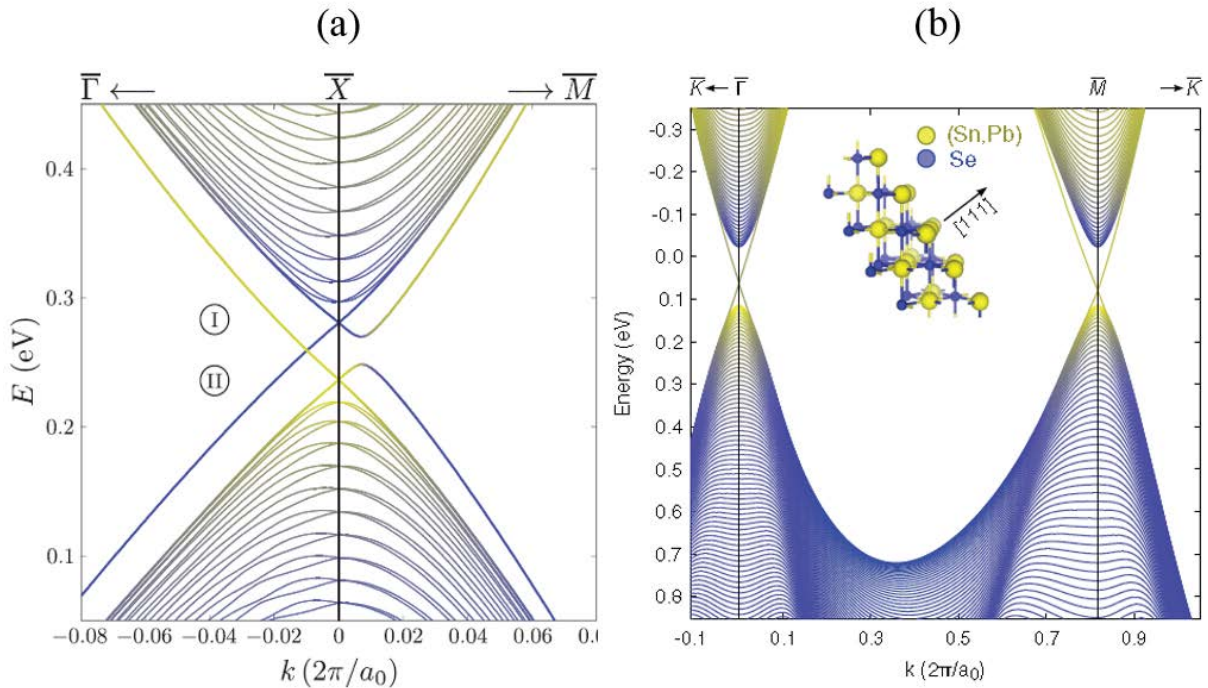


**Figure 3.20. Theoretical calculations of the electronic band structure of nontrivial  $\text{Pb}_{1-x}\text{Sn}_x\text{Se}$ .** (a) The calculated band structure of the (001)-oriented surface of  $\text{Pb}_{0.73}\text{Sn}_{0.27}\text{Se}$  along the  $\bar{\Gamma}$ - $\bar{X}$ - $\bar{M}$  direction at temperature  $T = 80$  K. (b) The calculated band structure of the (111)-oriented surface of cation terminated  $\text{Pb}_{0.64}\text{Sn}_{0.36}\text{Se}$  along the  $\bar{K}$ - $\bar{\Gamma}$ - $\bar{M}$ - $\bar{K}$  direction at temperature  $T = 100$  K. The inset shows the lattice model of a (111) crystal terminated with cations (Pb,Sn), not with anions (Se). Yellow and blue colors denote the relative

## CHAPTER 3

### A brief overview of topological matter

contribution of cation and anion p-type orbitals to the wave function, respectively. The  $k$  values are in the unity of  $2\pi/a_0$ , where  $a_0$  is the lattice parameter. (a) is adapted from <sup>61</sup>. (b) is adapted from <sup>62</sup>.

The (001)-oriented surface band structure was calculated in  $\text{Pb}_{0.73}\text{Sn}_{0.27}\text{Se}$  along the  $\bar{\Gamma}$ - $\bar{X}$ - $\bar{M}$  high-symmetry line for parameters corresponding to a temperature  $T = 80$  K <sup>61</sup>. The obtained results shown in Fig. 3.20(a) are similar to those obtained in (001)  $\text{Pb}_{0.4}\text{Sn}_{0.6}\text{Te}$  in Fig. 3.18(a). Four Dirac cones are situated around the  $\bar{X}$ -points, along the  $\bar{\Gamma}$ - $\bar{X}$  linecuts, and in the 2DBZ. However, we notice that the band structure of (001)  $\text{Pb}_{1-x}\text{Sn}_x\text{Se}$  is nearly isotropic, in contrast to that of (001)  $\text{Pb}_{1-x}\text{Sn}_x\text{Te}$  which is anisotropic <sup>63,64</sup>. ARPES experiments evidencing the double Dirac cones along the high-symmetry lines through the  $\bar{X}$ -points were also carried out in (001)  $\text{Pb}_{0.73}\text{Sn}_{0.27}\text{Se}$  <sup>61</sup>. Moreover, a systematic study of the temperature dependence of the TCI phase was done in (001)  $\text{Pb}_{0.77}\text{Sn}_{0.23}\text{Se}$  monocrystals <sup>39</sup>. Fig. 3.21(a) shows the ARPES spectra of (001)  $\text{Pb}_{0.77}\text{Sn}_{0.23}\text{Se}$  monocrystals measured at different temperatures for a direction perpendicular to the linecut  $\bar{\Gamma}$ - $\bar{X}$  (Fig. 3.21(b)) of the momentum space in the 2DBZ. Experimental results confirm the existence of four surface Dirac cones inside the 2DBZ and along the high-symmetry lines  $\bar{\Gamma}$ - $\bar{X}$ .

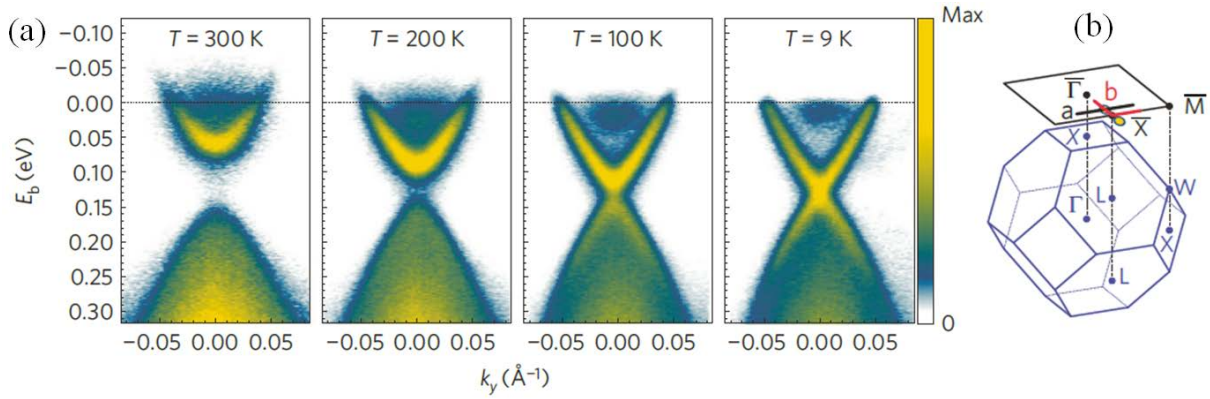


**Figure 3.21. Temperature dependence of the ARPES spectra measured in (001)  $\text{Pb}_{0.77}\text{Sn}_{0.23}\text{Se}$  monocrystals.** (a) ARPES studies along the line “a” depicted in (b). They clearly show the topological surface states for  $T \leq 100$  K. (b) A sketch of the rocksalt 3DBZ showing the selected study lines “a” and “b” for ARPES measurements. Adapted from <sup>39</sup>.

The calculated band structure of the (111)-oriented surface was done in cation terminated  $\text{Pb}_{0.64}\text{Sn}_{0.36}\text{Se}$  along the  $\bar{K}$ - $\bar{\Gamma}$ - $\bar{M}$ - $\bar{K}$  high-symmetry line for parameters corresponding to a temperature  $T = 100$  K <sup>62</sup> (Fig. 3.20(b)). The lattice model with cation termination (Pb,Sn) is shown in the inset. The obtained findings of (111)  $\text{Pb}_{1-x}\text{Sn}_x\text{Se}$  are comparable to those of (111)  $\text{Pb}_{1-x}\text{Sn}_x\text{Te}$  (Fig. 3.18(c)) with an isotropic surface Dirac cone at the  $\bar{\Gamma}$ -point. However, the other three Dirac cones at the  $\bar{M}$ -points are found to be slightly anisotropic in the case of (111)  $\text{Pb}_{1-x}\text{Sn}_x\text{Se}$ , while they are highly anisotropic in (111)  $\text{Pb}_{1-x}\text{Sn}_x\text{Te}$ . ARPES studies of (111)  $\text{Pb}_{0.64}\text{Sn}_{0.36}\text{Se}$  epitaxial films were also done and they show the existence of a surface Dirac cone at the  $\bar{\Gamma}$ -point and three surface Dirac cones at the  $\bar{M}$ -points <sup>62</sup> (Fig. 3.22).

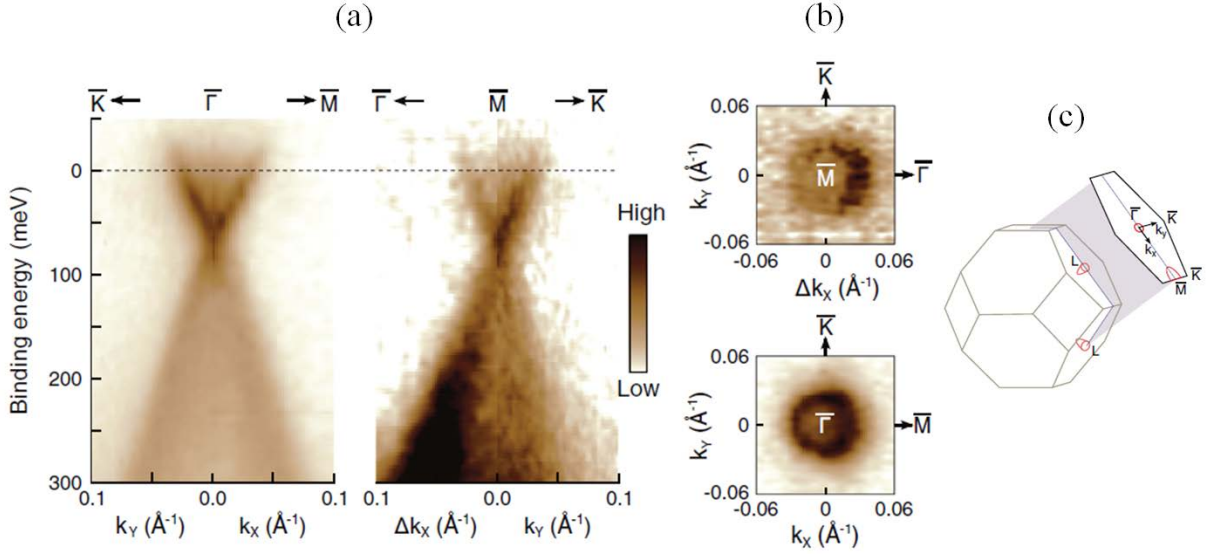


**Figure 3.22. ARPES spectra of the surface states of (111)  $\text{Pb}_{0.64}\text{Sn}_{0.36}\text{Se}$  epitaxial films.** (a) Band structures measured at two locations ( $\bar{\Gamma}$ - and  $\bar{M}$ -points) of the 2DBZ and along the high-symmetry lines indicated in (c). (b) Fermi surface maps at both locations at the Fermi level, showing circularly symmetrical surface states at the  $\bar{\Gamma}$ -point and slightly anisotropic surface states at the  $\bar{M}$ -points. (c) A rocksalt 3DBZ with bulk Fermi ellipsoids at the  $L$ -points. Their projection onto the corresponding 2DBZ is shown on top with Fermi surfaces at the  $\bar{\Gamma}$ - and  $\bar{M}$ -points. Adapted from <sup>62</sup>.

Fig. 3.23 shows the temperature dependence of ARPES intensity map measured in the vicinity of the  $\bar{\Gamma}$ -point of high-quality epitaxial (111)  $\text{Pb}_{1-x}\text{Sn}_x\text{Se}$  epilayers grown on  $\text{BaF}_2$  substrates by G. Springholz et al.. In  $\text{Pb}_{0.9}\text{Sn}_{0.1}\text{Se}$ , the energy gap increases with increasing temperature (Fig. 3.23(a)). The scenario is different in  $\text{Pb}_{0.8}\text{Sn}_{0.2}\text{Se}$  (Fig. 3.23(b)) and  $\text{Pb}_{0.72}\text{Sn}_{0.28}\text{Se}$  (Fig. 3.23(c)) since the gapless Dirac-like band dispersion was observed in both samples at temperatures  $T \leq 130$  K and the gapped band dispersion appears at higher temperatures  $T \geq 200$  K. This study allows one to determine, for each compound, the critical temperature of the topological phase transition.

## CHAPTER 3

### A brief overview of topological matter

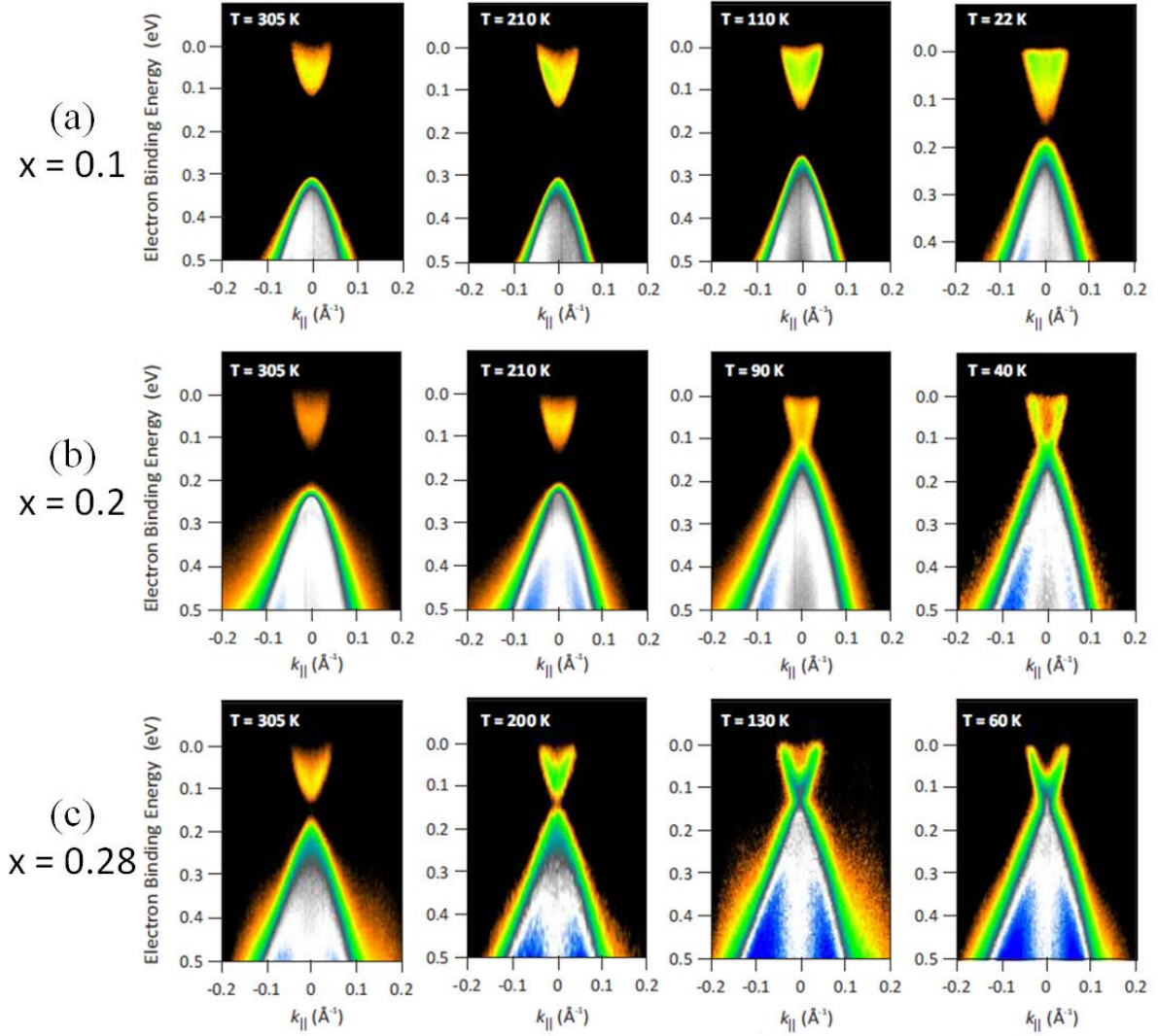


**Figure 3.23. Temperature dependence of ARPES spectra measured in high-quality epitaxial (111)  $\text{Pb}_{1-x}\text{Sn}_x\text{Se}$  films in the vicinity of the  $\bar{\Gamma}$ -point.** (111)-oriented  $\text{Pb}_{1-x}\text{Sn}_x\text{Se}$  films for (a)  $x = 0.1$ , (b)  $x = 0.2$  and (c)  $x = 0.28$  grown on  $\text{BaF}_2$  substrates were measured as a function of temperature. This experiment provides the study of the evolution of the band gap in each sample. Private communication of G. Springholz et al.

## 2.5. Valley anisotropy

IV-VI semiconductors possess four bulk ellipsoids<sup>54,63</sup> located at the  $L$ -points of the bulk Brillouin zone. Different configurations of the 3DBZ result in different orientations of the ellipsoidal bulk carrier pockets (Fig. 3.24). When a magnetic field is applied perpendicular to the sample surface, Landau quantization of the electron energy will be on planes parallel to this surface.



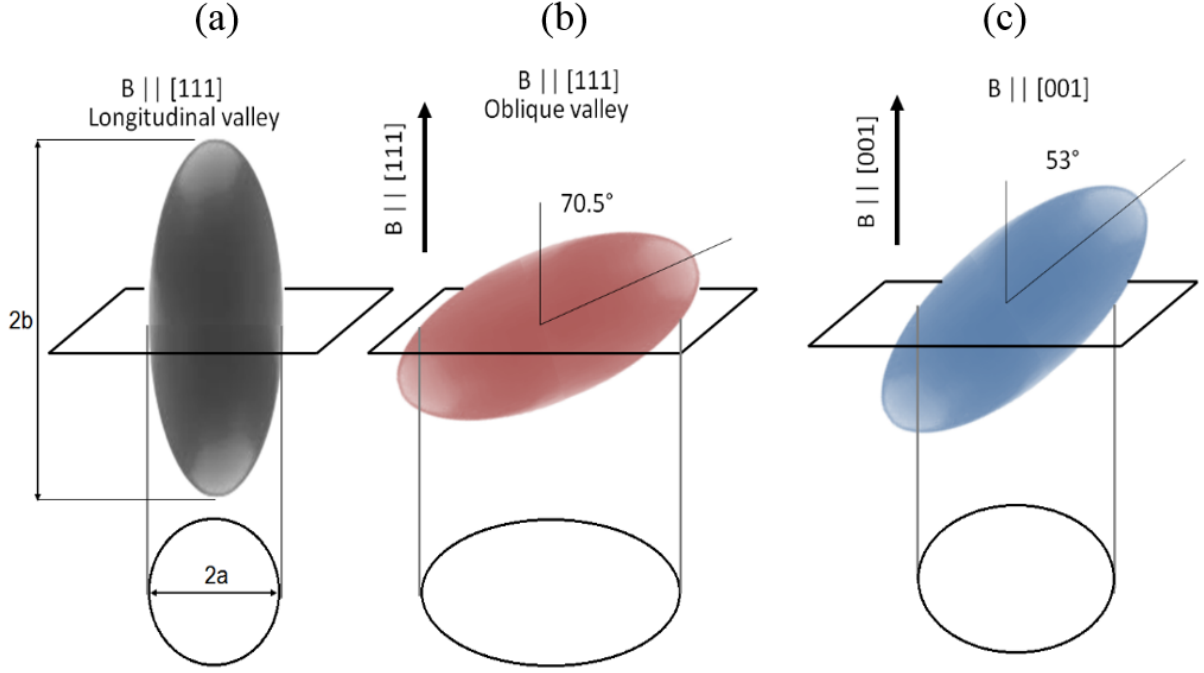


**Figure 3.24. Illustration of bulk carrier ellipsoids in different surface orientations.** (a) Bulk ellipsoid in the (111) longitudinal valley of IV-VI semiconductors with its major axis “2b” oriented parallel to the [111] direction and its minor axis “2a”. An applied magnetic field yields the cyclotron motion of electrons on a plane perpendicular to the field. The cross section of the Fermi ellipsoid by this plane results in a circular 2D Fermi surface shown below the ellipsoid. (b) In the (111) oblique valley, the ellipsoid is tilted by an angle  $70.5^\circ$  with respect to the [111] direction and the direction of the applied field. The 2D cross section is an ellipse. (c) In (001)-oriented crystals, the magnetic field is oriented parallel to the [001] direction. The ellipsoid is tilted by an angle  $53^\circ$  and the cross section also yields an ellipse.

For a (111)-oriented sample (Fig. 3.16(c)), the longitudinal valley is defined from the ellipsoidal bulk carrier pocket that is oriented parallel to the [111] direction. This longitudinal ellipsoid has its major axis “2b” parallel to the [111] direction and its minor axis “2a” (Fig. 3.24(a)). An applied magnetic field in the [111] direction will quantize the cyclotron orbits of electrons on the plane perpendicular to the [111] direction, yielding a 2D circular Fermi surface with a diameter “2a” (Fig. 3.24(a)). The three remaining ellipsoids have their major axes tilted by  $\theta = 70.5^\circ$  with respect to the [111] direction, defining the oblique valleys (Fig. 3.24(b)). The cross sections of the oblique ellipsoids are ellipses (Fig. 3.24(b)). For a (001)-oriented sample (Fig. 3.16(a)), the ellipsoids situated at the *L*-points are equivalent with their great axes tilted by  $\theta = 53^\circ$  with respect to the [001] direction (Fig. 3.24(c)), leading to 2D elliptic Fermi surfaces (Fig. 3.24(c)).

We can define the valley anisotropy factor  $K$  as the area anisotropy factor  $K = (b/a)^2$ . This is equivalent to the  $\mathbf{k} \cdot \mathbf{p}$  matrix element anisotropy factor  $K = (P_\perp/P_\parallel)^2$ <sup>54</sup>, where  $P_\perp$  and  $P_\parallel$  are respectively transverse and longitudinal momentum matrix elements. Note that  $K$  is found to depend on the Sn content of the  $\text{Pb}_{1-x}\text{Sn}_x\text{Se}$  or  $\text{Pb}_{1-x}\text{Sn}_x\text{Te}$  alloys.



### 3. Bernevig-Hughes-Zhang Hamiltonian for topological matter

The notions of TIs and TCIs have been previously presented. In this section, the models in physics allowing us to understand the topological character of a material will be introduced. B. A. Bernevig, T. L. Hughes and S. C. Zhang (BHZ) proposed for the first time in 2006 an explicit model Hamiltonian to describe the QSHE that was theoretically predicted to be realized in HgTe/CdTe quantum wells, known as the first 2D TI<sup>19</sup>. For 3D TIs with a single Dirac cone on the surface, in the Bi<sub>2</sub>Se<sub>3</sub> family, their topological nature can be similarly described by the model Hamiltonian developed by H. Zhang et al. in 2009<sup>27,65</sup>. Here, the multiband  $\mathbf{k} \cdot \mathbf{p}$  perturbation theory used to study TCI materials<sup>54,66–68</sup> will be demonstrated to be equivalent to the BHZ Hamiltonian for TIs. This model is equivalent to a 3D Dirac Hamiltonian that reliably describes relativistic-like Dirac fermions in topological matter.

For the sake of simplicity, the longitudinal valley ( $\theta = 0$ ) of (111)-oriented surface TCI material will be considered. Following<sup>54</sup>, the Hamiltonian of a 2-band  $\mathbf{k} \cdot \mathbf{p}$  model including the lowest conduction and the highest valence levels ( $L_6^\pm$ ), for  $\vec{z} // [111]$ , reads:

$$H(\vec{k}) = \begin{pmatrix} \frac{E_g}{2} & 0 & \frac{\hbar}{m_0} P_{\parallel} k_z & \frac{\hbar}{m_0} P_{\perp} k_{-} \\ 0 & \frac{E_g}{2} & \frac{\hbar}{m_0} P_{\perp} k_{+} & -\frac{\hbar}{m_0} P_{\parallel} k_z \\ \frac{\hbar}{m_0} P_{\parallel} k_z & \frac{\hbar}{m_0} P_{\perp} k_{-} & -\frac{E_g}{2} & 0 \\ \frac{\hbar}{m_0} P_{\perp} k_{+} & -\frac{\hbar}{m_0} P_{\parallel} k_z & 0 & -\frac{E_g}{2} \end{pmatrix} \quad (3.6)$$

where  $E_g$  is the band gap,  $P_{\perp}$  and  $P_{\parallel}$  are respectively transverse and longitudinal momentum matrix elements,  $k_{\pm} = k_x \pm ik_y$ , and  $m_0$  is the electron rest mass.

In the Dirac formalism, three new parameters are defined as follows:  $\Delta = E_g/2$ ,  $v_c = P_{\perp}/m_0$  and  $v'_c = P_{\parallel}/m_0$ . Here,  $v_c$  is the velocity perpendicular to the  $z$ -axis and  $v'_c$  is the velocity parallel to the  $z$ -axis. Thus, a massive Dirac Hamiltonian with uniaxial anisotropy along the  $z$ -direction can be written as:

$$H(\vec{k}) = \begin{pmatrix} \Delta & 0 & \hbar v'_c k_z & \hbar v_c k_{-} \\ 0 & \Delta & \hbar v_c k_{+} & -\hbar v'_c k_z \\ \hbar v'_c k_z & \hbar v_c k_{-} & -\Delta & 0 \\ \hbar v_c k_{+} & -\hbar v'_c k_z & 0 & -\Delta \end{pmatrix} \quad (3.7)$$

The eigenvalues of the above Hamiltonian yield the following Dirac dispersion:

$$E^{c,v}(\vec{k}) = \pm \sqrt{\Delta^2 + \hbar^2 v_c^2 k_{\perp}^2 + \hbar^2 v_c'^2 k_z^2} \quad (3.8)$$

where  $k_{\perp}^2 = k_x^2 + k_y^2$  and the  $\pm$  signs refer respectively to the energy of the conduction  $E^c(\vec{k})$  and valence  $E^v(\vec{k})$  bands. In this 2-band model, the Dirac transverse mass is given by  $m = \Delta/v_c^2$ .

If the effect of the four far-bands (two conduction ( $L_{4,5}^-$  and  $L_6^-$ ) and two valence ( $L_{4,5}^+$  and  $L_6^+$ ) bands) are treated in  $k^2$ -approximation<sup>54,66–68</sup>, the diagonal terms of the Hamiltonian in Eq. 3.7 will be changed. Here,  $\tilde{m}_c^t$  and  $\tilde{m}_v^t$  represent the far-band contributions to the transverse ( $t$ ) Dirac masses of the conduction ( $c$ ) and valence ( $v$ ) bands. Similarly,  $\tilde{m}_c^l$  and  $\tilde{m}_v^l$  denote the contributions to the longitudinal ( $l$ ) Dirac masses. Note that since the four far-bands are nearly equally distant from the main conduction and valence bands ( $L_6^{\pm}$ ), thereby these two bands are supposed to remain symmetric. We thus get:

$$\tilde{m}_c^t = -\tilde{m}_v^t = \tilde{m} > 0 \quad (3.9a)$$

$$\tilde{m}_c^l = -\tilde{m}_v^l = \tilde{\mu} > 0 \quad (3.9b)$$

For the following calculations in this thesis, we use  $\tilde{m}$  and  $\tilde{\mu}$  as the far-band contributions to the transverse and longitudinal Dirac masses in the conduction and valence bands, respectively.

The diagonal terms of Eq. 3.7 are thus replaced by:

$$H_{11} = H_{22} = \Delta + \frac{\hbar^2}{2\tilde{m}} k_{\perp}^2 + \frac{\hbar^2}{2\tilde{\mu}} k_z^2 \quad (3.10a)$$

$$H_{33} = H_{44} = -\Delta - \frac{\hbar^2}{2\tilde{m}} k_{\perp}^2 - \frac{\hbar^2}{2\tilde{\mu}} k_z^2 \quad (3.10b)$$

Therefore, the diagonal terms can be written as the  $\vec{k}$ -dependent mass term  $M(\vec{k}) = \Delta + \frac{\hbar^2}{2\tilde{m}} k_{\perp}^2 + \frac{\hbar^2}{2\tilde{\mu}} k_z^2$  and the Hamiltonian reads:

$$H(\vec{k}) = \begin{pmatrix} M(\vec{k}) & 0 & \hbar v_c' k_z & \hbar v_c k_- \\ 0 & M(\vec{k}) & \hbar v_c k_+ & -\hbar v_c' k_z \\ \hbar v_c' k_z & \hbar v_c k_- & -M(\vec{k}) & 0 \\ \hbar v_c k_+ & -\hbar v_c' k_z & 0 & -M(\vec{k}) \end{pmatrix} \quad (3.11)$$

## CHAPTER 3

### *A brief overview of topological matter*

If we swap the lines 2 and 3, then the columns 2 and 3 of the above Hamiltonian, we will exactly obtain the BHZ Hamiltonian for 3D TIs as expressed in <sup>27,65</sup>:

$$H(\vec{k}) = \begin{pmatrix} M(\vec{k}) & A_1 k_z & 0 & A_2 k_- \\ A_1 k_z & -M(\vec{k}) & A_2 k_- & 0 \\ 0 & A_2 k_+ & M(\vec{k}) & -A_1 k_z \\ A_2 k_+ & 0 & -A_1 k_z & -M(\vec{k}) \end{pmatrix} \quad (3.12)$$

where  $M(\vec{k}) = \Delta - B_1 k_\perp^2 - B_2 k_z^2$ . We can thus identify that  $A_1 = \hbar v'_c$ ,  $A_2 = \hbar v_c$ ,  $B_1 = -\frac{\hbar^2}{2\tilde{m}}$  and  $B_2 = -\frac{\hbar^2}{2\tilde{\mu}}$ . This Hamiltonian is nothing but the 3D Dirac Hamiltonian with uniaxial anisotropy along the  $z$ -direction and  $\vec{k}$ -dependent mass terms.

Neglecting the  $k^4$  terms, the dispersion relation of the conduction and valence bands is given by:

$$E^{c,v}(\vec{k}) = \pm \sqrt{\Delta^2 + \hbar^2(v_c^2 + \frac{\Delta}{\tilde{m}})k_\perp^2 + \hbar^2(v_c'^2 + \frac{\Delta}{\tilde{\mu}})k_z^2} \quad (3.13)$$

The topological nature of massive bulk Dirac fermions can be identified by the sign of  $\Delta/\tilde{m}$ :

If  $\Delta/\tilde{m} > 0$ , the material is trivial and its band structure is in the normal regime.

If  $\Delta/\tilde{m} < 0$ , the material is topological and its band structure is in the inverted regime.

The dispersion relation of massless surface Dirac fermions can be obtained by setting  $\Delta = 0$ .

## References

1. Moore, J. E. The birth of topological insulators. *Nature* **464**, 194–198 (2010).
2. Qi, X. L. & Zhang, S. C. The quantum spin Hall effect and topological insulators. *Phys. Today* **63**, 33–38 (2010).
3. Hasan, M. Z. & Kane, C. L. Colloquium: Topological insulators. *Rev. Mod. Phys.* **82**, 3045–3067 (2010).
4. Qi, X.-L. & Zhang, S.-C. Topological insulators and superconductors. *Rev. Mod. Phys.* **83**, 1057–1110 (2011).
5. Hall, E. H. On a New Action of the Magnet on Electric Currents. *Am. J. Math.* **2**, 287–292 (1879).
6. Klitzing, K. V., Dorda, G. & Pepper, M. New method for high-accuracy determination of the fine-structure constant based on quantized hall resistance. *Phys. Rev. Lett.* **45**, 494–497 (1980).
7. Laughlin, R. B. Quantized Hall conductivity in two dimensions. *Phys. Rev. B* **23**, 5632–5633 (1981).
8. Haldane, F. D. M. Model for a Quantum Hall Effect without Landau Levels: Condensed-Matter Realization of the ‘Parity Anomaly’. *Phys. Rev. Lett.* **61**, 2015–2018 (1988).
9. Onoda, M. & Nagaosa, N. Quantized anomalous Hall effect in two-dimensional ferromagnets: quantum Hall effect in metals. *Phys. Rev. Lett.* **90**, 206601 (2003).
10. Liu, C. X., Qi, X. L., Dai, X., Fang, Z. & Zhang, S. C. Quantum anomalous Hall effect in Hg<sub>1-y</sub>Mn<sub>y</sub>Te quantum wells. *Phys. Rev. Lett.* **101**, 146802 (2008).
11. Chang, C.-Z. *et al.* Experimental Observation of the Quantum Anomalous Hall Effect in a Magnetic Topological Insulator. *Science* **340**, 167–170 (2013).
12. Chang, C.-Z. *et al.* High-precision realization of robust quantum anomalous Hall state in a hard ferromagnetic topological insulator. *Nat Mater* **14**, 473–477 (2015).
13. Kane, C. L. & Mele, E. J. Quantum Spin Hall effect in graphene. *Phys. Rev. Lett.* **95**, 226801 (2005).
14. Bernevig, B. A. & Zhang, S. C. Quantum spin Hall effect. *Phys. Rev. Lett.* **96**, 106802 (2006).
15. Berry, M. V. Quantal Phase Factors Accompanying Adiabatic Changes. *Proc. R. Soc. London A Math. Phys. Eng. Sci.* **392**, 45–57 (1984).
16. Thouless, D. J., Kohmoto, M., Nightingale, M. & den Nijs, M. Quantized Hall Conductance in a Two-Dimensional Periodic Potential. *Phys. Rev. Lett.* **49**, 405–408 (1982).
17. Kane, C. L. & Mele, E. J. Z<sub>2</sub> topological order and the quantum spin Hall effect. *Phys. Rev. Lett.* **95**, 146802 (2005).
18. Altland, A. & Zirnbauer, M. R. Nonstandard symmetry classes in mesoscopic normal-superconducting hybrid structures. *Phys. Rev. B* **55**, 1142–1161 (1997).
19. Bernevig, B. A., Hughes, T. L. & Zhang, S.-C. Quantum spin Hall effect and topological phase transition in HgTe quantum wells. *Science* **314**, 1757–1762 (2006).

## CHAPTER 3

### A brief overview of topological matter

---

20. König, M. *et al.* Quantum Spin Hall Insulator State in HgTe Quantum Wells. *Science* **318**, 766–771 (2007).
21. Fu, L., Kane, C. L. & Mele, E. J. Topological insulators in three dimensions. *Phys. Rev. Lett.* **98**, 106803 (2007).
22. Moore, J. E. & Balents, L. Topological invariants of time-reversal-invariant band structures. *Phys. Rev. B* **75**, 121306(R) (2007).
23. Roy, R. Topological phases and the quantum spin Hall effect in three dimensions. *Phys. Rev. B* **79**, 195322 (2009).
24. Fu, L. & Kane, C. L. Topological insulators with inversion symmetry. *Phys. Rev. B* **76**, 045302 (2007).
25. Hsieh, D. *et al.* A topological Dirac insulator in a quantum spin Hall phase. *Nature* **452**, 970–974 (2008).
26. Schafgans, A. A. *et al.* Landau level spectroscopy of surface states in the topological insulator Bi<sub>0.91</sub>Sb<sub>0.09</sub> via magneto-optics. *Phys. Rev. B* **85**, 195440 (2012).
27. Zhang, H. *et al.* Topological insulators in Bi<sub>2</sub>Se<sub>3</sub>, Bi<sub>2</sub>Te<sub>3</sub> and Sb<sub>2</sub>Te<sub>3</sub> with a single Dirac cone on the surface. *Nat. Phys.* **5**, 438–442 (2009).
28. Xia, Y. *et al.* Observation of a large-gap topological-insulator class with a single Dirac cone on the surface. *Nat. Phys.* **5**, 398–402 (2009).
29. Chen, Y. L. *et al.* Experimental Realization of a Three-Dimensional Topological Insulator, Bi<sub>2</sub>Te<sub>3</sub>. *Science* **325**, 178–181 (2009).
30. Hsieh, D. *et al.* A tunable topological insulator in the spin helical Dirac transport regime. *Nature* **460**, 1101–1105 (2009).
31. Hsieh, D. *et al.* Observation of time-reversal-protected single-Dirac-cone topological-insulator states in Bi<sub>2</sub>Te<sub>3</sub> and Sb<sub>2</sub>Te<sub>3</sub>. *Phys. Rev. Lett.* **103**, 146401 (2009).
32. Orlita, M. *et al.* Magneto-Optics of Massive Dirac Fermions in Bulk Bi<sub>2</sub>Se<sub>3</sub>. *Phys. Rev. Lett.* **114**, 186401 (2015).
33. Fu, L. Topological crystalline insulators. *Phys. Rev. Lett.* **106**, 106802 (2011).
34. Ando, Y. Topological Insulator Materials. *J. Phys. Soc. Japan* **82**, 102001 (2013).
35. Ando, Y. & Fu, L. Topological Crystalline Insulators and Topological Superconductors: From Concepts to Materials. *Annu. Rev. Condens. Matter Phys.* **6**, 361–381 (2015).
36. Teo, J. C. Y., Fu, L. & Kane, C. L. Surface states and topological invariants in three-dimensional topological insulators: Application to Bi<sub>1-x</sub>Sb<sub>x</sub>. *Phys. Rev. B* **78**, 045426 (2008).
37. Hsieh, T. H. *et al.* Topological crystalline insulators in the SnTe material class. *Nat. Commun.* **3**, 982 (2012).
38. Tanaka, Y. *et al.* Experimental realization of a topological crystalline insulator in SnTe. *Nat. Phys.* **8**, 800–803 (2012).
39. Dziawa, P. *et al.* Topological crystalline insulator states in Pb(1-x)Sn(x)Se. *Nat. Mater.* **11**, 1023–1027 (2012).
40. Xu, S.-Y. *et al.* Observation of a topological crystalline insulator phase and topological phase transition in Pb<sub>1-x</sub>Sn<sub>x</sub>Te. *Nat. Commun.* **3**, 1192 (2012).
41. Taskin, A. A., Yang, F., Sasaki, S., Segawa, K. & Ando, Y. Topological surface

- transport in epitaxial SnTe thin films grown on Bi<sub>2</sub>Te<sub>3</sub>. *Phys. Rev. B* **89**, 121302(R) (2014).
42. Gyeen, A. *et al.* Quasiparticle interference on the surface of the topological crystalline insulator Pb<sub>1-x</sub>Sn<sub>x</sub>Se. *Phys. Rev. B* **88**, 125414 (2013).
  43. Okada, Y. *et al.* Observation of Dirac node formation and mass acquisition in a topological crystalline insulator. *Science* **341**, 1496–1499 (2013).
  44. Fang, C., Gilbert, M. J. & Bernevig, B. A. Large- Chern-number quantum anomalous Hall effect in thin-film topological crystalline insulators. *Phys. Rev. Lett.* **112**, 046801 (2014).
  45. Zeljkovic, I. *et al.* Strain engineering Dirac surface states in heteroepitaxial topological crystalline insulator thin films. *Nat. Nanotechnol.* **10**, 849–853 (2015).
  46. Li, C. H., Robinson, J. T., Liu, Y., Li, L. & Jonker, B. T. Electrical detection of charge-current-induced spin polarization due to spin-momentum locking in Bi<sub>2</sub>Se<sub>3</sub>. *Nat. Nanotechnol.* **9**, 218–224 (2014).
  47. Assaf, B. A. *et al.* Inducing magnetism onto the surface of a topological crystalline insulator. *Phys. Rev. B* **91**, 195310 (2015).
  48. Dimmock, J. O., Melngailis, I. & Strauss, A. J. Band Structure and Laser Action in Pb<sub>x</sub>Sn<sub>1-x</sub>Te. *Phys. Rev. Lett.* **16**, 1193–1196 (1966).
  49. Strauss, A. J. Inversion of Conduction and Valence Bands in Pb<sub>1-x</sub>Sn<sub>x</sub>Se Alloys. *Phys. Rev.* **157**, 608–611 (1967).
  50. Martinez, G. Band Inversion of Pb<sub>1-x</sub>Sn<sub>x</sub>Se Alloys under Hydrostatic Pressure. I. Theoretical Band Structure Analysis. *Phys. Rev. B* **8**, 4678–4685 (1973).
  51. Springholz, G. in *Molecular Beam Epitaxy* (ed. Henini, M.) 263–310 (Elsevier, 2013). doi:10.1016/B978-0-12-387839-7.00013-0
  52. Yan, C. *et al.* Experimental observation of Dirac-like surface states and topological phase transition in Pb<sub>1-x</sub>Sn<sub>x</sub>Te (111) films. *Phys. Rev. Lett.* **112**, 186801 (2014).
  53. Calawa, A. R., Dimmock, J. O., Harman, T. C. & Melngailis, I. Magnetic Field Dependence of Laser Emission in Pb<sub>1-x</sub>Sn<sub>x</sub>Se Diodes. *Phys. Rev. Lett.* **23**, 7–10 (1969).
  54. Bauer, G. in *Narrow Gap Semiconductors Physics and Applications: Proceeding of the International Summer School* (ed. Zawadzki, W.) **133**, 427–446 (Springer Berlin Heidelberg, 1980).
  55. Assaf, B. A. *et al.* Magneto-optical determination of a topological index. *npj Quantum Mater.* **2**, 26 (2017).
  56. Dimmock, J. O. & Wright, G. B. Band edge structure of PbS, PbSe, and PbTe. *Phys. Rev.* **135**, A821–A830 (1964).
  57. Dimmock, J. O. k.p theory for the conduction and valence bands of Pb<sub>1-x</sub>Sn<sub>x</sub>Te and Pb<sub>1-x</sub>Sn<sub>x</sub>Se alloys. in *Proceedings of the International Conference on the Physics of Semimetals and Narrow Gap Semiconductors 1969* (ed. Carter, D. L. & Bate, R. T.) 319 (Pergamon, 1971).
  58. Safaei, S., Kacman, P. & Buczko, R. Topological crystalline insulator (Pb,Sn)Te: Surface states and their spin polarization. *Phys. Rev. B* **88**, 045305 (2013).
  59. Liu, J., Duan, W. & Fu, L. Two types of surface states in topological crystalline

## CHAPTER 3

### *A brief overview of topological matter*

---

- insulators. *Phys. Rev. B* **88**, 241303(R) (2013).
60. Tanaka, Y. *et al.* Two types of Dirac-cone surface states on the ( 111 ) surface of the topological crystalline insulator SnTe. *Phys. Rev. B* **88**, 235126 (2013).
  61. Wojek, B. M. *et al.* Spin-polarized (001) surface states of the topological crystalline insulator Pb<sub>0.73</sub>Sn<sub>0.27</sub>Se. *Phys. Rev. B* **87**, 115106 (2013).
  62. Polley, C. M. *et al.* Observation of topological crystalline insulator surface states on (111)-oriented Pb<sub>1-x</sub>Sn<sub>x</sub>Se films. *Phys. Rev. B* **89**, 075317 (2014).
  63. Burke, J. R., Houston, B. & Savage, H. T. Anisotropy of the Fermi surface of p-type PbTe. *Phys. Rev. B* **2**, 1977–1988 (1970).
  64. Yusheng, H. & Grassie, A. D. C. The electronic band structure of Pb<sub>1-x</sub>Sn<sub>x</sub>Te alloys. III : Implications for the Fermi surface of SnTe. *J. Phys. F Met. Phys.* **15**, 363–376 (1985).
  65. Liu, C. X. *et al.* Model Hamiltonian for topological insulators. *Phys. Rev. B* **82**, 045122 (2010).
  66. Mitchell, D.L. & Wallis, R. F. Theoretical energy-band parameters for the lead salts. *Phys. Rev.* **151**, 581–595 (1966).
  67. Burkhard, H., Bauer, G. & Zawadzki, W. Band-population effects and intraband magneto-optical properties of a many-valley semiconductor: PbTe. *Phys. Rev. B* **19**, 5149–5159 (1979).
  68. Pascher, H., Bauer, G. & Grisar, R. Magneto-optical investigations and four-wave-mixing spectroscopy of PbSe. *Phys. Rev. B* **38**, 3383–3390 (1988).

# Chapter 4

## Magneto-optical investigation of topological crystalline insulators: IV-VI compounds

The concept of band topology has revolutionized our understanding of quantum phases of condensed matter. Fundamentally, the topological nature of materials is controlled by the orbital and parity ordering of the conduction and valence bands. When the parity of the conduction and valence bands of a material is inverted compared to conventional case with positive band gap in the trivial regime, the material is said to be nontrivial and has negative band gap. It undergoes a topological phase transition between two topologically distinct phases. Several theoretical and experimental works have recently demonstrated that the topological phase transition can be studied via the inversion of the bulk bands of a solid, the basis of a topological insulator (TI). Narrow gap rocksalt IV-VI semiconductors such as  $\text{Pb}_{1-x}\text{Sn}_x\text{Se}$  and  $\text{Pb}_{1-x}\text{Sn}_x\text{Te}$  could be considered as an ideal system to study the bulk band inversion by changing Sn composition, temperature or pressure of the system owing to their mirror-like conduction and valence bands  $L_6^\pm$  which are nearly symmetric. The electronic band structure of IV-VI compounds is therefore relatively simple when compared to II-VI and V-VI materials that possess asymmetric bulk conduction and valence bands.

In this chapter, we present a systematic study of the topological character of (111)  $\text{Pb}_{1-x}\text{Sn}_x\text{Se}$  and  $\text{Pb}_{1-x}\text{Sn}_x\text{Te}$  topological crystalline insulators (TCIs) across the topological phase transition occurring at the critical Sn content  $x_c$  using Dirac Landau level magneto-spectroscopy. With this powerful bulk sensitive probe, we are able to precisely measure the band parameters of our systems in the entire composition range such as the absolute value of the energy gap and the Dirac velocity of the bulk bands using massive Dirac fermion model analysis.



## CHAPTER 4

### *Magneto-optical investigation of TCIs: IV-VI compounds*

---

#### Chapter 4 – Magneto-optical investigation of TCIs: IV-VI compounds

<b>1. Dirac Landau levels of IV-VI semiconductors</b>	<b>111</b>
1.1. Landau levels of the longitudinal valley	111
1.2. Landau levels of the oblique valleys	116
1.3. Landau levels of the topological surface states	116
<b>2. Growth and characterization of (111) <math>\text{Pb}_{1-x}\text{Sn}_x\text{Se}</math> and <math>\text{Pb}_{1-x}\text{Sn}_x\text{Te}</math> epilayers</b>	<b>117</b>
2.1. Molecular beam epitaxy growth	117
2.2. X-ray diffraction	118
2.3. Electrical transport characterization	119
<b>3. Magneto-optical Landau level spectroscopy of Dirac fermions in (111) <math>\text{Pb}_{1-x}\text{Sn}_x\text{Se}</math></b>	<b>121</b>
3.1. Bulk states in (111) $\text{Pb}_{1-x}\text{Sn}_x\text{Se}$	121
3.2. Topological surface states in (111) $\text{Pb}_{1-x}\text{Sn}_x\text{Se}$	131
<b>4. Magneto-optical Landau level spectroscopy of Dirac fermions in (111) <math>\text{Pb}_{1-x}\text{Sn}_x\text{Te}</math></b>	<b>133</b>
4.1. Bulk states in (111) $\text{Pb}_{1-x}\text{Sn}_x\text{Te}$	133
4.2. Topological surface states in (111) $\text{Pb}_{1-x}\text{Sn}_x\text{Te}$	142
<b>5. Magneto-optical determination of a topological index</b>	<b>145</b>
5.1. (111) $\text{Pb}_{1-x}\text{Sn}_x\text{Se}$	146
5.2. (111) $\text{Pb}_{1-x}\text{Sn}_x\text{Te}$	149
<b>6. Validity of the massive Dirac approximation</b>	<b>151</b>
<b>7. Valley anisotropy in IV-VI compounds</b>	<b>153</b>
7.1. $\text{Pb}_{1-x}\text{Sn}_x\text{Se}$	154
7.2. $\text{Pb}_{1-x}\text{Sn}_x\text{Te}$	155
<b>8. Absence of the band gap closure across the topological phase transition in <math>\text{Pb}_{1-x}\text{Sn}_x\text{Te}</math></b>	<b>157</b>
<b>9. Conclusion and perspectives</b>	<b>159</b>
<b>References</b>	<b>162</b>

Our investigation technique does not only give access to the information of the band structure of the bulk states, but also a quantitative assessment of the gapless band structure of the topological surface states in the samples with  $x > x_c$  using the massless Dirac fermion model. Extracting the Dirac velocity of different bulk valleys allows us to study the valley anisotropy in (111)  $\text{Pb}_{1-x}\text{Sn}_x\text{Se}$  and  $\text{Pb}_{1-x}\text{Sn}_x\text{Te}$  as a function of Sn content. The most important aspect of our analysis is the ability to verify whether a material is trivial (with positive gap) or nontrivial (with negative gap) via the measure of its topological index defined by L. Fu. Here, we show that we can experimentally determine the topological index of the material. The results were analyzed using the Bernevig-Hughes-Zhang (BHZ) Hamiltonian. We can measure the sign of the band gap and we can experimentally extract  $x_c$  corresponding to the topological phase transition occurring when the gap changes sign from positive ( $x < x_c$ ) to negative ( $x > x_c$ ). This is the first magneto-optical demonstration that the topological index can be measured and the topological character of the material can be directly determined by the bulk properties, and not just inferred from the observation of the topological surface states. We argue that our approach is more or less general and can be applied to other material families that host a trivial to nontrivial topological phase transition and can be described by a BHZ model Hamiltonian.

## 1. Dirac Landau levels of IV-VI semiconductors

In this section, we will study the behavior of Dirac fermions in IV-VI lead-salt compounds subjected to the magnetic field via the quantization of their energy into discrete Landau levels. We define  $\theta$  as the angle between the direction of the magnetic field and the major axis of the ellipsoids of bulk carriers. The longitudinal valley corresponds to the bulk ellipsoids with a major axis oriented parallel to the magnetic field direction. Other ellipsoidal bulk carrier pockets whose major axes are tilted by an angle  $\theta$  with respect to the direction of the applied magnetic field are defined as oblique valleys.

### 1.1. Landau levels of the longitudinal valley

We will first treat the Landau quantization problem for the longitudinal valley of (111)-oriented narrow gap rocksalt IV-VI semiconductors using the description proposed by D. L. Mitchell and R. F. Wallis<sup>1-5</sup>. Their approach is a 6-band  $\mathbf{k} \cdot \mathbf{p}$  approach where the  $L_6^\pm$  conduction and valence bands are exactly accounted for and the effect of four far-bands (two conduction ( $L_{4,5}^-$  and  $L_6^-$ ) and two valence ( $L_{4,5}^+$  and  $L_6^+$ ) bands) is included perturbatively in  $k^2$ -approximation. Since the far-bands are nearly equally distant from the  $L_6^\pm$  conduction and valence bands (Fig. 3.14(b)), we assume that these two bands are symmetric. In the trivial regime where the  $L_6^-$  band is above the  $L_6^+$  band, the Dirac transverse band edge mass  $m^*$  can be written as:

## CHAPTER 4

### Magneto-optical investigation of TCIs: IV-VI compounds

$$\text{For the conduction band } (L_6^-): \quad \frac{1}{m^*} = \frac{1}{m} + \frac{1}{\tilde{m}} \quad (4.1a)$$

$$\text{For the valence band } (L_6^+): \quad \frac{1}{m^*} = -\frac{1}{m} - \frac{1}{\tilde{m}} \quad (4.1b)$$

Here,  $m$  is due to the interactions between the  $L_6^\pm$  bands in a 2-band  $\mathbf{k.p}$  model where  $\frac{1}{m} = \frac{v_c^2}{\Delta}$ .  $\Delta$  represents the half band gap ( $\Delta = E_g/2$ ) and  $v_c$  is the velocity perpendicular to the  $z$ -direction defined as  $v_c = P_\perp/m_0$ , where  $P_\perp$  is the transverse momentum matrix element.  $\tilde{m}$  is due to the interactions between the main conduction/valence bands ( $L_6^\pm$ ) and the four far-bands (Fig. 3.14(b)). In the following text, we denote  $B$  as the applied magnetic field and  $\mu_B = e\hbar/2m_0$  as the Bohr magneton. From Eq. 4.1(a,b), the cyclotron frequencies ( $eB/m^*$ ) of the conduction ( $\omega_c$ ) and valence ( $\omega_v$ ) bands are defined respectively as  $\omega_c = \omega + \tilde{\omega}$  and  $\omega_v = -\omega - \tilde{\omega}$ , where  $\omega = eB/m$  is the cyclotron frequency in the 2-band  $\mathbf{k.p}$  approach and the tilde term  $\tilde{\omega} = eB/\tilde{m}$  represents the far-band contributions. The Landé factors of the conduction ( $g_c$ ) and valence ( $g_v$ ) bands are given by  $g_c = g + \tilde{g}_c$  and  $g_v = -g + \tilde{g}_v$ , where  $g\mu_B B = \hbar\omega$ , and  $\tilde{g}_c$  and  $\tilde{g}_v$  are the far-band contributions. The far-band cyclotron energy contribution is assumed to be equal to the effective spin splitting. We thus obtain  $\tilde{g}_c\mu_B B = -\tilde{g}_v\mu_B B = -\hbar\tilde{\omega}$ .

Therefore, the matrix Hamiltonian of Mitchell and Wallis that describes the  $L_6^\pm$  conduction and valence levels in the trivial regime,  $\Delta > 0$ , is given by:

$$\begin{pmatrix} \Delta + n\hbar\tilde{\omega} & (2v_c^2\hbar eB(n+1))^{1/2} & 0 & \hbar k_z v_c \\ (2v_c^2\hbar eB(n+1))^{1/2} & -\Delta - (n+2)\hbar\tilde{\omega} & \hbar k_z v_c & 0 \\ 0 & \hbar k_z v_c & \Delta + (n+2)\hbar\tilde{\omega} & (2v_c^2\hbar eB(n+1))^{1/2} \\ \hbar k_z v_c & 0 & (2v_c^2\hbar eB(n+1))^{1/2} & -\Delta - n\hbar\tilde{\omega} \end{pmatrix} \quad (4.2)$$

where the Landau level (LL) index is denoted by  $n = -1, 0, 1, \dots$ .

Solving the eigenvalues of the above Hamiltonian, we get the LLs of the conduction ( $c$ ) and valence ( $v$ ) bands for the  $\sigma = \pm 1/2$  states, at  $k_z = 0$ , that are expressed as:

$$E_{v,n,-}^{c,n,+} = \frac{1}{2}(a_n + b_n) \pm \frac{1}{2}[(a_n - b_n)^2 + 8v_c^2\hbar eB(n+1)]^{1/2} \quad (4.3a)$$

$$E_{v,n,+}^{c,n,-} = \frac{1}{2}(c_n + d_n) \pm \frac{1}{2}[(c_n - d_n)^2 + 8v_c^2\hbar eB(n+1)]^{1/2} \quad (4.3b)$$

with

$$a_n = \Delta + n\hbar\tilde{\omega} \quad (4.3c)$$

$$b_n = -\Delta - (n+2)\hbar\tilde{\omega} \quad (4.3d)$$

$$c_n = \Delta + (n+2)\hbar\tilde{\omega} \quad (4.3e)$$

$$d_n = -\Delta - n\hbar\tilde{\omega} \quad (4.3f)$$

Note that the term that varies in  $B^2$  under the square root of the LLs given in Eq. 4.3(a,b) are explicitly neglected. This is equivalent to neglecting the  $k^4$  terms in the BHZ eigenvalues (see the section 3 of the Chapter 3). We have to keep in mind that the lowest conduction and the highest valence LLs are respectively  $E_{c,n=-1,-}$  and  $E_{v,n=-1,-}$ . The conduction and valence LL energies, for  $n = -1, 0, 1, \dots$ , read finally as follows:

$$E_{n \geq 0}^{c,\pm} = \mp \hbar\tilde{\omega} + \sqrt{\Delta^2 + 2 \left( v_c^2 + \frac{\Delta}{\tilde{m}} \right) \hbar e B (n+1)} \quad (4.4a)$$

and

$$E_{n=-1}^{c,-} = \hbar\tilde{\omega} + \Delta \quad (4.4b)$$

$$E_{n \geq 0}^{v,\pm} = \pm \hbar\tilde{\omega} - \sqrt{\Delta^2 + 2 \left( v_c^2 + \frac{\Delta}{\tilde{m}} \right) \hbar e B (n+1)} \quad (4.4c)$$

and

$$E_{n=-1}^{v,-} = -\hbar\tilde{\omega} - \Delta \quad (4.4d)$$

The LL index can be redefined such that  $N^+ = n^+ + 1$  for spin  $\sigma = +1/2$  states (+) and  $N^- = n^- + 1$  for spin  $\sigma = -1/2$  states (-). Note, however, that special care has to be taken when dealing with the  $N = 0$  ( $n^- = -1^-$ ) LL which is non-degenerate in spin. Finally, the above equations can be reduced to:

$$E_{N > 0}^{c,\pm} = \mp \hbar\tilde{\omega} + \sqrt{\Delta^2 + 2 \left( v_c^2 + \frac{\Delta}{\tilde{m}} \right) \hbar e B N} \quad (4.5a)$$

and

$$E_0^c = \hbar\tilde{\omega} + \Delta \quad (4.5b)$$

$$E_{N > 0}^{v,\pm} = \pm \hbar\tilde{\omega} - \sqrt{\Delta^2 + 2 \left( v_c^2 + \frac{\Delta}{\tilde{m}} \right) \hbar e B N} \quad (4.5c)$$

and

$$E_0^v = -\hbar\tilde{\omega} - \Delta \quad (4.5d)$$

## CHAPTER 4

### *Magneto-optical investigation of TCIs: IV-VI compounds*

We can extract the Dirac velocity  $v_D$  from Eq. 4.5(a,c) as the renormalization of  $v_c$  by the far-band correction term  $\tilde{m}$  to the band edge mass. Thus, the expression of  $v_D$  can be written as:

$$v_D = \sqrt{v_c^2 + \frac{\Delta}{\tilde{m}}} \quad (4.6)$$

We define the Dirac transverse band edge mass as:

$$m^* = |\Delta|/v_D^2 \quad (4.7)$$

The LL energies for the LL index  $N = 0, 1, 2, \dots$ , in the trivial regime with  $\Delta > 0$ , are finally written as:

$$E_{N>0}^{c,\pm} = \mp \hbar \tilde{\omega} + \sqrt{\Delta^2 + 2v_D^2 \hbar e B N} \quad (4.8a)$$

and

$$E_0^c = \hbar \tilde{\omega} + \Delta \quad (4.8b)$$

$$E_{N>0}^{v,\pm} = \pm \hbar \tilde{\omega} - \sqrt{\Delta^2 + 2v_D^2 \hbar e B N} \quad (4.8c)$$

and

$$E_0^v = -\hbar \tilde{\omega} - \Delta \quad (4.8d)$$

They correspond to the levels of a massive Dirac fermion model with the velocity  $v_D$  plus a linear far-band cyclotron energy contribution term  $\pm \hbar \tilde{\omega}$  <sup>6</sup>.

In our experimental setup, magneto-optical spectroscopy is performed in the Faraday geometry where the applied magnetic field is oriented parallel to the propagation direction of the light beam and the [111] growth direction of the sample. In this geometry, the selection rules are given by  $\Delta N = \pm 1$  and  $\Delta \sigma = \pm 1$ . Fig. 4.1 schematically illustrates the equivalence between the Landau levels in the 6-band  $\mathbf{k} \cdot \mathbf{p}$  model proposed by Mitchell and Wallis and in the massive Dirac fermion model with the far-band contributions. Accordingly, the interband transition energies from the level  $N$  of the valence band to the level  $N \pm 1$  of the conduction band, occurring at  $k_z = 0$  where the joint density of states is optimal, simply yield:

$$E_{N\pm 1}^{c,\pm} - E_N^{v,\mp} = \sqrt{\Delta^2 + 2v_D^2 \hbar e B (N \pm 1)} + \sqrt{\Delta^2 + 2v_D^2 \hbar e B N} \quad (4.9)$$

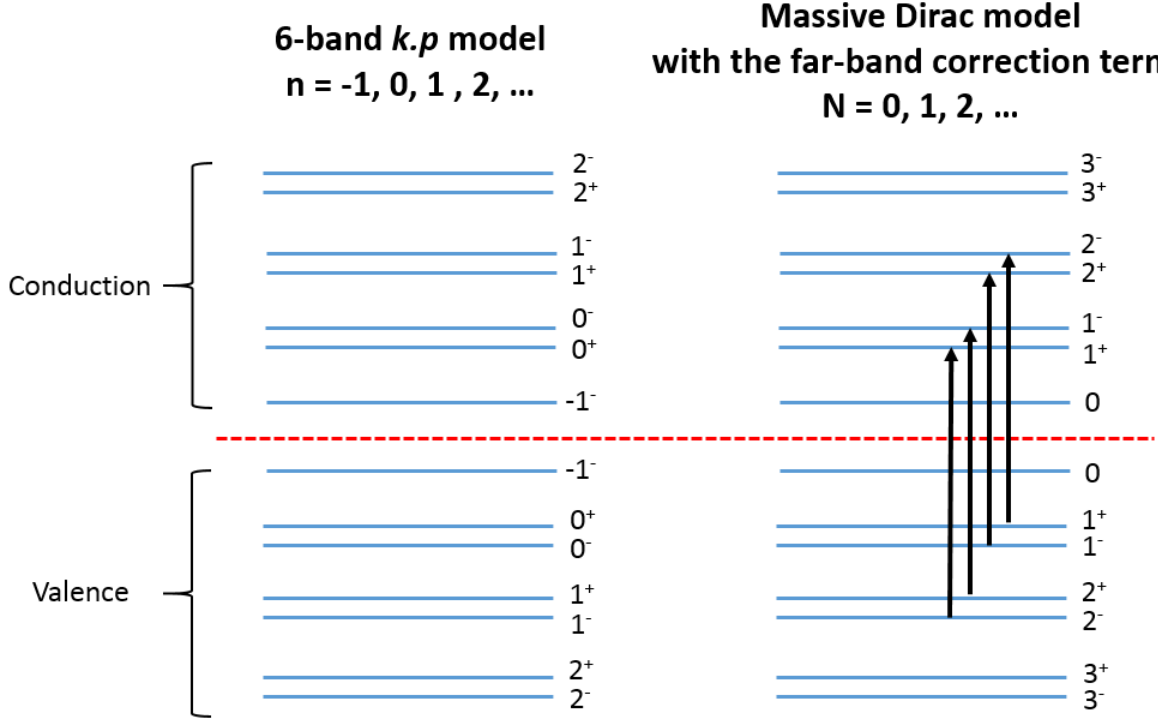


**Figure 4.1.** Equivalence between the Landau levels in the 6-band  $k.p$  model of Mitchell and Wallis and in the massive Dirac fermion model including the far-band correction terms (for the trivial case). In the massive Dirac model, the  $N = 0$  LL is non-degenerate in spin. Black arrows indicate the interband transitions of the same energy in the Faraday geometry where the selection rules are given by  $\Delta N = \pm 1$  and  $\Delta\sigma = \pm 1$ .

We notice that the interband transition energy is independent of the linear far-band contribution term  $\pm\hbar\tilde{\omega}$ . Hence, the transitions are insensitive to the effective spin. This is characteristic of the transitions in an ideal massive Dirac fermion model. To summarize, in the Faraday geometry the LL interband transitions can be effectively described by an ideal massive Dirac model even if the far-band correction terms are present. Note that the velocity of massive Dirac fermions is not a constant but it has to be modified as given by Eq. 4.6 across the topological phase transition.

The intraband or cyclotron resonance (CR) transition energies, obeying  $\Delta N = \pm 1$  and  $\Delta\sigma = 0$ , from the level  $N$  to the level  $N + 1$  of the conduction and valence bands similarly read, at  $k_z = 0$ :

$$E_{N+1}^{c/v,\pm} - E_N^{c/v,\pm} = \sqrt{\Delta^2 + 2v_D^2\hbar eB(N+1)} - \sqrt{\Delta^2 + 2v_D^2\hbar eBN} \quad (4.10)$$

The ground state CR transition energies from the level  $N = 0$  to the level  $N = 1$  of the conduction and valence bands, at  $k_z = 0$ , are given by:

$$E_1^{c/v,-} - E_0^{c/v} = \sqrt{\Delta^2 + 2v_D^2\hbar eB} - |\Delta| \quad (4.11)$$

## CHAPTER 4

### *Magneto-optical investigation of TCIs: IV-VI compounds*

---

#### 1.2. Landau levels of the oblique valleys

The massive Dirac fermions in any tilted bulk valleys  $\theta \neq 0$  undergo the same physics as in the longitudinal valley  $\theta = 0$ . As a consequence, the expressions of interband and intraband transition energies remain unchanged. However, we have to consider the Dirac velocity  $v_D$  that varies as a function of  $\theta$ . In this section, useful formulas for the calculation of  $v_D$  in a tilted valley are given.

The electronic bulk band structure of (111)-oriented  $\text{Pb}_{1-x}\text{Sn}_x\text{Se}$  and  $\text{Pb}_{1-x}\text{Sn}_x\text{Te}$  is four-fold degenerate. The magnetic field is applied along the growth axis [111] and perpendicular to the sample surface. Hence, four band minima occurring at four equivalent  $L$ -points yield a longitudinal valley for an ellipsoidal bulk carrier pocket oriented parallel to the [111] direction  $\theta = 0$  and remaining three oblique valleys for ellipsoidal pockets tilted by  $\theta = 70.5^\circ$  with respect to the [111] direction. For this matter, we define the Dirac velocity in the longitudinal valley as  $v_D(111)$ . We can then derive the expression of  $v_D$  as a function of  $\theta$  from the expression of the cyclotron frequency of the band edge mass in the tilted valleys given by H. Pascher, G. Bauer and R. Grisar<sup>4</sup> that reads:

$$v_D(\theta) = v_D(111) \left( \frac{1}{K} \sin^2 \theta + \cos^2 \theta \right)^{1/4} \quad (4.12)$$

Here,  $K$  is the valley anisotropy factor defined as  $K = (P_\perp/P_\parallel)^2$ , where  $P_\perp$  and  $P_\parallel$  are respectively the transverse and longitudinal momentum matrix elements<sup>2-4</sup>. Note that this anisotropy factor is found to be dependent on the Sn composition of the  $\text{Pb}_{1-x}\text{Sn}_x\text{Se}$  or  $\text{Pb}_{1-x}\text{Sn}_x\text{Te}$  compounds.

For the oblique valleys of (111)-oriented surface, we have:

$$v_D(\theta = 70.5^\circ) = v_D(111) \left( \frac{8}{9} \frac{1}{K} + \frac{1}{9} \right)^{1/4} \quad (4.13)$$

For (001)-oriented surface, we get:

$$v_D(\theta = 53^\circ) = v_D(111) \left( \frac{16}{25} \frac{1}{K} + \frac{9}{25} \right)^{1/4} \quad (4.14)$$

#### 1.3. Landau levels of the topological surface states

The LLs of massive Dirac fermions in  $\text{Pb}_{1-x}\text{Sn}_x\text{Se}$  and  $\text{Pb}_{1-x}\text{Sn}_x\text{Te}$  are represented in the previous two subsections. For massless Dirac fermions in the topological surface states (TSS) that satisfy the linear energy-momentum relation dispersing in the band gap, we can imagine the simplest case of their LL energies when the energy gap  $2\Delta$  in Eq. 4.8 becomes zero and the linear far-band contribution terms are absent. The optical transitions of the TSS obey the same selection rules for the ideal massive Dirac fermion model:  $\Delta N = \pm 1$ . The

Dirac velocities  $v_D$  of massless Dirac fermions in the  $\bar{\Gamma}$ - and  $\bar{M}$ -Dirac cones are not necessary the same and they can be different from those of the bulk bands.

The interband transitions of the TSS are given by:

$$E_{N\pm 1}^c - E_N^v = \sqrt{2v_D^2 \hbar e B (N \pm 1)} + \sqrt{2v_D^2 \hbar e B N} \quad (4.15)$$

The intraband or CR transition energies read as follows:

$$E_{N+1}^{c/v} - E_N^{c/v} = \sqrt{2v_D^2 \hbar e B (N + 1)} - \sqrt{2v_D^2 \hbar e B N} \quad (4.16)$$

The ground CR transition energies from the level  $N = 0$  to the level  $N = 1$  of the same band are written as:

$$E_1^c - E_0^c = E_0^v - E_1^v = \sqrt{2v_D^2 \hbar e B} \quad (4.17)$$

## 2. Growth and characterization of (111) $\text{Pb}_{1-x}\text{Sn}_x\text{Se}$ and $\text{Pb}_{1-x}\text{Sn}_x\text{Te}$ epilayers

High-quality (111)-oriented epitaxial  $\text{Pb}_{1-x}\text{Sn}_x\text{Se}$  and  $\text{Pb}_{1-x}\text{Sn}_x\text{Te}$  films were grown and characterized by G. Springholz, V.V. Volobuev and G. Bauer at the Institut für Halbleiter und Festkörperphysik, Johannes Kepler Universität, in Linz, Austria.

### 2.1. Molecular beam epitaxy growth

(111)-oriented  $\text{Pb}_{1-x}\text{Sn}_x\text{Se}$  and  $\text{Pb}_{1-x}\text{Sn}_x\text{Te}$  films were grown by means of molecular beam epitaxy (MBE) on freshly cleaved (111)  $\text{BaF}_2$  substrates using a Riber 1000 and a Varian GEN-II MBE setups, respectively <sup>7,8</sup>. The epilayers were grown under ultra-high vacuum (UHV) conditions with a pressure better than  $5 \times 10^{-10}$  mbar. Material sources employed for the growth are effusion cells filled with stoichiometric PbSe, PbTe, SnSe and SnTe. The chemical composition of the ternary compounds can be varied over a wide range by controlling the SnSe/PbSe or SnTe/PbTe beam flux ratio that is measured precisely using a quartz microbalance moved into the substrate position. The Sn content of the layers is  $0 \leq x \leq 0.30$  for  $\text{Pb}_{1-x}\text{Sn}_x\text{Se}$  and  $0 \leq x \leq 0.56$  for  $\text{Pb}_{1-x}\text{Sn}_x\text{Te}$ . The growth rate is typically 1  $\mu\text{m}/\text{hour}$  or 1 monolayer/second. The film thickness is between 1 and 3  $\mu\text{m}$  for the magneto-optical absorption measurement. The temperature growth was set to 380 °C. Note that the epilayers have intrinsic p-type carrier concentration (typically  $p > 10^{19} \text{ cm}^{-3}$ ), originating from native Pb and Sn vacancies, that strongly increases with higher Sn composition in  $\text{Pb}_{1-x}\text{Sn}_x\text{Se}$  and  $\text{Pb}_{1-x}\text{Sn}_x\text{Te}$ . In order to compensate this high carrier density, n-type Bi-doping ( $< 10^{19} \text{ cm}^{-3}$ ) was eventually supplied by  $\text{Bi}_2\text{Se}_3$  and  $\text{Bi}_2\text{Te}_3$  effusion cells <sup>9</sup>. When Bi atom is substitutionally incorporated on group IV lattice sites, it acts as a charged donor and thus compensates the background hole concentration. This mechanism leads to achieve the low carrier density



## CHAPTER 4

### *Magneto-optical investigation of TCIs: IV-VI compounds*

without compromising the mobility of the films. The growth of epitaxial films was monitored in-situ by reflection high energy electron diffraction (RHEED). Additionally, the atomically flat surface of the films was visualized using atomic force microscopy (AFM).

## 2.2. X-ray diffraction

(111)  $\text{Pb}_{1-x}\text{Sn}_x\text{Se}$  and  $\text{Pb}_{1-x}\text{Sn}_x\text{Te}$  samples were characterized by high resolution X-ray diffraction (XRD) that was performed in a Seifert XRD3003 diffractometer using  $\text{Cu-K}\alpha_1$  radiation. The diffractometer is equipped with a  $\text{Ge}(220)$  primary beam Bartels monochromator, a parabolic mirror, and a Meteor 1D linear pixel detector. This technique was used to determine the composition and thus the lattice constant of the films with a precision better than 2%. Fig. 4.2 shows the XRD characterization of (111)  $\text{Pb}_{1-x}\text{Sn}_x\text{Se}$  and  $\text{Pb}_{1-x}\text{Sn}_x\text{Te}$  films. Fig. 4.2(a) a  $\{111\}$  Bragg series of (111)  $\text{Pb}_{1-x}\text{Sn}_x\text{Te}$  with  $x = 0.46$  can be clearly observed<sup>10</sup>. In this study, all the epilayers with the thickness higher than  $0.5 \mu\text{m}$  were demonstrated to be fully relaxed<sup>10</sup>. Fig. 4.2(b,c) show only the (222) Bragg reflection for two series of  $\text{Pb}_{1-x}\text{Sn}_x\text{Se}$  ( $0 \leq x \leq 0.30$ ) (Fig. 4.2(b)) and  $\text{Pb}_{1-x}\text{Sn}_x\text{Te}$  ( $0 \leq x \leq 1$ ) (Fig. 4.2(c)) films. The (222) diffraction peaks were observed to monotonically shift to higher diffraction angles with increasing Sn concentration. The lattice constant of the ternary compounds can be directly obtained from the peak position. Fig. 4.2(d) shows the Sn content determined from XRD as a function of the beam flux ratio  $\text{Sn}/(\text{Sn}+\text{Pb})$  measured by the quartz balance method in the growth of  $\text{Pb}_{1-x}\text{Sn}_x\text{Se}$  (●) and  $\text{Pb}_{1-x}\text{Sn}_x\text{Te}$  (◆). The dashed green line represents the calculated nominal values of the Sn content from the change in lattice constant using the Vegard's law that is written as:

- For  $\text{Pb}_{1-x}\text{Sn}_x\text{Se}$ :  $a_{\text{Pb}_{1-x}\text{Sn}_x\text{Se}}(x) = (6.124 - 0.123x) \text{ \AA}$  (4.18)

- For  $\text{Pb}_{1-x}\text{Sn}_x\text{Te}$ :  $a_{\text{Pb}_{1-x}\text{Sn}_x\text{Te}}(x) = (6.462 - 0.162x) \text{ \AA}$  (4.19)

Here, the lattice constants of pure PbSe and PbTe are respectively  $6.124 \text{ \AA}$  and  $6.462 \text{ \AA}$ . As can be seen, the data points are in very good agreement with the nominal values within  $\pm 1\%$  without any adjustable parameters. Note that  $\text{Pb}_{1-x}\text{Sn}_x\text{Se}$  films with  $x > 0.40$  have orthorhombic crystal structure and are no longer single phase, resulting in a splitting of the diffraction peaks. Therefore, their Sn content results are not shown here. For this reason, only  $\text{Pb}_{1-x}\text{Sn}_x\text{Se}$  films with single phase cubic rocksalt structure in the Sn solubility limit  $x \sim 0.45$  were studied. For  $\text{Pb}_{1-x}\text{Sn}_x\text{Te}$ , complete miscibility exists over the entire composition range.

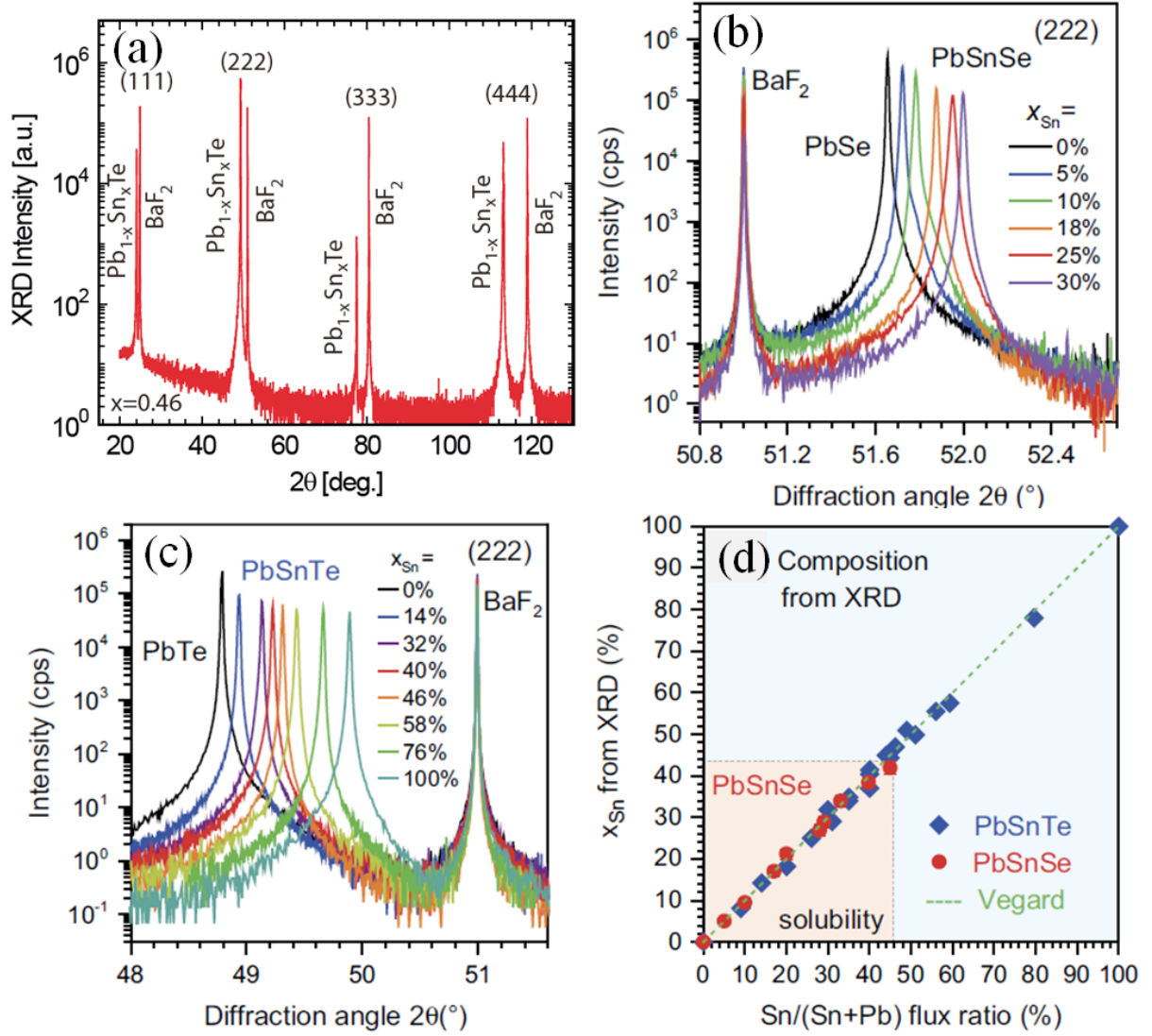


**Figure 4.2. X-ray diffraction characterization and analysis.** (a) Symmetric X-ray diffraction scan of (111)  $\text{Pb}_{1-x}\text{Sn}_x\text{Te}$  with  $x = 0.46$  using  $\text{Cu-K}\alpha_1$  radiation shows the diffraction peaks of the epitaxial layer with respect to the substrate (111)  $\text{BaF}_2$ . (222) Bragg diffraction peaks of  $\text{Pb}_{1-x}\text{Sn}_x\text{Se}$  films for  $0 \leq x \leq 0.30$  (b) and  $\text{Pb}_{1-x}\text{Sn}_x\text{Te}$  films for  $0 \leq x \leq 1$  (c). (d) The Sn content extracted from X-ray diffraction as a function of the beam flux ratio  $\text{Sn}/(\text{Sn}+\text{Pb})$  measured during the MBE growth of  $\text{Pb}_{1-x}\text{Sn}_x\text{Se}$  (●) and  $\text{Pb}_{1-x}\text{Sn}_x\text{Te}$  (◆) films. A very good agreement is obtained between the data points and the dashed green line representing the nominal values of the Sn concentration calculated from the change in lattice constant using the Vegard's law. All the figures are adapted from our papers ((a) from <sup>10</sup> and (b-d) from <sup>11</sup>).

### 2.3. Electrical transport characterization

Transport measurements using a van der Pauw geometry were carried out at 77 K to determine the Hall carrier density and mobility. For (111)  $\text{Pb}_{1-x}\text{Sn}_x\text{Te}$ , moderate Bi-doping ( $< 10^{19} \text{ cm}^{-3}$ )<sup>9</sup> was applied for  $x > 0.28$  to limit the carrier concentration to no more than  $4 \times 10^{18} \text{ cm}^{-3}$  and mobilities are between 5,000 and 30,000  $\text{cm}^2/(\text{V.s})$ . For (111)  $\text{Pb}_{1-x}\text{Sn}_x\text{Se}$ , carrier densities as low as  $10^{17} \text{ cm}^{-3}$  were achieved and mobilities were measured to be

## CHAPTER 4

### *Magneto-optical investigation of TCIs: IV-VI compounds*

between 10,000 and 40,000  $\text{cm}^2/(\text{V.s})$ . Table 4.1 show the carrier concentration and the mobility of (111)  $\text{Pb}_{1-x}\text{Sn}_x\text{Se}$  and  $\text{Pb}_{1-x}\text{Sn}_x\text{Te}$  films measured at 77 K. Thanks to these good transport properties, Landau quantization can be observed at low magnetic fields. Additionally, these electrical transport measurements allow us to know whether the sample has n- or p-type carriers, being the useful information for the magneto-optical determination of the Fermi energy of the sample.

Composition $\text{Pb}_{1-x}\text{Sn}_x\text{Se}$	Thickness ( $\mu\text{m}$ )	Carrier type	Bi- doping	Carrier density ( $\text{cm}^{-3}$ )	Carrier mobility ( $\text{cm}^2/(\text{V.s})$ )
<b>PbSe</b>	3	n	No	$1.5 \times 10^{17}$	29,700
<b>Pb<sub>0.95</sub>Sn<sub>0.05</sub>Se</b>	2	n	No	$2.4 \times 10^{17}$	32,800
<b>Pb<sub>0.90</sub>Sn<sub>0.10</sub>Se</b>	2	n	No	$1.7 \times 10^{17}$	35,800
<b>Pb<sub>0.86</sub>Sn<sub>0.14</sub>Se</b>	2	p	No	$9.77 \times 10^{16}$	14,900
<b>Pb<sub>0.835</sub>Sn<sub>0.165</sub>Se</b>	2	n	No	$1.43 \times 10^{17}$	29,500
<b>Pb<sub>0.81</sub>Sn<sub>0.19</sub>Se</b>	2	n	Yes	$2.6 \times 10^{17}$	34,600
<b>Pb<sub>0.76</sub>Sn<sub>0.24</sub>Se</b>	3	n	No	$1.86 \times 10^{17}$	15,900
<b>Pb<sub>0.70</sub>Sn<sub>0.30</sub>Se</b>	2.6	p	No	$1.20 \times 10^{18}$	9,540

Composition $\text{Pb}_{1-x}\text{Sn}_x\text{Te}$	Thickness ( $\mu\text{m}$ )	Carrier type	Bi- doping	Carrier density ( $\text{cm}^{-3}$ )	Carrier mobility ( $\text{cm}^2/(\text{V.s})$ )
<b>PbTe</b>	1	n	No	$5.24 \times 10^{16}$	30,100
<b>Pb<sub>0.92</sub>Sn<sub>0.08</sub>Te</b>	1	n	No	$2.82 \times 10^{17}$	17,600
<b>Pb<sub>0.89</sub>Sn<sub>0.11</sub>Te</b>	1	p	No	$9.14 \times 10^{17}$	6,820
<b>Pb<sub>0.86</sub>Sn<sub>0.14</sub>Te</b>	1	p	No	$6.71 \times 10^{17}$	4,410
<b>Pb<sub>0.85</sub>Sn<sub>0.15</sub>Te</b>	1	p	No	$2.09 \times 10^{18}$	7,160
<b>Pb<sub>0.80</sub>Sn<sub>0.20</sub>Te</b>	2	n	Yes	$5.18 \times 10^{18}$	10,000
<b>Pb<sub>0.75</sub>Sn<sub>0.25</sub>Te</b>	1	p	No	$1.01 \times 10^{18}$	7,640
<b>Pb<sub>0.72</sub>Sn<sub>0.28</sub>Te</b>	1	p	No	$1.83 \times 10^{18}$	8,520
<b>Pb<sub>0.69</sub>Sn<sub>0.31</sub>Te</b>	1	p	Yes	$7.91 \times 10^{17}$	8,100
<b>Pb<sub>0.66</sub>Sn<sub>0.34</sub>Te</b>	1	p	Yes	$1.31 \times 10^{18}$	10,000
<b>Pb<sub>0.65</sub>Sn<sub>0.35</sub>Te</b>	1	n	Yes	$6.54 \times 10^{17}$	19,900
<b>Pb<sub>0.63</sub>Sn<sub>0.37</sub>Te</b>	1	n	Yes	$2.34 \times 10^{18}$	11,300
<b>Pb<sub>0.60</sub>Sn<sub>0.40</sub>Te</b>	1	p	Yes	$1.09 \times 10^{18}$	9,630
<b>Pb<sub>0.59</sub>Sn<sub>0.41</sub>Te</b>	1	p	Yes	$1.81 \times 10^{18}$	11,100
<b>Pb<sub>0.56</sub>Sn<sub>0.44</sub>Te</b>	1	p	Yes	$2.89 \times 10^{18}$	9,810
<b>Pb<sub>0.55</sub>Sn<sub>0.45</sub>Te</b>	1	n	Yes	$1.16 \times 10^{18}$	7,480
<b>Pb<sub>0.54</sub>Sn<sub>0.46</sub>Te</b>	2	p	Yes	$8.2 \times 10^{17}$	7,000
<b>Pb<sub>0.50</sub>Sn<sub>0.50</sub>Te</b>	1	p	Yes	$1.81 \times 10^{18}$	6,990
<b>Pb<sub>0.49</sub>Sn<sub>0.51</sub>Te</b>	1	p	Yes	$3.04 \times 10^{18}$	9,060
<b>Pb<sub>0.44</sub>Sn<sub>0.56</sub>Te</b>	1	p	Yes	$3.94 \times 10^{18}$	7,430

Table 4.1. Carrier concentration and mobility of (111)  $\text{Pb}_{1-x}\text{Sn}_x\text{Se}$  and  $\text{Pb}_{1-x}\text{Sn}_x\text{Te}$  epilayers characterized by electrical transport measurements at 77 K (at the Institut für Halbleiter und Festkörperphysik, Johannes Kepler Universität, in Linz, Austria)

### **3. Magneto-optical Landau level spectroscopy of Dirac fermions in (111) $\text{Pb}_{1-x}\text{Sn}_x\text{Se}$**

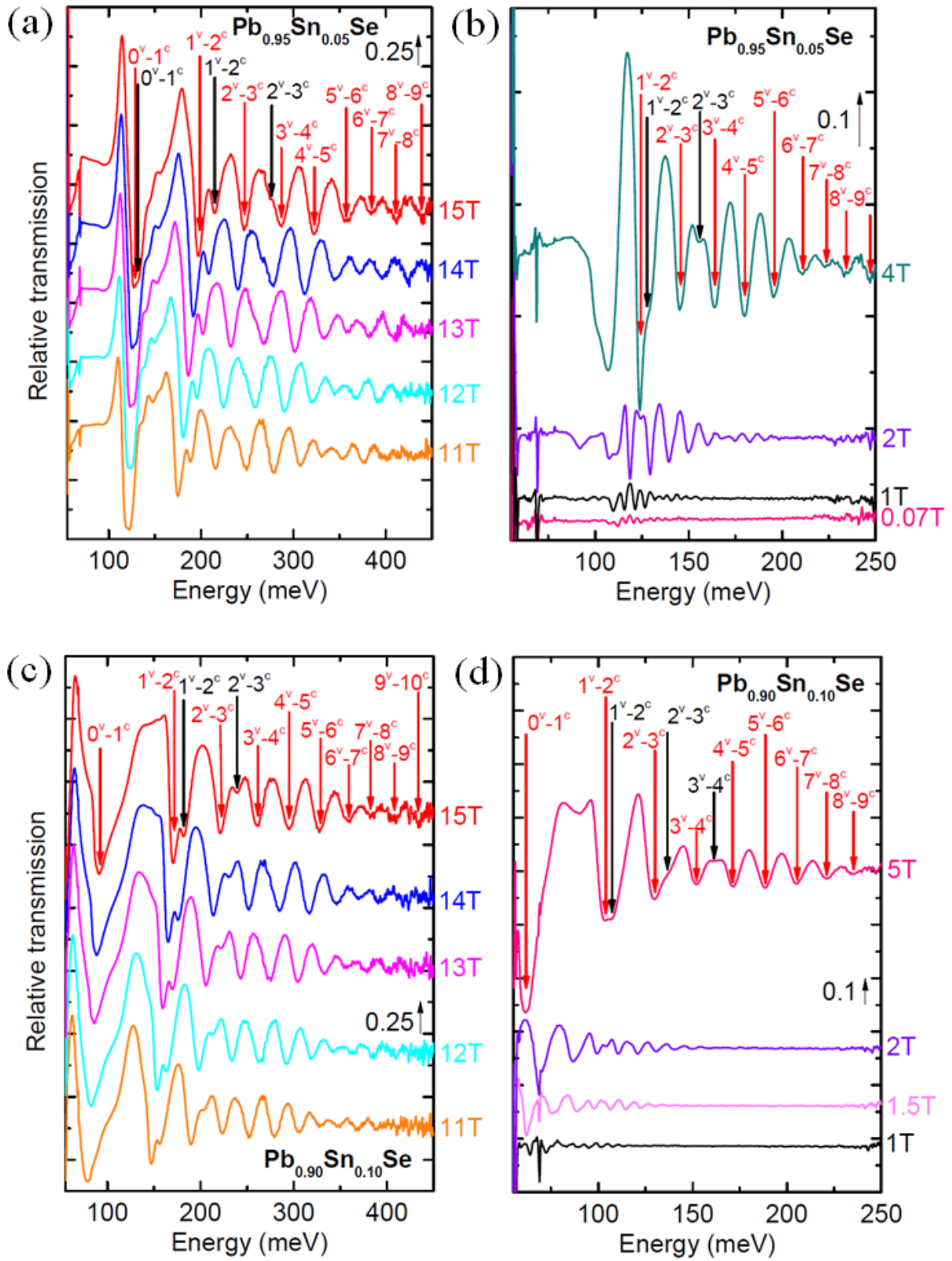
Magneto-optical IR Landau level spectroscopy was performed in eight (111)  $\text{Pb}_{1-x}\text{Sn}_x\text{Se}$  samples ( $0 \leq x \leq 0.30$ ) in the Faraday geometry for  $B = 0-17$  T and  $T = 4.5$  K in the FIR and MIR spectral ranges (4-600 meV). The applied magnetic field was oriented along the [111] direction or the growth axis and thus perpendicular to the sample surface. The relative transmission spectra at fixed fields  $T(B)/T(0)$  of each sample were acquired and analyzed using the Dirac fermion model as presented in the section 1.

#### **3.1. Bulk states in (111) $\text{Pb}_{1-x}\text{Sn}_x\text{Se}$**

The typical MIR magneto-optical transmission spectra measured at different magnetic fields of six representative samples are shown in Fig. 4.3(a,b) for  $x = 0.05$ , Fig. 4.3(c,d) for  $x = 0.10$ , Fig. 4.3(e,f) for  $x = 0.14$ , Fig. 4.4(a,b) for  $x = 0.19$ , Fig. 4.4(c,d) for  $x = 0.24$  and Fig. 4.4(e,f) for  $x = 0.30$ . A number of strong absorption minima dispersing as a function of field can be clearly seen in all the samples. Two series of transitions were observed and are associated with different bulk valleys. The series depicted by black arrows is attributed to the transitions in the bulk longitudinal valley. Other transitions marked by red arrows originate from the bulk oblique valleys, tilted with the angle  $\theta = 70.5^\circ$  with respect to the [111] direction. The intensity and broadening of the absorption lines increase when two contributions resulting from the transitions in both types of valleys occur at about the same energy. For high LL index  $N$  of the transitions, the longitudinal and oblique transitions of massive Dirac fermions are mixed. For the sake of simplicity, only the oblique ones are represented. Narrow absorption lines observed in the transmission spectra indicate the high crystalline quality of the epilayers. We observe that a strong and clear modulation can be followed down to low fields, evidencing the high mobility and low carrier concentration of the films. The transmission curves are vertically shifted for clarity purposes.

## CHAPTER 4

### Magneto-optical investigation of TCIs: IV-VI compounds



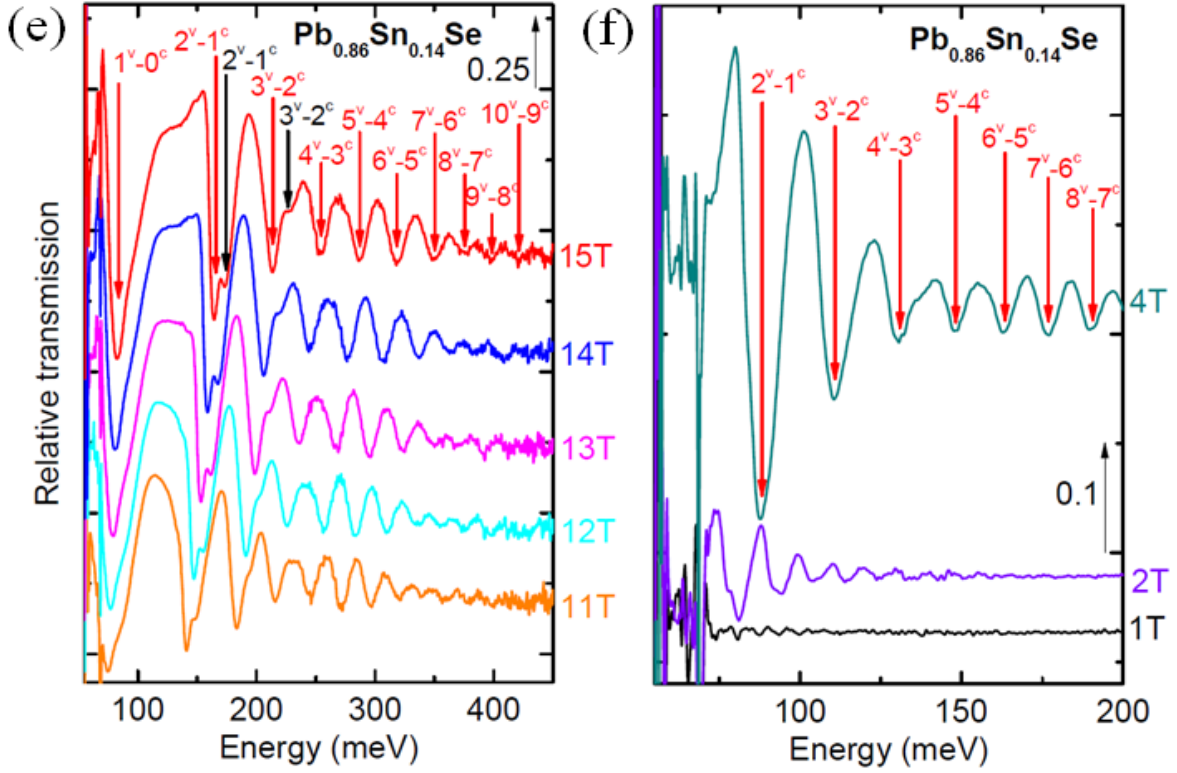
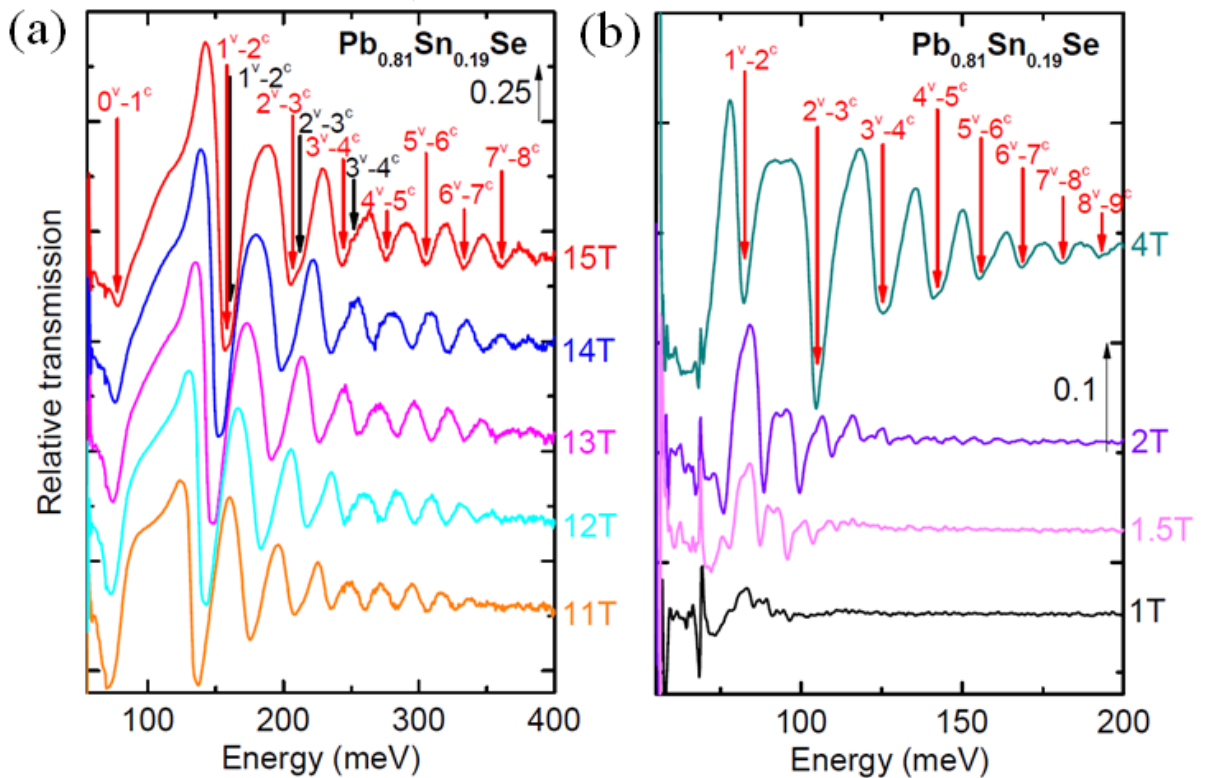


**Figure 4.3. MIR transmission spectra of trivial  $\text{Pb}_{1-x}\text{Sn}_x\text{Se}$ .** MIR magneto-optical transmission spectra of  $\text{Pb}_{1-x}\text{Sn}_x\text{Se}$  measured at 4.5 K for  $x = 0.05$  (a,b),  $x = 0.10$  (c,d) and  $x = 0.14$  (e,f). Black and red arrows mark the transmission minima resulting from the transitions in the bulk longitudinal and oblique valleys, respectively. At high LL index  $N$ , the bulk longitudinal and oblique transitions are mixed and only the oblique ones are shown by red arrows. Narrow absorption lines evidence the high crystalline quality of the films. Transitions can be observed at low fields, indicating the high mobility and low carrier density of the films. All the spectra are shifted vertically for clarity.





## CHAPTER 4

### Magneto-optical investigation of TCIs: IV-VI compounds

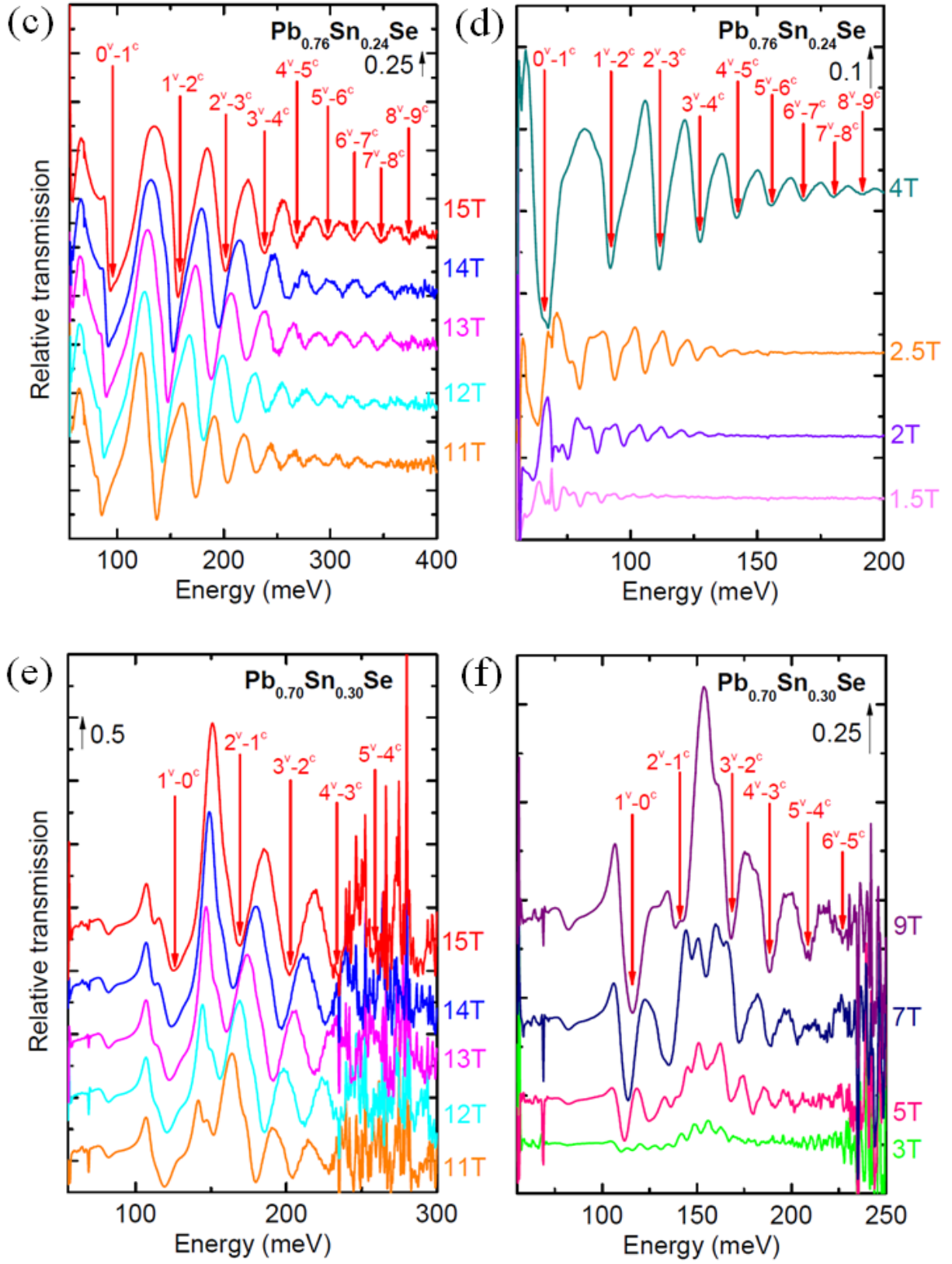


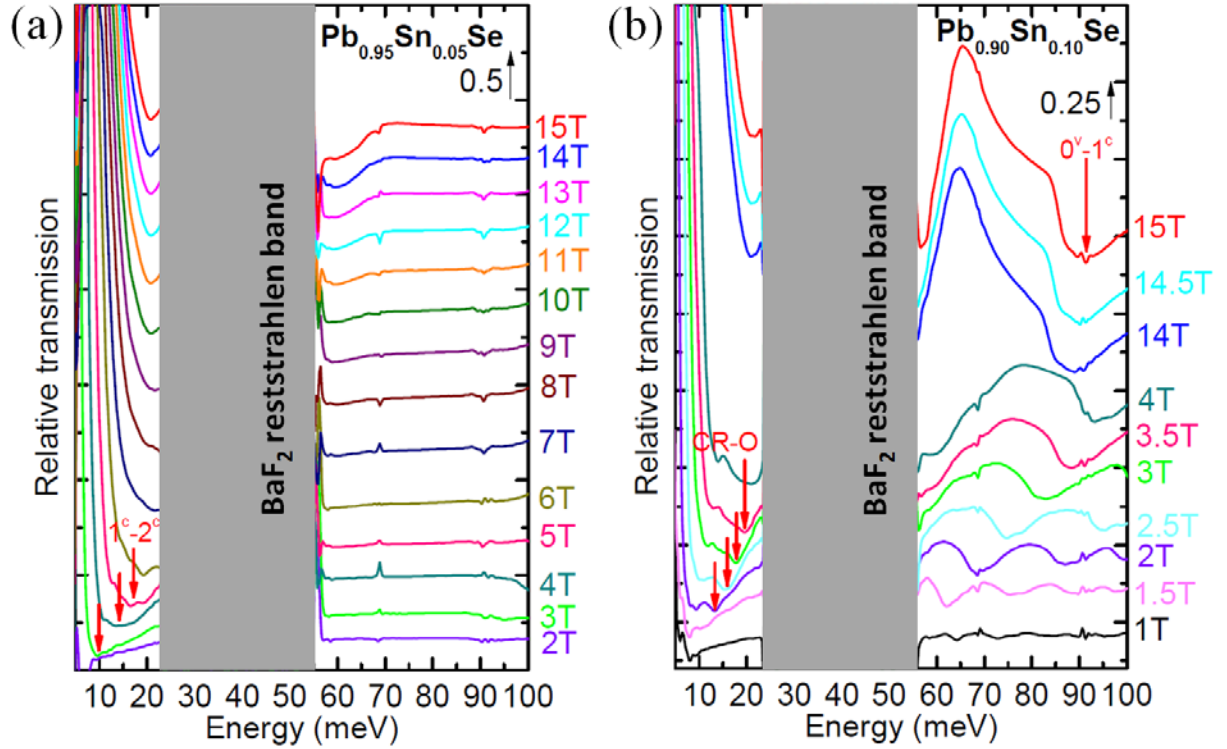
**Figure 4.4. MIR transmission spectra of nontrivial  $\text{Pb}_{1-x}\text{Sn}_x\text{Se}$ .** MIR magneto-optical transmission spectra of  $\text{Pb}_{1-x}\text{Sn}_x\text{Se}$  measured at 4.5 K for  $x = 0.19$  (a,b),  $x = 0.24$  (c,d) and  $x = 0.30$  (e,f). Black and red arrows mark the transmission minima resulting from the transitions in the bulk longitudinal and oblique valleys,

## CHAPTER 4

### *Magneto-optical investigation of TCIs: IV-VI compounds*

respectively. At high LL index  $N$ , the bulk longitudinal and oblique transitions are mixed and only the oblique ones are shown by red arrows. Narrow absorption lines evidence the high crystalline quality of the films. Transitions can be observed at low fields, indicating the high mobility and low carrier density of the films. All the spectra are shifted vertically for clarity.

FIR magneto-optical absorption measurements were also performed in the eight samples. Typical FIR transmission spectra at several magnetic fields are shown in Fig. 4.5(a) for  $x = 0.05$ , Fig. 4.5(b) for  $x = 0.10$ , Fig. 4.5(c) for  $x = 0.14$ , Fig. 4.5(d) for  $x = 0.19$ , Fig. 4.5(e) for  $x = 0.24$  and Fig. 4.5(f) for  $x = 0.30$ . Some transmission minima were observed in both FIR and MIR ranges. All the samples are opaque in the region covering the energy range from 22 to 55 meV. This is due to the phonon-related absorption in the  $\text{BaF}_2$  substrate resulting in the reststrahlen band where we cannot observe any transition. However, since our samples have low carrier densities, we can thus observe intraband transitions between low indices  $N$  dispersing down to low fields below the reststrahlen band.





## CHAPTER 4

### Magneto-optical investigation of TCIs: IV-VI compounds

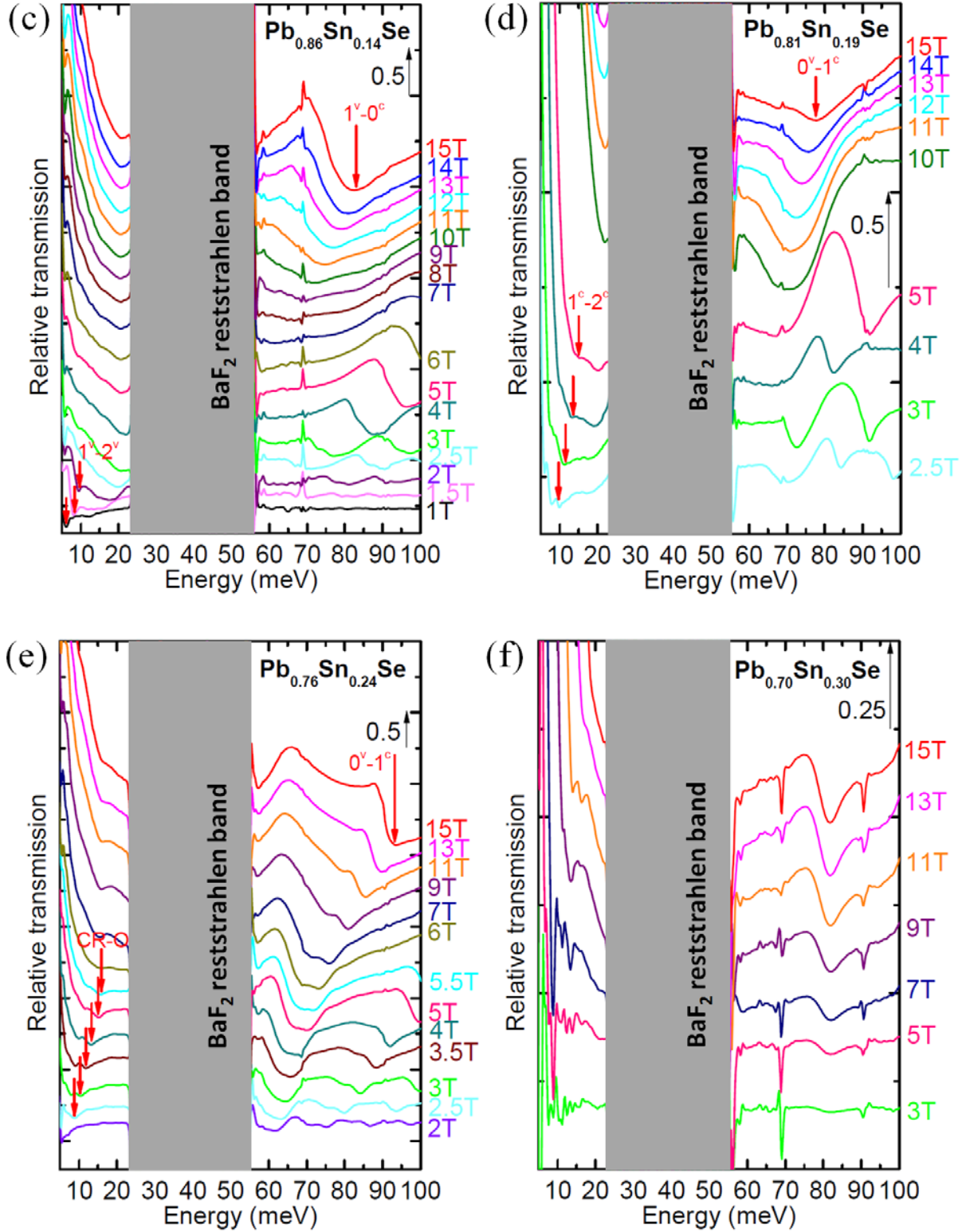


**Figure 4.5. FIR transmission spectra of trivial  $\text{Pb}_{1-x}\text{Sn}_x\text{Se}$ .** FIR magneto-optical transmission spectra of  $\text{Pb}_{1-x}\text{Sn}_x\text{Se}$  measured at 4.5 K for  $x = 0.05$  (a),  $x = 0.10$  (b),  $x = 0.14$  (c),  $x = 0.19$  (d),  $x = 0.24$  (e), and  $x = 0.30$  (f). Arrows mark the transmission minima originating from the transitions in the bulk valleys. The samples are opaque in the energy range from 22 to 55 meV (reststrahlen band) due to the phonon-related absorption in the  $\text{BaF}_2$  substrate. All the spectra are shifted vertically for clarity.

Note that baseline signal contributions from the response of the bolometer to the applied magnetic field have a negligible impact on the position of the transmission minima thanks to the large amplitude and narrowness of the observed absorption lines. Nevertheless, we also verified the change in the position of the minima in the transmission spectra taken at each field and found that it is negligible after removing the baseline slope originating from the detector's response. Accordingly, the error resulting from the presence of the baseline is significantly smaller than the error bars represented by the size of the markers on the LL transition diagrams (shown later). For our experimental results, we can directly extract the transition energies from the measured transmission spectra.

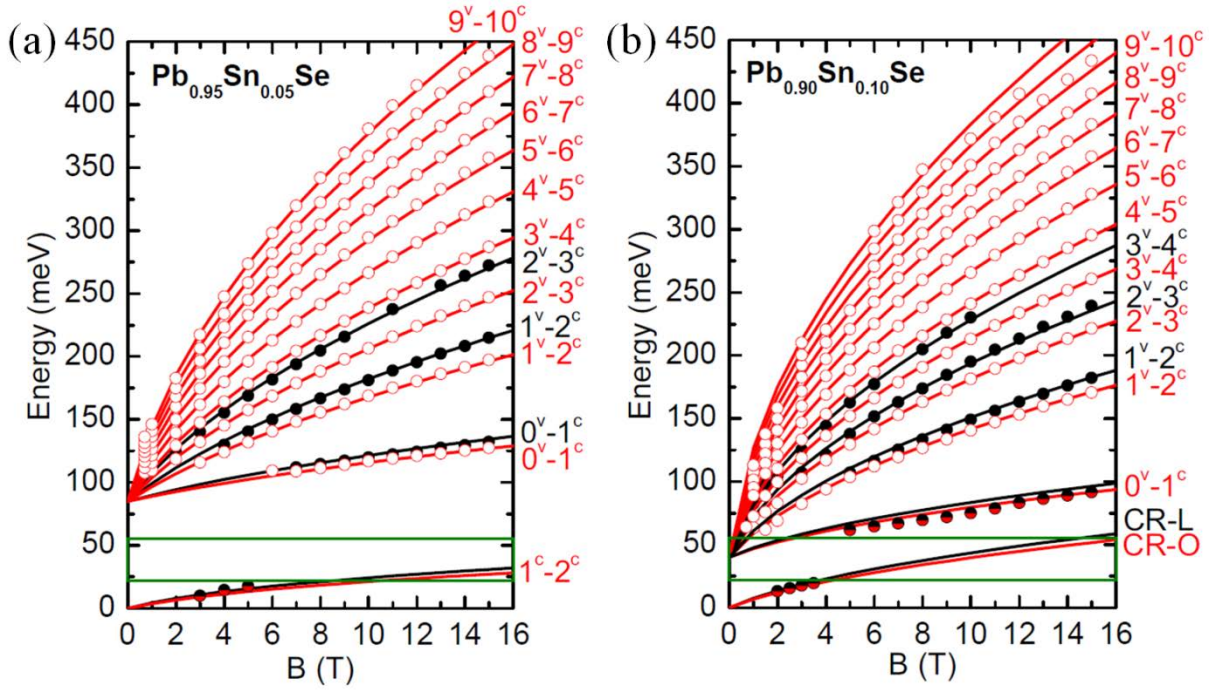
The transmission minima were identified and plotted as circles versus magnetic field in Fig. 4.6(a) for  $x = 0.05$ , Fig. 4.6(b) for  $x = 0.10$ , Fig. 4.6(c) for  $x = 0.14$ , Fig. 4.6(d) for  $x = 0.19$ , Fig. 4.6(e) for  $x = 0.24$  and Fig. 4.6(f) for  $x = 0.30$  in order to construct LL transition fan diagrams. Full black circles and empty red circles denote respectively the transitions resulting from the bulk longitudinal and oblique valleys. Bicolor circles (black and red) represent the minima originating from the transitions in both longitudinal and oblique valleys that occur very nearly at or exactly at the same energy. The green frame covering the energies between 22 and 55 meV is the BaF<sub>2</sub> substrate reststrahlen band where no absorption can be observed. The massive Dirac model was used to fit the experimental data for both types of valleys. Note that the magneto-optical absorption experiment measures the absolute value of the energy gap. For a given Sn content, the interband (Eq. 4.9), intraband (Eq. 4.10), and ground CR (Eq. 4.11) transition energies for the bulk states were calculated with two parameters for both types of valleys: the half band gap  $|\Delta|$  and the Dirac velocity  $v_D$ . Black and red solid lines are the calculated curve fits for the transitions in the bulk longitudinal and oblique valleys, respectively. Interband transitions from the level  $N$  of the valence band ( $v$ ) to the level  $N \pm 1$  of the conduction band ( $c$ ) are denoted as  $N^v - (N \pm 1)^c$ . CR-L and CR-O refer to the ground cyclotron resonance of the valence ( $0^v - 1^v$ ) or conduction ( $0^c - 1^c$ ) bands of the longitudinal and oblique valleys, respectively.  $N^v - (N + 1)^v$  and  $N^c - (N + 1)^c$  are used respectively as notation for intraband transitions with  $N > 0$  between two adjacent levels of the valence and conduction bands. An excellent agreement between the theory and the experimental data is obtained in the eight samples. Their band parameters precisely determined from the massive Dirac model analysis are represented in Table 4.2 as well as the corresponding Dirac transverse band edge masses  $m^* = |\Delta|/v_D^2$ .

## CHAPTER 4

### Magneto-optical investigation of TCIs: IV-VI compounds

Composition $\text{Pb}_{1-x}\text{Sn}_x\text{Se}$	$2 \Delta $ (meV)	$v_D$ (long.) ( $\times 10^5$ m/s)	$v_D$ (obl.) ( $\times 10^5$ m/s)	$m^*$ (long.) ( $\times m_0$ )	$m^*$ (obl.) ( $\times m_0$ )
<b>PbSe</b>	$146 \pm 4$	$6.4 \pm 0.1$	$5.6 \pm 0.1$	$0.031 \pm 0.001$	$0.041 \pm 0.002$
<b>Pb<sub>0.95</sub>Sn<sub>0.05</sub>Se</b>	$85 \pm 5$	$5.8 \pm 0.1$	$5.2 \pm 0.1$	$0.022 \pm 0.002$	$0.028 \pm 0.002$
<b>Pb<sub>0.90</sub>Sn<sub>0.10</sub>Se</b>	$40 \pm 5$	$5.25 \pm 0.10$	$4.9 \pm 0.1$	$0.013 \pm 0.002$	$0.015 \pm 0.002$
<b>Pb<sub>0.86</sub>Sn<sub>0.14</sub>Se</b>	$25 \pm 5$	$5.05 \pm 0.10$	$4.8 \pm 0.1$	$0.009 \pm 0.002$	$0.010 \pm 0.002$
<b>Pb<sub>0.835</sub>Sn<sub>0.165</sub>Se</b>	$15 \pm 5$	$4.9 \pm 0.1$	$4.7 \pm 0.1$	$0.005 \pm 0.002$	$0.006 \pm 0.002$
<b>Pb<sub>0.81</sub>Sn<sub>0.19</sub>Se</b>	$25 \pm 10$	$4.8 \pm 0.1$	$4.6 \pm 0.1$	$0.010 \pm 0.004$	$0.010 \pm 0.004$
<b>Pb<sub>0.76</sub>Sn<sub>0.24</sub>Se</b>	$55 \pm 5$	$4.4 \pm 0.1$	$4.4 \pm 0.1$	$0.025 \pm 0.003$	$0.025 \pm 0.003$
<b>Pb<sub>0.70</sub>Sn<sub>0.30</sub>Se</b>	$100 \pm 10$	$4.0 \pm 0.1$	$4.0 \pm 0.1$	$0.055 \pm 0.006$	$0.055 \pm 0.006$

**Table 4.2.** Magneto-optical band parameters determined from the massive Dirac model analysis in eight (111)  $\text{Pb}_{1-x}\text{Sn}_x\text{Se}$  samples measured at  $T = 4.5$  K.  $2|\Delta|$  is the band gap. The Dirac velocities  $v_D$  in the longitudinal and oblique valleys are represented for each compound. The band edge masses can be deduced from those two parameters  $m^* = |\Delta|/v_D^2$  for both types of valleys.  $m_0$  is the electron rest mass.



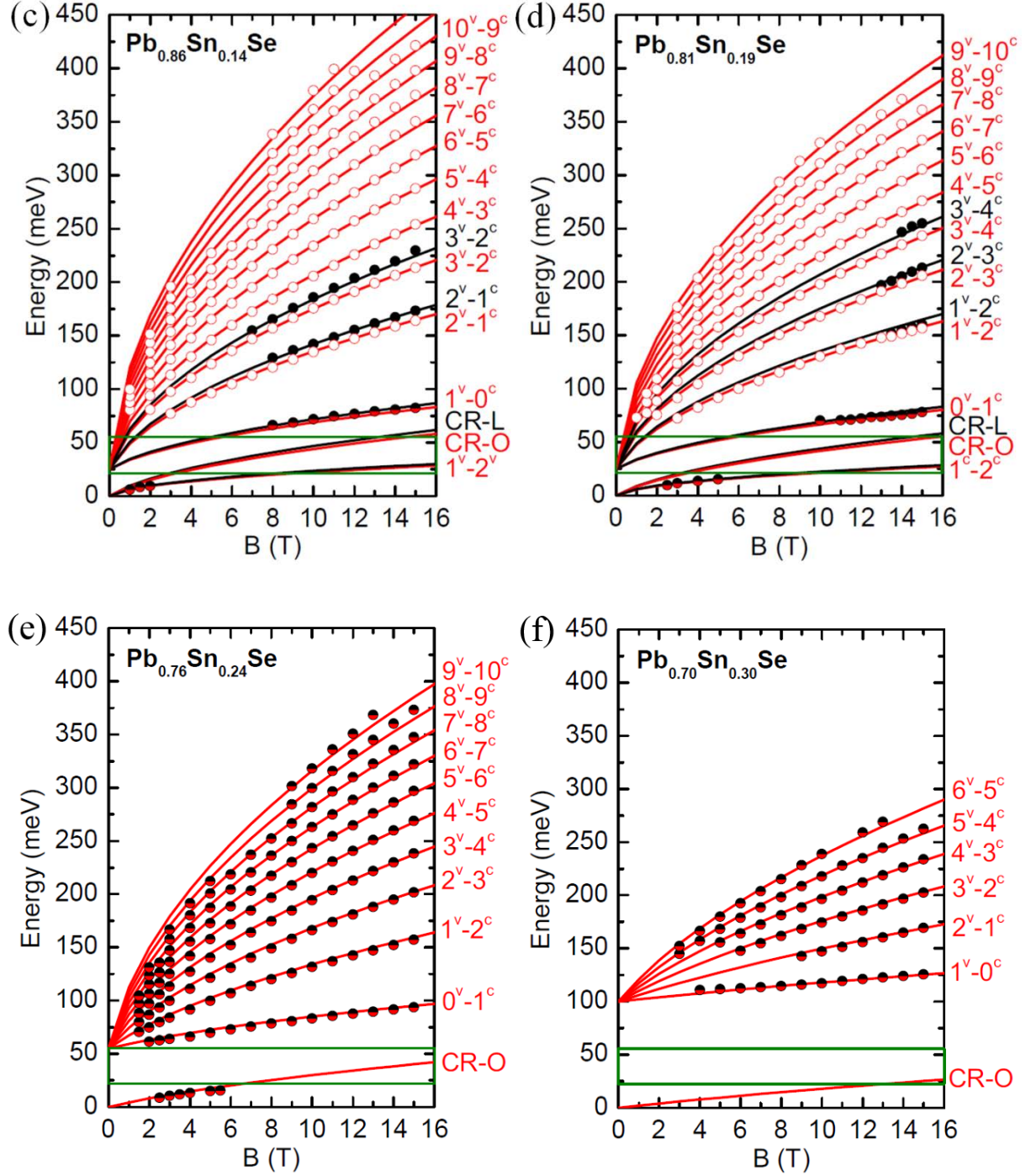


**Figure 4.6. Landau level transition diagrams of (111)  $\text{Pb}_{1-x}\text{Sn}_x\text{Se}$ .** Landau level transition fan charts of (111)  $\text{Pb}_{1-x}\text{Sn}_x\text{Se}$  for  $x = 0.05$  (a),  $x = 0.10$  (b),  $x = 0.14$  (c),  $x = 0.19$  (d),  $x = 0.24$  (e) and  $x = 0.30$  (f). Full black and empty red circles denote respectively the transitions in the bulk longitudinal and oblique valleys. Circles with two colors (black and red) mark the transitions in both types of valleys that occur very nearly at or exactly at the same energy. The green rectangle located between 22 and 55 meV is the BaF<sub>2</sub> substrate reststrahlen band. The experimental data were analyzed using the massive Dirac fermion model. Black and red curve fits were calculated for the transition energies in the longitudinal and oblique bulk valleys. Experimental results agree very well with the theory.

## CHAPTER 4

### Magneto-optical investigation of TCIs: IV-VI compounds

We notice that the band gap is the same in both types of valleys, while the Dirac velocity is found to be different due to the bulk valley anisotropy<sup>2-4</sup>. The larger value corresponds to the Dirac velocity of massive Dirac fermions in the bulk longitudinal valley, whereas the smaller one corresponds to that in the bulk oblique valleys. A decrease in  $v_D$  when  $x$  is increased is observed in both types of bulk valleys and this will be discussed in the sections 5 and 7. From Fig. 4.6, it is clear that the anisotropy decreases as  $x$  increases. For  $x \geq 0.24$ , we observe that the Dirac velocity is the same for the longitudinal and oblique valleys. This indicates that the longitudinal and oblique bulk pockets are nearly spherical. The anisotropy of ellipsoidal bulk carrier pockets of  $\text{Pb}_{1-x}\text{Sn}_x\text{Se}$  demonstrated by magneto-optics will be discussed in detail in the section 7.

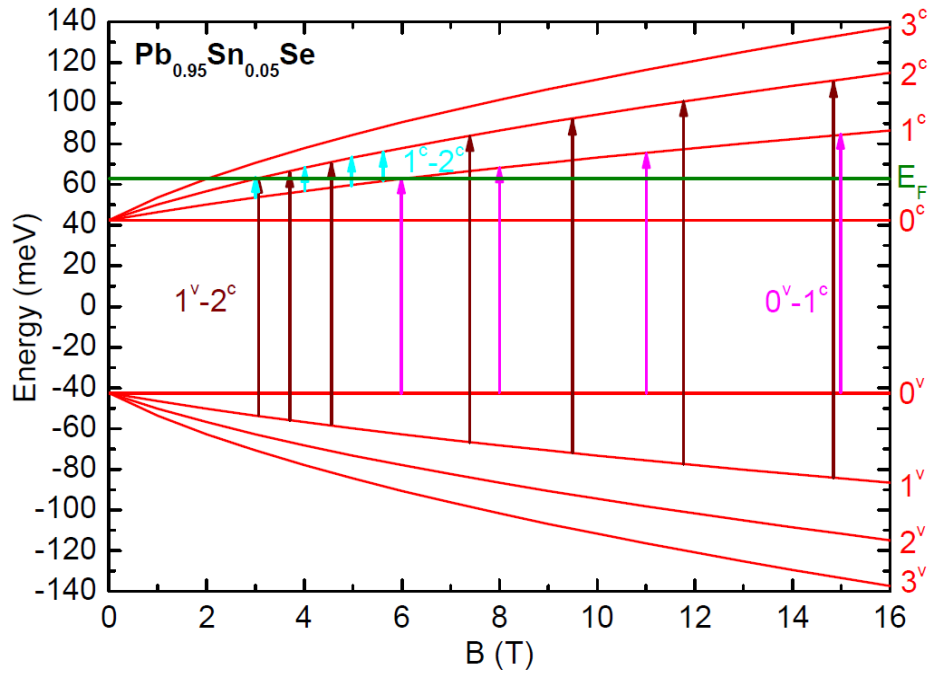


**Figure 4.7. Dirac Landau level dispersion and examples of Landau level transitions in (111)  $\text{Pb}_{0.95}\text{Sn}_{0.05}\text{Se}$  with n-type carriers.** The massive Dirac Landau levels in the oblique valleys (red curves) are calculated using the band gap  $2|\Delta| = 85$  meV and the Dirac velocity  $v_D = 5.2 \times 10^5$  m/s. Pink arrows show the first interband transition  $0^v - 1^c$  that can be observed down to  $B \sim 6$  T. Since the level  $1^c$  is depopulated from  $B \sim 6$  T, the Fermi energy  $E_F$  is estimated to be  $E_F \sim E_1^c \sim 20$  meV in the bulk conduction band edge. Brown arrows show the interband transition  $1^v - 2^c$  that can be followed down to  $B \sim 3$  T. Since the level  $2^c$  is depopulated from  $B \sim 3$  T, therefore  $E_F \sim E_2^c \sim 20$  meV above the bulk conduction band edge.  $E_F$  is depicted by green horizontal line, allowing the intraband transition  $1^c - 2^c$  (sky blue arrows) to occur between 3 and 6 T ( $E_1^c < E_F < E_2^c$ ).

We can estimate the Fermi energy  $E_F$  in the bulk band edge by calculating the LL energy at a fixed  $B$  where the transmission appears. For example, as shown in Fig. 4.7, in  $\text{Pb}_{0.95}\text{Sn}_{0.05}\text{Se}$  with n-type carriers (Fig. 4.6(a)) the first interband transition  $0^v - 1^c$  (pink arrows) of the bulk oblique valleys was observed down to  $B \sim 6$  T. By considering the level  $1^c$  that is depopulated from  $B \sim 6$  T, therefore  $E_F \sim E_1^c \sim 20$  meV above the bulk conduction band edge of the oblique valleys. This agrees very well with the interband transition  $1^v - 2^c$  (brown arrows) of the oblique valleys that was observed down to  $B \sim 3$  T because the level  $2^c$



is depopulated from  $B \sim 3$  T, therefore  $E_F \sim E_2^c \sim 20$  meV above the bulk conduction band edge of the oblique valleys. According to the theoretical calculation in the massive Dirac fermion model, the ground cyclotron resonance CR-O of this sample exists because the level  $1^c$  of the oblique valleys is depopulated from  $B \sim 6$  T, but this transition is masked in the reststrahlen band. The intraband transition  $1^c - 2^c$  (sky blue arrows) below the reststrahlen band can then occur below  $B \sim 6$  T down to  $B \sim 3$  T. The same scenario occurs in the bulk longitudinal valley, exhibiting  $E_F \sim 24$  meV above the bulk conduction band edge. This indicates that, in our sample  $\text{Pb}_{0.95}\text{Sn}_{0.05}\text{Se}$ , the bulk longitudinal and oblique conduction band edges are situated at about the same energy from the zero energy taken at the mid gap. This agrees well with the electronic band structure calculation of (111)  $\text{Pb}_{0.64}\text{Sn}_{0.36}\text{Se}$  <sup>12</sup> (Fig. 3.20(b)). It is known that one can estimate the carrier mobility from the necessary condition for electrons or holes to create a cyclotron orbit:  $\mu B \geq 1$ . In  $\text{Pb}_{0.95}\text{Sn}_{0.05}\text{Se}$ , we observed transitions down to  $B \sim 0.07$  T, evidencing a carrier mobility  $\mu \geq 140,000$  cm<sup>2</sup>/(V.s) at 4.5 K.

### 3.2. Topological surface states in (111) $\text{Pb}_{1-x}\text{Sn}_x\text{Se}$

The interband and CR transitions occurring in the bulk longitudinal and oblique valleys of the eight (111)  $\text{Pb}_{1-x}\text{Sn}_x\text{Se}$  samples were interpreted using the massive Dirac fermion model as shown in the previous subsection. Besides those transitions, some additional transmission minima cannot be fit with the Dirac LL transitions of massive Dirac fermions. Such minima could be pertaining to the transitions resulting from the TSS. To demonstrate this, we compare two samples  $x = 0.14$  and  $x = 0.19$  with the Sn compositions that are nearly “symmetric” with respect to the critical Sn content  $x_c = 0.16$  of the bulk band crossing in  $\text{Pb}_{1-x}\text{Sn}_x\text{Se}$  measured at 4.5 K. Magneto-spectroscopy was then carried out up to  $B = 17$  T at  $T = 4.5$  K. The ground CR transitions (CR-O and CR-L) and the first interband transition  $1^v - 0^c$  of the bulk valleys can be observed in  $\text{Pb}_{0.86}\text{Sn}_{0.14}\text{Se}$  (Fig. 4.8(a)). In  $\text{Pb}_{0.81}\text{Sn}_{0.19}\text{Se}$  (Fig. 4.8(b)), two transitions can be resolved: the first interband transition  $0^v - 1^c$  of the bulk valleys and the additional transition depicted by blue arrow which is only visible at 15 T and above. The additional transition occurs in topologically nontrivial  $\text{Pb}_{0.81}\text{Sn}_{0.19}\text{Se}$  ( $x > x_c$  with negative band gap) but not in topologically trivial  $\text{Pb}_{0.86}\text{Sn}_{0.14}\text{Se}$  ( $x < x_c$  with positive band gap) <sup>11</sup>.

The LL transitions in the FIR range are represented in Fig. 4.8(c) for  $\text{Pb}_{0.86}\text{Sn}_{0.14}\text{Se}$  and Fig. 4.8(d) for  $\text{Pb}_{0.81}\text{Sn}_{0.19}\text{Se}$ . Supplementary experimental data from 16 to 17 T were extracted from the transmission spectra of  $\text{Pb}_{0.86}\text{Sn}_{0.14}\text{Se}$  (Fig. 4.8(a)) and  $\text{Pb}_{0.81}\text{Sn}_{0.19}\text{Se}$  (Fig. 4.8(b)). The data points were added on the corresponding LL transition fan charts. The ground CR and the first interband transitions of the bulk valleys are marked by bicolor circles (black and red). The additional transmission minima of  $\text{Pb}_{0.81}\text{Sn}_{0.19}\text{Se}$  denoted as blue circles are seen to satisfy a massless Dirac dispersion and could thus be interpreted as the ground CR of the TSS (CR-TSS) of massless Dirac fermions. The additional transition occurs at energies higher than 60 meV where the CR-O and CR-L of the bulk bands are expected. Using the massless Dirac fermion model to calculate the transition energy of the CR-TSS as a function of magnetic field (Eq. 4.17), we obtain the blue solid line as curve fit for the CR-TSS in the  $\bar{\Gamma}$

## CHAPTER 4

### Magneto-optical investigation of TCIs: IV-VI compounds

and  $\bar{M}$  valleys. The Dirac velocity of massless Dirac fermions is  $v_D = (4.7 \pm 0.1) \times 10^5$  m/s, almost equal to that of the bulk valleys ( $(4.8 \pm 0.1) \times 10^5$  m/s for the longitudinal valley and  $(4.6 \pm 0.1) \times 10^5$  m/s for the oblique valleys). This is in good agreement with the theoretical calculation of the band structure of (111)  $\text{Pb}_{0.64}\text{Sn}_{0.36}\text{Se}$ <sup>12</sup> (Fig. 3.20(b)) where we can clearly see that the slope of the  $\bar{\Gamma}$ - and  $\bar{M}$ -Dirac cones is nearly equal to that of the bulk longitudinal and oblique bands.

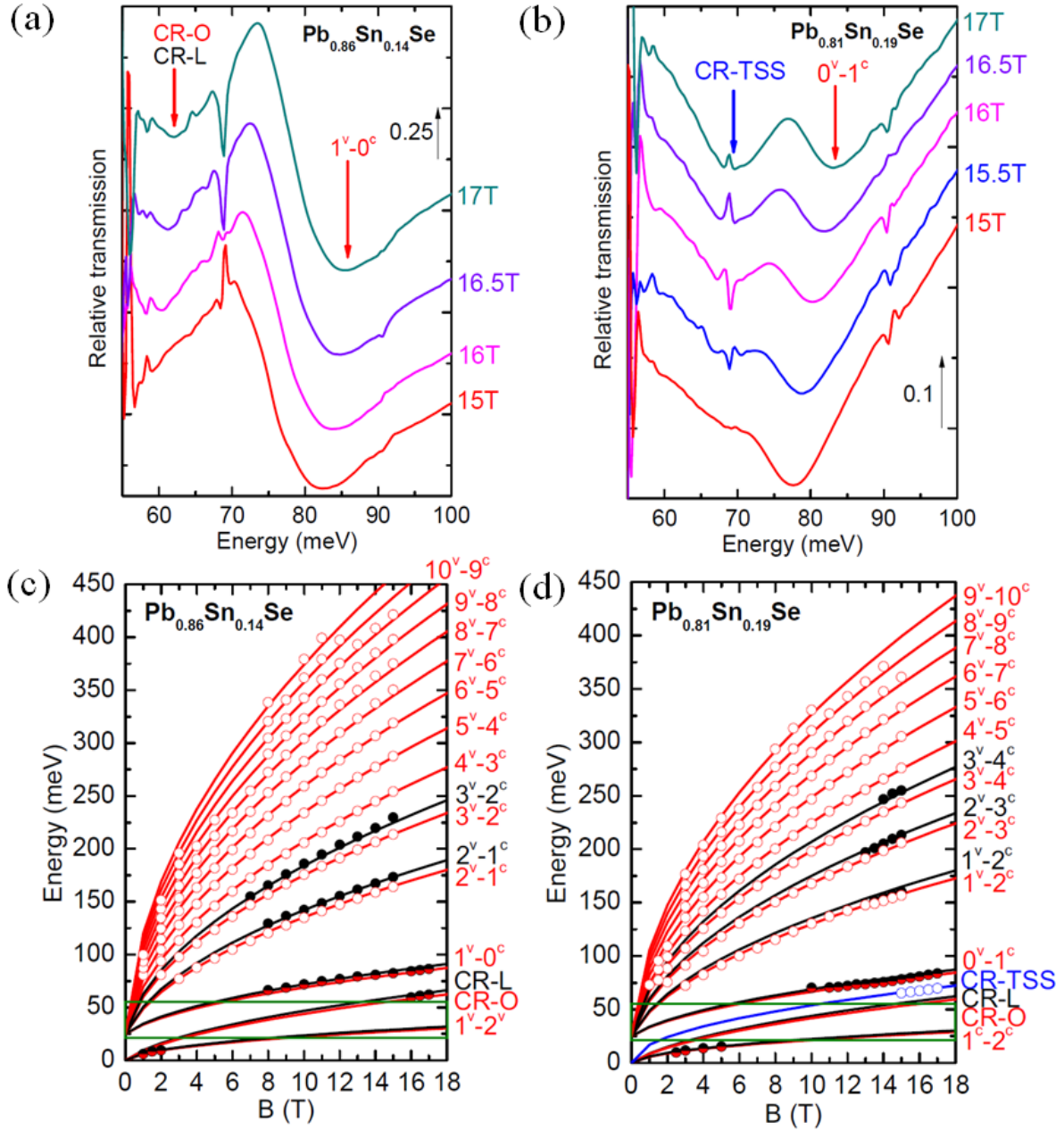


**Figure 4.8. Magneto-optical Landau level spectroscopy of the topological surface states in (111)  $\text{Pb}_{1-x}\text{Sn}_x\text{Se}$ .** FIR magneto-optical transmission spectra measured up to 17 T at 4.5 K of  $\text{Pb}_{0.86}\text{Sn}_{0.14}\text{Se}$  (a) and  $\text{Pb}_{0.81}\text{Sn}_{0.19}\text{Se}$  (b). Red arrows depict the ground CR and the first interband transitions in the bulk valleys. Additional transition associated with the cyclotron resonance of the topological surface states (CR-TSS) of massless Dirac fermions is labeled by blue arrow. Dirac Landau level transition diagrams of  $\text{Pb}_{0.86}\text{Sn}_{0.14}\text{Se}$  (c) and  $\text{Pb}_{0.81}\text{Sn}_{0.19}\text{Se}$  (d) are shown. Data points of the CR-TSS denoted by blue circles were added on (d). Other

circles refer to the bulk longitudinal (black) and oblique (red) transitions. Black and red solid lines are curve fits calculated using the massive Dirac model for the bulk longitudinal and oblique valleys. Blue solid line is the calculated curve fit derived from the massless Dirac model for the CR-TSS. The BaF<sub>2</sub> reststrahlen band is shown by green rectangle. Adapted from our previous work <sup>11</sup>.

We cannot distinguish the transitions of massless Dirac fermions in the  $\bar{\Gamma}$ -Dirac cone from the  $\bar{M}$ -Dirac cones in Pb<sub>0.81</sub>Sn<sub>0.19</sub>Se since they have very similar Dirac velocities and hence their ground CR are overlapping. This might also explain why the intensity of the ground CR transition attributed to the TSS is large, as can be seen in the transmission spectra. Since the CR-TSS can be observed for  $B \geq 15$  T, the Fermi level measured from the Dirac point can be estimated to be around 60 meV for the  $\bar{\Gamma}$ - and  $\bar{M}$ -Dirac cones in Pb<sub>0.81</sub>Sn<sub>0.19</sub>Se.

We also calculated the interband transitions of the TSS and they are found to be nearly located at the energy of the interband transitions of the bulk states. This can be easily understood by considering the square root terms of the interband transition energies in Eq. 4.9 for the bulk states and Eq. 4.15 for the TSS. In narrow gap semiconductors as our samples, for  $N \geq 1$  and  $B > 1$  T, we obtain  $(\Delta^2 + 2v_D^2 \hbar e B N)^{1/2} \approx (2v_D^2 \hbar e B N)^{1/2}$  since  $\Delta^2$  becomes smaller than  $2v_D^2 \hbar e B N$ . Hence, the TSS interband transitions cannot be experimentally resolved from the bulk interband transitions.

Finally, note that we also observed the CR-TSS in all the topologically nontrivial (111) Pb<sub>1-x</sub>Sn<sub>x</sub>Te samples (see the subsection 4.2).

## **4. Magneto-optical Landau level spectroscopy of Dirac fermions in (111) Pb<sub>1-x</sub>Sn<sub>x</sub>Te**

Magneto-optical IR Landau level spectroscopy was performed in twenty (111) Pb<sub>1-x</sub>Sn<sub>x</sub>Te samples ( $0 \leq x \leq 0.56$ ) in the Faraday geometry for  $B = 0-15$  T and  $T = 4.5$  K in the FIR and MIR spectral ranges (4-600 meV). The applied magnetic field was oriented parallel to the [111] direction (the growth axis) and thus perpendicular to the sample surface. The relative transmission spectra of each sample can be obtained from the normalization of the sample transmission at a fixed field  $T(B)$  by the zero-field transmission  $T(0)$  of the sample. The Dirac fermion model as described in the section 1 was used to analyze the experimental results.

### **4.1. Bulk states in (111) Pb<sub>1-x</sub>Sn<sub>x</sub>Te**

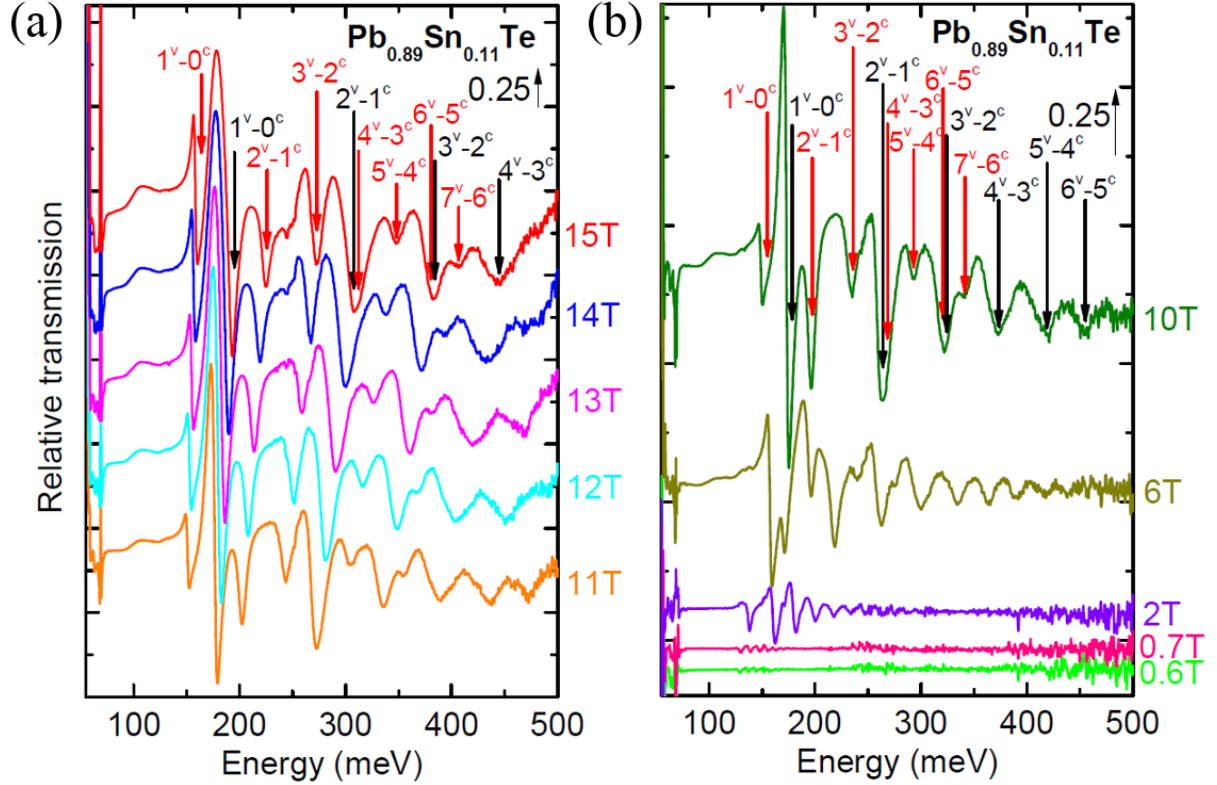
The magneto-optical MIR transmission spectra taken at various magnetic fields of six representative samples are represented in Fig. 4.9(a,b) for  $x = 0.11$ , Fig. 4.9(c,d) for  $x = 0.14$ , Fig. 4.9(e,f) for  $x = 0.25$ , Fig. 4.10(a,b) for  $x = 0.35$ , Fig. 4.10(c,d) for  $x = 0.46$  and Fig. 4.10(e,f) for  $x = 0.56$ . The observed transmission minima dispersing with increasing field correspond to absorptions due to the presence of LL transitions of Dirac fermions. Black and red arrows mark respectively the transitions originating from the bulk longitudinal and



## CHAPTER 4

### *Magneto-optical investigation of TCIs: IV-VI compounds*

oblique valleys. The absorption lines are broadened and their intensity increases when two transitions in both types of valleys occur at about the same energy. For high LL index  $N$  of the transitions, only the transitions from the bulk longitudinal valley are shown. A large number of strong interband transitions were observed down to low fields and low energies in these samples, evidencing the Fermi energy close to the bulk band edge in both types of valleys. The samples possess high mobilities and low carrier densities. The sharpness of the absorption lines assures the high crystalline quality of the films.



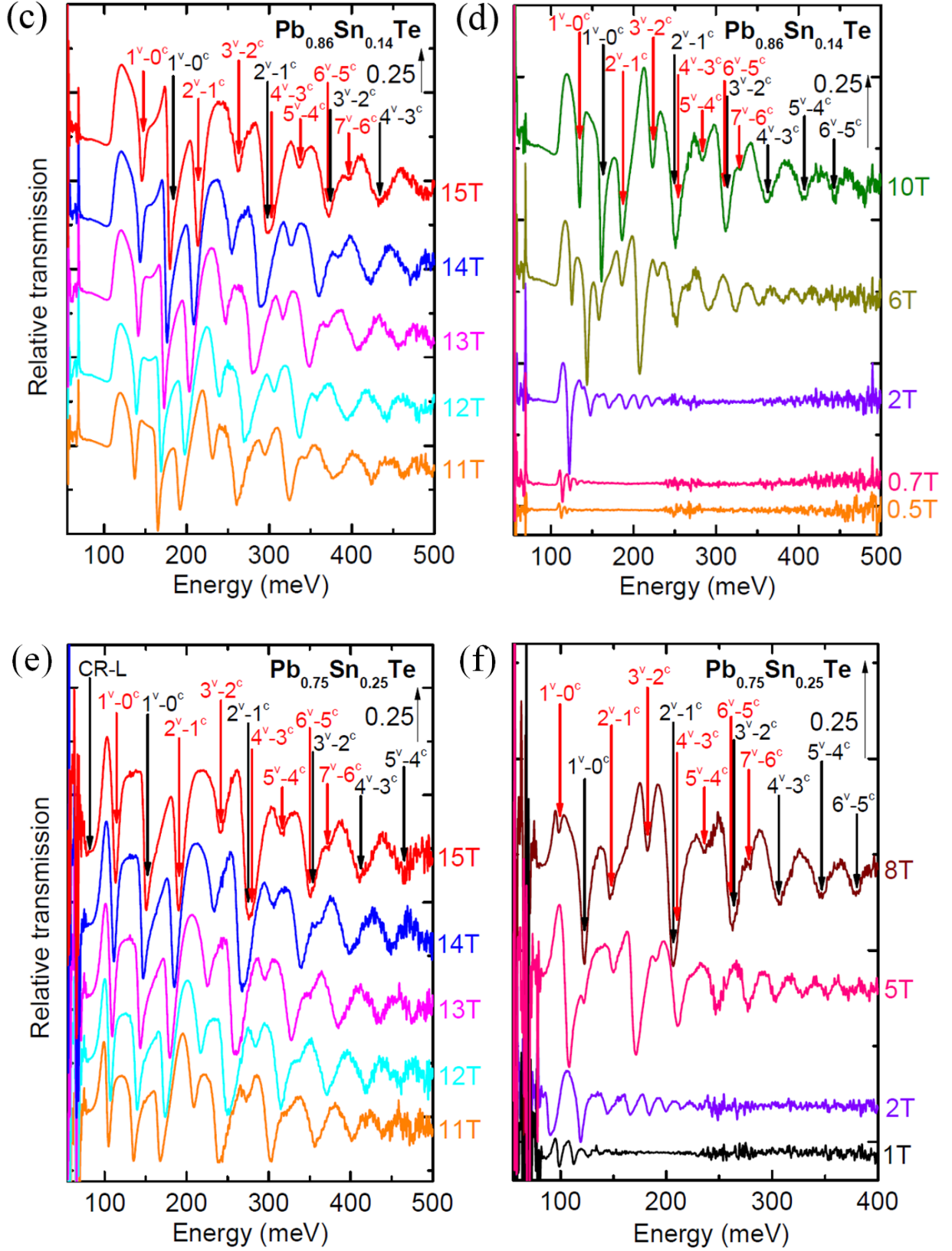
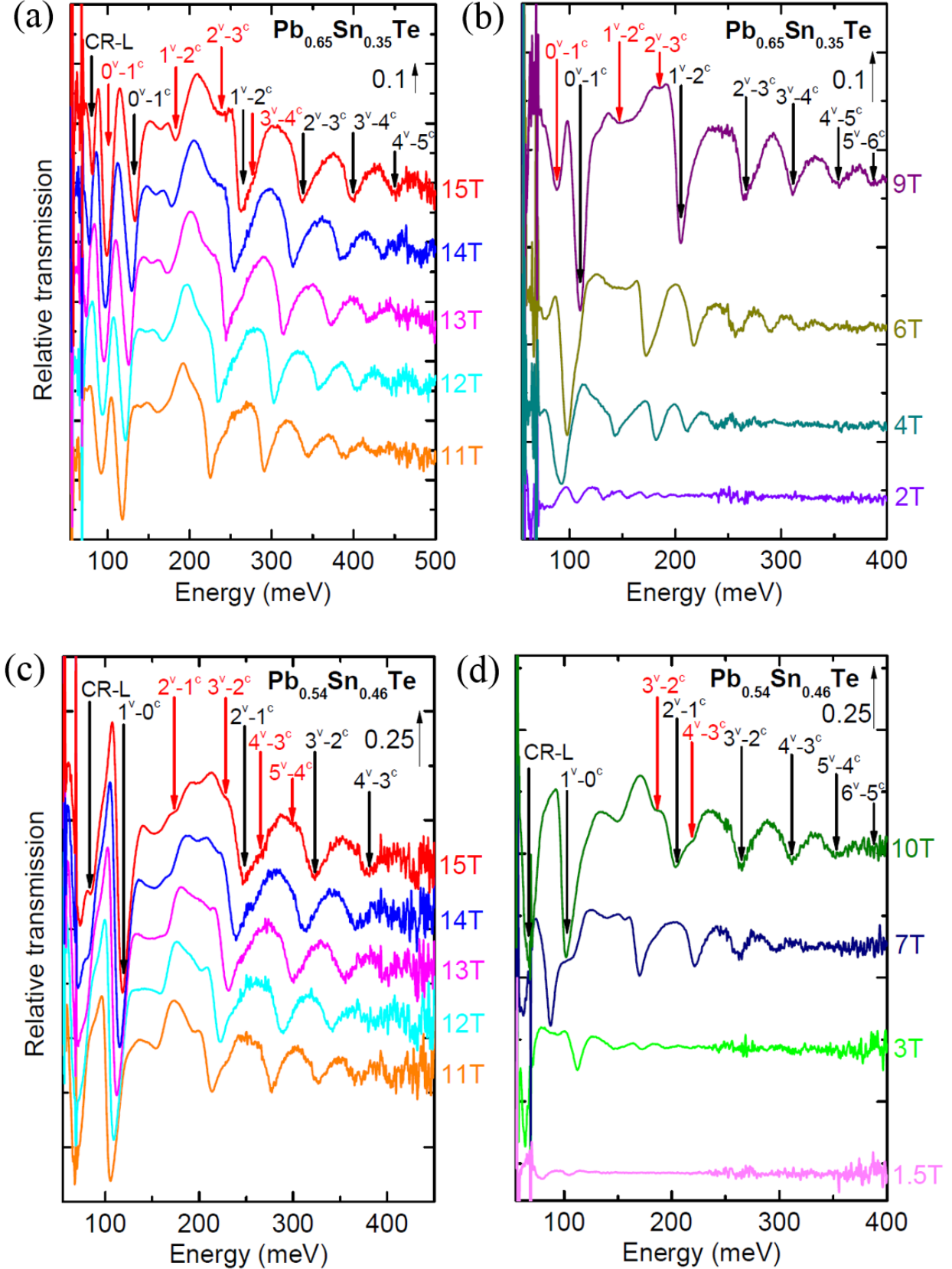


**Figure 4.9. MIR transmission spectra of trivial  $\text{Pb}_{1-x}\text{Sn}_x\text{Te}$ .** MIR magneto-optical transmission spectra of  $\text{Pb}_{1-x}\text{Sn}_x\text{Te}$  measured at 4.5 K for  $x = 0.11$  (a,b),  $x = 0.14$  (c,d) and  $x = 0.25$  (e,f) at different magnetic fields. Black and red arrows depict the transmission minima originating from the transitions in the bulk

## CHAPTER 4

### Magneto-optical investigation of TCIs: IV-VI compounds

longitudinal and oblique valleys, respectively. At high LL index  $N$ , the bulk longitudinal and oblique transitions are mixed and only the longitudinal ones are represented by black arrows. Narrow absorption lines evidence the high crystalline quality of the films. Transitions can be observed down to low fields, indicating the low carrier density and high mobility of the samples. All the spectra are shifted vertically for clarity



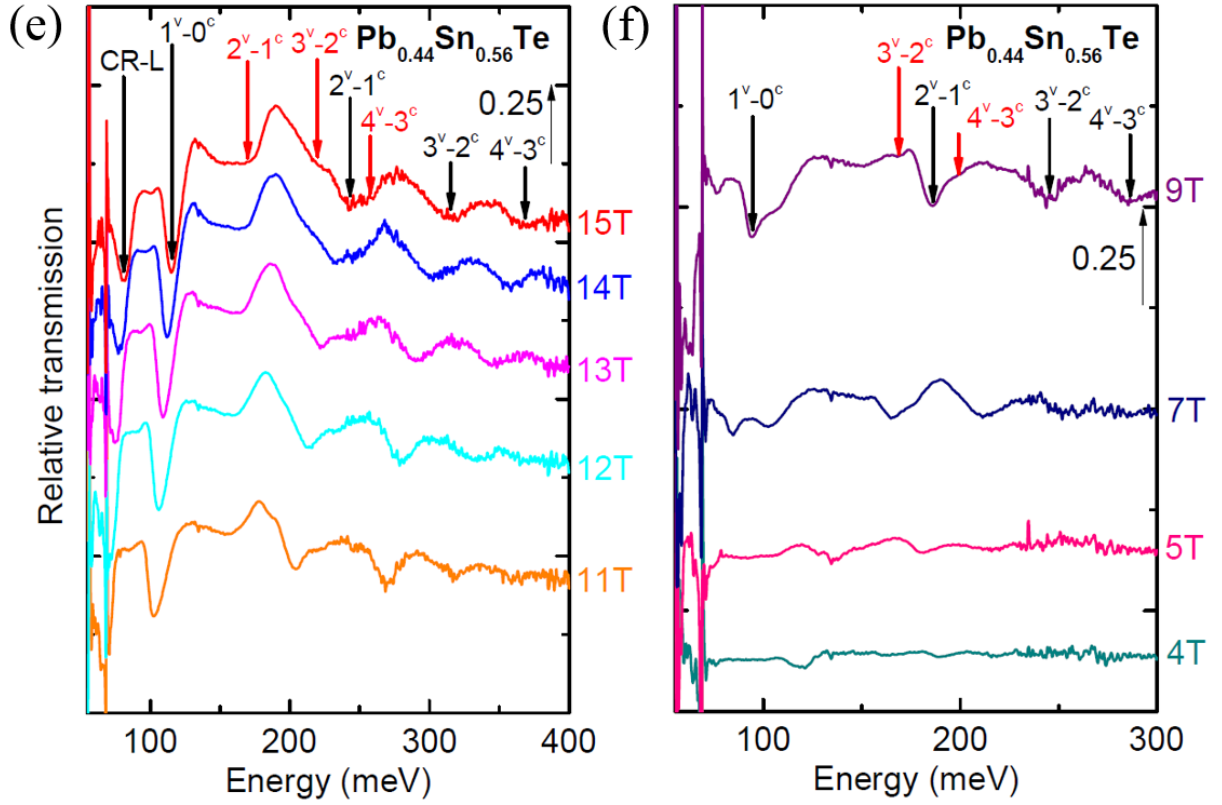


**Figure 4.10. MIR transmission spectra of  $\text{Pb}_{1-x}\text{Sn}_x\text{Te}$  around the topological phase transition.** MIR magneto-optical transmission spectra of  $\text{Pb}_{1-x}\text{Sn}_x\text{Te}$  measured at 4.5 K for  $x = 0.35$  (a,b),  $x = 0.46$  (c,d) and  $x = 0.56$  (e,f) at different magnetic fields. Black and red arrows depict the transmission minima originating from the transitions in the bulk longitudinal and oblique valleys, respectively. At high LL index  $N$ , the bulk longitudinal and oblique transitions are mixed and only the longitudinal ones are represented by black arrows. Narrow absorption lines evidence the high crystalline quality of the films. Transitions can be observed down to low fields, indicating the low carrier density and high mobility of the samples. All the spectra are shifted vertically for clarity.

The eight samples were also examined by magneto-optical spectroscopy in the FIR range. Here, we will show the typical FIR transmission spectra measured at several magnetic fields of  $\text{Pb}_{0.89}\text{Sn}_{0.11}\text{Te}$  (Fig. 4.11(a)),  $\text{Pb}_{0.86}\text{Sn}_{0.14}\text{Te}$  (Fig. 4.11(b)),  $\text{Pb}_{0.65}\text{Sn}_{0.35}\text{Te}$  (Fig. 4.11(c)) and  $\text{Pb}_{0.54}\text{Sn}_{0.46}\text{Te}$  (Fig. 4.11(d)). In spite of the  $\text{BaF}_2$  substrate reststrahlen band between 22 and 55 meV, the ground CR and intraband transitions in high-mobility samples were observed at low fields below the reststrahlen band.

## CHAPTER 4

### Magneto-optical investigation of TCIs: IV-VI compounds

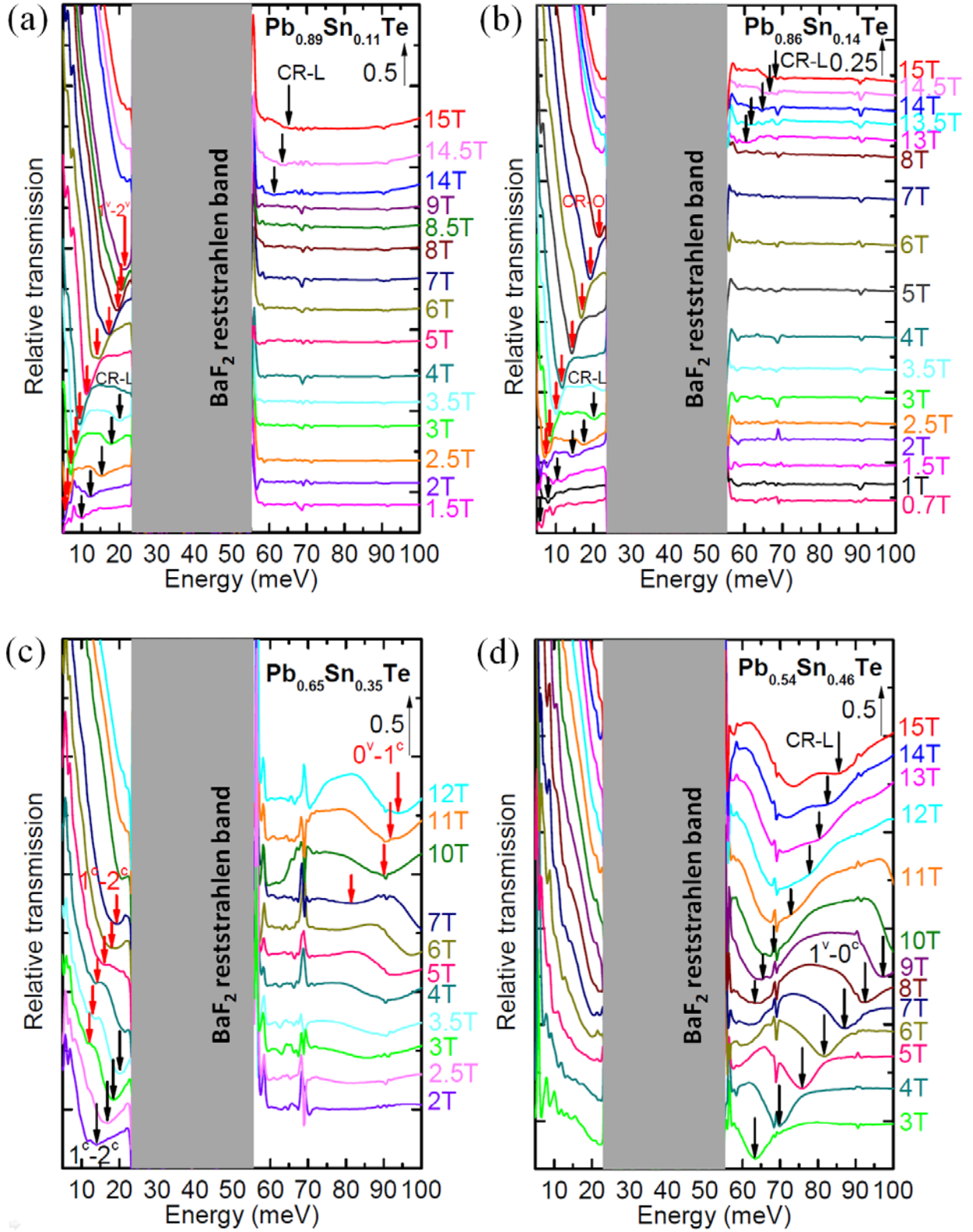


**Figure 4.11. FIR transmission spectra of  $\text{Pb}_{1-x}\text{Sn}_x\text{Te}$ .** FIR magneto-optical transmission spectra of  $\text{Pb}_{1-x}\text{Sn}_x\text{Te}$  measured at 4.5 K for  $x = 0.11$  (a),  $x = 0.14$  (b),  $x = 0.35$  (c) and  $x = 0.46$  (d). The ground state CR, intraband and interband transitions associated with the bulk valleys are shown by black (longitudinal valley) and

## CHAPTER 4

### Magneto-optical investigation of TCIs: IV-VI compounds

red (oblique valleys) arrows. The reststrahlen band of the BaF<sub>2</sub> substrate is from 22 to 55 meV. All the curves are shifted vertically for clarity.

To construct LL transition fan charts, experimental transmission minima were then plotted as a function of magnetic field in Fig. 4.12(a) for  $x = 0.11$ , Fig. 4.12(b) for  $x = 0.14$ , Fig. 4.12(c) for  $x = 0.25$ , Fig. 4.12(d) for  $x = 0.35$ , Fig. 4.12(e) for  $x = 0.46$  and Fig. 4.12(f) for  $x = 0.56$ . Full black circles and empty red circles are used respectively for the absorption minima originating from the bulk longitudinal and oblique transitions. The green rectangle represents the reststrahlen band of the BaF<sub>2</sub> substrate (22-55 meV) which limits our observation. Similar analysis using the massive Dirac fermion model was carried out in these representative samples as in Pb<sub>1-x</sub>Sn<sub>x</sub>Se films seen in the subsection 3.1. The black and red solid lines are the transition energies calculated using Eq. 4.9 for interband transitions, Eq. 4.10 for intraband transitions and Eq. 4.11 for the ground CR for the bulk longitudinal and oblique valleys, respectively. We used the same notation as in the case of Pb<sub>1-x</sub>Sn<sub>x</sub>Se for intraband and interband transitions. Again, an excellent agreement theory/experiment is obtained in these representative Pb<sub>1-x</sub>Sn<sub>x</sub>Te films. Magneto-optical band parameters ( $|\Delta|$  and  $v_D$ ) of these twenty Pb<sub>1-x</sub>Sn<sub>x</sub>Te samples precisely extracted from the massive Dirac model are represented in Table 4.3. The Dirac transverse band edge mass of each valley can then be deduced from those two principle parameters:  $m^* = |\Delta|/v_D^2$ .

Composition Pb <sub>1-x</sub> Sn <sub>x</sub> Te	$2 \Delta $ (meV)	$v_D$ (long.) ( $\times 10^5$ m/s)	$v_D$ (obl.) ( $\times 10^5$ m/s)	$m^*$ (long.) ( $\times m_0$ )	$m^*$ (obl.) ( $\times m_0$ )
PbTe	$190 \pm 5$	$9.0 \pm 0.2$	$6.0 \pm 0.1$	$0.021 \pm 0.001$	$0.046 \pm 0.002$
Pb <sub>0.92</sub> Sn <sub>0.08</sub> Te	$145 \pm 5$	$8.3 \pm 0.1$	$5.6 \pm 0.1$	$0.019 \pm 0.001$	$0.041 \pm 0.002$
Pb <sub>0.89</sub> Sn <sub>0.11</sub> Te	$125 \pm 5$	$8.15 \pm 0.10$	$5.4 \pm 0.1$	$0.017 \pm 0.001$	$0.038 \pm 0.002$
Pb <sub>0.86</sub> Sn <sub>0.14</sub> Te	$110 \pm 5$	$8.0 \pm 0.1$	$5.3 \pm 0.1$	$0.015 \pm 0.001$	$0.034 \pm 0.002$
Pb <sub>0.85</sub> Sn <sub>0.15</sub> Te	$105 \pm 5$	$8.0 \pm 0.1$	$5.3 \pm 0.1$	$0.014 \pm 0.001$	$0.033 \pm 0.002$
Pb <sub>0.80</sub> Sn <sub>0.20</sub> Te	$90 \pm 5$	$8.0 \pm 0.1$	$5.3 \pm 0.1$	$0.012 \pm 0.001$	$0.028 \pm 0.002$
Pb <sub>0.75</sub> Sn <sub>0.25</sub> Te	$70 \pm 5$	$7.75 \pm 0.10$	$5.15 \pm 0.10$	$0.010 \pm 0.001$	$0.023 \pm 0.002$
Pb <sub>0.72</sub> Sn <sub>0.28</sub> Te	$62.5 \pm 7.5$	$7.65 \pm 0.10$	$5.15 \pm 0.10$	$0.009 \pm 0.001$	$0.021 \pm 0.003$
Pb <sub>0.69</sub> Sn <sub>0.31</sub> Te	$55 \pm 5$	$7.6 \pm 0.1$	$5.15 \pm 0.10$	$0.008 \pm 0.001$	$0.018 \pm 0.002$
Pb <sub>0.66</sub> Sn <sub>0.34</sub> Te	$55 \pm 5$	$7.575 \pm 0.075$	$5.1 \pm 0.1$	$0.008 \pm 0.001$	$0.019 \pm 0.002$
Pb <sub>0.65</sub> Sn <sub>0.35</sub> Te	$50 \pm 10$	$7.55 \pm 0.10$	$5.2 \pm 0.1$	$0.008 \pm 0.002$	$0.016 \pm 0.003$
Pb <sub>0.63</sub> Sn <sub>0.37</sub> Te	$45 \pm 15$	$7.5 \pm 0.1$	$5.2 \pm 0.1$	$0.007 \pm 0.002$	$0.015 \pm 0.005$
Pb <sub>0.60</sub> Sn <sub>0.40</sub> Te	$50 \pm 10$	$7.4 \pm 0.1$	$5.2 \pm 0.1$	$0.008 \pm 0.002$	$0.016 \pm 0.003$
Pb <sub>0.59</sub> Sn <sub>0.41</sub> Te	$50 \pm 10$	$7.4 \pm 0.1$	$5.2 \pm 0.1$	$0.008 \pm 0.002$	$0.016 \pm 0.003$
Pb <sub>0.56</sub> Sn <sub>0.44</sub> Te	$40 \pm 5$	$7.3 \pm 0.1$	$5.1 \pm 0.1$	$0.007 \pm 0.001$	$0.014 \pm 0.002$
Pb <sub>0.55</sub> Sn <sub>0.45</sub> Te	$40 \pm 5$	$7.3 \pm 0.1$	$5.1 \pm 0.1$	$0.007 \pm 0.001$	$0.014 \pm 0.002$
Pb <sub>0.54</sub> Sn <sub>0.46</sub> Te	$30 \pm 5$	$7.3 \pm 0.1$	$5.0 \pm 0.1$	$0.005 \pm 0.001$	$0.011 \pm 0.002$
Pb <sub>0.50</sub> Sn <sub>0.50</sub> Te	$35 \pm 5$	$7.1 \pm 0.1$	$4.9 \pm 0.1$	$0.006 \pm 0.001$	$0.013 \pm 0.002$
Pb <sub>0.49</sub> Sn <sub>0.51</sub> Te	$35 \pm 5$	$7.2 \pm 0.1$	$5.05 \pm 0.10$	$0.006 \pm 0.001$	$0.012 \pm 0.002$
Pb <sub>0.44</sub> Sn <sub>0.56</sub> Te	$30 \pm 10$	$7.1 \pm 0.1$	$4.9 \pm 0.1$	$0.005 \pm 0.002$	$0.011 \pm 0.004$

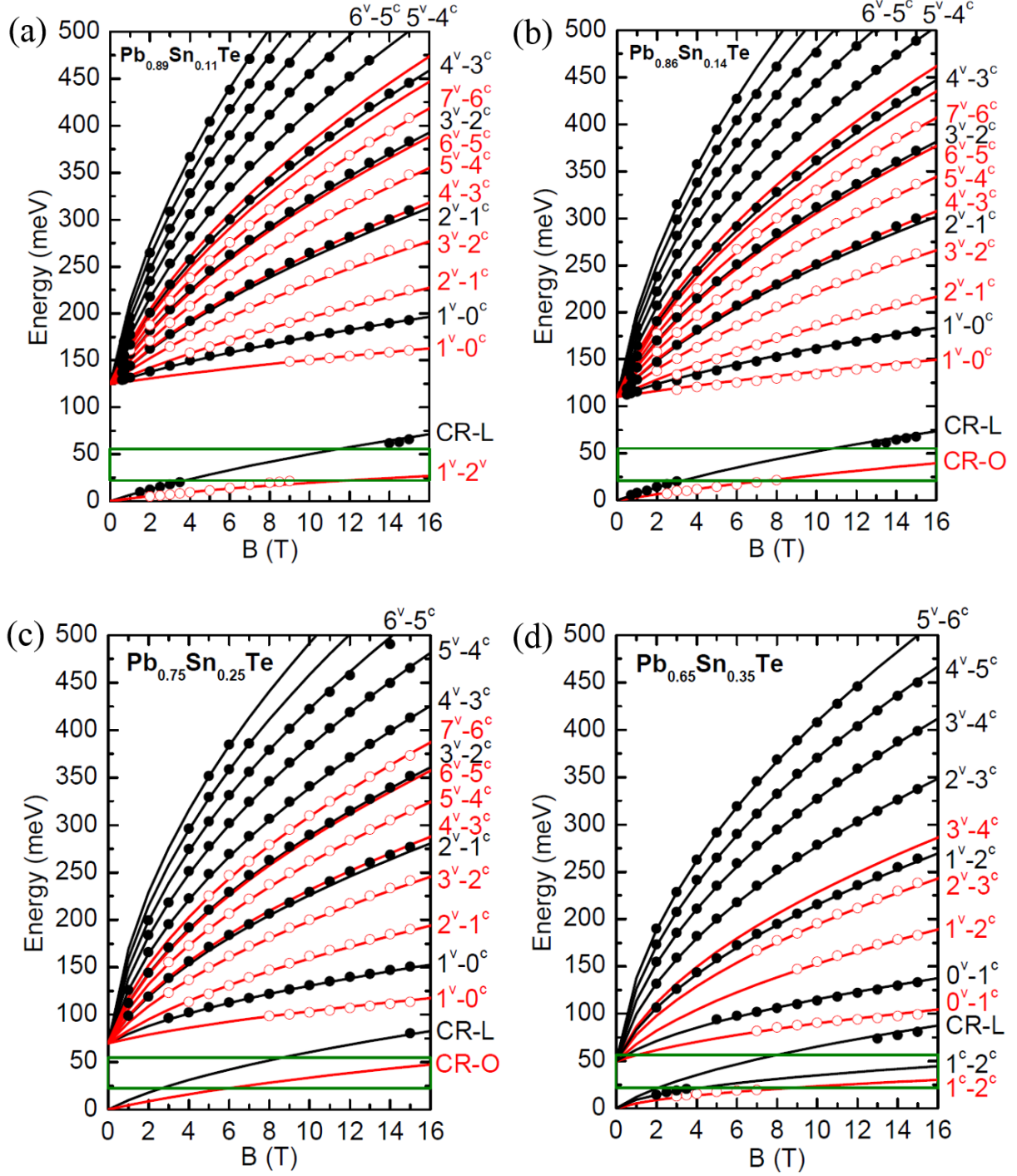
Table 4.3. Magneto-optical band parameters determined from the massive Dirac model analysis in twenty (111) Pb<sub>1-x</sub>Sn<sub>x</sub>Te samples measured at  $T = 4.5$  K.  $2|\Delta|$  is the energy gap. The Dirac velocities  $v_D$  in



## CHAPTER 4

### Magneto-optical investigation of TCIs: IV-VI compounds

the longitudinal and oblique valleys are represented for each composition. The band edge masses are deduced from the previous two parameters  $m^* = |\Delta|/v_D^2$  for both types of valleys.  $m_0$  is the electron rest mass.



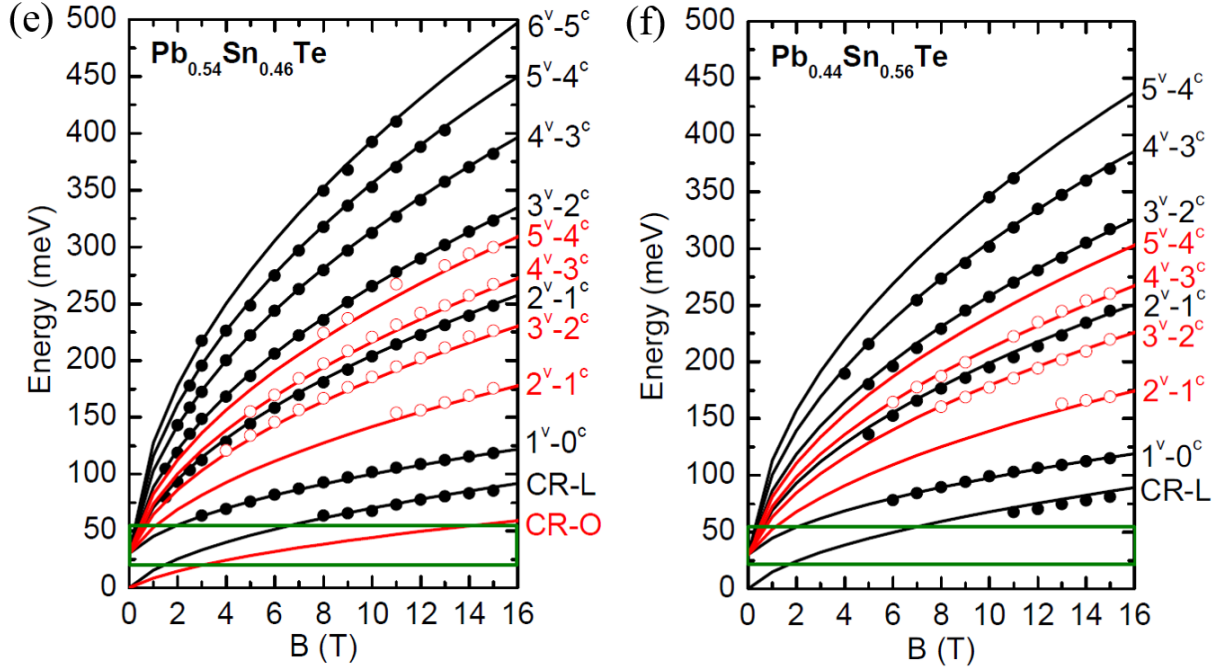


**Figure 4.12. Landau level transition fan charts of (111)  $\text{Pb}_{1-x}\text{Sn}_x\text{Te}$ .** Landau level transition fan charts of (111)  $\text{Pb}_{1-x}\text{Sn}_x\text{Te}$  for  $x = 0.11$  (a),  $x = 0.14$  (b),  $x = 0.25$  (c),  $x = 0.35$  (d),  $x = 0.46$  (e) and  $x = 0.56$  (f). Full black and empty red circles mark respectively the transitions in the bulk longitudinal and oblique valleys. The  $\text{BaF}_2$  substrate reststrahlen band between 22 and 55 meV is represented by green rectangle. The experimental results were analyzed using the massive Dirac model. Black and red curve fits were calculated for the transition energies in the longitudinal and oblique bulk valleys.

The energy gap takes the same value for both types of valleys. The Dirac velocity decreases as  $x$  increases in both types of bulk valleys, as discussed in the sections 5 and 7. The Dirac velocity of the bulk states in the longitudinal valley is larger than that in the oblique valleys as seen previously in (111)  $\text{Pb}_{1-x}\text{Sn}_x\text{Se}$  system, but the ratio of the longitudinal and oblique Dirac velocities of (111)  $\text{Pb}_{1-x}\text{Sn}_x\text{Te}$  is always large through the Sn composition range. This can be explained by the fact that the valley anisotropy in  $\text{Pb}_{1-x}\text{Sn}_x\text{Te}$  is higher than that in  $\text{Pb}_{1-x}\text{Sn}_x\text{Se}$ . This topic will be further clarified in the section 7.

The Fermi energy  $E_F$  in the bulk band edge of  $\text{Pb}_{1-x}\text{Sn}_x\text{Te}$  can be estimated as presented previously for  $\text{Pb}_{1-x}\text{Sn}_x\text{Se}$ . For example, in p-type  $\text{Pb}_{0.54}\text{Sn}_{0.46}\text{Te}$  (Fig. 4.12(e)), the interband transitions  $1^v - 0^c$  and  $2^v - 1^c$  of the longitudinal bulk valley were respectively observed down to  $B \sim 3$  T and  $B \sim 1.5$  T, indicating  $E_F \sim 35$  meV below the valence band edge of the longitudinal valley. In the oblique bulk valleys, the interband transitions  $3^v - 2^c$  and  $4^v - 3^c$  were measured down to  $B \sim 4$  T and  $B \sim 3$  T, we thus get  $E_F \sim 50$  meV below the bulk valence band edge of the oblique valleys. Note that it is not surprising that the Fermi energy in the valence band edge in both types of valleys is slightly different. Since the system of  $\text{Pb}_{1-x}\text{Sn}_x\text{Te}$  grown on  $\text{BaF}_2(111)$  substrate has been reported to exhibit a mismatch at low temperatures due to a strong thermal expansion, therefore the bulk oblique bands could be shifted up in energy with respect to the longitudinal bands<sup>14-16</sup>. In  $\text{Pb}_{0.54}\text{Sn}_{0.46}\text{Se}$ , we



## CHAPTER 4

### *Magneto-optical investigation of TCIs: IV-VI compounds*

---

observed transitions down to  $B \sim 1.5$  T, evidencing a carrier mobility  $\mu \geq 6,500$  cm<sup>2</sup>/(V.s) at 4.5 K.

#### 4.2. Topological surface states in (111) Pb<sub>1-x</sub>Sn<sub>x</sub>Te

To study the TSS in (111) Pb<sub>1-x</sub>Sn<sub>x</sub>Te, we applied the same analysis as used for (111) Pb<sub>1-x</sub>Sn<sub>x</sub>Se to interpret additional transmission minima that seem to evade the expected physics of the carriers in the bulk longitudinal and oblique valleys. Here, we show two couples of samples that possess nearly “*symmetric*” Sn contents with respect to the critical concentration  $x_c \sim 0.4$  of the bulk band inversion in Pb<sub>1-x</sub>Sn<sub>x</sub>Te measured at 4.5 K:  $x = 0.35$  and  $x = 0.46$ , and  $x = 0.25$  and  $x = 0.56$ . Fig. 4.13 and Fig. 4.14 show a zoomed in view of the transmission spectra measured at 4.5 K and at high magnetic fields  $B = 11 - 15$  T of Pb<sub>0.65</sub>Sn<sub>0.35</sub>Te (Fig. 4.13(a)), Pb<sub>0.54</sub>Sn<sub>0.46</sub>Te (Fig. 4.13(b)), Pb<sub>0.75</sub>Sn<sub>0.25</sub>Te (Fig. 4.14(a)) and Pb<sub>0.44</sub>Sn<sub>0.56</sub>Te (Fig. 4.14(b)) in the spectral range 55 - 150 meV. The ground CR transition in the bulk longitudinal valley (CR-L) and the first interband transitions of the bulk valleys can be observed in these four samples. We observed the additional transition indicated by blue arrows that occurs between the CR-L and the first interband transition. This transition is only measured in nontrivial Pb<sub>0.54</sub>Sn<sub>0.46</sub>Te and Pb<sub>0.44</sub>Sn<sub>0.56</sub>Te samples ( $x > x_c$  with negative band gap), but not in trivial Pb<sub>0.75</sub>Sn<sub>0.25</sub>Te and Pb<sub>0.65</sub>Sn<sub>0.35</sub>Te samples ( $x < x_c$  with positive band gap). We have shown the magneto-optical results of (111) Pb<sub>0.54</sub>Sn<sub>0.46</sub>Te and (111) Pb<sub>0.44</sub>Sn<sub>0.56</sub>Te in our works <sup>10,17</sup>.

We added the additional minima as represented by blue circles on the LL transition fan charts of Pb<sub>0.54</sub>Sn<sub>0.46</sub>Te (Fig. 4.13(d)) and Pb<sub>0.44</sub>Sn<sub>0.56</sub>Te (Fig. 4.14(d)). Using the massless Dirac model (Eq. 4.17), the additional transmission minima observed in Pb<sub>0.54</sub>Sn<sub>0.46</sub>Te and Pb<sub>0.44</sub>Sn<sub>0.56</sub>Te could be interpreted as the ground CR-TSS of massless Dirac fermions. The blue solid lines are the calculated CR-TSS using the same Dirac velocity as in the bulk longitudinal valley:  $v_D = (7.3 \pm 0.1) \times 10^5$  m/s for Pb<sub>0.54</sub>Sn<sub>0.46</sub>Te and  $v_D = (7.1 \pm 0.1) \times 10^5$  m/s for Pb<sub>0.44</sub>Sn<sub>0.56</sub>Te. As the Dirac velocities of the longitudinal bulk states and the TSS are equivalent, the observed CR-TSS could thus be associated with the massless Dirac fermions in the  $\bar{\Gamma}$  valley, in good agreement with theoretical calculations shown in Fig. 3.18(c,d) <sup>13</sup>. Since the CR-TSS transition was observed down to  $\sim 11$  T in Pb<sub>0.54</sub>Sn<sub>0.46</sub>Te and  $\sim 9$  T in Pb<sub>0.44</sub>Sn<sub>0.56</sub>Te, the Fermi energy measured from the Dirac point is estimated to be  $E_F \sim 85$  meV and  $E_F \sim 75$  meV in the  $\bar{\Gamma}$ -Dirac cone, respectively. Note that the interband transitions of the TSS cannot be experimentally resolved since they are nearly located at the energy of the bulk interband transitions.

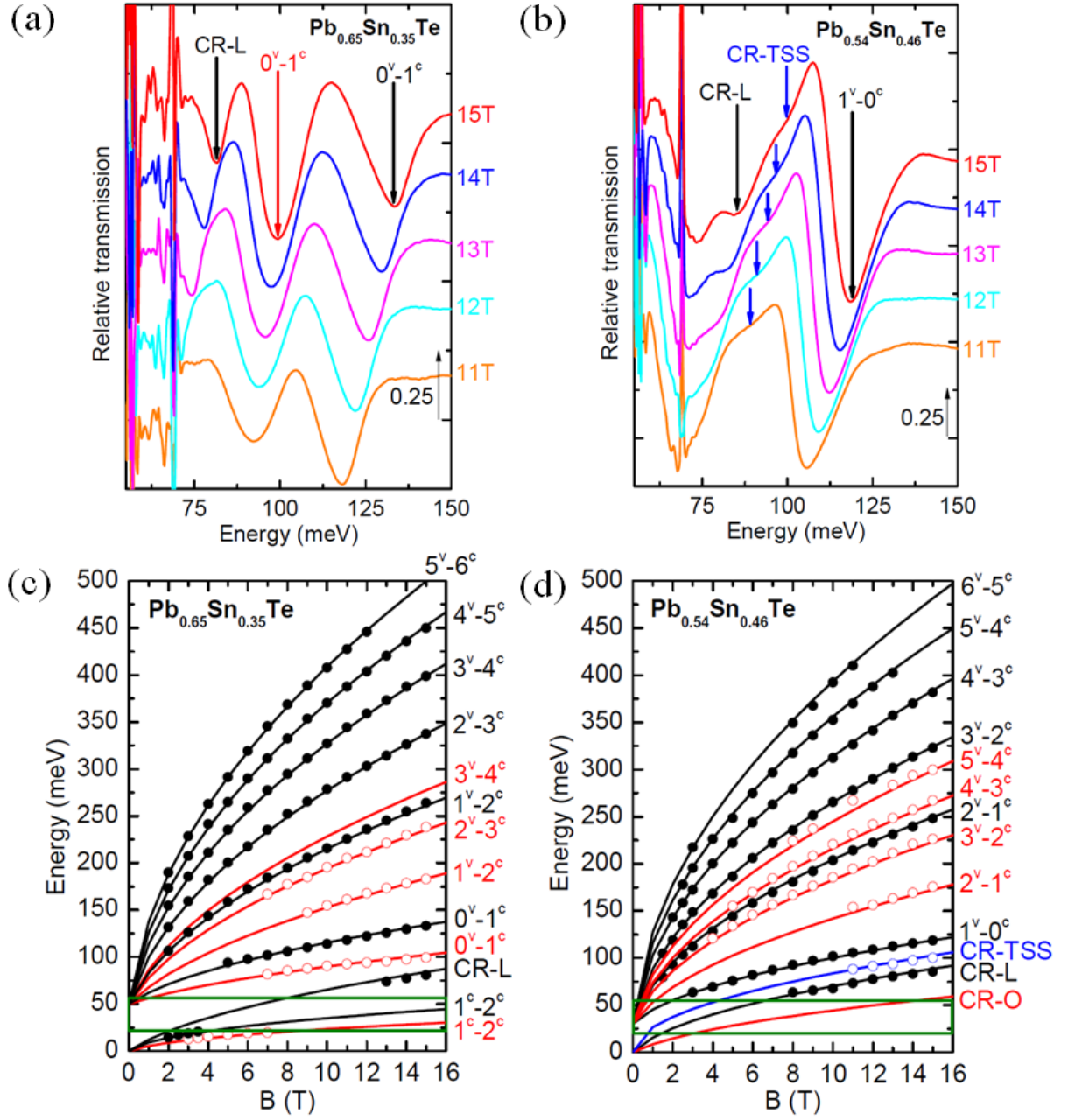


**Figure 4.13. Magneto-optical Landau level spectroscopy of the topological surface states in (111)  $\text{Pb}_{1-x}\text{Sn}_x\text{Te}$ .** A zoomed in view of the magneto-optical transmission spectra measured between 11 and 15 T at 4.5 K of  $\text{Pb}_{0.65}\text{Sn}_{0.35}\text{Te}$  (a) and  $\text{Pb}_{0.54}\text{Sn}_{0.46}\text{Te}$  (b). The ground CR and the first interband transitions in the bulk valleys are depicted by black (for the longitudinal valley) or red (for the oblique valleys) arrows. Additional transition associated with the ground cyclotron resonance of the topological surface states (CR-TSS) of massless Dirac fermions is labeled by blue arrow. Dirac Landau level transition diagrams of  $\text{Pb}_{0.65}\text{Sn}_{0.35}\text{Te}$  (c) and  $\text{Pb}_{0.54}\text{Sn}_{0.46}\text{Te}$  (d) are shown. Data points of the CR-TSS denoted by blue circles were added on (d). Other circles refer to the bulk longitudinal (black) and oblique (red) transitions. Black and red solid lines are curve fits calculated using the massive Dirac model for the bulk longitudinal and oblique valleys. Blue solid line is the calculated curve fit derived from the massless Dirac model for the CR-TSS. The  $\text{BaF}_2$  reststrahlen band is shown by green rectangle. (b) and (d) is adapted from our paper <sup>10</sup>.

## CHAPTER 4

### Magneto-optical investigation of TCIs: IV-VI compounds

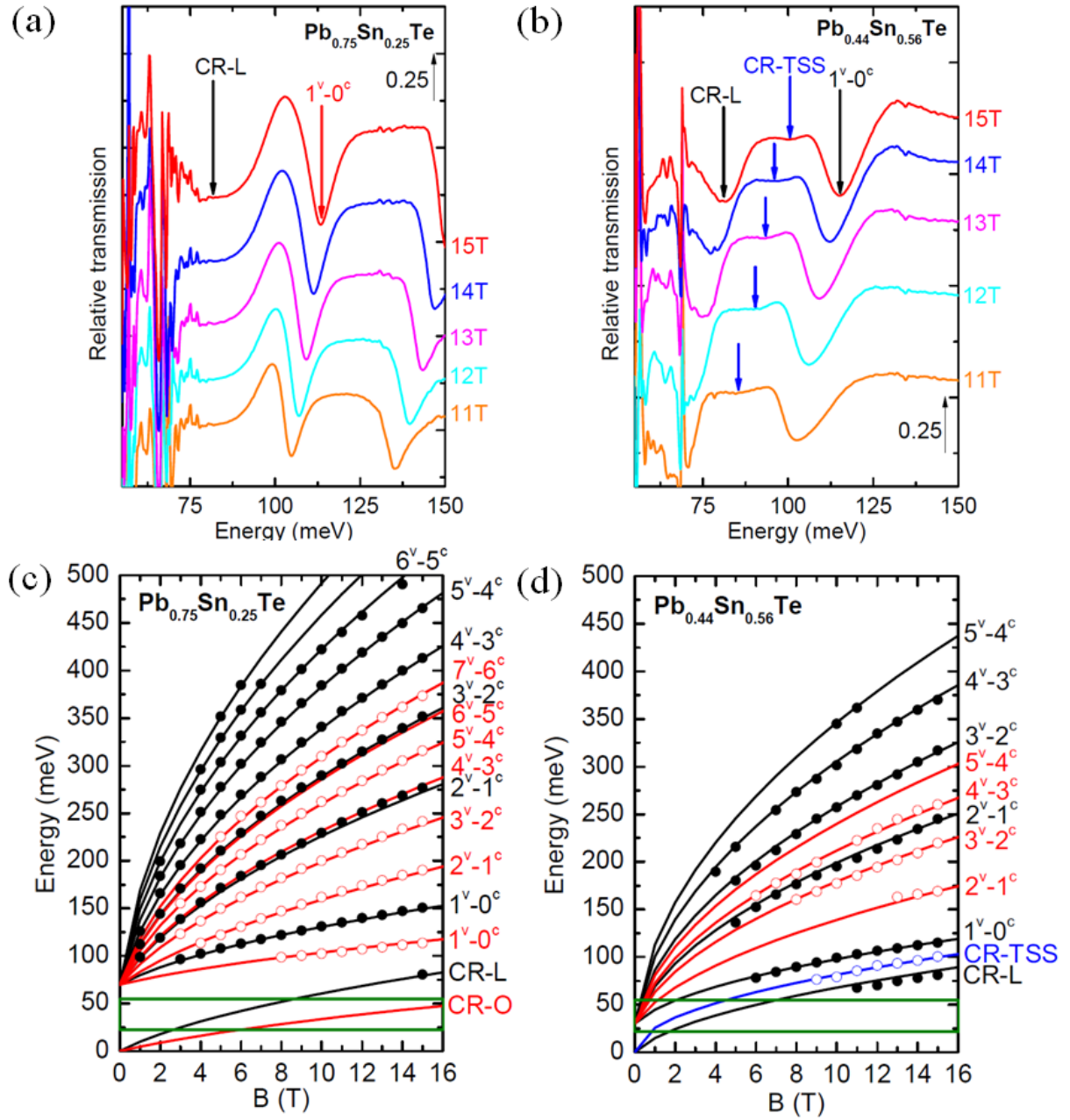


**Figure 4.14. Magneto-optical Landau level spectroscopy of the topological surface states in (111)  $\text{Pb}_{1-x}\text{Sn}_x\text{Te}$ .** A zoomed view of the magneto-optical transmission spectra measured between 11 and 15 T at 4.5 K of  $\text{Pb}_{0.75}\text{Sn}_{0.25}\text{Te}$  (a) and  $\text{Pb}_{0.44}\text{Sn}_{0.56}\text{Te}$  (b). The ground CR and the first interband transitions in the bulk longitudinal valley are depicted by black arrows. Additional transition associated with the ground cyclotron resonance of the topological surface states (CR-TSS) of massless Dirac fermions is labeled by blue arrow. Dirac Landau level transition diagrams of  $\text{Pb}_{0.75}\text{Sn}_{0.25}\text{Te}$  (c) and  $\text{Pb}_{0.44}\text{Sn}_{0.56}\text{Te}$  (d) are shown. Data points of the CR-TSS denoted by blue circles were added on (d). Other circles refer to the bulk longitudinal (black) and oblique (red) transitions. Black and red solid lines are curve fits calculated using the massive Dirac model for the bulk longitudinal and oblique valleys. Blue solid line is the calculated curve fit derived from the massless Dirac model for the CR-TSS. The  $\text{BaF}_2$  reststrahlen band is shown by green rectangle. (b) and (d) is adapted from <sup>17</sup>.

In this analysis, we did not observe any LL transition pertaining to the TSS in the  $\bar{M}$  valleys in  $\text{Pb}_{0.54}\text{Sn}_{0.46}\text{Te}$  and  $\text{Pb}_{0.44}\text{Sn}_{0.56}\text{Te}$ . This might be due to the fact that the Dirac velocity of the massless Dirac fermions in the  $\bar{M}$ -Dirac cones is almost equal to that of the oblique bulk bands. As a consequence, the interband transitions of the TSS in the  $\bar{M}$  valleys and those of the bulk states in the oblique valleys are overlapping. Moreover, the search for the ground CR-TSS transition of the  $\bar{M}$ -Dirac cones is not that easy since it lies within the  $\text{BaF}_2$  reststrahlen band. If we consider the fact that the bulk oblique bands of p-type  $\text{Pb}_{0.54}\text{Sn}_{0.46}\text{Te}$  and  $\text{Pb}_{0.44}\text{Sn}_{0.56}\text{Te}$  samples are shifted up in energy due to the thermal expansion mismatch at low temperatures, the Fermi energy in the  $\bar{M}$ -Dirac cones seems to be located at the energy higher than that estimated from the Dirac point of the  $\bar{\Gamma}$ -Dirac cone. Therefore, further experiments up to high magnetic fields ( $B > 20$  T) should be carried out in order to find out the CR-TSS related-feature of the  $\bar{M}$ -points.

The magneto-optical determination of the Dirac velocity in the oblique valleys of (111)  $\text{Pb}_{1-x}\text{Sn}_x\text{Te}$  is not precise as in the case of (111)  $\text{Pb}_{1-x}\text{Sn}_x\text{Se}$  where the oblique bands are nearly isotropic (Fig. 3.20(b)). The high anisotropy of the oblique bands found in (111)  $\text{Pb}_{1-x}\text{Sn}_x\text{Te}$  results in different Dirac velocities in different directions along the high-symmetry line cuts  $\bar{K}-\bar{\Gamma}-\bar{M}-\bar{K}$  of the 2DBZ (Fig. 3.18(c,d)). Our experimental value of the oblique  $v_D$  is actually an effective result derived from  $v_D(\text{obl.}) = \sqrt{v_{\bar{M}-\bar{K}}v_{\bar{M}-\bar{\Gamma}}}$ , where  $v_{\bar{M}-\bar{K}}$  and  $v_{\bar{M}-\bar{\Gamma}}$  denote respectively the Dirac velocities along the  $\bar{M}-\bar{K}$  and  $\bar{M}-\bar{\Gamma}$  directions. The Dirac velocity for the  $\bar{M}$ -Dirac cones is also an effective value.  $v_{\bar{M}-\bar{K}}$  is expected to be almost equal to the Dirac velocity measured in the longitudinal valley. We can thus extract  $v_{\bar{M}-\bar{\Gamma}}$ , for example in (111)  $\text{Pb}_{0.54}\text{Sn}_{0.46}\text{Te}$ , that is given by  $v_{\bar{M}-\bar{\Gamma}} \sim (3.4 \pm 0.2) \times 10^5$  m/s.

## 5. Magneto-optical determination of a topological index

Now, we will turn our attention to the notion of the topological index that can be used to describe the parity ordering of the conduction and valence bands of a Dirac fermion system. When the Dirac system is said to have positive energy gap, i.e.  $L_6^-$  is above  $L_6^+$  in  $\text{Pb}_{1-x}\text{Sn}_x\text{Se}$  and  $\text{Pb}_{1-x}\text{Sn}_x\text{Te}$  (Fig. 3.14(a)), their bulk bands exhibit trivial topology. On the contrary, the Dirac system possesses negative energy gap when their bulk bands are in the inverted regime and shown to have nontrivial topology. In this work, we show that the topological index of a material can be determined via the effective velocity of bulk massive Dirac fermions. This has been described in our previous paper<sup>11</sup>. Starting from solving the eigenvalue problem for a Dirac system that can be described by the general BHZ Hamiltonian<sup>18,19</sup>, shown in the section 3 of the Chapter 3, we obtain the Dirac velocity as:

$$v_D^2 = v_c^2 - \frac{2B_1\Delta}{\hbar^2} \quad (4.20)$$

Here,  $v_c$  is the critical velocity of a gapless 3D Dirac state that could take place at the critical composition  $x_c$  of the topological phase transition. Comparing the above equation to Eq. 4.6 derived from the 6-band  $\mathbf{k} \cdot \mathbf{p}$  approach for the lead salts proposed by Mitchell and Wallis<sup>1</sup>,

## CHAPTER 4

### *Magneto-optical investigation of TCIs: IV-VI compounds*

we can identify  $B_1 = -\frac{\hbar^2}{2\tilde{m}}$ .  $B_1$  is typically negative in the sign convention of BHZ<sup>18</sup> and the far-band contribution to the band edge mass  $\tilde{m}$  has a positive sign<sup>1</sup>.  $\tilde{m}$  is due to interactions between the valence/conduction bands ( $L_6^\pm$ ) and the four far-bands lying far away in energy from the band gap (Fig. 3.14(b)). When the main valence and conduction bands invert, the far-bands are still in the same ordering. Consequently,  $\tilde{m}$  does not change sign for fundamental reasons. Note that the term  $1/\tilde{m}$  is always small as compared to the term  $1/m$  in Eq. 4.1 in lead-salt systems. For example, in PbSe<sup>3,4</sup>, for the longitudinal valley  $1/m$  ( $\sim 1/0.04m_0$ ) is 6.25 times greater than  $1/\tilde{m}$  ( $\sim 1/0.25m_0$ ).

Interestingly, the term  $-\frac{2B_1\Delta}{\hbar^2}$  in Eq. 4.20 has been previously defined in the literature to be related to the topological index  $\eta$  as follows<sup>20-23</sup>:

$$(-1)^\eta = \text{sign}\left(-\frac{2B_1\Delta}{\hbar^2}\right) \quad (4.21)$$

We thus finally get:

$$(-1)^\eta = \text{sign}\left(\frac{\Delta}{\tilde{m}}\right) = \text{sign}(v_D^2 - v_C^2) \quad (4.22)$$

As  $\tilde{m}$  is always positive,  $\Delta$  can thus change sign through the topological phase transition when the conduction and valence bands swap. For a TCI system,  $\eta$  is a valley topological index that can be related to the mirror Chern number via the definition given by T. H. Hsieh et al.<sup>24</sup> and L. Fu<sup>20,25</sup>. In the trivial regime,  $\Delta > 0$ , the material is attributed a zero topological index ( $\eta = 0$ ). The material in the nontrivial regime,  $\Delta < 0$ , is identified by the emergence of the TSS that disperse in the bulk band gap and has a nonzero topological index ( $\eta = 1$ ). However, Eq. 4.22 demonstrates that by measuring  $v_D$  and  $v_C$  of the bulk states, we can determine the topological index  $\eta$  (modulo 2) of the topological matter. This approach is a new way for measuring  $\eta$  that is usually inferred from the direct observation of the TSS by ARPES or STM experiments as seen in the Chapter 3.

In this section, we will experimentally extract  $\eta$  in  $\text{Pb}_{1-x}\text{Sn}_x\text{Se}$  and  $\text{Pb}_{1-x}\text{Sn}_x\text{Te}$  IV-VI TCI systems via the study of the variation of  $v_D$ , measured from magneto-spectroscopy, through the topological phase transition.

#### **5.1. (111) $\text{Pb}_{1-x}\text{Sn}_x\text{Se}$**

We systematically investigated a total of eight (111)  $\text{Pb}_{1-x}\text{Sn}_x\text{Se}$  films in the Sn composition range  $0 \leq x \leq 0.30$  using IR magneto-optical LL spectroscopy. The massive Dirac model was used to extract, for each compound, the magneto-optical band parameters  $2|\Delta|$  and  $v_D$  in the longitudinal and oblique valleys as reported in Table 4.2.

The longitudinal and oblique velocities of massive Dirac fermions were respectively plotted as a function of Sn content in Fig. 4.15(a,b) in order to study their variation across the topological phase transition. We observe a decrease of the longitudinal and oblique Dirac velocities when  $x$  increases. The measured band gaps  $2|\Delta|$  were also plotted versus  $x$  in Fig. 4.15(c). We observe at the beginning a decrease of the energy gaps, then they show a minimum about  $15 \pm 5$  meV at  $x = 0.165$  that is followed by an increase with increasing Sn composition. Hence, we can estimate the critical Sn content where the topological phase transition occurs at 4.5 K as  $x_c = 0.16$  for  $\text{Pb}_{1-x}\text{Sn}_x\text{Se}$ . We can then deduce  $v_c = 5 \times 10^5$  m/s for the longitudinal valley and  $v_c = 4.7 \times 10^5$  m/s for the oblique valleys in (111)  $\text{Pb}_{1-x}\text{Sn}_x\text{Se}$ . Overall, we found that  $v_D > v_c$  for  $x < x_c$  in the topologically trivial regime and  $v_D < v_c$  for  $x > x_c$  in the topologically nontrivial regime. Additionally, we observed in the magneto-optical transmission spectra that the decrease in bulk Dirac velocity correlates with the emergence of the CR-TSS beyond the crossing over point  $x_c$  of the topological phase transition.

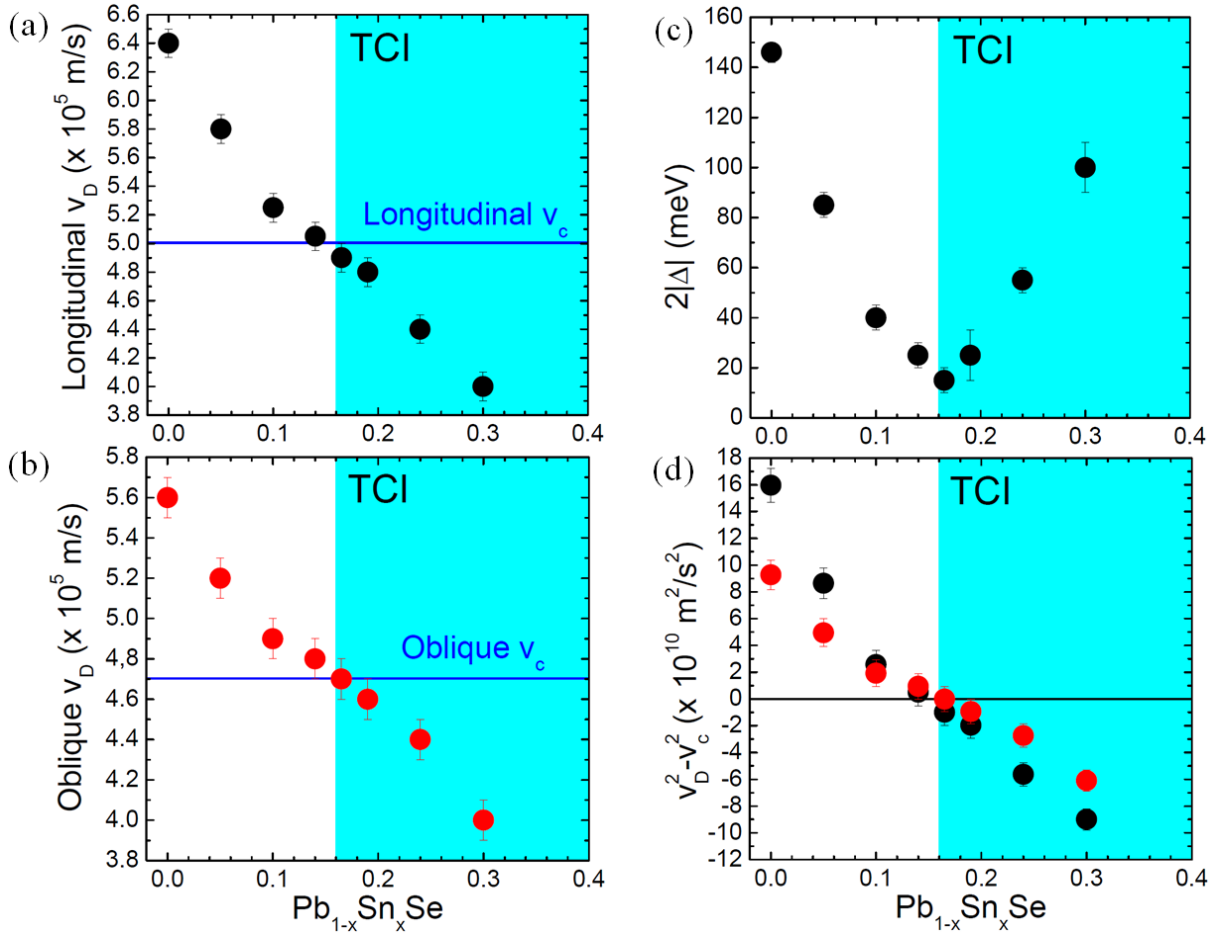


**Figure 4.15. Magneto-optical spectroscopy of bulk (111)  $\text{Pb}_{1-x}\text{Sn}_x\text{Se}$  measured at 4.5 K.** Longitudinal (a) and oblique (b) velocities of massive Dirac fermions as a function of Sn content. A decrease in bulk velocity as  $x$  is increased is observed. Blue lines in (a) and (b) indicate the values of the critical velocity:  $v_c = 5 \times 10^5$  m/s for the longitudinal valley and  $v_c = 4.7 \times 10^5$  m/s for the oblique valleys. (c) Energy gap  $2|\Delta|$  versus  $x$  shows a minimum at  $x = 0.165$ . We estimate the critical composition to be  $x_c = 0.16$  at 4.5 K. (d)  $v_D^2 - v_c^2 = \Delta/\tilde{m}$  plotted as a function of  $x$  for the longitudinal (black) and oblique (red) valleys. We observe  $v_D^2 - v_c^2 > 0$  for  $x < x_c$  and  $v_D^2 - v_c^2 < 0$  for  $x > x_c$ . This indicates the sign change of  $\Delta$  from positive to negative for  $x > x_c$ .

## CHAPTER 4

### Magneto-optical investigation of TCIs: IV-VI compounds

which can be seen in (c) when  $2|\Delta|$  turns to be increased beyond  $x_c$ . Shaded region represents the topological regime. Adapted from our previous work <sup>11</sup>.

The topological index  $\eta$  of  $\text{Pb}_{1-x}\text{Sn}_x\text{Se}$  can then be extracted by studying  $v_D^2 - v_c^2$  as a function of  $x$ , as shown in Fig. 4.15(d) for both types of bulk valleys. We observe  $v_D^2 - v_c^2$  decrease with increasing  $x$  such that  $v_D^2 - v_c^2 > 0$  for  $x < x_c$  and  $v_D^2 - v_c^2 < 0$  for  $x > x_c$ . Therefore, we can determine from Eq. 4.22 that  $\eta = 0$  for  $x < x_c$  when  $\text{Pb}_{1-x}\text{Sn}_x\text{Se}$  is in the trivial regime and  $\eta = 1$  for  $x > x_c$  when  $\text{Pb}_{1-x}\text{Sn}_x\text{Se}$  is in the nontrivial regime. A first magneto-optical determination of the topological index in a material of 3D TI family is thus confirmed in our investigation. Moreover, since  $v_D^2 - v_c^2 = \Delta/\tilde{m}$  and  $\tilde{m} > 0$ , we can determine the sign of the band gap. We observe  $\Delta > 0$  for  $x < x_c$  and  $\Delta < 0$  for  $x > x_c$ . In other words,  $\text{Pb}_{1-x}\text{Sn}_x\text{Se}$  has a positive band gap when it is topologically trivial ( $x < x_c$ ) and its band structure is in the normal regime, and it has a negative band gap when it is topologically nontrivial ( $x > x_c$ ) and its band structure is in the inverted regime. Table 4.4 represents the values of the energy gap with sign and Dirac velocities in both types of bulk valleys.

Composition $\text{Pb}_{1-x}\text{Sn}_x\text{Se}$	$2\Delta$ (meV)	$v_D$ (long.) ( $\times 10^5$ m/s)	$v_D$ (obl.) ( $\times 10^5$ m/s)
<b>PbSe</b>	$146 \pm 4$	$6.4 \pm 0.1$	$5.6 \pm 0.1$
<b>Pb<sub>0.95</sub>Sn<sub>0.05</sub>Se</b>	$85 \pm 5$	$5.8 \pm 0.1$	$5.2 \pm 0.1$
<b>Pb<sub>0.90</sub>Sn<sub>0.10</sub>Se</b>	$40 \pm 5$	$5.25 \pm 0.10$	$4.9 \pm 0.1$
<b>Pb<sub>0.86</sub>Sn<sub>0.14</sub>Se</b>	$25 \pm 5$	$5.05 \pm 0.10$	$4.8 \pm 0.1$
<b>Pb<sub>0.835</sub>Sn<sub>0.165</sub>Se</b>	$-15 \pm 5$	$4.9 \pm 0.1$	$4.7 \pm 0.1$
<b>Pb<sub>0.81</sub>Sn<sub>0.19</sub>Se</b>	$-25 \pm 10$	$4.8 \pm 0.1$	$4.6 \pm 0.1$
<b>Pb<sub>0.76</sub>Sn<sub>0.24</sub>Se</b>	$-55 \pm 5$	$4.4 \pm 0.1$	$4.4 \pm 0.1$
<b>Pb<sub>0.70</sub>Sn<sub>0.30</sub>Se</b>	$-100 \pm 10$	$4.0 \pm 0.1$	$4.0 \pm 0.1$

**Table 4.4.** Magneto-optical band parameters extracted from the massive Dirac model analysis in eight (111)  $\text{Pb}_{1-x}\text{Sn}_x\text{Se}$  films ( $0 \leq x \leq 0.30$ ) measured at  $T = 4.5$  K. The band gap  $2\Delta$  is shown with sign. Longitudinal and oblique bulk velocities  $v_D$  are represented for each compound.

We can deduce the value of  $\tilde{m}$  of (111)  $\text{Pb}_{1-x}\text{Sn}_x\text{Se}$  samples for each respective valley by studying the variation of  $v_D^2 - v_c^2$  in the longitudinal (black points) and oblique (red points) valleys as a function of  $\Delta$ , as shown in Fig. 4.16. From the fitting parameters, we deduced  $\tilde{m} \sim (0.09 \pm 0.01)m_0$  in the longitudinal valley and  $\tilde{m} \sim (0.15 \pm 0.01)m_0$  in the oblique valleys.



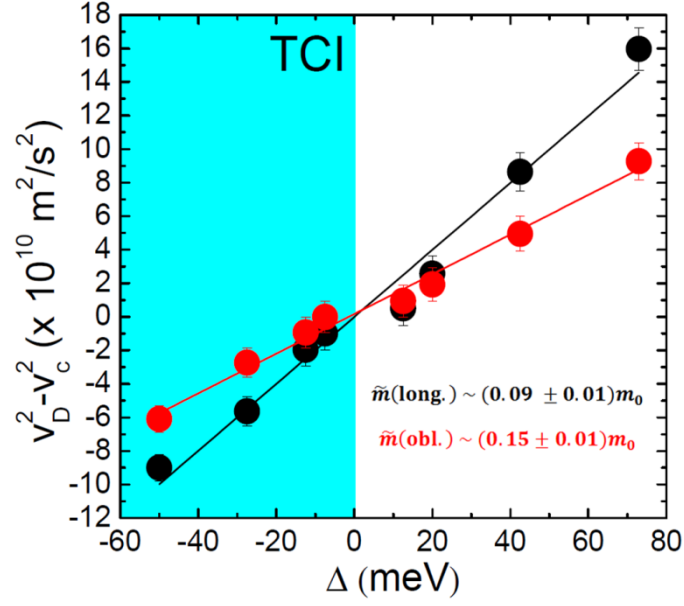


**Figure 4.16.** Determination of the far-band contribution to the band edge mass  $\tilde{m}$  in the longitudinal and oblique bulk valleys. The variation of  $v_D^2 - v_c^2$  in the longitudinal (black points) and oblique (red points) valleys is shown as a function of half band gap  $\Delta$ .  $\tilde{m}$  is the inverse of the slope of the linear curve fit.

## 5.2. (111) $\text{Pb}_{1-x}\text{Sn}_x\text{Te}$

In order to consolidate the general aspect of our magneto-optical results obtained in (111)  $\text{Pb}_{1-x}\text{Sn}_x\text{Se}$ , a total of twenty (111)  $\text{Pb}_{1-x}\text{Sn}_x\text{Te}$  samples for  $0 \leq x \leq 0.56$  were also systematically examined by means of IR magneto-optical LL spectroscopy. For each composition,  $v_D$  in the longitudinal and oblique valleys were obtained from the massive Dirac model analysis and are listed in Table 4.3.

Similar to (111)  $\text{Pb}_{1-x}\text{Sn}_x\text{Se}$ , we proceeded the same analysis to study the variation of the longitudinal and oblique bulk velocities (Fig. 4.17(a,b)) as a function of Sn composition through the topological phase transition in (111)  $\text{Pb}_{1-x}\text{Sn}_x\text{Te}$ . The critical Sn content where the bulk bands  $L_6^\pm$  invert can be estimated to be  $x_c \approx 0.42 \pm 0.02$  for  $\text{Pb}_{1-x}\text{Sn}_x\text{Te}$  measured at 4.5 K. We can then deduce  $v_c = 7.4 \times 10^5$  m/s for the longitudinal valley and  $v_c = 5.1 \times 10^5$  m/s for the oblique valleys in (111)  $\text{Pb}_{1-x}\text{Sn}_x\text{Te}$ . Again, we found that  $v_D > v_c$  for  $x < x_c$  in the topologically trivial regime and  $v_D < v_c$  for  $x > x_c$  in the topologically nontrivial regime, being identified by the observation of the CR-TSS related feature in the transmission spectra after  $x_c$ .

## CHAPTER 4

### Magneto-optical investigation of TCIs: IV-VI compounds

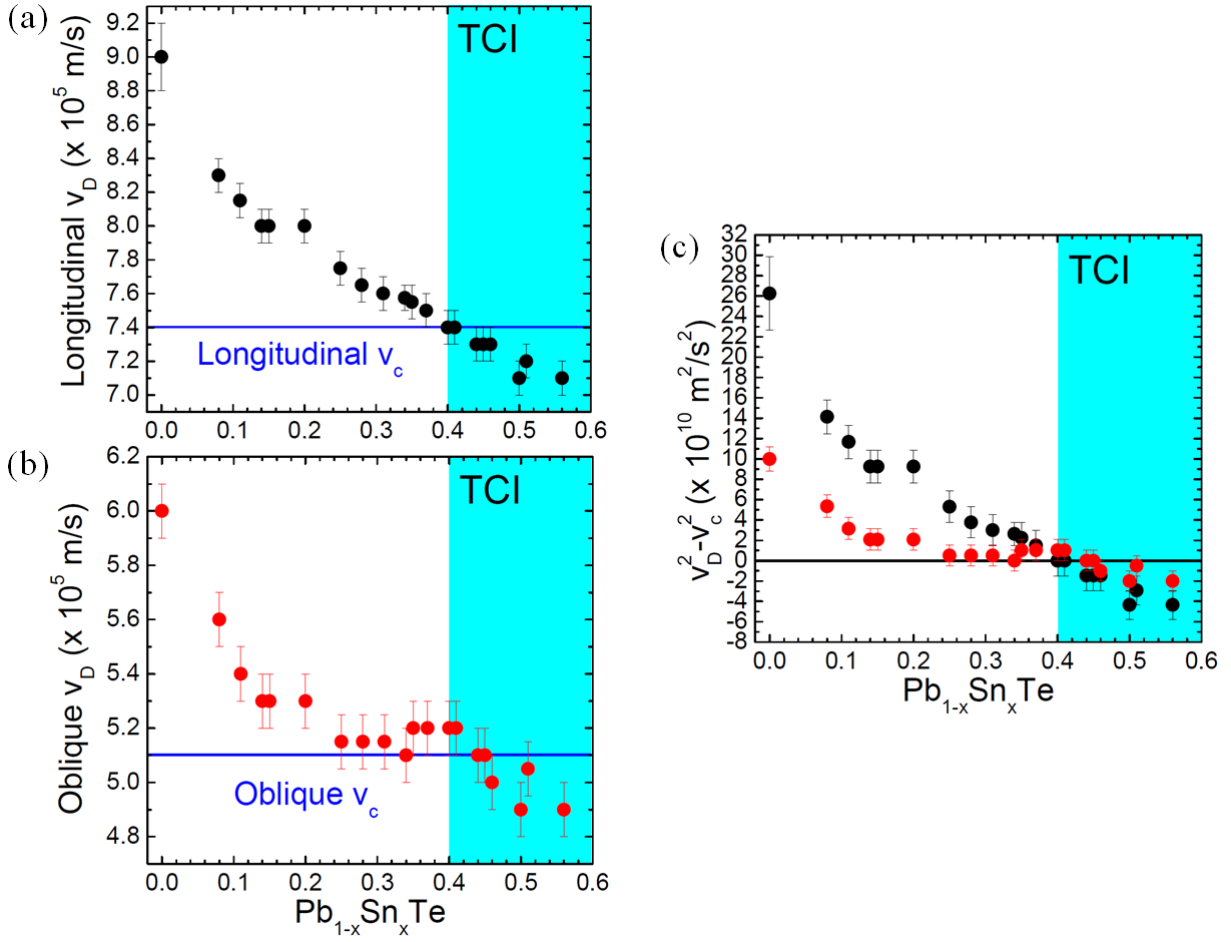


**Figure 4.17. Magneto-optical spectroscopy of bulk (111)  $\text{Pb}_{1-x}\text{Sn}_x\text{Te}$  measured at 4.5 K.** Longitudinal (a) and oblique (b) velocities of massive Dirac fermions as a function of Sn content. A decrease in bulk velocity as  $x$  is increased is observed. Blue lines in (a) and (b) indicate the values of the critical velocity:  $v_c = 7.4 \times 10^5 \text{ m/s}$  for the longitudinal valley and  $v_c = 5.1 \times 10^5 \text{ m/s}$  for the oblique valleys. We estimate the critical composition to be  $x_c \approx 0.42 \pm 0.02$  at 4.5 K. (c)  $v_D^2 - v_c^2 = \Delta/\tilde{m}$  plotted as a function of  $x$  for the longitudinal (black) and oblique (red) valleys. We observe  $v_D^2 - v_c^2 > 0$  for  $x < x_c$  and  $v_D^2 - v_c^2 < 0$  for  $x > x_c$ . This indicates the sign change of  $\Delta$  from positive to negative for  $x > x_c$ . Shaded region represents the topological regime.

Studying the sign of  $v_D^2 - v_c^2$  as a function of  $x$  for both types of bulk valleys, as illustrated in Fig. 4.17(c), we can determine the topological index  $\eta$  of  $\text{Pb}_{1-x}\text{Sn}_x\text{Te}$  using Eq. 4.22. We observe that  $v_D^2 - v_c^2 > 0$  for  $x < x_c$  and  $v_D^2 - v_c^2 < 0$  for  $x > x_c$ , thereby,  $\eta = 0$  for  $x < x_c$  when  $\text{Pb}_{1-x}\text{Sn}_x\text{Te}$  is in the trivial regime and  $\eta = 1$  for  $x > x_c$  when  $\text{Pb}_{1-x}\text{Sn}_x\text{Te}$  is in the nontrivial regime. Subsequently, we can give the sign to the band gap as we know that  $v_D^2 - v_c^2 = \Delta/\tilde{m}$ , with  $\tilde{m} > 0$ :  $\Delta > 0$  for  $x < x_c$  and  $\Delta < 0$  for  $x > x_c$ . The values of the energy gap with sign and Dirac velocities in both types of bulk valleys are listed in Table 4.5.

Composition $\text{Pb}_{1-x}\text{Sn}_x\text{Te}$	$2\Delta$ (meV)	$v_D$ (long.) ( $\times 10^5$ m/s)	$v_D$ (obl.) ( $\times 10^5$ m/s)
<b>PbTe</b>	$190 \pm 5$	$9.0 \pm 0.2$	$6.0 \pm 0.1$
<b>Pb<sub>0.92</sub>Sn<sub>0.08</sub>Te</b>	$145 \pm 5$	$8.3 \pm 0.1$	$5.6 \pm 0.1$
<b>Pb<sub>0.89</sub>Sn<sub>0.11</sub>Te</b>	$125 \pm 5$	$8.15 \pm 0.10$	$5.4 \pm 0.1$
<b>Pb<sub>0.86</sub>Sn<sub>0.14</sub>Te</b>	$110 \pm 5$	$8.0 \pm 0.1$	$5.3 \pm 0.1$
<b>Pb<sub>0.85</sub>Sn<sub>0.15</sub>Te</b>	$105 \pm 5$	$8.0 \pm 0.1$	$5.3 \pm 0.1$
<b>Pb<sub>0.80</sub>Sn<sub>0.20</sub>Te</b>	$90 \pm 5$	$8.0 \pm 0.1$	$5.3 \pm 0.1$
<b>Pb<sub>0.75</sub>Sn<sub>0.25</sub>Te</b>	$70 \pm 5$	$7.75 \pm 0.10$	$5.15 \pm 0.10$
<b>Pb<sub>0.72</sub>Sn<sub>0.28</sub>Te</b>	$62.5 \pm 7.5$	$7.65 \pm 0.10$	$5.15 \pm 0.10$
<b>Pb<sub>0.69</sub>Sn<sub>0.31</sub>Te</b>	$55 \pm 5$	$7.6 \pm 0.1$	$5.15 \pm 0.10$
<b>Pb<sub>0.66</sub>Sn<sub>0.34</sub>Te</b>	$55 \pm 5$	$7.575 \pm 0.075$	$5.1 \pm 0.1$
<b>Pb<sub>0.65</sub>Sn<sub>0.35</sub>Te</b>	$50 \pm 10$	$7.55 \pm 0.10$	$5.2 \pm 0.1$
<b>Pb<sub>0.63</sub>Sn<sub>0.37</sub>Te</b>	$45 \pm 15$	$7.5 \pm 0.1$	$5.2 \pm 0.1$
<b>Pb<sub>0.60</sub>Sn<sub>0.40</sub>Te</b>	$50 \pm 10$	$7.4 \pm 0.1$	$5.2 \pm 0.1$
<b>Pb<sub>0.59</sub>Sn<sub>0.41</sub>Te</b>	$50 \pm 10$	$7.4 \pm 0.1$	$5.2 \pm 0.1$
<b>Pb<sub>0.56</sub>Sn<sub>0.44</sub>Te</b>	$-40 \pm 5$	$7.3 \pm 0.1$	$5.1 \pm 0.1$
<b>Pb<sub>0.55</sub>Sn<sub>0.45</sub>Te</b>	$-40 \pm 5$	$7.3 \pm 0.1$	$5.1 \pm 0.1$
<b>Pb<sub>0.54</sub>Sn<sub>0.46</sub>Te</b>	$-30 \pm 5$	$7.3 \pm 0.1$	$5.0 \pm 0.1$
<b>Pb<sub>0.50</sub>Sn<sub>0.50</sub>Te</b>	$-35 \pm 5$	$7.1 \pm 0.1$	$4.9 \pm 0.1$
<b>Pb<sub>0.49</sub>Sn<sub>0.51</sub>Te</b>	$-35 \pm 5$	$7.2 \pm 0.1$	$5.05 \pm 0.10$
<b>Pb<sub>0.44</sub>Sn<sub>0.56</sub>Te</b>	$-30 \pm 10$	$7.1 \pm 0.1$	$4.9 \pm 0.1$

**Table 4.5.** Magneto-optical band parameters extracted from the massive Dirac model analysis in twenty (111)  $\text{Pb}_{1-x}\text{Sn}_x\text{Te}$  films ( $0 \leq x \leq 0.56$ ) measured at  $T = 4.5$  K. The band gap  $2\Delta$  is shown with sign. Longitudinal and oblique bulk velocities  $v_D$  are represented for each compound.

Similar to (111)  $\text{Pb}_{1-x}\text{Sn}_x\text{Se}$ , we can deduce the value of  $\tilde{m}$  of (111)  $\text{Pb}_{1-x}\text{Sn}_x\text{Te}$  samples for each respective valley by studying the variation of  $v_D^2 - v_C^2$  in the longitudinal and oblique valleys versus  $\Delta$ . From the linear curve fit parameter, we deduced  $\tilde{m} \sim (0.09 \pm 0.01)m_0$  in the longitudinal valley and  $\tilde{m} \sim (0.20 \pm 0.01)m_0$  in the oblique valleys.

## 6. Validity of the massive Dirac approximation

We have previously seen that the LLs in the massive Dirac fermion model given in Eq. 4.8 describe very well the optical transitions in  $\text{Pb}_{1-x}\text{Sn}_x\text{Se}$  and  $\text{Pb}_{1-x}\text{Sn}_x\text{Te}$  IV-VI semiconductors. Note that they are obtained by neglecting the  $k^4$  terms in the BHZ eigenvalues or equivalently the term that varies in  $B^2$  under the square root of the LLs expressed in Eq. 4.3(a,b). In the following, we will verify and show that our assumptions for neglecting these terms are valid. If we do not neglect any term, the LL energies in the trivial regime (Eq. 4.8) become:

## CHAPTER 4

### Magneto-optical investigation of TCIs: IV-VI compounds

$$E_{N>0}^{c,\pm} = \mp \hbar \tilde{\omega} + \sqrt{(\Delta + \frac{\hbar e B N}{\tilde{m}})^2 + 2v_c^2 \hbar e B N} \quad (4.23a)$$

and

$$E_0^c = \hbar \tilde{\omega} + \Delta \quad (4.23b)$$

$$E_{N>0}^{v,\pm} = \pm \hbar \tilde{\omega} - \sqrt{(\Delta + \frac{\hbar e B N}{\tilde{m}})^2 + 2v_c^2 \hbar e B N} \quad (4.23c)$$

and

$$E_0^v = -\hbar \tilde{\omega} - \Delta \quad (4.23d)$$

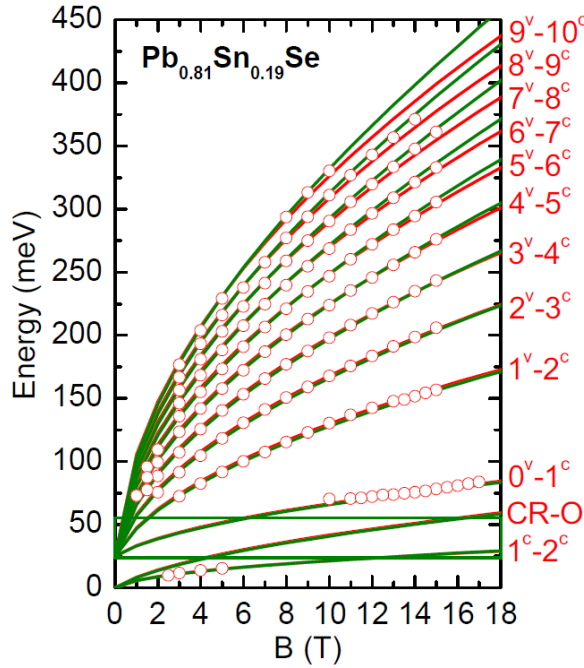


**Figure 4.18. Comparison between the Landau level transitions obtained from the massive Dirac model and the full  $\mathbf{k} \cdot \mathbf{p}$  model including the  $B^2$  term.** Only experimental data in the bulk oblique valleys of (111)  $\text{Pb}_{0.81}\text{Sn}_{0.19}\text{Se}$  investigated by magneto-spectroscopy at 4.5 K are fit by the Landau level transitions calculated using the massive Dirac model (red curves) and the full model with the  $B^2$  term (green curves). Adapted from the supplementary material for our previous work <sup>11</sup>.

For this matter, the magneto-optical transmission minima associated with the bulk oblique valleys of (111)  $\text{Pb}_{0.81}\text{Sn}_{0.19}\text{Se}$  will be fit using the LL transitions calculated from the massive Dirac model (red curves) and the full  $\mathbf{k} \cdot \mathbf{p}$  model taking into account the  $B^2$  term (green curves), as shown in Fig. 4.18. We clearly see that our data points are mostly constrained by the curve fits of low index LLs resulting from both models and are therefore little affected by the  $B^2$  term. The discrepancy between both models can be seen at high LL indices and high magnetic fields. However, both of them agree with the data within experimental uncertainty. The band parameters extracted from the massive Dirac model are  $2\Delta = -25 \pm 10$  meV and  $v_D = (4.6 \pm 0.1) \times 10^5$  m/s for the bulk oblique valleys. The systematic study by magneto-optics allows us to estimate the critical oblique Dirac velocity to

be  $v_c = (4.7 \pm 0.1) \times 10^5$  m/s. Using the relation  $v_D^2 - v_c^2 = \frac{\Delta}{\tilde{m}}$ , we can then deduce  $\tilde{m} \approx 0.24m_0$  for the bulk oblique valleys in (111)  $\text{Pb}_{0.81}\text{Sn}_{0.19}\text{Se}$ . The band parameters obtained from the full model are  $2\Delta = -25 \pm 5$  meV,  $v_c = (4.6 \pm 0.1) \times 10^5$  m/s for the oblique valleys and  $\tilde{m} = 0.24m_0$ , in good agreement with the massive Dirac model. For a typical value of  $\tilde{m}$  for  $\text{Pb}_{1-x}\text{Sn}_x\text{Se}$  and  $\text{Pb}_{1-x}\text{Sn}_x\text{Te}$ , we can safely neglect the  $B^2$  term for  $N \leq 7$  and  $B < 15$  T.

Note that, even if the  $B^2$  term are not neglected, we can still extract the Dirac velocity from the LLs given in Eq. 4.23, allowing the determination of the topological index  $\eta$ . By expanding Eq. 4.23, we obtain:

$$E_{N>0}^{c,\pm} = \mp \hbar \tilde{\omega} + \sqrt{\Delta^2 + 2 \left( v_c^2 + \frac{\Delta}{\tilde{m}} \right) \hbar e B N + \left( \frac{\hbar e B N}{\tilde{m}} \right)^2} \quad (4.24a)$$

$$\text{and} \\ E_0^c = \hbar \tilde{\omega} + \Delta \quad (4.24b)$$

$$E_{N>0}^{v,\pm} = \pm \hbar \tilde{\omega} - \sqrt{\Delta^2 + 2 \left( v_c^2 + \frac{\Delta}{\tilde{m}} \right) \hbar e B N + \left( \frac{\hbar e B N}{\tilde{m}} \right)^2} \quad (4.24c)$$

$$\text{and} \\ E_0^v = -\hbar \tilde{\omega} - \Delta \quad (4.24d)$$

The Dirac velocity can still be defined as before  $v_D^2 = v_c^2 + \frac{\Delta}{\tilde{m}}$ , and varies as expected when the sign of  $\Delta$  changes.

## 7. Valley anisotropy in IV-VI compounds

In the previous sections, we have seen that magneto-optical investigation allows us to precisely determine the band parameters such as the band gap, the Dirac velocity and the effective band edge mass of  $\text{Pb}_{1-x}\text{Sn}_x\text{Se}$  and  $\text{Pb}_{1-x}\text{Sn}_x\text{Te}$  systems. Furthermore, the magneto-spectroscopy technique is also capable of studying the Sn composition dependence of the valley anisotropy in these IV-VI compounds at low temperatures. The valley anisotropy factor  $K$  must be defined as the square of the ratio of the maximum ( $A_{max}$ ) and minimum ( $A_{min}$ ) cross-sectional areas of the Fermi surface:  $K = (A_{max}/A_{min})^2 = (b/a)^2$ <sup>26</sup>. Here,  $2a$  and  $2b$  are respectively the minor and major axes of a 3D Fermi ellipsoid, as shown in the subsection 2.5 of the Chapter 3. This area anisotropy factor can also be determined directly by the  $\mathbf{k} \cdot \mathbf{p}$  transverse ( $P_{\perp}$ ) and longitudinal ( $P_{\parallel}$ ) momentum matrix elements<sup>2-4,27</sup>:  $K = (P_{\perp}/P_{\parallel})^2$ .

Using the massive Dirac model, we are able to extract  $v_D$  in the longitudinal and oblique bulk valleys for each (111)  $\text{Pb}_{1-x}\text{Sn}_x\text{Se}$  and  $\text{Pb}_{1-x}\text{Sn}_x\text{Te}$  compound. Hence, we can determine  $K$  of each lead-tin salt composition using Eq. 4.13. Finally, we can deduce the shape ( $b/a$ ) of the corresponding 3D bulk carrier ellipsoids and study their evolution as a function of  $x$ .

## CHAPTER 4

### Magneto-optical investigation of TCIs: IV-VI compounds

#### 7.1. $\text{Pb}_{1-x}\text{Sn}_x\text{Se}$

(111)  $\text{Pb}_{1-x}\text{Sn}_x\text{Se}$  films ( $0 \leq x \leq 0.30$ ) were systematically investigated by magneto-optical absorption measurement. Their bulk band parameters are reported in Table 4.6. For a given Sn composition, the band gap is the same for both types of bulk valleys, while the difference in bulk velocity is observed and it results originally from the valley anisotropy. Fig. 4.19 shows the evolution of the bulk velocities in the longitudinal (black circles) and oblique (red circles) valleys as a function of  $x$ , represented in the same scale. We observe that the anisotropy in bulk Dirac velocity in  $\text{Pb}_{1-x}\text{Sn}_x\text{Se}$  depends on  $x$  as the difference between the longitudinal  $v_D$  and the oblique  $v_D$  decreases with increasing  $x$ . They become equivalent when  $x \geq 0.24$  (bicolor circles) since the bulk transitions in both types of valleys occur at the same energy. This can be more clearly observed in the transmission spectra as well as in the LL transition fan charts of (111)  $\text{Pb}_{1-x}\text{Sn}_x\text{Se}$  shown in the subsection 3.1.

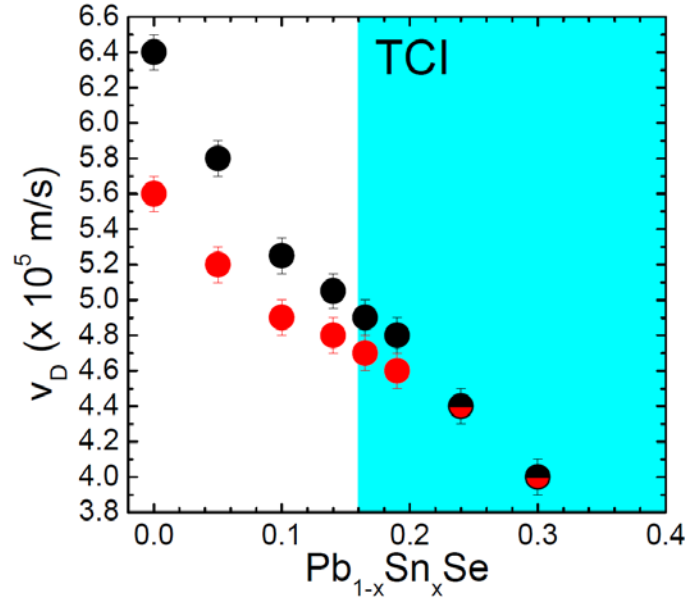


**Figure 4.19.** Study of valley anisotropy factor  $K$  via the evolution of the bulk velocities in the longitudinal and oblique valleys as a function of Sn content in (111)  $\text{Pb}_{1-x}\text{Sn}_x\text{Se}$ . The longitudinal (black circles) and oblique (red circles) velocities are plotted versus  $x$  in the same scale. The difference between them diminishes as  $x$  is increased. They are equivalent when  $x \geq 0.24$ .

A quantitative study of the valley anisotropy factor can be done by calculating  $K$  for each compound using Eq. 4.13. The values of  $K$  and the ratio  $b/a$  are listed in Table 4.6.

Composition $\text{Pb}_{1-x}\text{Sn}_x\text{Se}$	$2\Delta$ (meV)	$v_D$ (long.) ( $\times 10^5$ m/s)	$v_D$ (obl.) ( $\times 10^5$ m/s)	$K$	$b/a$
<b>PbSe</b>	$146 \pm 4$	$6.4 \pm 0.1$	$5.6 \pm 0.1$	$1.87 \pm 0.22$	$1.37 \pm 0.08$
<b>Pb<sub>0.95</sub>Sn<sub>0.05</sub>Se</b>	$85 \pm 5$	$5.8 \pm 0.1$	$5.2 \pm 0.1$	$1.66 \pm 0.21$	$1.29 \pm 0.08$
<b>Pb<sub>0.90</sub>Sn<sub>0.10</sub>Se</b>	$40 \pm 5$	$5.25 \pm 0.10$	$4.9 \pm 0.1$	$1.37 \pm 0.18$	$1.17 \pm 0.08$
<b>Pb<sub>0.86</sub>Sn<sub>0.14</sub>Se</b>	$25 \pm 5$	$5.05 \pm 0.10$	$4.8 \pm 0.1$	$1.26 \pm 0.17$	$1.12 \pm 0.07$
<b>Pb<sub>0.835</sub>Sn<sub>0.165</sub>Se</b>	$-15 \pm 5$	$4.9 \pm 0.1$	$4.7 \pm 0.1$	$1.21 \pm 0.16$	$1.10 \pm 0.07$
<b>Pb<sub>0.81</sub>Sn<sub>0.19</sub>Se</b>	$-25 \pm 10$	$4.8 \pm 0.1$	$4.6 \pm 0.1$	$1.21 \pm 0.17$	$1.10 \pm 0.08$
<b>Pb<sub>0.76</sub>Sn<sub>0.24</sub>Se</b>	$-55 \pm 5$	$4.4 \pm 0.1$	$4.4 \pm 0.1$	$1 \pm 0.14$	$1 \pm 0.07$
<b>Pb<sub>0.70</sub>Sn<sub>0.30</sub>Se</b>	$-100 \pm 10$	$4.0 \pm 0.1$	$4.0 \pm 0.1$	$1 \pm 0.16$	$1 \pm 0.08$

**Table 4.6. Magneto-optical band parameters of eight (111)  $\text{Pb}_{1-x}\text{Sn}_x\text{Se}$  ( $0 \leq x \leq 0.30$ ) measured at  $T = 4.5$  K and their valley anisotropy factor  $K$ .** The band gap  $2\Delta$ , the longitudinal and oblique bulk velocities  $v_D$  are listed for each compound. The valley anisotropy factor  $K = (b/a)^2$  can be deduced from both Dirac velocities. The ratio  $b/a$  gives the information about the shape of the 3D Fermi ellipsoid.

We measured  $K = 1.87 \pm 0.22$  in the PbSe sample. This agrees very well with the results obtained from previous magneto-optical studies in PbSe reporting  $K = 1.82 \pm 0.3$ <sup>3</sup> or  $K = 1.82 \pm 0.05$ <sup>4</sup>. The Sn content dependence of  $K$  in  $\text{Pb}_{1-x}\text{Sn}_x\text{Se}$  is not high.  $K$  decreases with increasing  $x$  and becomes equal to 1 when  $x \geq 0.24$ , evidencing a nearly isotropic Fermi surface. The ratio  $b/a$  gives access to study the geometry of the ellipsoidal bulk carrier pockets in  $\text{Pb}_{1-x}\text{Sn}_x\text{Se}$  in the whole range of  $x$ . This is a demonstration of the transformation from ellipsoidal ( $b/a > 1$ ) to spherical ( $b/a = 1$ ) shape of the 3D bulk carrier pockets when  $x$  increases. Note that  $\text{Pb}_{1-x}\text{Sn}_x\text{Se}$  displays a very low anisotropy in the vicinity of the topological phase transition ( $K < 1.2$ ). Therefore,  $\text{Pb}_{1-x}\text{Sn}_x\text{Se}$  alloys are an ideal system allowing to investigate such phase transition owing to their two mirror-like bands  $L_6^+$  and  $L_6^-$  which are nearly spherical, and the absence of a heavy hole band as for instance in the  $\text{Hg}_{1-x}\text{Cd}_x\text{Te}$  system.

## 7.2. $\text{Pb}_{1-x}\text{Sn}_x\text{Te}$

We have also studied the valley anisotropy factor in (111)  $\text{Pb}_{1-x}\text{Sn}_x\text{Te}$  films ( $0 \leq x \leq 0.56$ ) in order to study the anisotropy factor of the Fermi surface. Their bulk band parameters are listed in Table 4.7, leading to study the evolution of the longitudinal (black circles) and oblique (red circles) bulk velocities versus  $x$  as shown in Fig. 4.20. In contrast to  $\text{Pb}_{1-x}\text{Sn}_x\text{Se}$ , the anisotropy in bulk Dirac velocity in  $\text{Pb}_{1-x}\text{Sn}_x\text{Te}$  is much more important. This is evidenced by the observation of a number of bulk transitions originating from both types of valleys in the transmission spectra as well as in the LL transition fan diagrams of (111)  $\text{Pb}_{1-x}\text{Sn}_x\text{Te}$  (see the subsection 3.1).



## CHAPTER 4

### Magneto-optical investigation of TCIs: IV-VI compounds

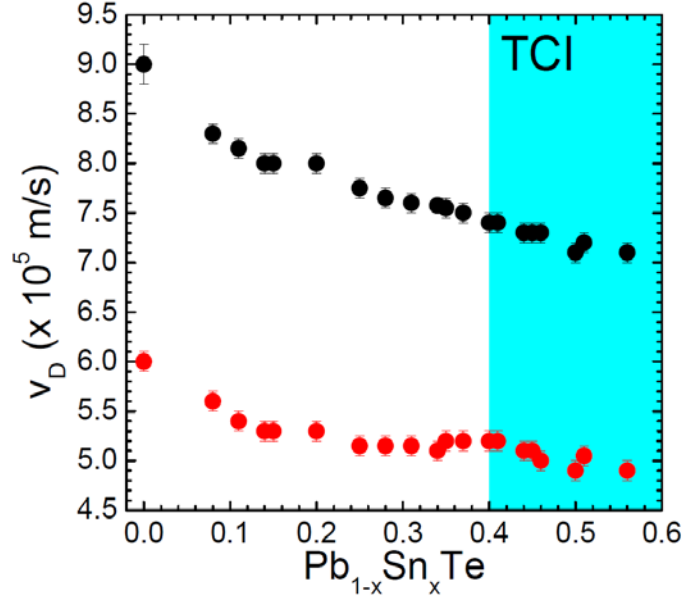


Figure 4.20. Study of valley anisotropy factor  $K$  via the evolution of the bulk velocities in the longitudinal and oblique valleys as a function of Sn content in (111)  $\text{Pb}_{1-x}\text{Sn}_x\text{Te}$ . The longitudinal (black circles) and oblique (red circles) velocities are plotted versus  $x$  in the same scale. The difference between them remains high in the whole range of  $x$ .

Using Eq. 4.13, we obtain the value of  $K$  for each composition and subsequently the corresponding ratio  $b/a$  that are given in Table 4.7.

Composition $\text{Pb}_{1-x}\text{Sn}_x\text{Te}$	$2\Delta$ (meV)	$v_D$ (long.) ( $\times 10^5$ m/s)	$v_D$ (obl.) ( $\times 10^5$ m/s)	$K$	$b/a$
<b>PbTe</b>	$190 \pm 5$	$9.0 \pm 0.2$	$6.0 \pm 0.1$	$10.3 \pm 2.6$	$3.2 \pm 0.4$
<b>Pb<sub>0.92</sub>Sn<sub>0.08</sub>Te</b>	$145 \pm 5$	$8.3 \pm 0.1$	$5.6 \pm 0.1$	$9.3 \pm 1.7$	$3.0 \pm 0.3$
<b>Pb<sub>0.89</sub>Sn<sub>0.11</sub>Te</b>	$125 \pm 5$	$8.15 \pm 0.10$	$5.4 \pm 0.1$	$10.9 \pm 2.3$	$3.3 \pm 0.4$
<b>Pb<sub>0.86</sub>Sn<sub>0.14</sub>Te</b>	$110 \pm 5$	$8.0 \pm 0.1$	$5.3 \pm 0.1$	$10.9 \pm 2.3$	$3.3 \pm 0.4$
<b>Pb<sub>0.85</sub>Sn<sub>0.15</sub>Te</b>	$105 \pm 5$	$8.0 \pm 0.1$	$5.3 \pm 0.1$	$10.9 \pm 2.3$	$3.3 \pm 0.4$
<b>Pb<sub>0.80</sub>Sn<sub>0.20</sub>Te</b>	$90 \pm 5$	$8.0 \pm 0.1$	$5.3 \pm 0.1$	$10.9 \pm 2.3$	$3.3 \pm 0.4$
<b>Pb<sub>0.75</sub>Sn<sub>0.25</sub>Te</b>	$70 \pm 5$	$7.75 \pm 0.10$	$5.15 \pm 0.10$	$10.6 \pm 2.3$	$3.3 \pm 0.4$
<b>Pb<sub>0.72</sub>Sn<sub>0.28</sub>Te</b>	$62.5 \pm 7.5$	$7.65 \pm 0.10$	$5.15 \pm 0.10$	$9.4 \pm 1.9$	$3.1 \pm 0.3$
<b>Pb<sub>0.69</sub>Sn<sub>0.31</sub>Te</b>	$55 \pm 5$	$7.6 \pm 0.1$	$5.15 \pm 0.10$	$8.9 \pm 1.8$	$3.0 \pm 0.3$
<b>Pb<sub>0.66</sub>Sn<sub>0.34</sub>Te</b>	$55 \pm 5$	$7.575 \pm 0.075$	$5.1 \pm 0.1$	$9.4 \pm 1.8$	$3.1 \pm 0.3$
<b>Pb<sub>0.65</sub>Sn<sub>0.35</sub>Te</b>	$50 \pm 10$	$7.55 \pm 0.10$	$5.2 \pm 0.1$	$7.8 \pm 1.4$	$2.8 \pm 0.3$
<b>Pb<sub>0.63</sub>Sn<sub>0.37</sub>Te</b>	$45 \pm 15$	$7.5 \pm 0.1$	$5.2 \pm 0.1$	$7.4 \pm 1.3$	$2.7 \pm 0.3$
<b>Pb<sub>0.60</sub>Sn<sub>0.40</sub>Te</b>	$50 \pm 10$	$7.4 \pm 0.1$	$5.2 \pm 0.1$	$6.7 \pm 1.2$	$2.6 \pm 0.2$
<b>Pb<sub>0.59</sub>Sn<sub>0.41</sub>Te</b>	$50 \pm 10$	$7.4 \pm 0.1$	$5.2 \pm 0.1$	$6.7 \pm 1.2$	$2.6 \pm 0.2$
<b>Pb<sub>0.56</sub>Sn<sub>0.44</sub>Te</b>	$-40 \pm 5$	$7.3 \pm 0.1$	$5.1 \pm 0.1$	$7.0 \pm 1.3$	$2.6 \pm 0.2$
<b>Pb<sub>0.55</sub>Sn<sub>0.45</sub>Te</b>	$-40 \pm 5$	$7.3 \pm 0.1$	$5.1 \pm 0.1$	$7.0 \pm 1.3$	$2.6 \pm 0.2$
<b>Pb<sub>0.54</sub>Sn<sub>0.46</sub>Te</b>	$-30 \pm 5$	$7.3 \pm 0.1$	$5.0 \pm 0.1$	$8.2 \pm 1.6$	$2.9 \pm 0.3$
<b>Pb<sub>0.50</sub>Sn<sub>0.50</sub>Te</b>	$-35 \pm 5$	$7.1 \pm 0.1$	$4.9 \pm 0.1$	$7.7 \pm 1.5$	$2.8 \pm 0.3$
<b>Pb<sub>0.49</sub>Sn<sub>0.51</sub>Te</b>	$-35 \pm 5$	$7.2 \pm 0.1$	$5.05 \pm 0.10$	$6.8 \pm 1.2$	$2.6 \pm 0.2$
<b>Pb<sub>0.44</sub>Sn<sub>0.56</sub>Te</b>	$-30 \pm 10$	$7.1 \pm 0.1$	$4.9 \pm 0.1$	$7.7 \pm 1.5$	$2.8 \pm 0.3$

**Table 4.7. Magneto-optical band parameters of twenty (111)  $\text{Pb}_{1-x}\text{Sn}_x\text{Te}$  ( $0 \leq x \leq 0.56$ ) measured at  $T = 4.5$  K and their valley anisotropy factor  $K$ .** The band gap  $2\Delta$ , the longitudinal and oblique bulk velocities  $v_D$  are listed for each compound. The valley anisotropy factor  $K = (b/a)^2$  can be deduced from both Dirac velocities. The ratio  $b/a$  gives the information about the shape of the 3D Fermi ellipsoid.

We obtain  $K = 10.3 \pm 2.6$  for the PbTe sample, in good agreement with previous magneto-optical measurements in PbTe having  $K = 10.24 \pm 0.6$ <sup>2</sup> or  $K = 10.9 \pm 0.6$ <sup>3</sup>.  $K$  decreases with increasing  $x$ . However, for the same  $x$ ,  $K$  in the case of  $\text{Pb}_{1-x}\text{Sn}_x\text{Te}$  is more significant than that in the case of  $\text{Pb}_{1-x}\text{Sn}_x\text{Se}$ . The values  $b/a$  indicate that the bulk carrier pockets of  $\text{Pb}_{1-x}\text{Sn}_x\text{Te}$  are always ellipsoidal for the whole range of  $x$ .

## 8. Absence of band gap closure across the topological phase transition in $\text{Pb}_{1-x}\text{Sn}_x\text{Te}$

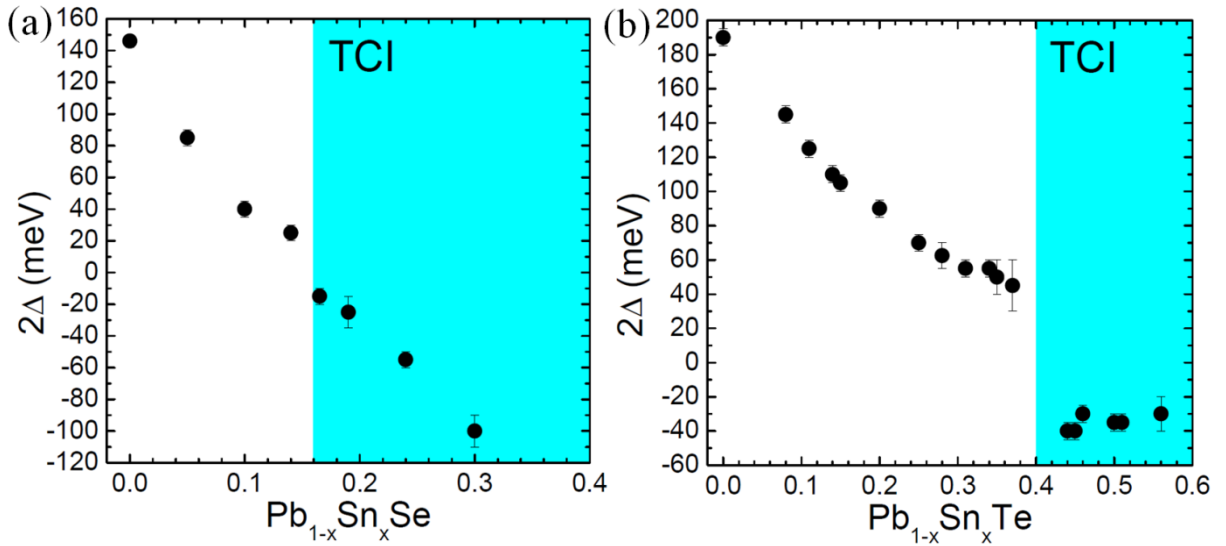


**Figure 4.21. Variation of the band gap of IV-VI topological crystalline insulators across the topological phase transition at 4.5 K.** (a) The band gap  $2\Delta$  of  $\text{Pb}_{1-x}\text{Sn}_x\text{Se}$  ( $0 \leq x \leq 0.30$ ) is plotted as a function of Sn content. The critical composition where the bulk band inversion occurs is  $x_c = 0.16$  at 4.5 K. We have  $\Delta > 0$  for  $x < x_c$  and  $\Delta < 0$  for  $x > x_c$ . A gradual decrease in energy gap is observed through the topological phase transition. (b) The band gap  $2\Delta$  of  $\text{Pb}_{1-x}\text{Sn}_x\text{Te}$  ( $0 \leq x \leq 0.56$ ) is represented versus  $x$ . The band crossing occurs at the critical Sn content  $x_c \approx 0.42 \pm 0.02$  at 4.5 K. We plotted  $\Delta > 0$  for  $x < x_c$  and  $\Delta < 0$  for  $x > x_c$ . The positive gap continuously decreases as  $x$  increases only for  $x < x_c$ , then beyond  $x_c$  the gap changes sign from positive to negative and jumps abruptly without gap closure. Shaded region represents the nontrivial regime.

We have shown in the previous sections that IR magneto-spectroscopy allows us to gain valuable information about the properties of the electronic bulk bands of  $\text{Pb}_{1-x}\text{Sn}_x\text{Se}$  and  $\text{Pb}_{1-x}\text{Sn}_x\text{Te}$  TCIs. Importantly, we are able to measure the sign of the energy gap and the topological index in these Dirac systems. Now, an unexplained issue is raised when we study the variation of the band gap across the topological phase transition. Fig. 4.21 shows the band

## CHAPTER 4

### *Magneto-optical investigation of TCIs: IV-VI compounds*

gap  $2\Delta$  varying as a function of Sn content in  $\text{Pb}_{1-x}\text{Sn}_x\text{Se}$  for  $0 \leq x \leq 0.30$  (Fig. 4.21(a)) and  $\text{Pb}_{1-x}\text{Sn}_x\text{Te}$  for  $0 \leq x \leq 0.56$  (Fig. 4.21(b)). We observe in  $\text{Pb}_{1-x}\text{Sn}_x\text{Se}$  that the gap decreases gradually with increasing  $x$  through the topological phase transition occurring at  $x_c = 0.16$  at 4.5 K. In  $\text{Pb}_{1-x}\text{Sn}_x\text{Te}$ , the inversion of the bulk bands is experimentally observed at  $x_c \approx 0.42 \pm 0.02$  at 4.5 K. The gap decreases continuously as  $x$  increases in the trivial regime  $x < x_c$ , it then changes sign from positive to negative at the critical Sn content  $x_c$  of the topological phase transition and jumps abruptly into the nontrivial regime  $x > x_c$  without gap closure. Our observation is similar to recent ARPES experiments in IV-VI materials measured in the temperature range  $9 \text{ K} \leq T \leq 300 \text{ K}$  that show the anomaly of the zero-gap state of the bulk bands and the discontinuous process of band inversion <sup>29</sup>.

It is commonly assumed that a solid material cannot undergo a topological phase transition without closing its band gap. Consequently, a gapless 3D Dirac state is expected to exist at the critical point between two topologically distinct trivial and nontrivial phases. Our (111)  $\text{Pb}_{1-x}\text{Sn}_x\text{Se}$  samples were shown to exhibit a zero-gap 3D Dirac state owing to the continuous evolution of the band gap through the entire Sn composition range. This matter is found to be completely different in (111)  $\text{Pb}_{1-x}\text{Sn}_x\text{Te}$  samples since the variation of the band gap is discontinuous in the vicinity of the bulk band crossing. Several following hypotheses that could probably describe the dynamics of the topological phase transition in  $\text{Pb}_{1-x}\text{Sn}_x\text{Te}$  will be addressed.

A first explanation for the absence of the band gap closure in  $\text{Pb}_{1-x}\text{Sn}_x\text{Te}$  is the fact that Bi-doping (0.01%-0.2%) was used to compensate the high intrinsic hole carrier concentration from (Pb,Sn) vacancies in  $\text{Pb}_{1-x}\text{Sn}_x\text{Te}$  with high Sn composition ( $x > 0.28$ ) <sup>30</sup>, as shown in Table 4.1. The Bi content could have some disorder impacts on the band gap and could explain the behavior of the gap observed in Fig. 4.21(b) in the vicinity of the phase transition.

A second hypothesis could be related to the alloy disorder of which the effective potential varies as  $x(1-x)$  and becomes very significant around the critical Sn composition  $x_c \approx 0.42$  in  $\text{Pb}_{1-x}\text{Sn}_x\text{Te}$  measured at 4.5 K. Thus, we get  $x_c(1-x_c) \approx 0.24$  for  $\text{Pb}_{1-x}\text{Sn}_x\text{Te}$ . This is not the case for  $\text{Pb}_{1-x}\text{Sn}_x\text{Se}$  where  $x_c(1-x_c) \approx 0.13$ , with  $x_c = 0.16$  at 4.5 K.

Recent theoretical work has demonstrated that the topological phase transition in a TCI family can be argued to be first-order and discontinuous (without closing the gap) <sup>21</sup>. This could also be used to explain our magneto-optical results in  $\text{Pb}_{1-x}\text{Sn}_x\text{Te}$ . The BHZ Hamiltonian model for a 3D TI was treated in order to compute the free energy of the system that has been shown to exhibit a jump between the minima corresponding to the topological phase transition.

Further measurements would be necessary in order to better understand whether the topological phase transition without gap closure in  $\text{Pb}_{1-x}\text{Sn}_x\text{Te}$  is fundamentally discontinuous or caused by disorder (alloy scattering or Bi-doping). For instance, temperature-driven magneto-optical absorption experiments would provide a demonstration of the evolution of the band gap of a nontrivial  $\text{Pb}_{1-x}\text{Sn}_x\text{Te}$  sample at 4.5 K that is expected to become closer to

zero and change sign from negative to positive when the temperature is increased, as demonstrated by F. Teppe et al. in  $\text{Hg}_{1-x}\text{Cd}_x\text{Te}$  crystals<sup>31</sup>.

## 9. Conclusion and perspectives

Magneto-optical absorption measurement in the FIR and MIR ranges allows us to map out the LL spectrum of high-quality (111)-oriented  $\text{Pb}_{1-x}\text{Sn}_x\text{Se}$  ( $0 \leq x \leq 0.30$ ) and  $\text{Pb}_{1-x}\text{Sn}_x\text{Te}$  ( $0 \leq x \leq 0.56$ ) TCIs grown on  $\text{BaF}_2(111)$  substrates by means of MBE. The band parameters such as the absolute value of the band gap, the Dirac velocity and the effective band edge mass in the longitudinal and oblique bulk valleys of all the investigated samples were accurately measured using the massive Dirac fermion model including the far-band contributions to the band edge mass. Our investigation technique, highly sensitive to the bulk states but yet not blind to the surface states, also provides a quantitative assessment of the gapless band structure via the observation of the ground CR transition of the TSS using the massless Dirac fermion model. The observed CR-TSS signature is attributed to the TSS in the  $\bar{\Gamma}$ - and  $\bar{M}$ -Dirac cones in  $\text{Pb}_{1-x}\text{Sn}_x\text{Se}$  samples with  $x > 0.16$ , while it is attributed to the TSS in the  $\bar{\Gamma}$ -Dirac cone in  $\text{Pb}_{1-x}\text{Sn}_x\text{Te}$  samples with  $x > 0.4$ . Further measurements up to high magnetic fields ( $B > 20$  T) would allow us to probe the CR-TSS in the  $\bar{M}$ -Dirac cones in  $\text{Pb}_{1-x}\text{Sn}_x\text{Te}$  ( $x > 0.4$ ) that may be shifted with respect to the  $\bar{\Gamma}$ -Dirac cone and may have Fermi energy lying farther from the  $\bar{M}$  Dirac point. Finally, the electronic band structure of each lead-tin salt sample was established in the vicinity of the band gap.

The magneto-optical band parameters of (111)  $\text{Pb}_{1-x}\text{Sn}_x\text{Se}$  and  $\text{Pb}_{1-x}\text{Sn}_x\text{Te}$  were extracted from the massive Dirac model analysis. By studying the evolution of the absolute value of the band gap  $2|\Delta|$  as a function of  $x$ , we can estimate the critical Sn content  $x_c$  when  $2|\Delta|$  reaches a minimum:  $x_c = 0.16$  for  $\text{Pb}_{1-x}\text{Sn}_x\text{Se}$  and  $x_c \approx 0.42 \pm 0.02$  for  $\text{Pb}_{1-x}\text{Sn}_x\text{Te}$  at 4.5 K. This is relevant to the observation of the CR-TSS related feature in  $\text{Pb}_{1-x}\text{Sn}_x\text{Se}$  for  $x > 0.16$  and in  $\text{Pb}_{1-x}\text{Sn}_x\text{Te}$  for  $x > 0.4$ . The critical velocity  $v_c$  in both the longitudinal and oblique bulk valleys can then be estimated:  $v_c(\text{long.}) = 5 \times 10^5$  m/s and  $v_c(\text{obl.}) = 4.7 \times 10^5$  m/s for  $\text{Pb}_{1-x}\text{Sn}_x\text{Se}$ , and  $v_c(\text{long.}) = 7.4 \times 10^5$  m/s and  $v_c(\text{obl.}) = 5.1 \times 10^5$  m/s for  $\text{Pb}_{1-x}\text{Sn}_x\text{Te}$ . From the variation of the bulk Dirac velocity  $v_D$  as a function of  $x$  in both types of valleys in  $\text{Pb}_{1-x}\text{Sn}_x\text{Se}$  and  $\text{Pb}_{1-x}\text{Sn}_x\text{Te}$ , we can conclude that a material is in the topologically trivial regime when  $v_D > v_c$  and  $x < x_c$ , or is in the topologically nontrivial regime when  $v_D < v_c$  and  $x > x_c$ . We can then experimentally measure the topological index  $\eta$  of a material satisfying the BHZ Hamiltonian from the fundamental relation  $(-1)^\eta = \text{sign}(v_D^2 - v_c^2) = \text{sign}(\Delta/\tilde{m})$ , where  $\tilde{m} > 0$  is the far-band correction to the band edge mass. If  $\eta = 0$  we have  $v_D > v_c$  and  $\Delta > 0$ , the material is said to be trivial and has a positive gap in the normal band structure. If  $\eta = 1$  we get  $v_D < v_c$  and  $\Delta < 0$ , the material is said to be nontrivial and has a negative gap in the inverted band structure. We have shown that our analysis is important and powerful since we are able to directly determine the topological character associated with the topological index of a material via its bulk band parameters. Our approach is argued to be more or less general and is expected to be valid for other systems that can be described by a BHZ Hamiltonian and exhibit a trivial to nontrivial topological phase transition such as tunable 3D TIs

## CHAPTER 4

### *Magneto-optical investigation of TCIs: IV-VI compounds*

$\text{BiTl}(\text{S}_{1-\delta}\text{Se}_\delta)_2$ <sup>32,33</sup> and  $(\text{Bi}_{1-x}\text{In}_x)_2\text{Se}_3$ <sup>34,35</sup>, 3D Dirac semimetals  $\text{Na}_3\text{Bi}$ <sup>36,37</sup> and  $\text{Cd}_3\text{As}_2$ <sup>38,39</sup>, topological Heusler materials<sup>40</sup>, and  $\text{Hg}_{1-x}\text{Cd}_x\text{Te}$ <sup>28</sup> (see the supplementary material for our previous work<sup>11</sup>).

For most (111)  $\text{Pb}_{1-x}\text{Sn}_x\text{Se}$  and  $\text{Pb}_{1-x}\text{Sn}_x\text{Te}$  samples, the Dirac velocity of massive Dirac fermions in the longitudinal valley is larger than that in the oblique valleys due to the anisotropy of 3D Fermi ellipsoids of bulk carriers. We studied this anisotropy in the whole range of Sn composition by calculating the valley anisotropy factor  $K$  for each compound from its bulk velocities in both types of bulk valleys. A decrease of  $K$  with increasing  $x$  is observed in both materials. In  $\text{Pb}_{1-x}\text{Sn}_x\text{Te}$ ,  $K$  ( $\sim 7$ -11) is highly dependent on  $x$ , while  $K$  ( $\leq 2$ ) in  $\text{Pb}_{1-x}\text{Sn}_x\text{Se}$  is much smaller and becomes nearly equal to 1 when  $x \geq 0.24$ , indicating the quasi-isotropy of the ellipsoidal bulk carrier pockets. Subsequently, we studied the evolution of the geometry ( $b/a = \sqrt{K}$ ) of the bulk carrier ellipsoids in  $\text{Pb}_{1-x}\text{Sn}_x\text{Se}$  and  $\text{Pb}_{1-x}\text{Sn}_x\text{Te}$  in the entire Sn content range. In  $\text{Pb}_{1-x}\text{Sn}_x\text{Se}$ , the ellipsoids transform gradually into spheres when  $x$  increases, whereas the bulk carrier pockets in  $\text{Pb}_{1-x}\text{Sn}_x\text{Te}$  remain ellipsoidal. It is worthwhile noting that in the vicinity of the topological phase transition,  $\text{Pb}_{1-x}\text{Sn}_x\text{Se}$  displays a very low valley anisotropy. This makes  $\text{Pb}_{1-x}\text{Sn}_x\text{Se}$  system an ideal test-bed to study the topological phase transition since their conduction and valence bands ( $L_6^\pm$ ) are mirror-like and nearly spherical. Moreover, since these ternary alloys possess low carrier density and high mobility, they deserve great interest in fundamental research and could lead to significant achievements in the application of topological matter.

The systematic study by magneto-optics allows us to better understand the mechanism of the topological phase transition in  $\text{Pb}_{1-x}\text{Sn}_x\text{Se}$  and  $\text{Pb}_{1-x}\text{Sn}_x\text{Te}$ . However, a challenging issue regarding the absence of the band gap closure that gives rise to the discontinuous topological phase transition in  $\text{Pb}_{1-x}\text{Sn}_x\text{Te}$  needs to be addressed. Several arguments have been proposed to explain this phenomenon. Further experiments by varying temperature are required to be done for clarifying whether the unclosed gap is fundamental or results from the disorder (alloy scattering or Bi-doping used to control the carrier concentration).

In this work, we have shown that magneto-spectroscopy allows us to precisely gain the bulk band parameters of 3D tunable (111)  $\text{Pb}_{1-x}\text{Sn}_x\text{Se}$  and  $\text{Pb}_{1-x}\text{Sn}_x\text{Te}$  systems, and these quantities of each compound can then be directly used to determine the topological nature of the system: trivial phase or nontrivial phase relating to the TSS. Nevertheless, the direct observation of the TSS by magneto-optics has always been a topic that requires high-quality samples, accuracy of theoretical models, or experiments up to high magnetic fields ( $B > 17$  T). For some high-quality nontrivial (111)  $\text{Pb}_{1-x}\text{Sn}_x\text{Se}$  and  $\text{Pb}_{1-x}\text{Sn}_x\text{Te}$  samples, the CR-TSS seems to occur at energies within the reststrahlen band of the  $\text{BaF}_2$  substrates (22-55 meV), limiting our observation of the TSS. A next hard but feasible step that could bring us to probe the TSS is the  $\text{BaF}_2$  substrate removal from the epilayers and the deposition of these layers onto substrates such as Si that is not opaque. Additionally, a study of thickness dependence in nontrivial samples, where the CR-TSS is already observed, could also be performed to confirm the surface origin of this transition.

Our magneto-optical findings obtained in (111)  $\text{Pb}_{1-x}\text{Sn}_x\text{Se}$  and  $\text{Pb}_{1-x}\text{Sn}_x\text{Te}$  will pave the way for further magneto-transport studies on these materials as well as magneto-optical absorption measurements on other surfaces such as (001)  $\text{Pb}_{1-x}\text{Sn}_x\text{Se}$  and  $\text{Pb}_{1-x}\text{Sn}_x\text{Te}$  films grown on  $\text{KCl}(001)$  substrates by MBE. The latter could allow us to study how to control over band topology and the TSS by strain imposed by different kinds of substrates.

Besides the TSS occurring in 3D topological matter, it has been known that 2D TIs such as  $\text{HgTe}/\text{CdTe}$  quantum wells provide a platform to study the band topology via the observation of the quantum spin Hall effect stemming from the helical edge states. Inspired by this discovery, single- and multi-quantum well structures of  $\text{Pb}_{1-x}\text{Sn}_x\text{Se}/\text{Pb}_{1-x}\text{Eu}_x\text{Se}$  and  $\text{Pb}_{1-x}\text{Sn}_x\text{Te}/\text{Pb}_{1-x}\text{Eu}_x\text{Te}$  will be realized using MBE and examined by magneto-spectroscopy to study the quantum spin Hall state in 2D TCI quantum wells at higher temperature than that in  $\text{HgTe}/\text{CdTe}$  quantum wells.

## CHAPTER 4

### Magneto-optical investigation of TCIs: IV-VI compounds

---

## References

1. Mitchell, D.L. & Wallis, R. F. Theoretical energy-band parameters for the lead salts. *Phys. Rev.* **151**, 581–595 (1966).
2. Burkhard, H., Bauer, G. & Zawadzki, W. Band-population effects and intraband magneto-optical properties of a many-valley semiconductor: PbTe. *Phys. Rev. B* **19**, 5149–5159 (1979).
3. Bauer, G. in *Narrow Gap Semiconductors Physics and Applications: Proceeding of the International Summer School* (ed. Zawadzki, W.) **133**, 427–446 (Springer Berlin Heidelberg, 1980).
4. Pascher, H., Bauer, G. & Grisar, R. Magneto-optical investigations and four-wave-mixing spectroscopy of PbSe. *Phys. Rev. B* **38**, 3383–3390 (1988).
5. Burkhard, H., Bauer, G. & Zawadzki, W. Magneto-optical properties of semimagnetic lead chalcogenides. *Semicond. Sci. Technol.* **7**, 703–723 (1999).
6. Phuphachong, T. *et al.* Dirac Landau Level Spectroscopy in  $\text{Pb}_{1-x}\text{Sn}_x\text{Se}$  and  $\text{Pb}_{1-x}\text{Sn}_x\text{Te}$  across the Topological Phase Transition: A Review. *Crystals* **7**, 29 (2017).
7. Springholz, G., Ueta, A. Y., Frank, N. & Bauer, G. Spiral growth and threading dislocations for molecular beam epitaxy of PbTe on  $\text{BaF}_2$  (111) studied by scanning tunneling microscopy. *Appl. Phys. Lett.* **69**, 2822–2824 (1996).
8. Springholz, G. in *Molecular Beam Epitaxy* 263–310 (2013). doi:10.1016/B978-0-12-387839-7.00013-0
9. Ueta, A. Y., Springholz, G., Schinagl, F., Marschner, G. & Bauer, G. Doping studies for molecular beam epitaxy of PbTe and  $\text{Pb}_{1-x}\text{Eu}_x\text{Te}$ . *Thin Solid Films* **306**, 320–325 (1997).
10. Assaf, B. A. *et al.* Massive and massless Dirac fermions in  $\text{Pb}_{1-x}\text{Sn}_x\text{Te}$  topological crystalline insulator probed by magneto-optical absorption. *Sci. Rep.* **6**, 20323 (2016).
11. Assaf, B. A. *et al.* Magneto-optical determination of a topological index. *npj Quantum Mater.* **2**, 26 (2017).
12. Polley, C. M. *et al.* Observation of topological crystalline insulator surface states on (111)-oriented  $\text{Pb}_{1-x}\text{Sn}_x\text{Se}$  films. *Phys. Rev. B* **89**, 075317 (2014).
13. Safaei, S., Kacman, P. & Buczko, R. Topological crystalline insulator (Pb,Sn)Te: Surface states and their spin polarization. *Phys. Rev. B* **88**, 045305 (2013).
14. Olver, M. M. *et al.* The observation of the integral quantum Hall effect in  $\text{PbTe}/\text{Pb}_{1-x}\text{Eu}_x\text{Te}$  quantum well structures. *Solid State Commun.* **89**, 693–696 (1994).
15. Chitta, V. A. *et al.* Multivalley transport and the integer quantum Hall effect in a PbTe quantum well. *Phys. Rev. B* **72**, 195326 (2005).
16. Burke, J. R. & Carver, G. P. Magnetophonon and Shubnikov-de Haas oscillations in n-type PbTe epitaxial films. *Phys. Rev. B* **17**, 2719–2727 (1978).
17. Phuphachong, T. *et al.* Magneto-optical evidence of the topological phase transition in (111)- $\text{Pb}_{1-x}\text{Sn}_x\text{Te}$ . in *Proceedings of the International Conference on the Physics of Semiconductors ICPS 2016* (2016).

## CHAPTER 4

### Magneto-optical investigation of TCIs: IV-VI compounds

18. Zhang, H. *et al.* Topological insulators in Bi<sub>2</sub>Se<sub>3</sub>, Bi<sub>2</sub>Te<sub>3</sub> and Sb<sub>2</sub>Te<sub>3</sub> with a single Dirac cone on the surface. *Nat. Phys.* **5**, 438–442 (2009).
19. Liu, C. X. *et al.* Model Hamiltonian for topological insulators. *Phys. Rev. B* **82**, 045122 (2010).
20. Fu, L. Topological crystalline insulators. *Phys. Rev. Lett.* **106**, 106802 (2011).
21. Juricic, V., Abergel, D. S.L. & Balatsky, A. V. First-order quantum phase transition in three-dimensional topological band insulators. *Phys. Rev. B* **95**, 161403(R) (2017).
22. Shen, S.-Q. *Topological Insulators: Dirac Equation in Condensed Matters*. (Springer Science & Business Media, 2013).
23. Bernevig, B. A. & Hughes, T. L. *Topological Insulators and Topological Superconductors*. (Princeton University Press, 2013).
24. Hsieh, T. H. *et al.* Topological crystalline insulators in the SnTe material class. *Nat. Commun.* **3**, 982 (2012).
25. Ando, Y. & Fu, L. Topological Crystalline Insulators and Topological Superconductors: From Concepts to Materials. *Annu. Rev. Condens. Matter Phys.* **6**, 361–381 (2015).
26. Yusheng, H. & Grassie, A. D. C. The electronic band structure of Pb<sub>1-x</sub>Sn<sub>x</sub>Te alloys. III: Implications for the Fermi surface of SnTe. *J. Phys. F Met. Phys.* **15**, 363–376 (1985).
27. Burke, J. R., Houston, B. & Savage, H. T. Anisotropy of the Fermi surface of p-type PbTe. *Phys. Rev. B* **2**, 1977–1988 (1970).
28. Guldner, Y., Rigaux, C., Mycielski, A. & Couder, Y. Magneto-optical Investigation of Hg<sub>1-x</sub>Cd<sub>x</sub>Te Mixed Crystals II. Semiconducting Configuration and Semimetal → Semiconductor Transition. *Phys. Status Solidi* **82**, 149–158 (1977).
29. Wojek, B. M. *et al.* Band inversion and the topological phase transition in (Pb,Sn)Se. *Phys. Rev. B* **90**, 161202(R) (2014).
30. Volobuev, V. V. *et al.* Giant Rashba Splitting in Pb<sub>1-x</sub>Sn<sub>x</sub>Te (111) Topological Crystalline Insulator Films Controlled by Bi Doping in the Bulk. *Adv. Mater.* **29**, 1604185 (2017).
31. Teppe, F. *et al.* Temperature-driven massless Kane fermions in HgCdTe crystals. *Nat. Commun.* **7**, 12576 (2016).
32. Xu, S.-Y. *et al.* Topological Phase Transition and Texture Inversion in a Tunable Topological Insulator. *Science* **332**, 560–564 (2011).
33. Sato, T. *et al.* Unexpected mass acquisition of Dirac fermions at the quantum phase transition of a topological insulator. *Nat. Phys.* **7**, 840–844 (2011).
34. Brahlek, M. *et al.* Topological-metal to band-insulator transition in (Bi<sub>1-x</sub>In<sub>x</sub>)<sub>2</sub>Se<sub>3</sub> thin films. *Phys. Rev. Lett.* **109**, 186403 (2012).
35. Wu, L. *et al.* A sudden collapse in the transport lifetime across the topological phase transition in (Bi<sub>1-x</sub>In<sub>x</sub>)<sub>2</sub>Se<sub>3</sub>. *Nat. Phys.* **9**, 410–414 (2013).
36. Wang, Z. *et al.* Dirac semimetal and topological phase transitions in A<sub>3</sub>Bi (A = Na, K, Rb). *Phys. Rev. B* **85**, 195320 (2012).
37. Pan, H., Wu, M., Liu, Y. & Yang, S. A. Electric control of topological phase transitions in Dirac semimetal thin films. *Sci. Rep.* **5**, 14639 (2015).



## CHAPTER 4

### *Magneto-optical investigation of TCIs: IV-VI compounds*

---

38. Jeon, S. *et al.* Landau quantization and quasiparticle interference in the three-dimensional Dirac semimetal Cd<sub>3</sub>As<sub>2</sub>. *Nat. Mater.* **13**, 851–856 (2014).
39. Yuan, X. *et al.* Direct Observation of Landau Level Resonance and Mass Generation in Dirac Semimetal Cd<sub>3</sub>As<sub>2</sub> Thin Films. *Nano Lett.* **17**, 2211–2219 (2017).
40. Chadov, S. *et al.* Tunable multifunctional topological insulators in ternary Heusler compounds. *Nat. Mater.* **9**, 541–545 (2010).



# Conclusion & outlook

Using magneto-spectroscopy performed with magnetic field up to 17 T at 4.5 K, we have successfully studied the electronic properties of two Dirac materials: graphene and topological crystalline insulators.

High-quality C- and Si-terminated face MEG prepared by means of thermal decomposition of SiC substrates were investigated. The graphene layers of MEG were shown to be electronically disconnected due to the rotational stacking occurring during the heating process of fabrication. Therefore, the graphene sheets of C-face MEG behave as graphene monolayers. The interband and intraband magneto-optical transitions were clearly observed and interpreted using a massless Dirac fermion model analysis. Beside the principal transitions, transitions involving point defects in the graphene lattice were also observed and could be interpreted using a short-range impurity model. Moreover, the existence of bilayer graphene was evidenced in C-face MEG, indicating the stacking faults in the fabrication. Si-face MEG was also examined and shown to exhibit the electronic band structure of trilayer graphene. High mobility and low carrier density make graphene a prototype system to study the Dirac matter. We have also shown that magneto-optical absorption spectroscopy is an efficient investigation technique since it provides an accurate determination of the band parameters of graphene stacks.

High-quality (111)-oriented  $\text{Pb}_{1-x}\text{Sn}_x\text{Se}$  and  $\text{Pb}_{1-x}\text{Sn}_x\text{Te}$  TCIs grown on  $\text{BaF}_2(111)$  substrates using MBE were investigated across the topological phase transition by varying the Sn concentration. Magneto-spectroscopy allows us to accurately extract the bulk band parameters in both systems using the massive Dirac fermion model including the far-band contribution to the band edge mass. Our investigation technique, highly sensitive to the bulk states but yet not blind to the surface states, also provides a quantitative information about the gapless band structure of the topological surface states using the massless Dirac fermion model. The electronic band structure of each IV-VI compound was accurately established.

## CONCLUSION & OUTLOOK

---

The heart of this thesis is the ability to determine experimentally the topological character of  $\text{Pb}_{1-x}\text{Sn}_x\text{Se}$  and  $\text{Pb}_{1-x}\text{Sn}_x\text{Te}$  systems, satisfying the BHZ Hamiltonian, via its bulk band properties. In other words, we have shown that we can experimentally measure the topological index of a TCI system and give the sign to its band gap. A zero topological index implies that the system is in the topologically trivial regime and has a positive gap since the band ordering is normal ( $x < x_c$ ). A nonzero topological index indicates that the system is in the topologically nontrivial regime and has a negative gap as the bands are inverted ( $x > x_c$ ). Our approach can be argued to be more or less general to be applied to other systems that can be described by a BHZ-like Hamiltonian and exhibit a topological phase transition.

The valley anisotropy study in the entire range of Sn composition demonstrates that  $\text{Pb}_{1-x}\text{Sn}_x\text{Se}$  has a very low valley anisotropy in the vicinity of the topological phase transition. The fact that the mirror-like conduction and valence bands of  $\text{Pb}_{1-x}\text{Sn}_x\text{Se}$  alloys are nearly spherical, combined with their high mobility and low carrier concentration, makes  $\text{Pb}_{1-x}\text{Sn}_x\text{Se}$  an ideal system to study the topological phase transition in topological matter.

Once again, we conclude that magneto-spectroscopy is a very powerful investigation technique that not only gives us an accurate information about the bulk band parameters of materials, but also allows us to determine the topological character of materials via the bulk band properties.

The magneto-optical results obtained in (111)  $\text{Pb}_{1-x}\text{Sn}_x\text{Se}$  and  $\text{Pb}_{1-x}\text{Sn}_x\text{Te}$  TCIs provide a solid basis for further studies aimed at manipulating the band topology of topological material such as magneto-transport experiment performed in (111)  $\text{Pb}_{1-x}\text{Sn}_x\text{Se}$  films that will be presented in the Appendix. A complete magneto-optical study of (111)  $\text{Pb}_{1-x}\text{Sn}_x\text{Se}$  and  $\text{Pb}_{1-x}\text{Sn}_x\text{Te}$  by varying temperature would be necessary to confirm the gap closure in the vicinity of the topological phase transition. Moreover, magneto-optical absorption measurements on other surface orientations such as (001)  $\text{Pb}_{1-x}\text{Sn}_x\text{Se}$  and  $\text{Pb}_{1-x}\text{Sn}_x\text{Te}$  epilayers grown on KCl(001) substrates by MBE would also be interesting since this could allow us to study the band topology via the influence of the strain imposed by KCl substrates compared to  $\text{BaF}_2$  substrates. Last but not least, inspired by the QSHE observed in the first 2D TI HgTe/CdTe quantum wells, single- and multi-quantum wells of  $\text{Pb}_{1-x}\text{Sn}_x\text{Se}/\text{Pb}_{1-x}\text{Eu}_x\text{Se}$  and  $\text{Pb}_{1-x}\text{Sn}_x\text{Te}/\text{Pb}_{1-x}\text{Eu}_x\text{Te}$  fabricated using MBE would provide a study of the QSHE in 2D TCI quantum wells at temperature higher than that in HgTe/CdTe quantum wells.

# Appendix

## Negative longitudinal magnetoresistance from anomalous $N = 0$ Landau level in topological material

In this appendix, we present another approach to determine the topological character of quantum materials via their bulk properties. We performed magneto-transport measurement on high-quality (111)  $\text{Pb}_{1-x}\text{Sn}_x\text{Se}$  ( $0 \leq x \leq 0.30$ ) epilayers grown on  $\text{BaF}_2$  substrates using MBE in order to demonstrate the topological phase transition in this system. We observed, in the extreme quantum limit, the negative longitudinal magnetoresistance (NLMR) that only occurs in  $\text{Pb}_{1-x}\text{Sn}_x\text{Se}$  in the nontrivial regime ( $x > 0.16$ ) where the bulk bands are inverted. When the system is in the trivial regime ( $x < 0.16$ ) and has a normal band structure, this NLMR is shown to be positive. The NLMR results from the anomalous behavior of the lowest  $N = 0$  conduction and the highest  $N = 0$  valence Landau levels that disperse respectively down and up in energy as a function of increasing applied magnetic field.

In the following text, we present our recent manuscript entitled “Negative longitudinal magnetoresistance from anomalous  $N = 0$  Landau level in topological materials” and its supplementary material which are under peer review.

# Negative longitudinal magnetoresistance from anomalous $N = 0$ Landau level in topological materials

B. A. Assaf<sup>1</sup>, T. Phuphachong<sup>2</sup>, E. Kampert<sup>3</sup>, V. V. Volobuev<sup>4,5</sup>, P. S. Mandal<sup>6</sup>, J. Sánchez-Barriga<sup>6</sup>, O. Rader<sup>6</sup>, G. Bauer<sup>4</sup>, G. Springholz<sup>4</sup>, L. A. de Vaultier<sup>2</sup>, Y. Guldner<sup>2</sup>

<sup>1</sup> *Département de Physique, Ecole Normale Supérieure, PSL Research University,  
24 rue Lhomond, 75005 Paris, France*

<sup>2</sup> *Laboratoire Pierre Aigrain, Ecole Normale Supérieure, PSL Research University,  
Université Pierre et Marie Curie, Sorbonne Universités, Université Denis Diderot, Sorbonne Cité,  
24 rue Lhomond, 75005 Paris, France*

<sup>3</sup> *Dresden High Magnetic Field Laboratory (HLD-EMFL), Helmholtz-Zentrum Dresden-Rossendorf,  
01328 Dresden, Germany*

<sup>4</sup> *Institut für Halbleiter und Festkörperphysik, Johannes Kepler Universität, Altenberger Straße 69,  
4040 Linz, Austria*

<sup>5</sup> *National Technical University “Kharkiv Polytechnic Institute”, Frunze Str. 21, 61002 Kharkiv, Ukraine*

<sup>6</sup> *Helmholtz-Zentrum Berlin für Materialien und Energie, Albert-Einstein Str. 15, 12489 Berlin, Germany*

**Abstract:** Negative longitudinal magnetoresistance (NLMR) is shown to occur in topological materials in the extreme quantum limit, when a magnetic field is applied parallel to the excitation current. We perform pulsed and DC field measurements on  $\text{Pb}_{1-x}\text{Sn}_x\text{Se}$  epilayers where the topological state can be chemically tuned. The NLMR is observed in the topological state, but is suppressed and becomes positive when the system becomes trivial. In a topological material, the lowest ( $N=0$ ) conduction (valence) Landau disperses down (up) in energy as a function of increasing magnetic field. This is shown to be responsible for the observed NLMR. Our work provides an explanation of the outstanding question of NLMR in topological insulators and establishes this effect as a possible hallmark of bulk conduction in topological matter.

The emergence of topological insulators (TI) as novel quantum materials [1] [2] [3] has played a key role in the discovery of novel physical phenomena, [4] [5] [6] [7] [8] [9] such as the quantum spin Hall effect [4] [10] [11] and quantum anomalous Hall effect [5] [12] [13]. This stems from the helical Dirac nature of surface-states in 3D TIs or, that of edge-states in 2D TIs. In fact, a huge amount of literature (for a review: [14] [15] [16] [17]) took interest in this question and investigated electronic transport of 2D Dirac electrons in 3D-TIs. The majority of these studies were, however, impeded by the fact that bulk transport is usually significant in TIs, and thus dominates in most transport experiments. On the other hand, little attention has been given to signatures of non-trivial band topology in 3D electron transport in a TI.

Naively speaking, one can think of the bulk energy bands of a TI as being identical to those of conventional semiconductors and are, thus, unlikely to generate non-conventional physical phenomena. However, one should not forget that the basis of a topological insulator lies in the inverted orbital character of these bulk energy bands. [10], [18] Most interesting is the unusual

behavior of the Landau levels of TIs that one can analytically extract from a general Bernevig-Hughes-Zhang Hamiltonian (appendix of ref. [18]). In fact, it has been both theoretically [18] [19] [20] and experimentally [21] [22] [23] shown, that the energy of the lowest ( $N=0$ ) conduction (valence) Landau level in topological insulators decreases (increases) as a function of increasing magnetic field, opposite to what usually happens in a topologically trivial system (Fig. 1(a,b)). This behavior is anomalous and leads to a field-induced closure of the energy gap in a TI [21] (Fig. 1(b)), whereas in a trivial material, the energy gap usually opens as a function of magnetic field (Fig. 1(a)). This anomaly is a hallmark of the inverted band structure of topological materials. Its implications on magnetotransport have not yet been considered.

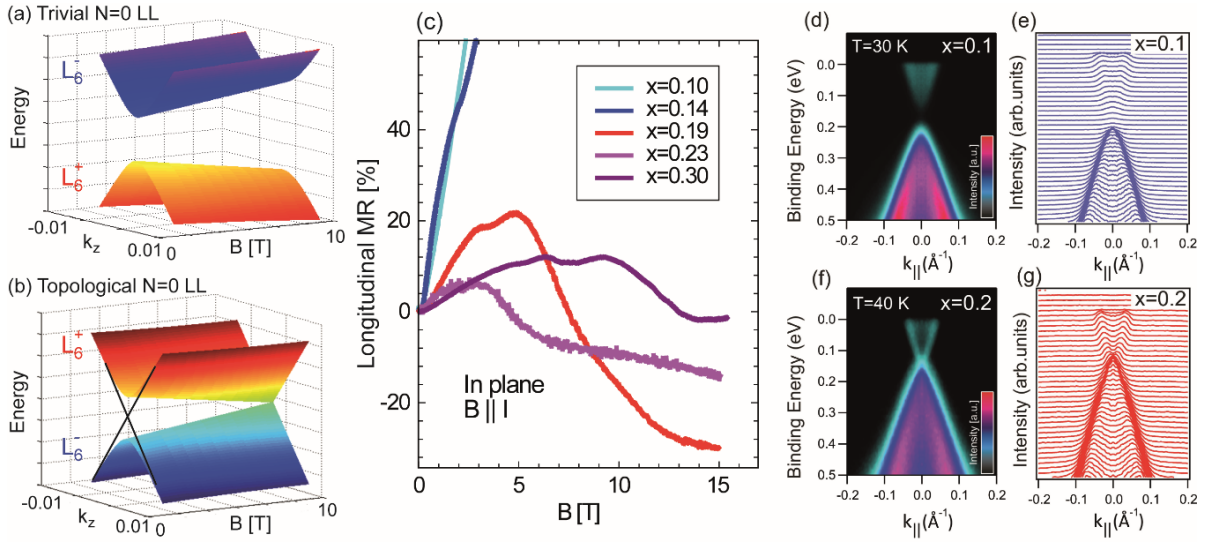


FIG 1. (Color Online) Sketch of the behavior of the  $N=0$  bulk Landau level (LL) as a function of magnetic field for a trivial (a) and a topological (b) system. The  $k$ -dispersion of the energy level in the direction of the applied field is shown ( $k_z$ ). Topological surface states are shown in black in (b) at  $B=0$ . (c) In-plane-MR measured with the magnetic field  $B \parallel I$  at 10K in two trivial  $\text{Pb}_{1-x}\text{Sn}_x\text{Se}$  epilayers ( $x=0.10$  and  $x=0.14$ ) and three topological ones ( $x=0.19$ ,  $x=0.23$  and  $x=0.3$ ) up to  $B=15$ T. ARPES dispersions and momentum distribution curves (MDC) for  $x=0.1$  (d,e) and  $x=0.2$  (f,g) measured with 18eV photons at 30K and 40K, respectively.

In the present work, we study the MR in topological insulators in the extreme quantum limit – the regime where only the lowest Landau level is occupied. We measure magnetotransport in pulsed magnetic field up to 61T in high mobility  $\text{Pb}_{1-x}\text{Sn}_x\text{Se}$  epitaxial layers. We show that, when all Lorentz components contributing to the MR are suppressed by applying the magnetic field in-plane and parallel to the excitation current, a negative longitudinal MR (NLMR) emerges near the onset of the quantum limit. This NLMR is only observed in  $\text{Pb}_{1-x}\text{Sn}_x\text{Se}$  in the topological regime ( $x>0.16$ ) and is absent in trivial samples ( $x<0.16$ ). We theoretically argue that this NLMR is a result of the anomalous behavior of the  $N=0$  Landau levels that leads to a field induced closure of the energy gap as a function of the applied magnetic field, thus enhancing the carriers' Fermi velocity and reducing electrical resistivity. Our findings establish that NLMR is a hallmark of the topological insulating state, and may reconcile controversial interpretations of axial anomaly-induced NLMR in such materials.

## APPENDIX

Magnetotransport measurements are performed on [111] oriented  $\text{Pb}_{1-x}\text{Sn}_x\text{Se}$  epilayers on (111)  $\text{BaF}_2$  substrates with different  $x$ . Growth by molecular beam epitaxy and characterization are described in our previous works [24] [25] [26]. We purposely study low carrier density samples that go into the quantum limit at low fields. A 15T/4.2K superconducting cryostat setup is used for in-house measurements. Further measurements are performed up to 61T using a 200ms pulsed-field coil at the Dresden High Magnetic Fields Lab. These measurements are carried out at 10K. Angle-resolved-photoemission (ARPES) experiments are performed with linearly-polarized undulator radiation at the UE112-PGM1 beamline of the synchrotron BESSY-II in Berlin.

Figure 1(c) shows the longitudinal MR measured at 10K, up to 15T for five  $\text{Pb}_{1-x}\text{Sn}_x\text{Se}$  samples, with the magnetic field applied in-plane parallel to the current ( $I \parallel B \parallel [1-10]$ ). For trivial samples having  $x < 0.16$ , [24] the MR rises fast. In non-trivial samples having  $x > 0.16$ , [24] [27] [28] although initially positive, the MR turns negative, and remains so over a wide field range. This sign of the MR hence depends of the topological character of the sample.

ARPES measurements [Figs. 1(d)-1(g)] for  $x=0.10$  and  $x=0.20$  below 50K clearly indicate the changing topological character for compositions across  $x=0.16$ . A gapped state is observed in the ARPES dispersion and momentum distribution curves (MDCs) for  $x=0.10$  (Figs 1(d,e)) whereas for  $x=0.20$  a gapless topological Dirac surface state is clearly resolved (Fig. 1(f,g)), in agreement with previous ARPES studies. [27] [28]. This ties the occurrence of the NLMR to the topologically non-trivial regime in  $\text{Pb}_{1-x}\text{Sn}_x\text{Se}$ .

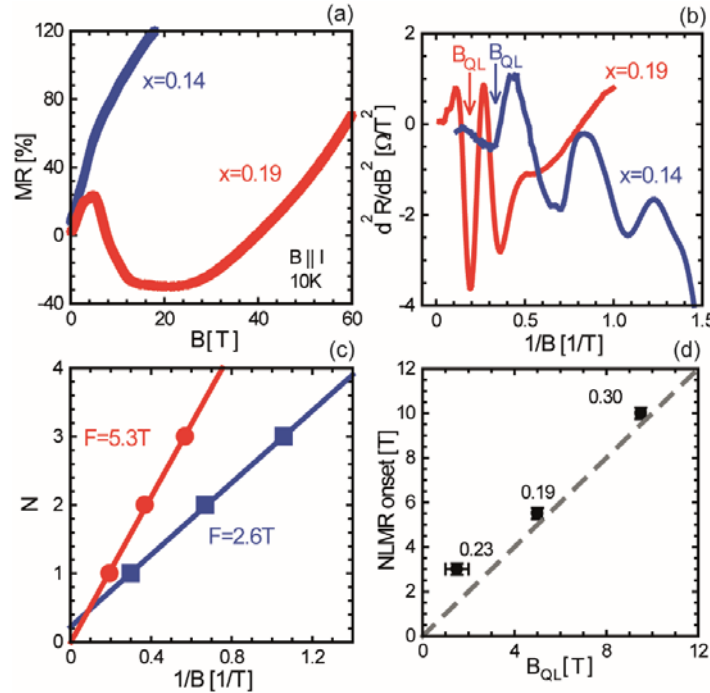


FIG 2. (Color Online). (a) In-plane MR measured up to 60T using pulsed magnetic field for  $\text{Pb}_{1-x}\text{Sn}_x\text{Se}$  with  $x=0.14$  (blue) and  $x=0.19$  (red). (b) Low-field Shubnikov-de-Haas oscillations and (c) Landau index versus  $1/B$

shown for both samples. Arrows mark the field at which the quantum limit is reached ( $B_{QL}$ ). (d) NLMR onset extracted from Fig. 1(c) versus  $B_{QL}$  for the three topological samples considered in this work. The dashed grey line is obtained for an onset exactly equal to  $B_{QL}$ . The Sn concentration 'x' corresponding to each sample is shown above the data points.

In order to confirm the robustness of the MR trend on either side of the topological phase transition, transport measurements for field up to 61T are performed on two selected samples with compositions close to the transition. Results are shown in Fig. 2(a). Comparing the sample  $x=0.14$  to  $x=0.19$  confirms that the MR in the trivial regime is robustly positive up to 60T, whereas in the topological regime, the MR is initially positive, then turns negative reaches a plateau-like behavior at intermediate fields, then increases again at very high fields.

We correlate the appearance of the NLMR to the crossing of the  $N=1$  Landau level with the Fermi level, by looking at 3D Shubnikov-de-Haas oscillations measured in the same geometry as the MR ( $I \parallel B \parallel [1-10]$ ). Fig. 2(b) shows SdH oscillations obtained from the second derivate of the resistance measured for  $x=0.14$  and  $x=0.19$  at 10K. The last oscillation minimum is observed at  $B_{QL} \approx 5T$  ( $0.2T^{-1}$ ) and  $\approx 2.8T$  ( $0.35T^{-1}$ ) for  $x=0.19$  and  $x=0.14$ , respectively; this is the onset of the extreme quantum limit (arrows in Fig.2(b)). The SdH frequency extracted from the plot of the Landau index  $N$  versus  $1/B$  (Fig. 2(c)) comes out close to 5T for  $x=0.19$  and 2.6T for  $x=0.14$ . For  $x=0.19$ , this yields a 3D carrier density of about  $6 \times 10^{16} \text{cm}^{-3}$  per valley or a total carrier density of  $2.4 \times 10^{17} \text{cm}^{-3}$  for the four valleys of  $\text{Pb}_{1-x}\text{Sn}_x\text{Se}$ . This also agrees with the Hall density  $n \approx 3 \times 10^{17} \text{cm}^{-3}$ . [20] For  $x=0.14$ , we find  $2 \times 10^{16} \text{cm}^{-3}$  per valley. [24] The Hall data yields  $p = 1 \times 10^{17} \text{cm}^{-3}$  for four valleys in good agreement with the SdH analysis. We also note that the SdH results nicely agree with our previous magneto-optical measurements on the same samples. [24] Note that even though the two samples studied here in detail have different carrier type, the other samples examined in Fig. 1(c) rule out any possible link between this and the NLMR. [20]

In  $x=0.19$ ,  $B_{QL}$  is close to the onset of the NLMR seen in Fig. 2(a). In  $x=0.14$ , even though  $B_{QL}$  is small, no NLMR is observed up to 60T. We consolidate the relation between the NLMR and the entrance into the quantum limit in the topological state by further investigating the behavior of the Landau levels in two additional samples ( $x=0.23$  and  $x=0.3$ ). Detailed Shubnikov-de-Haas and magneto-optical IR spectroscopy data shown in the supplement allow us to extract  $B_{QL}$  for both. [20] The onset of the NLMR extracted from Fig. 1(c) is plotted versus  $B_{QL}$  for  $x=0.19$ ,  $x=0.23$  and  $x=0.3$  in Fig. 2(d). A clear correlation of the onset of NLMR with increasing  $B_{QL}$  is observed, as indicated by the dashed line, confirming that the NLMR occurs when all electrons occupy the lowest  $N=0$  Landau level.

We next elucidate the origin of the NLMR occurring in topological materials in the quantum limit by investigating transport in the quantum regime. We have shown that the Landau levels in IV-IV TCIs can be well described by a massive Dirac spectrum that includes spin-splitting [24] [29] [30] [31]. At low fields, the spin splitting can be neglected yielding an ideal massive Dirac model identical to one used in ref. [32]. At high fields, when only the  $N=0$  level is occupied, Zeeman terms need to be taken into account.



## APPENDIX

The wavevector dispersion of the  $N=0$  Landau level and its field dependence can be treated in this regime starting from the Mitchell and Wallis Hamiltonian [30] [33] [34] [35]. Here, we highlight, that this Hamiltonian is similar to the Bernevig-Hughes-Zhang Hamiltonian [18] [10] [36] that generally describes topological systems. Our treatment can thus be generalized to any topological system exhibiting an  $N=0$  behavior similar to Fig. 1(b). We can write for the energy eigenvalue of the  $N=0$  Landau level of the conduction band [20]:

$$E_0 = \sqrt{(|\Delta| \pm \hbar\tilde{\omega})^2 + (\hbar v_z k_z)^2} \quad (1)$$

Here, the  $\pm$  sign refers to the trivial and topological regime respectively.  $\Delta$  is the half-band gap,  $k_z$  is wavevector in the  $z$ -direction ( $z//B$ ),  $v_z$  is the Dirac velocity in the  $z$ -direction, and  $\tilde{\omega} = eB/\tilde{m}$ .  $\tilde{m}$  is a mass term resulting from interactions between the band edges, and far-bands located about 1eV above and below the energy-gap in IV-VI semiconductors. [30][31] It also appears on the diagonal of the BHZ Hamiltonian as  $-M_1 k^2 = \frac{\hbar^2 (k_x + k_y)^2}{2\tilde{m}}$ . [10] [36]

In Eq. 1, the  $|\Delta| \pm \hbar\tilde{\omega}$  term describes whether the energy-gap closes (−) or opens (+) as a function of increasing magnetic field. Note that this equation remains valid as long as  $|\Delta| \geq \hbar\tilde{\omega}$ . At very high fields such that  $|\Delta| < \hbar\tilde{\omega}$ , for both the topological and trivial regime, the energy gap opens with increasing field and the  $N=0$  Landau level varies as given in Eq. 1 for the (+) case. [20]

The Landau level energies are plotted versus magnetic in Fig. 3(a,b) for  $x=0.19$  and  $x=0.14$ , respectively, (and in the supplement for  $x=0.23$  and  $x=0.3$ ). The parameters are given in the caption and table I. For  $N=0$ , Eq. (1) is used. In the topological state, the energy gap closes versus  $B$ , then reopens as dictated by eq. (1).

The dependence of the Fermi energy of magnetic field is then extracted using:

$$n_{sdH} = \frac{eB}{4\pi^2\hbar} \sum_N \int f(E_N, k_z) dk_z \quad (2)$$

Here  $n_{sdH}$  is the valley carrier density,  $f(E_N, k_z)$  is a Fermi-Dirac step function,  $E_N$  is the Landau level energy.  $E_f(B)$  is also shown in Fig. 3(a,b) for  $x=0.19$  and  $x=0.14$ . Eq. (2) also allows us to determine  $k_z(B)$  in the quantum limit:

$$k_z(B) = \frac{2\pi^2\hbar n_{sdH}}{eB}, \quad (3)$$

The magnetoconductivity for a 3D electron gas in the quantum limit has recently been treated for the case of short range impurities by Goswami et al. [37] Although ref. [37] has also treated the problem of scattering by long range ionic impurities, we neglect their impact in  $\text{Pb}_{1-x}\text{Sn}_x\text{Se}$  because of its very large dielectric constant ( $>280$ ). [38] [39] In IV-VI systems, the scattering rate from ionic impurities is thus expected to be at least two-orders of magnitude smaller than that of III-V or II-VI narrow gap materials. [37] [40] It is also well known that in  $\text{Pb}_{1-x}\text{Sn}_x\text{Se}$ , doping is essentially caused by atomic vacancies that can be treated as short range (point-like) defects. In this limit, the conductivity is given by [37]:

$$\sigma(B) = \frac{e^2 \hbar}{2\pi m_i U_0} v_f^2(B) \quad (4)$$

Here, in the notation of Goswami et al.  $n_i$  is the impurity density,  $U_0$  is the impurity potential and  $v_f(B)$  is the Fermi velocity as a function of magnetic field.

Using Eq. (1) and (3), it can be shown that [37]:

$$v_f(B) = \frac{\alpha v_z^2}{\sqrt{\left(|\Delta| \pm \frac{\hbar e B}{\tilde{m}}\right)^2 e^2 B^2 + \alpha^2 v_z^2}} \quad (5)$$

$\alpha = 2\pi^2 \hbar^2 n_{sdH}$ . The  $\pm$  sign is for the trivial and topological case respectively. Using this expression for the Fermi velocity and plugging it into Eq. (4), we finally get, the MR in the quantum limit:

$$MR = \frac{\rho(B)}{\rho(0)} - 1 = \frac{\sigma(0)}{\sigma(B)} - 1 \sim \left(|\Delta| \pm \frac{\hbar e B}{\tilde{m}}\right)^2 \frac{e^2 B^2}{\alpha^2 v_z^2} \quad (6)$$

We find,

$$\frac{dMR}{dB} \sim 2 \frac{e^2 B}{\alpha^2 v_z^2} \left(|\Delta| \pm \frac{\hbar e B}{\tilde{m}}\right) \left(|\Delta| \pm 2 \frac{\hbar e B}{\tilde{m}}\right) \quad (7)$$

It is obvious that for  $\Delta \tilde{m} / 2\hbar e < B < \Delta \tilde{m} / \hbar e$  the derivative becomes negative in the topological regime and resistance decreases as a function of magnetic field. Thus, a NLMR occurs in the quantum limit for topological materials.

In order to plot the MR versus B using Eq. (6), a knowledge of  $\Delta$ ,  $v_z$  and  $\tilde{m}$  is required. Note that the valley degeneracy of IV-VI materials, and the valley anisotropy for B||[1-10] also needs to

## APPENDIX

be carefully accounted for at high fields. When  $B \parallel [1-10]$ , the Fermi surface consists of two ellipsoidal valleys having their major axis tilted by  $\theta=90^\circ$ , and two others tilted by  $\theta=35^\circ$  with respect to  $B$ . [21] [20]  $\Delta$  and  $v_z(\theta)$  can be obtained from previous magnetooptical measurements. [24] Based on previous measurements of  $\tilde{m}$ , we can determine  $\tilde{m}(\theta)$ . [21] [24] We finally find  $\tilde{m}(90^\circ) \approx (0.25 \pm 0.03)m_0$  and  $\tilde{m}(35^\circ) \approx (0.20 \pm 0.02)m_0$ . [20]. All parameters are shown in table I. According to previous laser emission measurements, the far-band parameter  $\tilde{m}$  remains approximately constant over the concentration range  $0 < x < 0.28$ . [21]

<b>Pb<sub>1-x</sub>Sn<sub>x</sub>Se</b>	<b>n<sub>SdH</sub> [pervalley]</b>	<b> \Delta  [meV]</b>	<b><math>v_z</math> [<math>10^5</math> m/s] (<math>35^\circ</math>, <math>90^\circ</math>)</b>	<b><math>\tilde{m}/m_0</math> (<math>35^\circ</math>, <math>90^\circ</math>)</b>	<b>B<sub>c</sub> [T] (<math>35^\circ</math>, <math>90^\circ</math>)</b>
x=0.14	$2 \times 10^{16} \text{ cm}^{-3}$	10	5.0, 4.8	$0.20 \pm 0.02$ , $0.25 \pm 0.03$	N/A
x=0.19	$6 \times 10^{16} \text{ cm}^{-3}$	10	4.8, 4.6	$0.20 \pm 0.02$ , $0.25 \pm 0.03$	$17 \pm 2$ , $22 \pm 3$

Table I. Parameters used to compute the MR shown in Fig. 3(d). The carrier density is determined from SdH measurements shown in Fig. 2.  $B_c = \Delta\tilde{m}/\hbar e$  is the field at which the N=0 levels cross.

We compute the variation of the N=0 conduction and valence Landau levels as a function of magnetic field for both valleys for  $x=0.19$  (Fig. 3(c)) using the parameters listed in table I, and calculate the MR using Eq. (6) for both  $x=0.14$  and  $x=0.19$ . In the trivial case for  $x=0.14$ , the MR is positive (Fig. 3(d)), in agreement with the predictions of Goswami et al. for point defects [37] and with our experimental data (Fig. 2(a)). In the topological regime for  $x=0.19$ , the model yields a negative MR, when  $\Delta\tilde{m}/2\hbar e < B < \Delta\tilde{m}/\hbar e$ , for each valley. The simulated MR is plotted in Fig. 3(d). We get a NLMR between 11T and 22T for the  $90^\circ$  valley and between 8.5T and 17T for the  $35^\circ$  valley. Two MR minima are thus expected at 22T and 17T. Experimentally, we observe a wide MR minimum at around  $B_c=20$ T (Fig. 2(a)). The model thus agrees quantitatively with both the sign of the MR and position of the MR minimum. The broadening of the minimum can be explained by the coexistence of the two minima resulting from valley degeneracy [20] and an anticrossing of N=0 Landau levels (dashed line in Fig. 3(c)) near  $B_c$ . [41]

The experimental onset of the NLMR is 5T. The model predicts an onset of about 8.5T. The onset calculated in the model is, however, non-universal and might strongly depend on carrier population of different valleys. [42] Here, for simplicity, a constant carrier population of valleys is assumed, leading to Eq. (3). This is not always the case in IV-VI TCIs thin films grown on BaF<sub>2</sub> since the N=0 Landau levels disperse differently for different valleys and since a slight energy offset between different valleys may occur at low temperatures due to the mismatch of the expansion coefficients of the epilayers and the substrate. This causes a depopulation of one type of valleys and a repopulation of the other. [42] The most populated valley will then dictate the behavior in the quantum limit, however, the carrier density in this valley will no longer be constant resulting in a violation of Eq. (3). The onset of the NLMR will no longer be governed by the condition  $\Delta\tilde{m}/2\hbar e = B$  as inferred from Eq. (6) and will only be governed by the system entering the quantum limit.

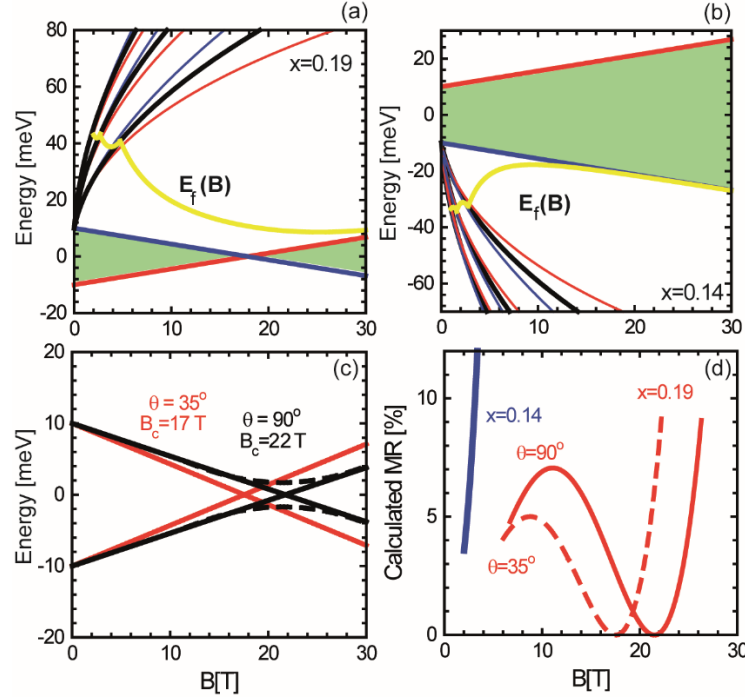


FIG 3. (Color Online). Massive Dirac Landau levels (black) of  $\text{Pb}_{1-x}\text{Sn}_x\text{Se}$  plotted versus magnetic field for  $x=0.19$  (a) and  $x=0.14$  (b) using an energy gap  $2\Delta=20\text{meV}$  and a Dirac velocity  $v_z=4.8\times10^5\text{m/s}$  for  $x=0.19$  and  $5.0\times10^5\text{m/s}$  for  $x=0.14$ . Spin-split Landau levels are plotted in blue and red,  $\tilde{m}=0.20m_0$  is used for both samples. [24] The variation of the Fermi energy  $E_f$  versus magnetic field is shown in yellow. The energy gap is shaded in green. (c)  $N=0$  Landau levels for the conduction and valence bands computed using the parameters in table I. (d) MR calculated using Eq. (6) for parameters shown in table I, for  $x=0.14$  and  $x=0.19$  above quantum limit.

Finally, the magnitude of the simulated MR is smaller than what is observed experimentally. This is due to the rescaling of the MR by  $R(B=0)$ , which in the model is assumed to be given by Eq. (6) at  $B=0$ . Nevertheless, the shape of the NLMR, and its minimum agree very well with our model, without the use of any fit parameters. Most importantly, the model elucidates why the NLMR is observed in topologically non-trivial samples, and absent in trivial ones, and establish a firm basis for further theoretical treatment of this effect.

In conclusion, we have shown that NLMR results from the anomalous behavior of the lowest bulk Landau level of topological materials (Fig. 1), when the system is in the quantum limit. This MR and its anisotropy [20] do not appear to be qualitatively different from what is observed in Dirac and Weyl semimetals. [43] [44] [45] [46] However, its origin is fundamentally different. It is a result of the topologically non-trivial (inverted) nature of bulk bands, the anomalous behavior of the  $N=0$  Landau level and is a direct consequence of the inverted band structure of topological materials. Our results establish that NLMR is a hallmark of the topological insulating state, and can reconcile controversial interpretations of axial anomalous-like [47] [48] NLMR in candidate topological insulators such as,  $\text{ZrTe}_5$ , [23]

## APPENDIX

[34] [49] and possibly  $\text{Pb}_{0.75}\text{Sn}_{0.25}\text{Te}$  under pressure. [50] Our proposed model also clarifies why an NLMR may occur in Dirac and Weyl semimetals under a magnetic field, even if the Fermi energy is high above the Weyl nodes and the chirality is ill-defined. [51] The implications of our work, may even be extended to the quasi-classical regime to explain the occurrence of NLMR in  $\text{Bi}_2\text{Se}_3$ . [52]

**Acknowledgements:** We acknowledge G. Bastard, S. Tchoumakov, and M. Goerbig for useful discussions. This work is supported by Agence Nationale de la Recherche LabEx grant ENS-ICFP (ANR-10-LABX-0010/ANR-10-IDEX-0001-02 PSL) and by the Austrian Science Fund, Project SFB F2504-N17 IRON. TP acknowledges support from Mahidol Wittayanusorn Scholarship and the Franco-Thai Scholarship. We also acknowledge the support of the HLD-HZDR, member of the European Magnetic Field Laboratory (EMFL).

- [1] M. Z. Hasan and C. L. Kane, Rev. Mod. Phys. **82**, 3045 (2010).
- [2] X.-L. Qi and S.-C. Zhang, Rev. Mod. Phys. **83**, 1057 (2011).
- [3] C. L. Kane and E. J. Mele, Phys. Rev. Lett. **95**, 226801 (2005).
- [4] M. König, S. Wiedmann, C. Brune, A. Roth, H. Buhmann, L. W. Molenkamp, X.-L. Qi, and S.-C. Zhang, Science. **318**, 766 (2007).
- [5] C.-Z. Chang, J. Zhang, X. Feng, J. Shen, Z. Zhang, M. Guo, K. Li, Y. Ou, P. Wei, L.-L. Wang, Z.-Q. Ji, Y. Feng, S. Ji, X. Chen, J. Jia, X. Dai, Z. Fang, S.-C. Zhang, K. He, Y. Wang, L. Lu, X.-C. Ma, and Q.-K. Xue, Science. **340**, 167 (2013).
- [6] E. Bocquillon, R. S. Deacon, J. Wiedenmann, P. Leubner, T. M. Klapwijk, C. Brüne, K. Ishibashi, H. Buhmann, and L. W. Molenkamp, Nat. Nanotechnol. **12**, 134 (2016).
- [7] P. Wei, F. Katmis, B. a. Assaf, H. Steinberg, P. Jarillo-Herrero, D. Heiman, and J. S. Moodera, Phys. Rev. Lett. **110**, 186807 (2013).
- [8] A. R. Mellnik, J. S. Lee, a. Richardella, J. L. Grab, P. J. Mintun, M. H. Fischer, a. Vaezi, a. Manchon, E. -a. Kim, N. Samarth, and D. C. Ralph, Nature **511**, 449 (2014).
- [9] B. A. Assaf, F. Katmis, P. Wei, C.-Z. Chang, B. Satpati, J. S. Moodera, and D. Heiman, Phys. Rev. B **91**, 195310 (2015).
- [10] B. A. Bernevig, T. L. Hughes, and S.-C. Zhang, Science. **314**, 1757 (2006).
- [11] I. Knez, R.-R. Du, and G. Sullivan, Phys. Rev. Lett. **107**, 136603 (2011).
- [12] R. Yu, W. Zhang, H.-J. Zhang, S.-C. Zhang, X. Dai, and Z. Fang, Science. **329**, 61 (2010).
- [13] C.-Z. Chang, W. Zhao, D. Y. Kim, H. Zhang, B. A. Assaf, D. Heiman, S.-C. Zhang, C. Liu, M. H. W. Chan, and J. S. Moodera, Nat. Mater. **14**, 473 (2015).
- [14] Y. Ando, J. Phys. Soc. Japan **82**, 102001 (2013).
- [15] M. Veldhorst, M. Snelder, M. Hoek, C. G. Molenaar, D. P. Leusink, A. A. Golubov, H. Hilgenkamp, and A. Brinkman, Phys. Status Solidi - Rapid Res. Lett. **7**, 26 (2013).
- [16] D. Culcer, Phys. E Low-Dimensional Syst. Nanostructures **44**, 860 (2012).
- [17] C.-Z. Chang, P. Wei, and J. S. Moodera, MRS Bull. **39**, 867 (2014).
- [18] B. A. Bernevig and T. L. Hughes, *Topological Insulator and Topological Superconductors* (Princeton University Press, 2013).
- [19] M. Orlita, B. A. Piot, G. Martinez, N. K. S. Kumar, C. Faugeras, M. Potemski, C. Michel, E. M. Hankiewicz, T. Brauner, Č. Drašar, S. Schreyeck, S. Grauer, K. Brunner, C. Gould, C. Brüne, and L. W. Molenkamp, Phys. Rev. Lett. **114**, 186401 (2015).
- [20] Supplementary Material.

- [21] A. Calawa, J. Dimmock, T. Harman, and I. Melngailis, Phys. Rev. Lett. **23**, 7 (1969).
- [22] M. Schultz, U. Merkt, A. Sonntag, U. Rossler, R. Winkler, T. Colin, P. Helgesen, T. Skauli, and S. Lovold, Phys. Rev. B **57**, 14772 (1998).
- [23] Z.-G. Chen, R. Y. Chen, R. D. Zhong, J. Schneeloch, C. Zhang, Y. Huang, F. Qu, R. Yu, Q. Li, G. D. Gu, and N. L. Wang, Proc. Natl. Acad. Sci. **114**, 816 (2017).
- [24] B. A. Assaf, T. Phuphachong, V. V Volobuev, G. Bauer, G. Springholz, L.-A. De Vaultchier, and Y. Guldner, in press, NPJ Quantum Materials. Arxiv 1608.08912.
- [25] G. Springholz and G. Bauer, in *Landolt-Bornstein*, edited by K. Klingsher (Springer Verlag, Berlin, 2013), pp. 415–561.
- [26] G. Springholz, in *Mol. Beam Ep.*, edited by M. Henini (Elsevier, 2013), pp. 263–310.
- [27] B. M. Wojek, P. Dziawa, B. J. Kowalski, A. Szczerbakow, A. M. Black-Schaffer, M. H. Berntsen, T. Balasubramanian, T. Story, and O. Tjernberg, Phys. Rev. B **90**, 161202 (2014).
- [28] P. Dziawa, B. J. Kowalski, K. Dybko, R. Buczko, a Szczerbakow, M. Szot, E. Łusakowska, T. Balasubramanian, B. M. Wojek, M. H. Berntsen, O. Tjernberg, and T. Story, Nat. Mater. **11**, 1023 (2012).
- [29] T. Phuphachong, B. Assaf, V. Volobuev, G. Bauer, G. Springholz, L.-A. de Vaultchier, and Y. Guldner, Crystals **7**, 29 (2017).
- [30] D. L. Mitchell and R. F. Wallis, Phys. Rev. **151**, 581 (1966).
- [31] G. Bauer, in *Narrow Gap Semicond. Phys. Appl. Proceeding Int. Summer Sch.*, edited by W. Zawadzki (Springer Berlin Heidelberg, Berlin, Heidelberg, 1980), pp. 427–446.
- [32] B. A. Assaf, T. Phuphachong, V. V. Volobuev, A. Inhofer, G. Bauer, G. Springholz, L. A. de Vaultchier, and Y. Guldner, Sci. Rep. **6**, 20323 (2016).
- [33] H. Burkhard, G. Bauer, and W. Zawadzki, Phys. Rev. B **19**, 5149 (1979).
- [34] G. Bauer, in *Narrow Gap Semicond. Phys. Appl. Proceeding Int. Summer Sch.*, edited by W. Zawadzki (Springer Berlin Heidelberg, Berlin, Heidelberg, 1980), pp. 427–446.
- [35] J. Dimmock, in *Proc. Int. Conf. Phys. Semimetals Narrow Gap Semicond. 1969, Ed. by D. L. Cart. R. T. Bate* (Pergamon, New York, 1971), p. 319.
- [36] C. X. Liu, X. L. Qi, H. Zhang, X. Dai, Z. Fang, and S. C. Zhang, Phys. Rev. B - Condens. Matter Mater. Phys. **82**, 045122 (2010).
- [37] P. Goswami, J. H. Pixley, and S. Das Sarma, Phys. Rev. B **92**, 075205 (2015).
- [38] H. Preier, Appl. Phys. **20**, 189 (1979).
- [39] E. Burstein, S. Perkowitz, and M. H. Brodsky, Le J. Phys. Colloq. **29**, C4 (1968).
- [40] G. Bastard, *Wave Mechanics Applied to Semiconductor Heterostructures* (Les éditions de physique, Les Ulis, France, 1996).
- [41] G. A. Baraff, Phys. Rev. **137**, A842 (1965).
- [42] J. Oswald, P. Pichler, B. B. Goldberg, and G. Bauer, Phys. Rev. B **49**, 017029 (1994).
- [43] J. Xiong, S. K. Kushwaha, T. Liang, J. W. Krizan, M. Hirschberger, W. Wang, R. J. Cava, and N. P. Ong, Science. **350**, 413 (2015).
- [44] Q. Li, D. E. Kharzeev, C. Zhang, Y. Huang, I. Pletikosić, A. V. Fedorov, R. D. Zhong, J. A. Schneeloch, G. D. Gu, and T. Valla, Nat. Phys. **12**, 550 (2016).
- [45] X. Huang, L. Zhao, Y. Long, P. Wang, D. Chen, Z. Yang, H. Liang, M. Xue, H. Weng, Z. Fang, X. Dai, and G. Chen, Phys. Rev. X **5**, 031023 (2015).
- [46] H.-J. Kim, K.-S. Kim, J.-F. Wang, M. Sasaki, N. Satoh, A. Ohnishi, M. Kitaura, M. Yang, and L. Li, Phys. Rev. Lett. **111**, 246603 (2013).
- [47] D. T. Son and B. Z. Spivak, Phys. Rev. B **88**, 104412 (2013).
- [48] H. B. Nielsen and M. Ninomiya, Phys. Lett. B **130**, 389 (1983).
- [49] G. Manzoni, L. Gragnaniello, G. Autès, T. Kuhn, A. Sterzi, F. Cilento, M. Zacchigna, V.

## APPENDIX

---

- Enenkel, I. Vobornik, L. Barba, F. Bisti, P. Bugnon, A. Magrez, V. N. Strocov, H. Berger, O. V. Yazyev, M. Fonin, F. Parmigiani, and A. Crepaldi, *Phys. Rev. Lett.* **117**, 237601 (2016).
- [50] T. Liang, S. Kushwaha, J. Kim, Q. Gibson, J. Lin, N. Kioussis, R. J. Cava, and N. P. Ong, *Arxiv* 1610.07565 (2016).
- [51] F. Arnold, C. Shekhar, S.-C. Wu, Y. Sun, R. D. dos Reis, N. Kumar, M. Naumann, M. O. Ajeesh, M. Schmidt, A. G. Grushin, J. H. Bardarson, M. Baenitz, D. Sokolov, H. Borrmann, M. Nicklas, C. Felser, E. Hassinger, and B. Yan, *Nat. Commun.* **7**, 11615 (2016).
- [52] S. Wiedmann, A. Jost, B. Fauqué, J. van Dijk, M. J. Meijer, T. Khouri, S. Pezzini, S. Grauer, S. Schreyeck, C. Brüne, H. Buhmann, L. W. Molenkamp, and N. E. Hussey, *Phys. Rev. B* **94**, 081302 (2016).

**Supplementary materials for:**  
**Negative longitudinal magnetoresistance from anomalous**  
**N = 0 Landau level in topological materials**

**S1. N=0 Landau level from Mitchell and Wallis Hamiltonian**

Using the Mitchell and Wallis (1966) formalism, we can write the following matrix Hamiltonian [1] [2]:

$$\begin{array}{cccc}
 c^{1/2}F_n & v^{-1/2}F_{n+1} & c^{-1/2}F_{n+1} & v^{1/2}F_n \\
 c^{1/2}F_n & v^{-1/2}F_{n+1} & c^{-1/2}F_{n+1} & v^{1/2}F_n \\
 v^{-1/2}F_{n+1} & c^{-1/2}F_{n+1} & v^{1/2}F_n & c^{1/2}F_n \\
 v^{1/2}F_n & c^{1/2}F_n & v^{-1/2}F_{n+1} & c^{-1/2}F_{n+1}
 \end{array}
 \begin{bmatrix}
 \Delta + \hbar\tilde{\omega}\left(n + \frac{1}{2}\right) + \frac{1}{2}g\mu_B B & \sqrt{2e\hbar v_c^2(n+1)B} & 0 & \hbar v_z k_z \\
 \sqrt{2e\hbar v_c^2(n+1)B} & -\Delta - \hbar\tilde{\omega}\left(n + \frac{3}{2}\right) + \frac{1}{2}g\mu_B B & \hbar v_z k_z & 0 \\
 0 & \hbar v_z k_z & \Delta + \hbar\tilde{\omega}\left(n + \frac{3}{2}\right) - \frac{1}{2}g\mu_B B & \sqrt{2e\hbar v_c^2(n+1)B} \\
 \hbar v_z k_z & 0 & \sqrt{2e\hbar v_c^2(n+1)B} & -\Delta - \hbar\tilde{\omega}\left(n + \frac{1}{2}\right) - \frac{1}{2}g\mu_B B
 \end{bmatrix}$$

With the following simplifications:

$$\begin{aligned}
 \overline{\omega}_c^l &= -\overline{\omega}_v^l = \tilde{\omega} = \frac{eB}{\tilde{m}} \\
 \overline{g}_c^l &= -\overline{g}_v^l = g
 \end{aligned}$$

The terms are defined in ref. [1].  $v_c$  is the critical Fermi velocity corresponding to each respective valley and  $v_z = \frac{P_z}{m_0}$  is the Fermi velocity in the z-direction (the direction of the applied field), given by the k.p matrix element in the z-direction ( $P_{||}$  is the case of the longitudinal valley).

The lowest Landau level is the N=0 ( $\sigma=-1/2$ ) level. It is obtained by solving the inner block Hamiltonian when  $n = -1$ :

$$\begin{array}{cccc}
 c^{1/2}F_{-1} & v^{-1/2}F_0 & c^{-1/2}F_0 & v^{1/2}F_{-1} \\
 c^{1/2}F_{-1} & v^{-1/2}F_0 & c^{-1/2}F_0 & v^{1/2}F_{-1} \\
 v^{-1/2}F_0 & c^{-1/2}F_0 & v^{1/2}F_{-1} & c^{1/2}F_{-1} \\
 v^{1/2}F_{-1} & c^{1/2}F_{-1} & v^{-1/2}F_0 & c^{-1/2}F_0
 \end{array}
 \begin{bmatrix}
 \Delta - \hbar\tilde{\omega}\left(\frac{1}{2}\right) + \frac{1}{2}g\mu_B B & 0 & 0 & \hbar v_z k_z \\
 0 & -\Delta - \hbar\tilde{\omega}\left(\frac{1}{2}\right) + \frac{1}{2}g\mu_B B & \hbar v_z k_z & 0 \\
 0 & \hbar v_z k_z & \Delta + \hbar\tilde{\omega}\left(\frac{1}{2}\right) - \frac{1}{2}g\mu_B B & 0 \\
 \hbar v_z k_z & 0 & 0 & -\Delta + \hbar\tilde{\omega}\left(\frac{1}{2}\right) - \frac{1}{2}g\mu_B B
 \end{bmatrix}$$



## APPENDIX

The inner block reduces to:

$$\begin{bmatrix} -\Delta - \hbar\tilde{\omega}\left(\frac{1}{2}\right) + \frac{1}{2}g\mu_B B & \hbar v_z k_z \\ \hbar v_z k_z & \Delta + \hbar\tilde{\omega}\left(\frac{1}{2}\right) - \frac{1}{2}g\mu_B B \end{bmatrix}$$

We make an even further simplifying assumption:

$$g\mu_B B \approx -\hbar\tilde{\omega}.$$

This is justified near the band inversion, since it has been shown that in the trivial regime  $|g\mu_B B| \leq |\hbar\tilde{\omega}|$  whereas in the topological regime  $|g\mu_B B| \geq |\hbar\tilde{\omega}|$ . [3]

We can now solve the eigenvalue problem for the  $N=0$  ( $\sigma = -1/2$ ) level:

$$\begin{vmatrix} -\Delta - \hbar\tilde{\omega} - E & \hbar v_z k_z \\ \hbar v_z k_z & \Delta + \hbar\tilde{\omega} - E \end{vmatrix} = 0$$

We get the following equation:

$$(E - \hbar\tilde{\omega} - \Delta)(E + \hbar\tilde{\omega} + \Delta) - (\hbar v_z k_z)^2 = 0$$

The energy eigenvalue to the lowest Landau level now rewritten as  $E_0$  is then given by:

$$E_0 = \pm \sqrt{(\Delta + \hbar\tilde{\omega})^2 + (\hbar v_z k_z)^2}$$

For the following we will only consider the  $N=0$  Landau level of the conduction band with the (+) sign, keeping in mind that that of the valence band is simply given by its opposite. Thus,

$$E_0 = \sqrt{(\Delta + \hbar\tilde{\omega})^2 + (\hbar v_z k_z)^2}$$

When going through the topological phase transition,  $\Delta$  changes sign yielding:

$$E_0 = \sqrt{(\pm \Delta + \hbar\tilde{\omega})^2 + (\hbar v_z k_z)^2}$$

$$E_0 = \sqrt{(|\Delta| \pm \hbar\tilde{\omega})^2 + (\hbar v_z k_z)^2} \quad (+ \text{ for trivial, } - \text{ for topological})$$

### **S2. Far-band mass correction anisotropy**

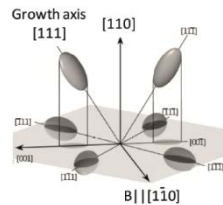


Figure S1. Ellipsoidal Fermi surface of  $\text{Pb}_{1-x}\text{Sn}_x\text{Se}$  at the L-points of the bulk Brillouin zone.

In our previous work on magnetooptical characterization of the band structure of  $\text{Pb}_{1-x}\text{Sn}_x\text{Se}$ , we measured  $\tilde{m} \approx (0.24 \pm 0.03)m_0$  for the oblique valleys in the Faraday geometry ( $\theta=71^\circ$ ). [4] From Calawa et al. we have  $\tilde{m} \approx (0.22)m_0$  for the [001] valleys having ( $\theta=53^\circ$ ). [5] Using these two experimental results and the fact that:

$$\tilde{m}(\theta) \approx m_t \left[ \frac{\sin^2(\theta)m_t}{m_l} + \cos^2(\theta) \right]^{-1/2}$$

We can find the anisotropy ratio for far-band contributions:

$$\frac{m_\ell}{m_t} \approx 1.7 \pm 0.1,$$

and estimate  $m_t \approx (0.19 \pm 0.02)m_0$  and  $m_l \approx (0.32 \pm 0.05)m_0$ . Here  $m_t$  and  $m_l$  are the transverse and longitudinal far-band mass correction terms as defined in ref. 1. We can now compute  $\tilde{m}(\theta)$  for any angle. When  $B \parallel [1-10]$ , it can easily be shown that two oblique valleys (the [1-11] and the [-111] valleys) are tilted by  $35^\circ$  with respect to the field and one longitudinal ([111]) and one oblique valley ([11-1]) are tilted by  $90^\circ$ .

$$\begin{aligned} \tilde{m}(90^\circ) &\approx m_t \left[ \frac{\sin^2(\theta)m_t}{m_l} + \cos^2(\theta) \right]^{-1/2} \approx (0.25 \pm 0.03)m_0 \\ \tilde{m}(35^\circ) &\approx m_t \left[ \frac{\sin^2(\theta)m_t}{m_l} + \cos^2(\theta) \right]^{-1/2} \approx (0.2 \pm 0.02)m_0 \end{aligned}$$

### S3. Hall effect

For DC fields	$n_1$ [cm <sup>-3</sup> ]	$n_2$ [cm <sup>-2</sup> ]	$\mu_1$ [cm <sup>2</sup> /Vs]	$\mu_2$ [cm <sup>2</sup> /Vs]	$\rho_{\text{tot}}$ [Ω.m]
x=0.10	<b>3.0 x 10<sup>17</sup> elec.</b>	7 x 10 <sup>17</sup> holes	<b>50000</b>	1500	4 x 10 <sup>-7</sup>
x=0.14	<b>1.5 x 10<sup>17</sup> holes</b>	6 x 10 <sup>17</sup> holes	<b>60000</b>	1600	4 x 10 <sup>-6</sup>
x=0.19	<b>3.5 x 10<sup>17</sup> elec.</b>	1 x 10 <sup>18</sup> holes	<b>17000</b>	500	1 x 10 <sup>-6</sup>
x=0.23	<b>3 x 10<sup>16</sup> elec.</b>	8 x 10 <sup>17</sup> holes	<b>40000</b>	2000	2 x 10 <sup>-5</sup>
x=0.30	<b>4.5 x 10<sup>17</sup> holes</b>	9 x 10 <sup>17</sup> holes	<b>8500</b>	4500	3 x 10 <sup>-5</sup>

Table S1. Transport parameters determined from the Hall effect using a 2 parameters Drude fit. Note that all samples show two carrier transport. The low mobility channel is either due to a 2D Fermi surface channel or an interfacial layer. The bulk is found to have a low carrier density  $n_1$  and a high mobility  $\mu_1$  in all samples as confirmed by the low field Shubnikov-de-Haas oscillations and by magnetooptical data. [4]

## S4. Quantum oscillations in $x=0.23$ and $x=0.3$

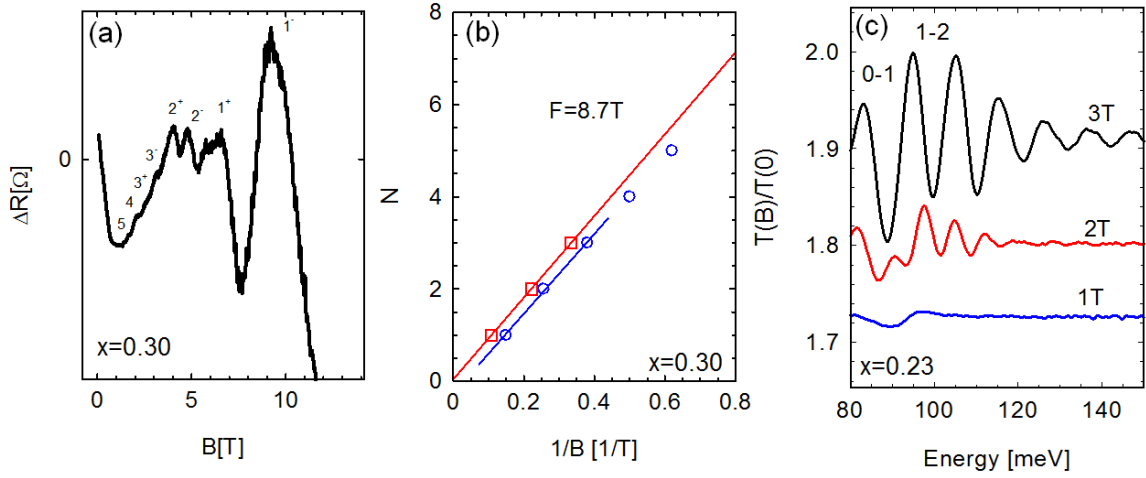


Figure S2. (a) Shubnikov-de-Haas oscillations in  $x=0.3$  at 10K. (b) Landau index versus  $1/B$  extracted from (a). Red and blue indicate series of opposite spin as indexed in (a). (c) Magneto-optical infrared absorption spectra taken between 1T and 3T for  $x=0.23$  at 4.5K. The  $N=0$ - $N=1$  interband transition is already visible and strong in amplitude at 2T.

Shubnikov-de-Haas data shown is Fig. S2(a) for  $x=0.3$ . Spin is taken into account in the plot of  $N$  versus  $1/B$  as shown Fig. S2(b) similarly to ref. [3]. The lowest  $N=1$  Landau level crosses the Fermi energy close to 9T. For  $x=0.23$ , magneto-optical Landau level spectroscopy measurements at low fields are performed. The details of these measurements are shown in ref. [4] The  $N=0$  to  $N=1$  interband Landau level transition is observed at 2T and above indicating that the  $N=1$  Landau level crosses the Fermi energy at 2T.

The Landau level energy for  $Pb_{1-x}Sn_xSe$  derived from the Mitchell and Wallis Hamiltonian for  $N>0$  has been discussed in our previous work [4] [6] as is given by:

$$E_{N>0}^{c,\pm} = \mp \hbar \tilde{\omega} + \sqrt{\Delta^2 + 2v_D^2 \hbar e B N}$$

$$E_{N>0}^{v,\pm} = -E_{N>0}^{c,\pm}$$

$\Delta$  is the half energy gap,  $v_D$  is the Dirac velocity, and  $\tilde{\omega} = eB/\tilde{m}$  as discussed in the main text. When spin splitting is neglected ( $\tilde{\omega} = 0$ ), we recover a classical massive Dirac dispersion. The Landau level dispersion versus  $B$  is plotted for  $x=0.23$  and  $x=0.30$  in Fig. S3.

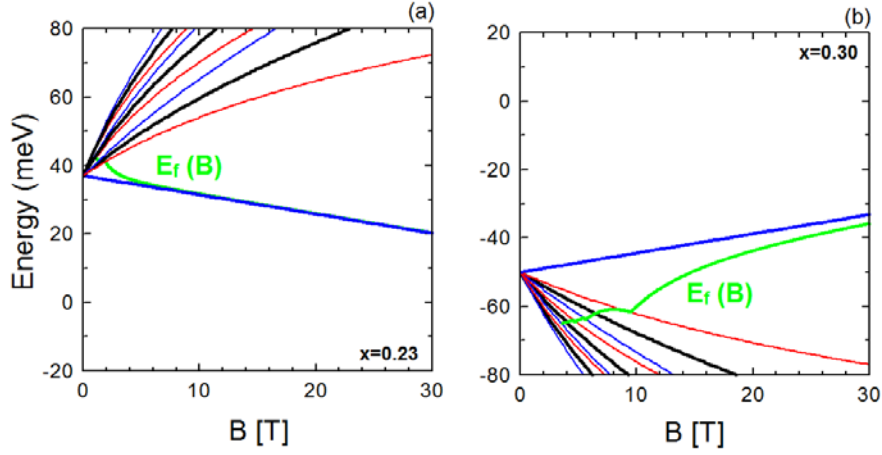


FIG S3. Landau level dispersion versus magnetic field for  $x=0.23$  (a) and  $x=0.3$  (d), with the field dependence of the Fermi energy. Landau levels from an ideal massive Dirac model (black) and a massive Dirac model that includes spin are also shown (red, blue). For  $N>0$ , spin splitting is only relevant and taken into for  $x=0.3$ , it is negligible in other samples at the fields of interest.

### S5. MR anisotropy

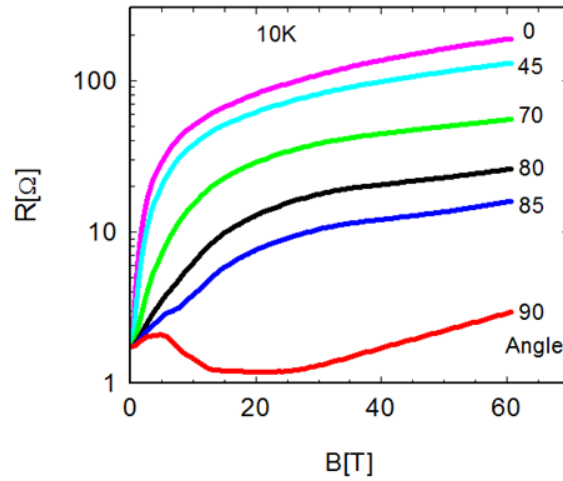


Figure S4. (a) Resistance as a function of magnetic field for different angles  $\theta$ , up to 60T at 10K.  $\theta$  is the angle between the applied field and the normal.  $\theta=0^\circ$  corresponds to an out-of-plane magnetic field, normal to the sample surface. When  $\theta=90^\circ$  the magnetic field is aligned parallel to the current. The MR is highly anisotropic and positive MR is restored as of  $\theta=85^\circ$ .

- [1] D. L. Mitchell and R. F. Wallis, Phys. Rev. **151**, 581 (1966).
- [2] G. Bauer, in *Narrow Gap Semicond. Phys. Appl. Proceeding Int. Summer Sch.*, edited by W. Zawadzki (Springer Berlin Heidelberg, Berlin, Heidelberg, 1980), pp. 427–446.
- [3] J. Melngailis, T. C. Harman, and W. C. Kernan, Phys. Rev. B **5**, 2250 (1972).
- [4] B. A. Assaf, T. Phuphachong, V. V. Volobuev, G. Bauer, G. Springholz, L.-A. De Vaultier, and Y. Guldner, arXiv 1608.08912 (n.d.).
- [5] A. Calawa, J. Dimmock, T. Harman, and I. Melngailis, Phys. Rev. Lett. **23**, 7 (1969).
- [6] T. Phuphachong, B. Assaf, V. Volobuev, G. Bauer, G. Springholz, L.-A. de Vaultier, and Y. Guldner, Crystals **7**, 29 (2017).



---

## Publications and presentations

---

### Publications

- [1] B. A. Assaf, **T. Phuphachong**, E. Kampert, V. V. Volobuev, P. S. Mandal, J. Sánchez-Barriga, O. Rader, G. Bauer, G. Springholz, L. A. de Vaultchier, and Y. Guldner. Negative longitudinal magnetoresistance from the anomalous  $N = 0$  Landau level in topological materials. *Phys. Rev. Lett.* **119**, 106602 (2017).
- [2] B. A. Assaf, **T. Phuphachong**, V. V. Volobuev, G. Bauer, G. Springholz, L. A. de Vaultchier, and Y. Guldner. Magneto-optical determination of a topological index. *npj Quantum Mater.* **2**, 26 (2017).
- [3] S. Massabeau, M. Baillergeau, **T. Phuphachong**, C. Berger, W. A. de Heer, S. Dhillon, J. Tignon, L. A. de Vaultchier, R. Ferreira and J. Mangeney. Evidence of Fermi level pinning at the Dirac point in epitaxial multilayer graphene. *Phys. Rev. B* **95**, 085311 (2017).
- [4] **T. Phuphachong**, B. A. Assaf, V. V. Volobuev, G. Bauer, G. Springholz, L. A. de Vaultchier, and Y. Guldner. Dirac Landau level spectroscopy in  $\text{Pb}_{1-x}\text{Sn}_x\text{Se}$  and  $\text{Pb}_{1-x}\text{Sn}_x\text{Te}$  across the topological phase transition: A review. *Crystals* **7**, 29 (2017).
- [5] **T. Phuphachong**, B. A. Assaf, V. V. Volobuev, G. Bauer, G. Springholz, L. A. de Vaultchier, and Y. Guldner. Magneto-optical evidence of the topological phase transition in (111)- $\text{Pb}_{1-x}\text{Sn}_x\text{Te}$ . *J. Phys. Conf. Ser.* **864**, 012038 (2017).
- [6] B. A. Assaf, **T. Phuphachong**, V. V. Volobuev, A. Inhofer, G. Bauer, G. Springholz, L. A. de Vaultchier, and Y. Guldner. Massive and massless Dirac fermions in  $\text{Pb}_{1-x}\text{Sn}_x\text{Te}$  topological crystalline insulator probed by magneto-optical absorption. *Sci. Rep.* **6**, 20323 (2016).
- [7] M. Hajlaoui, H. Sediri, D. Pierucci, H. Henck, **T. Phuphachong**, M. G. Silly, L. A. de Vaultchier, F. Sirotti, Y. Guldner, R. Belkhou, and A. Ouerghi. High electron mobility in epitaxial trilayer graphene on off-axis SiC(0001). *Sci. Rep.* **6**, 18791 (2016).
- [8] S. Maëro, A. Torche, **T. Phuphachong**, E. Pallecchi, A. Ouerghi, R. Ferreira, L. A. de Vaultchier, and Y. Guldner. Disorder-perturbed Landau levels in high-electron-mobility epitaxial graphene. *Phys. Rev. B* **90**, 195433 (2014).

### **Presentations**

- [1] T. Phuphachong, B. A. Assaf, V. V. Volobuev, G. Bauer, G. Springholz, L. A. de Vaultchier, and Y. Guldner, “*Topological phase transition in  $Pb_{1-x}Sn_xSe$  topological crystalline insulator*”, **The 2<sup>nd</sup> meeting of the NanoTeraMIR GDR**, Paris, France (24-25 November 2016).
- [2] T. Phuphachong, B. A. Assaf, V. V. Volobuev, G. Bauer, G. Springholz, L. A. de Vaultchier, and Y. Guldner, “*Magneto-optical investigation of Dirac fermions in  $Pb_{1-x}Sn_xTe$  topological crystalline insulator*”, **The 33<sup>rd</sup> International Conference on the Physics of Semiconductors (ICPS 2016)**, Beijing, China (31 July - 5 August 2016).
- [3] T. Phuphachong, B. A. Assaf, V. V. Volobuev, G. Bauer, G. Springholz, L. A. de Vaultchier, and Y. Guldner, “*Magneto-optical investigation of Dirac fermions in  $Pb_{1-x}Sn_xTe$  and  $Pb_{1-x}Sn_xSe$  topological crystalline insulators*”, **The 5<sup>th</sup> Thai Student Academic Conference (TSAC 2016)**, Alghero, Italy (11-14 May 2016).
- [4] T. Phuphachong, B. A. Assaf, A. Inhofer, V. V. Volobuev, G. Bauer, G. Springholz, L. A. de Vaultchier, and Y. Guldner, “*Landau levels in topological crystalline insulator  $Pb_{1-x}Sn_xTe$  probed by magneto-optics*”, **La 3<sup>ème</sup> Rencontre des Jeunes Physiciens (RJP)**, Paris, France (10 November 2015).
- [5] T. Phuphachong, B. A. Assaf, A. Inhofer, V. V. Volobuev, G. Bauer, G. Springholz, L. A. de Vaultchier, and Y. Guldner, “*Massive and massless Dirac fermions in  $Pb_{1-x}Sn_xTe$  topological crystalline insulator probed by magneto-optical absorption*”, **Young physicists’ seminar of Laboratoire Pierre Aigrain of Ecole Normale Supérieure**, Paris, France (21 October 2015).
- [6] T. Phuphachong, A. Ouerghi, M. Eddrief, L. A. de Vaultchier, and Y. Guldner, “*Magneto-optical investigation of Dirac fermions in graphene and topological insulators*”, **The 4<sup>th</sup> Thai Student Academic Conference (TSAC 2015)**, Uppsala, Sweden (8-10 May 2015).





